Studies of Higgs Boson Signals Leading to Multi-Photon Final States with The ATLAS Detector

Neil Cooper-Smith

Department of Physics

Royal Holloway, University of London

A thesis submitted to the University of London for the

Degree of Doctor of Philosophy

February 9, 2011

DECLARATION

I confirm that the work presented in this thesis is my own. Where information has been derived from other sources, I confirm that this has been indicated in the document.

Neil Cooper-Smith

Abstract

The efficient identification of photons is a crucial aspect in the search for the Higgs boson at ATLAS. With the high luminosity and collision energies provided by the Large Hadron Collider, rejection of backgrounds to photons is of key importance. It is often not feasible to fully simulate background processes that require large numbers of events, due to processing time and disk space constraints. The standard fast simulation program, ATLFAST-I, is able to simulate events $\sim$1000 times faster than the full simulation program but does not always provide enough detailed information to make accurate background estimates. To bridge the gap, a set of photon reconstruction efficiency parameterisations, for converted and unconverted photons, have been derived from full simulation events and subsequently applied to ATLFAST-I photons. Photon reconstruction efficiencies for isolated photons from fully simulated and ATLFAST-I, plus parameterisations, events are seen to agree within statistical error.

A study into a newly proposed Two Higgs Doublet Model channel, $gg \rightarrow$ H $\rightarrow$ hh $\rightarrow \gamma\gamma\gamma\gamma$, where the light Higgs (h) boson is fermiophobic, has been investigated. The channel is of particular interest as it exploits the large production cross-section of a heavy Higgs (H) boson via gluon-fusion at the LHC in conjunction with the enhanced branching ratio of a light fermiophobic Higgs (h) boson to a pair of photons. This channel is characterised by a distinct signature of four high p_T photons in the final state. Samples of signal events have been generated across the $(\mathrm{m_h}, \mathrm{m_H})$ parameter space along with the dominant backgrounds. An event selection has been developed with the search performed at generator-level. In addition, the search was also performed with simulated ATLFAST-I events utilising the above photon reconstruction efficiency parameterisations. For both analyses, the expected upper limit on the cross-section at 95% confidence level is determined and exclusion regions of the $(\mathrm{m_h}, \mathrm{m_H})$ parameter space are defined for integrated luminosities of 1 fb^{-1} and 10 fb^{-1} in seven fermiophobic model benchmarks.

Acknowledgements

There are a large number of people without whom this thesis would never have been possible. Firstly I'd like to thank my supervisor Pedro Teixeira-Dias for his tireless support and understanding. Without a supervisor as knowledgeable and approachable as you I might not have made it this far. I would also like to thank Rui Santos for all his input and work, especially at the eleventh hour. Additionally, I'd like to thank all the past and present post-doctorates and academics in the Royal Holloway particle physics department who have helped me through many of the technical problems I encountered over these last four years.

Probably the greatest thanks must go to my family and friends. Without their support and encouragement over the years I might not have pursued a Doctorate, let alone a physics one. To my family: thank you for looking after me all those evenings I've spent at home whilst doing this PhD, especially the last month or so. Your love and support never gets taken for granted. To my fellow PhD colleagues at Royal Holloway, Matt and Max: thank you guys so much for all the good times we've enjoyed both at CERN and at Holloway. It was a pleasure to have spent so much time in your company.

Finally, but by no means least I want to thank my, now wife, Lisa. She has provided a constant source of support and guidance throughout my PhD and unselfishly agreed for me to extend my stay abroad. The best things that have happened in my life over these past four years have all involved Lisa and I know this will continue to be the case for many more years to come. Thank you.

This work was funded by the Science and Technology Facilities Council and undertaken at Royal Holloway, University of London.

To Lisa,

For all that time we spent apart,

the one thing that kept me going was

knowing that you'd be there when I came home.

Words cannot express how much I love you.

With each day that I get to spend with you,

I am reminded of how lucky I am to call you my wife.

This is for you, with all my love.

p.s. I'm not a student anymore!!!!!!

Contents

Preface

In March 2010, the Large Hadron Collider (LHC) started colliding beams at a centre-of mass of 7 TeV. This point marked the beginning of a new era in high-energy physics, which may potentially result in the ending of the long running search for the elusive Higgs boson. As one of the four main LHC experiments, the ATLAS detector has been designed to capture a broad range of physics signatures. Not only will the detector be able to make precision measurements of the electroweak parameters but it will also be able to detect the tell-tale signs of new physics beyond the Standard Model.

One of the potential signatures of a Higgs boson is its decay to a pair of photons. This signature is particularly attractive as photons passing through the detector leave identifiable energy deposits in the calorimeter system. Therefore, the ATLAS detector must be able to identify and reconstruct photons with high efficiency whilst at the same time be able to reject the background to them arising from electromagnetic components of hadronic jets.

This thesis will present the parameterisation of the photon reconstruction efficiency and its subsequent inclusion into the ATLAS fast simulation package, ATLFAST-I. Additionally, the analysis of a new Two Higgs Doublet Model channel, where a signature of four isolated photons is expected, will be presented at both generator-level and detector-level. This thesis is arranged into the following chapters:

- Chapter 1 provides an overview of the Standard Model of particle physics, and in particular the motivation for, and inclusion of, the Higgs mechanism into the theory.

- Chapter 2 will then describe the theoretical models which contain the simplest natural extension of the Higgs sector of the Standard Model. In these models, known as Two Higgs Doublet Models, a phenomenon called fermiophobia can arise where the coupling between the light Higgs boson and fermions vanishes. The phenomenology of a newly proposed fermiophobic Higgs channel with a characteristic final state of four isolated photons will then be explored. This channel is of particular interest as it has a potentially large signal cross-section at the LHC. Finally, seven fermiophobic model benchmarks have been defined and regions of allowed

parameter space will be shown. The analysis of this channel and the results for the seven benchmarks will be detailed in Chapter 7.

- Chapter 3 presents an overview of the ATLAS detector. Particular attention will be paid to the calorimetry and tracking system which are responsible for reconstructing and identifying photons from Higgs decays.

- Chapter 4 introduces the Monte Carlo and detector simulation methods used at ATLAS. In particular, this Chapter describes the Monte-Carlo event generators, used later in this thesis, and also the ATLAS fast detector simulation package, ATLFAST-I.

- Chapter 5 provides the reader with an overview of how photons are reconstructed within the ATLAS detector. The use of tracking and calorimeter information in recovering converted photons and the rejection of jets is also detailed. This chapter provides the final piece of introductory material needed before discussion of the author's own work can begin.

- Chapter 6 presents a new set of photon reconstruction efficiency parameterisations for the ATLAS fast simulation package, ATLFAST-I. It will be demonstrated that to create an effective set of parameterisations, converted and unconverted photons must be treated separately. Photon reconstruction efficiencies will be extracted from full simulation events and applied to ATLFAST-I photons to give realistic estimates of the reconstruction efficiency in the fast simulation.

- Chapter 7 details the search for a light fermiophobic Higgs boson in a new Two Higgs Doublet Model channel, described in Chapter 2. The main focus will be on a generator-level analysis of the new channel. Event samples of signals, with varying values of the light and heavy Higgs boson masses in the allowed search range, have been generated along with the identified backgrounds to the signal. An event selection will then be defined that has been designed to separate any signal, in the allowed search range, from the background. Results will be presented in terms of the upper limit on the signal cross-section at 95% confidence level and regions of exclusion will be shown in the seven benchmarks for integrated luminosities of $1\ fb^{-1}$ and $10\ fb^{-1}$. Finally, in addition to the generator-level analysis, the analysis has been repeated including detector effects, simulated with the ATLAS fast simulation package, ATLFAST-I. Here, photons from ATLFAST-I will have the photon reconstruction efficiency parameterisations, described in Chapter 6, applied to them to give a realistic estimation of the ATLAS detector's ability to reconstruct and identify photons. Results from the fast simulation analysis will then be compared to those from the generator-level analysis.

Chapters 6 and 7 represent the author's original work. The only exception is in Section 7.4.1 where the 95% confidence level upper limit on the signal cross-section is calculated using an existing external C++ coding of the CLs method [1, 2]. All the figures shown in these chapters were produced by the author.

Chapter 1

The Standard Model and The Higgs Boson

Particle physics can be viewed simply as the study of matter and energy. It attempts to explain and describe the elemental building blocks of nature and the forces that act between them. Currently, four fundamental forces are known: gravity, the electromagnetic force, the weak nuclear force and the strong nuclear force. Einstein's General Relativity theory [3] explains the gravitational force by the use of field equations relating the four-momenta of particles to the curvature of space-time. Whilst General Relativity has proven to be remarkably successful at describing gravity on a cosmological scale, it is still unclear as to how it can be reconciled with quantum physics. In the absence of gravity, quantum field theory (QFT) combines special relativity, quantum mechanics and classical field theory to describe the three other fundamental forces in a single framework known as The Standard Model (SM) [4, 5].

Despite the great success of the Standard Model in describing observed particles and phenomena, intrinsic problems exist, most notably the absence of the predicted Higgs boson which has so far eluded discovery. These problems motivate the extension of the Standard Model, which in the case of Two-Higgs Doublet Models (2HDMs), to name an example, predicts the existence of five Higgs bosons in contrast to the one Higgs boson of the SM. With the LHC now in operation it should only be a matter of time before many of the proposed extensions and indeed the presence of the elusive SM Higgs boson are either proven or excluded.

This chapter aims to provide the reader with an overview of the Standard Model. A more comprehensive description can be found in [4, 5].

1.1 The Standard Model

The Standard Model categorises fundamental particles according to their spins. Particles with half integer spins ($s = \frac{1}{2}, \frac{3}{2}$, etc.) obeying Fermi-Dirac statistics are called fermions whilst particles with integer spins ($s = 0, 1$, etc) obeying Bose-Einstein statistics are called bosons.

Fermions are the foundation for all matter and are sub-divided into two groups: *quarks*, which interact via the electromagnetic, weak and strong forces; and *leptons*, which only interact via the electromagnetic and weak forces. Each group contains six particles which are organised into three generations according to their properties. Figure 1.1 details the sub-division in the fermion sector, indicating the mass and charge of the twelve particles (twenty-four including anti-particles). Leptons

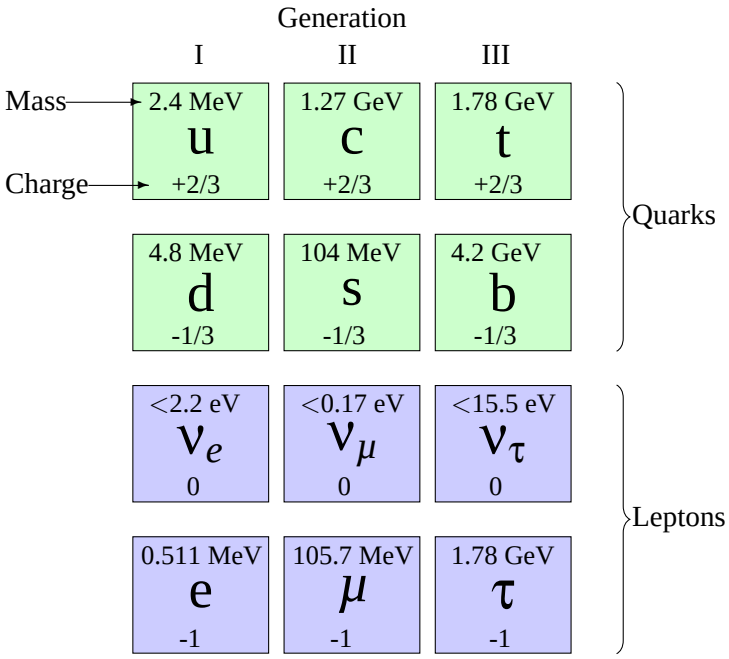

Figure 1.1: *Organisation of the fermion sector. Cells in green represent the quarks and in blue represent the leptons. Average measured mass is indicated for all fermions along with the charge, in units of qe.*

carry unit electric charge and can exist in a free state whereas quarks carry a fractional charge. In addition to the electrical charge, quarks (anti-quarks) also carry a quantum number known as *colour*, which has three states: *red*(*anti-red*); *green*(*anti-green*); and *blue*(*anti-blue*). Due to a phenomenon known as confinement, no quark can exist freely and must instead form integer-charged composite particles with neutral colour. These composite particles are called *hadrons* and come in two forms: *mesons*, containing quark-anitquark pairs; and *baryons*, containing three quarks. Colour also allows for states to exist that apparently violate the Pauli-Exclusion principle, e.g. $\Delta^{--}(ddd)$, where each

d-quark has a different colour.

As a note, two weaknesses of the Standard Model can be seen in the fermion sector. Firstly, large differences in mass between the families cannot be explained by the SM and secondly, neutrinos which are assumed to be massless in the SM have been shown to have non-zero mass [6, 7, 8].

Vector bosons are responsible for propagating the fundamental forces between fermions and in the Standard Model are split into three groups: electromagnetic force carrier (photon); weak force carriers ($W^{\pm}$, Z^0); and strong force carriers (gluons). Table 1.1 details the bosons associated with the three forces along with their respective masses and charges. Particles interact with each other via the

Interaction	**Particle**	**Mass [** GeV/c^2**]**	**Charge [q***e***]**
Electromagnetic	γ	0	0
Weak	$W^{\pm}$	80.4	± 1
	Z^0	91.2	0
Strong	g	0	0

Table 1.1: *Vector bosons in the Standard Model with their electric charges and masses.*

exchange of virtual[1] vector boson. The exchange of virtual photons between any electrically charged particles gives rise to the electromagnetic force. The strength of the interaction is proportional to the electrical charge of the particle and due to the zero mass of the photon, the force is felt at infinite range. The weak force arises from the exchanging of $W^{\pm}$ and Z^0 bosons and is felt by quarks and leptons. The weak force, due to the heavy mass of the mediating bosons, is relatively weak compared to the electromagnetic and strong forces and therefore is only felt over short ranges. Finally, the strong force arises from the exchange of gluons. There are eight types of gluon all of which are massless and carry colour-anti-colour, e.g. red-antiblue. As they carry colour, gluons can interact not only with quarks but also with themselves. Whilst the gluon is massless, like the photon, the strong force is not infinite in range. This is due to the self interactions of gluons which cause the force to increase as the distance between them grows.

The presence of another scalar boson, the Higgs boson, is predicted by the Standard Model but as of yet it has not been observed experimentally. The SM Higgs boson is associated with the Higgs field, which is introduced to give mass to the elementary particles. A more comprehensive description of the Higgs mechanism is given in Section 1.1.6.

[1] A *virtual* particle is one that is undetectable in the conventional sense and momentarily breaks the $E^2 = p^2 + m^2$ relationship.

The following sections detail the formalisation of the Standard Model as a local gauge theory.

1.1.1 The Lagrangian

The Lagrangian of a conserved energy system is defined as:

$$L = T - V \tag{1.1}$$

where T is the kinetic energy and V is the scalar potential energy. In classical mechanics, where the Lagrangian is a function of the coordinates q_i ($i = 1, ..., n$ where n is the number of dimensions) and their time derivatives $\dot{q}_i$, the equations of motion are specified by the Euler-Lagrange equation:

$$\frac{d}{dt}\left(\frac{\partial L}{\partial \dot{q}_i}\right) - \frac{\partial L}{\partial q_i} = 0 \tag{1.2}$$

In field theories, particles are not treated as localised entities but instead are treated as fields. This motivates the change from a discrete system with coordinates $q_i(t)$ to a continuous system with a field $\phi(\vec{x}, t)$. The Lagrangian is now replaced by a Lagrangian density (also often referred to as the Lagrangian):

$$L(q_i, \dot{q}_i, t) \rightarrow \mathcal{L}(\phi, \partial_\mu \phi, x_\mu) \tag{1.3}$$

where $\partial_\mu = \frac{\partial}{\partial x_\mu}$ and ϕ is a function of the continuous variable x_μ. In the classical form of the Euler-Lagrange equation, the left hand side is only a derivative of time. In a relativistic theory, space and time coordinates must be treated equally. Thus the Euler-Lagrange equation becomes:

$$\frac{\partial}{\partial x_\mu}\left(\frac{\partial \mathcal{L}}{\partial(\partial_\mu \phi)}\right) - \frac{\partial \mathcal{L}}{\partial \phi} = 0 \tag{1.4}$$

For example, consider the Lagrangian for a Dirac spinor ($s = \frac{1}{2}$) field, ψ:

$$\mathcal{L}_{Dirac} = \bar{\psi}(i\gamma^\mu \partial_\mu - m)\psi \tag{1.5}$$

Treating ψ and the adjoint spinor $\bar{\psi}$ as independent variables, the application of the Euler-Lagrange Equation, 1.4, results in, for $\bar{\psi}$:

$$i\gamma^\mu \partial_\mu \psi - m\psi = 0 \tag{1.6}$$

and for ψ:

$$i\partial_\mu \bar{\psi}\gamma^\mu + m\bar{\psi} = 0 \tag{1.7}$$

Equation 1.6 is the Dirac equation describing a fermion of mass, m, whilst Equation 1.7 is the adjoint of the Dirac equation.

1.1.2 Gauge Theories and Invariance

Gauge theories are defined as field theories which have the distinct property that physical observables remain unchanged by a defined transformation of the fields. Formally, this property is known as *gauge invariance* or *gauge symmetry*. Two distinct forms of invariance exist: *global invariance* where physical observables remain unchanged by a single transformation applied uniformly over all space-time points and *local invariance* where physical observables remain unchanged by a transformation that is a function of space-time, meaning that different transformations are applied at individual space-time points. In general, a theory that is globally gauge invariant is not locally invariant. However, by the introduction of new fields that transform in a specific way local invariance can be restored.

The principle of local gauge invariance dates back to 1918 with Hermann Weyl [9]. It was proposed that global invariance must hold locally under a phase transformation generated by a unitary 1×1 matrix. This type of local gauge invariance is referred to as U(1) symmetry, where the symmetry group U(1) represents all 1×1 unitary matrices. This principle of local gauge invariance under U(1) transformations forms the basis for Quantum Electrodynamics (QED). The principle of local gauge invariance, however, was not extended to other symmetry groups until 1957 when Yang and Mills [10] extended it to SU(2) to describe the weak force, and later to SU(3), producing Quantum Chromodynamics (QCD).

1.1.3 Quantum Electrodynamics

In the context of the Standard Model, gauge invariance is determined by the requirement that the Lagrangian must be invariant under phase transformations. For example, consider the global phase transformation, $U(\alpha) = e^{i\alpha}$ which forms the unitary abelian[2] group, $U(1)$. Under the transformation:

$$\psi \rightarrow \psi' = U(\alpha)\psi = e^{iq\alpha}\psi \tag{1.8}$$

where α is any real number, the Dirac Lagrangian, $\mathcal{L}_{Dirac} = \bar{\psi}(i\gamma^\mu\partial_\mu - m)\psi$ is invariant, since it follows that the adjoint spinor transforms as $\bar{\psi} \rightarrow \bar{\psi}' = e^{-iq\alpha}\bar{\psi}$. This form of invariance is global as α is independent of the coordinates. To test if the Dirac Lagrangian is invariant under local phase

[2] An abelian group is one in which the result of the group operation is unchanged by the order in which it acts on two elements. For $U(1)$ this means $U(\alpha)U(\beta) = U(\beta)U(\alpha)$.

transformations, α becomes a function of x^μ, such that:

$$\psi(x) \rightarrow \psi(x)' = e^{iq\alpha(x)}\psi(x) \tag{1.9}$$

Clearly, the Lagrangian is no longer invariant under this transformation since an extra term arises from the derivative of $\alpha(x)$:

$$\partial_\mu\psi(x)' = \partial_\mu(e^{iq\alpha(x)}\psi(x)) = iq(\partial_\mu\alpha(x))e^{i\alpha(x)}\psi(x) + e^{iq\alpha(x)}\partial_\mu\psi(x) \tag{1.10}$$

leading to the Lagrangian:

$$\mathcal{L}_{Dirac} \rightarrow \mathcal{L}_{Dirac} - (q\bar{\psi}\gamma^\mu\psi)\partial_\mu\alpha(x) \tag{1.11}$$

Therefore to eliminate this extra term in the Lagrangian and thus make the Lagrangian locally invariant something must be added to cancel it out. Hence, a new spin-1 field is introduced which transforms as:

$$A_\mu(x) \rightarrow A'_\mu(x) = A_\mu(x) - \partial_\mu\alpha(x) \tag{1.12}$$

Additionally the covariant derivative is defined as:

$$D_\mu = \partial_\mu + iqA_\mu(x) \tag{1.13}$$

which has the property that it transforms like the field itself:

$$D_\mu \rightarrow D'_\mu = e^{iq\alpha(x)}D_\mu \tag{1.14}$$

If the covariant derivative is substituted into the Dirac Lagrangian then the gauge transform of $A_\mu(x)$ will cancel out the extra term in Equation 1.11. The new covariant form of the Dirac Lagrangian reads:

$$\mathcal{L}_{covDirac} = \bar{\psi}\,(i\gamma^\mu D_\mu - m)\,\psi = \mathcal{L}_{Dirac} - q\bar{\psi}\gamma^\mu\psi A_\mu \tag{1.15}$$

where it is seen that a new term has been gained which can be interpreted as an interaction between the fermion field, ψ, and a new vector spin-1 field, A_μ. However, for A_μ to be associated with the photon, a gauge invariant Lagrangian term describing a propagating vector spin-1 field must be added to the new Lagrangian. The Proca Lagrangian describing such a field is:

$$\mathcal{L}_{Proca} = -\frac{1}{4}F_{\mu\nu}F^{\mu\nu} + \frac{1}{2}m_A^2A^\mu A_\mu \tag{1.16}$$

where $F^{\mu\nu} = \partial^\mu A^\nu - \partial^\nu A^\mu$ is the electro-magnetic tensor. This Lagrangian however must also be gauge invariant. Whilst the first term is invariant under the transform in Equation 1.12, the second term is not, since:

$$\frac{1}{2}m_A^2 A^\mu A_\mu \rightarrow \frac{1}{2}m_A^2 \left(A^\mu + \partial^\mu \alpha\right)\left(A_\mu + \partial_\mu \alpha\right) \neq \frac{1}{2}m_A^2 A^\mu A_\mu \tag{1.17}$$

Initially, this may appear to be problematic but it is resolved by the realisation that the $A_\mu(x)$ field is identified as the photon. The only solution is to set $m_A = 0$, which is in agreement with the observation that the photon is massless. Therefore, the second term in the Proca Lagrangian vanishes and the Lagrangian reduces to one that describes a massless vector spin-1 field, known as the Maxwell Lagrangian:

$$\mathcal{L}_{Max} = -\frac{1}{4}F_{\mu\nu}F^{\mu\nu} \tag{1.18}$$

Finally, the Lagrangian describing QED can be formed:

$$\begin{aligned} \mathcal{L}_{QED} &= \mathcal{L}_{covDirac} + \mathcal{L}_{Max} \\ &= \bar{\psi}\left(i\gamma^\mu \partial_\mu - m\right)\psi - q\bar{\psi}\gamma^\mu \psi A_\mu - \frac{1}{4}F_{\mu\nu}F^{\mu\nu} \end{aligned} \tag{1.19}$$

From this Lagrangian the form of interactions allowed in QED can be seen in the term: $q\bar{\psi}\gamma^\mu\psi A_\mu$. This term describes the interaction between a massless vector spin-1 field, the photon, with a fermion. The strength of the interaction is characterised by q which, in the case that the fermion is an electron, is $q = e$.

1.1.4 Quantum Chromodynamics

Quantum Chromodynamics (QCD) is a gauge theory characterising the strong force. It describes the interactions between particles that carry colour, namely quarks and gluons. QCD is based on the same concepts as QED but the requirement of U(1) gauge symmetry for QED is replaced with the requirement that QCD must be invariant under SU(3) phase transformations.

SU(3) is a subset of U(3), where 3×3 unitary matrices have the property that their determinant is 1. The SU(3) group is characterised by eight independent parameters, denoted $\alpha_a(x)$ where $a = 1,...,8$. The generators of the group are defined as:

$$T_a = \frac{\lambda_a}{2} \tag{1.20}$$

where λ_a are known as the Gell-Mann matrices. These generators do not commute and instead follow the relation:

$$\left[\frac{\lambda_i}{2}, \frac{\lambda_j}{2}\right] = i f_{ijk} \frac{\lambda_k}{2} \tag{1.21}$$

hence, the theory is non-abelian. The constants f_{ijk} are known as the structure constants of SU(3).

Since each quark appears in three colours (red, green, blue) it is convenient to replace the spinors of QED with quark fields where:

$$q(x) = \begin{pmatrix} \psi_R(x) \\ \psi_G(x) \\ \psi_B(x) \end{pmatrix} \qquad \bar{q}(x) = (\bar{\psi}_R(x), \bar{\psi}_G(x), \bar{\psi}_B(x)) \tag{1.22}$$

Therefore, the Dirac Lagrangian describing a free quark can be written as:

$$\mathcal{L} = \bar{q}(x)\,(i\gamma^\mu \partial_\mu - m)\,q(x) \tag{1.23}$$

Following the same formalism as QED, this Lagrangian must be locally gauge invariant under SU(3). The quark field transforms as:

$$q(x) \rightarrow q'(x) = Uq(x) = e^{i\alpha_a(x)\frac{\lambda_a}{2}} q(x) \tag{1.24}$$

with the infinitesimal transform defined as:

$$q(x) \rightarrow \left(1 + i\alpha_a(x)\frac{\lambda_a}{2}\right) q(x) \tag{1.25}$$

As is seen with QED, the Dirac Lagrangian is not gauge invariant since the derivative, $\partial_\mu q(x)$ transforms as:

$$\partial_\mu q(x) \rightarrow \left(1 + i\alpha_a(x)\frac{\lambda_a}{2}\right) \partial_\mu q(x) + i\frac{\lambda_a}{2} q(x) \partial_\mu \alpha_a \tag{1.26}$$

In QED, a vector spin-1 field, A_μ, was introduced to the Lagrangian to absorb the extra term from the derivative of $\partial_\mu \psi$. Likewise, new fields must also be introduced to the QCD Lagrangian. Instead of just one field, eight gauge fields, G^a_μ, must be introduced which transform as:

$$G^a_\mu \rightarrow G^a_\mu - \frac{1}{g_s}\partial_\mu \alpha_a \tag{1.27}$$

Again, all derivatives ∂_μ must be replaced by covariant derivatives, D_μ:

$$D_\mu = \partial_\mu + ig_s\frac{\lambda_a}{2}G_\mu^a \tag{1.28}$$

The Lagrangian in Equation 1.23 becomes:

$$\begin{aligned}\mathcal{L} &= \bar{q}(i\gamma^\mu D_\mu - m)\,q \\ &= \bar{q}(i\gamma^\mu\partial_\mu - m)\,q - g_s\left(\bar{q}\gamma^\mu\frac{\lambda_a}{2}q\right)G_\mu^a\end{aligned} \tag{1.29}$$

However, due to the non-abelian nature of SU(3), modifications to this Lagrangian are necessary for it to be invariant. It is observed that the gauge invariant QCD Lagrangian can be obtained if the gauge fields transforms as:

$$G_\mu^a \rightarrow G_\mu^{a\prime} = G_\mu^a - \frac{1}{g_s}\partial_\mu\alpha_a - f_{abc}\alpha_b G_\mu^c \tag{1.30}$$

The final piece is to add the free particle Maxwell Lagrangian for each of the eight gauge fields to yield the Lagrangian[3] describing QCD:

$$\mathcal{L}_{QCD} = \bar{q}(i\gamma^\mu\partial_\mu - m)\,q - g_s\left(\bar{q}\gamma^\mu\frac{\lambda_a}{2}q\right)G_\mu^a - \frac{1}{4}G_{\mu\nu}^a G_a^{\mu\nu} \tag{1.31}$$

where $G_{\mu\nu}^a = \partial_\mu G_\nu^a - \partial_\mu G_\nu^a - g_s f_{abc}G_\mu^b G_\nu^c$. From this Lagrangian the interactions allowed in QCD can be seen. In comparison with QED, interactions between the quark (fermion in QED) fields with the gauge fields are seen in the term $g_s\left(\bar{q}\gamma^\mu\frac{\lambda_a}{2}q\right)G_\mu^a$, where the strength of the coupling determined by the strong coupling constant g_s. Due to the non-Abelian nature of SU(3) and thus the form of the gauge field tensors, $G_{\mu\nu}^a$, self-interactions between the gauge fields are allowed. These forms of interaction have no analogue in QED since the photon does not carry charge. The consequence is that these self-interactions lead to differences in the properties of the strong force to those of electromagnetism. These differing properties are known as *asymptotic freedom* and *confinement*.

Asymptotic freedom is shorthand for saying that the relative strength of the coupling constant diminishes with decreasing distance, the so called running of the coupling constants. The reason QCD and not QED displays this phenomenon is best understood via the Feynman diagrams of the lowest-order loop corrections to a simple boson exchange process shown in Figures 1.2 and 1.3. For QED, loop corrections of the kind seen in Figure 1.2 contribute to the dependence of the coupling constant on the scale (Q^2). This is due to a process called *screening*, where virtual charged particles in the loop cause a polarization of charge in the vacuum. Therefore, as Q^2 increases, or equivalently

[3] In actual fact there are six Lagrangians, one for each flavour of quark and corresponding mass.

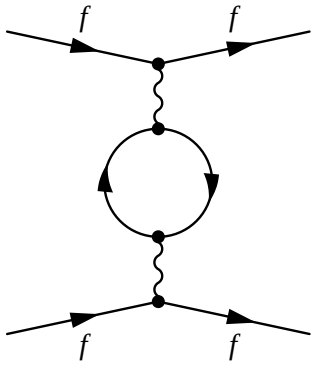

Figure 1.2: *Feynman diagram of the lowest order loop correction to QED quark-quark scattering.*

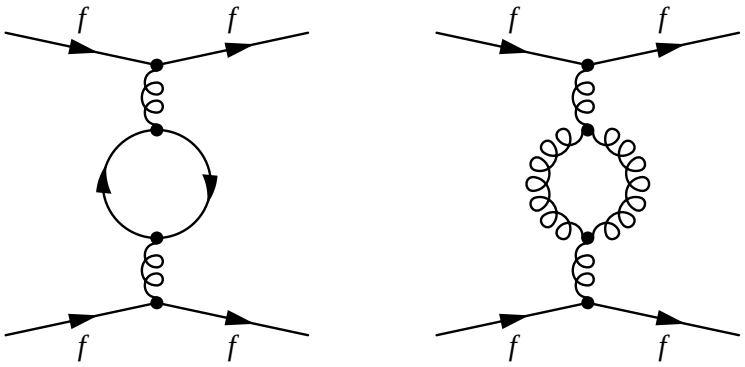

Figure 1.3: *Feynman diagrams of the lowest order loop corrections to QCD quark-quark scattering.*

the distance decreases, less and less effect of the vacuum polarisation is seen, resulting in an effective increase in the strength of the coupling. In QCD, the same thing occurs as quark-anti-quark pairs analogous to the QED charged fermion loops contribute to an effective increase in the coupling at short distances. However, due to the self-interaction of gluons there is also a second diagram, Figure 1.3(b), for quark-quark scattering that is not present in QED. This leads to an *antiscreening* effect meaning that there is an effective decrease in the coupling at short distances. This is more significant than the QCD screening effect leading to the net result that the interaction weakens at short distances or equivalently strengthens at larger distances. It is this strengthening at larger distances that results in no free objects of colour being identified by particle detectors. Instead, they are confined to colourless hadrons where their presence is inferred by the detection of collimated hadronic jets.

1.1.5 Electroweak Unification

The weak interaction theory is described using the non-abelian symmetry group SU(2). In analogy with the formalism of QCD the generators of the group give rise to the gauge fields. In QCD there are eight generators, the Gell-Mann matrices, that give rise to the introduction of eight gauge fields identified as gluons. Similarly, in the weak theory there are three generators, the Pauli-spin matrices, that give rise to three gauge fields identified as the Z^0, W^+ and W^- vector bosons. According to Noether's theorem[4], a quantity or current is conserved providing gauge invariance is shown. For example, in QED the electric charge is conserved and in QCD it is colour charge that is conserved. In the case of the weak interaction, the conserved quantity is called weak isopin, $T_{1,2.3}$.

The electromagnetic and weak interactions were unified by Glashow, Salam and Weinberg (GSW) in 1968 [11, 12, 13]. The GSW theory describes the electroweak interactions between fermions via the exchange of vector spin-1 gauge bosons. It is a gauge field theory based on the symmetry group $\mathrm{SU}(2)_L \otimes \mathrm{U}(1)_Y$. The $\mathrm{SU}(2)_L$ part refers to the symmetry group under which the Lagrangian, describing the weak interactions between left-handed fermion doublets and right-handed fermion singlets, is invariant. Experimental observations have shown that weak charged currents only involve left-handed chiral doublets and right-handed singlets:

$$\chi_{iL} = \begin{pmatrix} \psi_{\nu_i} \\ \psi_{l_i} \end{pmatrix}_L, \begin{pmatrix} \psi_{u_i} \\ \psi_{d_i'} \end{pmatrix} \qquad \psi_{iR} = \psi_{l_{iR}}, \psi_{u_{iR}}, \psi_{d_{iR}'} \tag{1.32}$$

where the index i runs over all lepton and quark flavours. Note that there are no right-handed neutrinos listed above since they only interact gravitationally. Additionally, the quark mass eigenstate (d_i) has been replaced by a linear combination of mass eigenstates (d_i') in accordance with the discovery of flavour changing currents. The transition between eigenstates is described by the Cabbibo-Kobayashi-Maskawa (CKM) matrix [14, 15]:

$$\begin{pmatrix} d' \\ s' \\ b' \end{pmatrix} = \begin{pmatrix} V_{ud} & V_{us} & V_{ub} \\ V_{cd} & V_{cs} & V_{cb} \\ V_{td} & V_{ts} & V_{tb} \end{pmatrix} \begin{pmatrix} d \\ s \\ b \end{pmatrix} \tag{1.33}$$

Whilst flavour mixing in the lepton sector is not included in the electroweak theory its existence was confirmed in 1998 by observation of neutrino oscillations [6, 7, 8].

The $\mathrm{U}(1)_Y$ symmetry in electroweak theory is generated by *hypercharge*, denoted Y. It is related

[4]Put simply, when Noether's theorem is applied to quantum field theory it states that if a Lagrangian is symmetric (invariant) under some transformation then there must a conserved quantity or *current*.

to the electric charge by:

$$Q = T_3 + \frac{Y}{2} \tag{1.34}$$

where T_3 is the third component of weak isospin.

The Lagrangian describing fermions in the electroweak formalism is:

$$\mathcal{L} = i\bar{\chi}_{iL}\gamma^{\mu}\partial_{\mu}\chi_{iL} + i\bar{\psi}_{iR}\gamma^{\mu}\partial_{\mu}\psi_{iR} \tag{1.35}$$

Mass terms such as:

$$-\bar{\psi}m\psi = -(\bar{\psi}_L + \bar{\psi}_R)m(\psi_L + \psi_R) \tag{1.36}$$

are omitted from the Lagrangian since they break gauge invariance by linking a left handed isopin doublet to a right handed singlet. For the time being the absence of mass terms is ignored.

Following the formalism of QCD, the Lagrangian is required to be invariant under $SU(2)_L$ and $U(1)_Y$ transformations. The fermion fields transform as:

$$\begin{aligned} \chi_{iL} &\rightarrow \chi'_{iL} = e^{\left(ig_w\alpha_a\frac{\tau_a}{2} + i\frac{g'}{2}\beta Y\right)}\chi_{iL} \\ \psi_{iR} &\rightarrow \psi'_{iR} = e^{\left(i\frac{g'}{2}\beta Y\right)}\psi_{iR} \end{aligned} \tag{1.37}$$

This motivates the introduction of four massless gauge fields W^1_{μ}, W^2_{μ}, W^3_{μ} and B_{μ} via the definition of the covariant derivatives:

$$\begin{aligned} D_{\mu}\chi_{iL} &= \left[\partial_{\mu} + ig_w\frac{\tau_a}{2}W^a_{\mu} + i\frac{g'}{2}YB_{\mu}\right]\chi_{iL} \\ D_{\mu}\psi_{iR} &= \left[\partial_{\mu} + i\frac{g'}{2}YB_{\mu}\right]\psi_{iR} \end{aligned} \tag{1.38}$$

Replacing all ∂_{μ} by D_{μ} in the Lagrangian (1.35), and adding the Maxwell Lagrangians for the four gauge fields, the electroweak Lagrangian is formed:

$$\begin{aligned} \mathcal{L}_{GSW} &= \sum_{i=flavour}\bar{\chi}_{iL}\gamma^{\mu}\left(i\partial_{\mu} - g_w\frac{\tau_a}{2}W^a_{\mu} - \frac{g'}{2}YB_{\mu}\right)\chi_{iL} && SU(2) \\ &+ \sum_{i=flavour}\bar{\psi}_{iR}\gamma^{\mu}\left(i\partial_{\mu} - \frac{g'}{2}YB_{\mu}\right)\psi_{iR} && U(1) \\ &- \frac{1}{4}W^a_{\mu\nu}W^{\mu\nu}_a - \frac{1}{4}B_{\mu\nu}B^{\mu\nu} && \textit{Maxwell Terms} \end{aligned} \tag{1.39}$$

where $B_{\mu\nu} = \partial_{\mu}B_{\nu} - \partial_{\nu}B_{\mu}$ and $W^a_{\mu\nu} = \partial_{\mu}W^a_{\nu} - \partial_{\nu}W^a_{\mu} - g_w\varepsilon_{abc}W^b_{\mu}W^c_{\nu}$, where the constants ε_{abc} are the structure constants of SU(2). The nature of allowed interactions in the electroweak theory can again

be derived from this Lagrangian. In similarity with QCD, the non-abelian nature of SU(2) introduces trilinear and quadrilinear self-coupling terms between the W_μ^a gauge fields. Naively, one might expect that the gauge fields $W_\mu^{1,2}$ are interpreted as the gauge fields of the charged weak interaction, mediated by the $W^\pm$ bosons, and W_μ^3 as the gauge field of the neutral weak interaction, mediated by the Z^0. If this were the case then charged and neutral weak interactions would have the same coupling, g_w, however, this is in contradiction with experimental observations. Instead the gauge fields are related to the mass eigenstates (physical bosons) by a linear transformation:

$$\begin{pmatrix} A_\mu \\ Z_\mu \end{pmatrix} = \begin{pmatrix} cos\,\theta_w & sin\,\theta_w \\ -sin\,\theta_w & cos\,\theta_w \end{pmatrix} \begin{pmatrix} B_\mu \\ W_\mu^3 \end{pmatrix} \tag{1.40}$$

$$W_\mu^\pm = \frac{1}{\sqrt{2}}\left(W_\mu^1 \mp iW_\mu^2\right) \tag{1.41}$$

where the mixing angle, θ_w, is known as the *weak mixing angle* or *Weinberg angle*. This angle also specifies the relation between the two coupling constants g' and g_w:

$$g' = g_w tan\,\theta_w \tag{1.42}$$

One fundamental question remains: Why are no mass terms for either the fermions or weak gauge bosons present in the Lagrangian? The answer, as demonstrated with the fermion mass terms above, is that they break gauge invariance. At first, this may appear catastrophic, since it is well known fermions along with $W^\pm$ and Z^0 are massive. The solution, which is subject of the following chapter, is to spontaneously break the symmetry via the Higgs mechanism.

1.1.6 Electroweak Symmetry Breaking: The Higgs Mechanism

Prior to the invention of the Higgs mechanism, it was not known how to formulate a consistent relativistic field theory with a local symmetry which could contain both massless and massive force carriers. In 1962, Goldstone's theorem had shown that spontaneous breaking of symmetry in a relativistic field theory results in massless spin-zero bosons, which are excluded experimentally. In his 1964 paper, Peter Higgs showed that Goldstone bosons need not occur when a local symmetry is spontaneously broken in a relativistic theory [16]. Instead, he postulated the presence of a new massive spin-zero particle - the Higgs boson.

In the formalism of the Higgs mechanism and its subsequent incorporation of it in the electroweak theory, it is often useful to consider a few simplistic models.

1.1.6.1 The Scalar Field Model

Following the classical form of the Lagrangian, $\mathcal{L} = T - V$ the Lagrangian for a free scalar field, ϕ, is:

$$\mathcal{L} = \frac{1}{2}(\partial_\mu \phi)^2 - V(\phi) \tag{1.43}$$

and the potential $V(\phi)$ is:

$$V(\phi) = \frac{1}{2}\mu^2\phi^2 + \frac{1}{4}\lambda^2\phi^4 \tag{1.44}$$

For a vacuum state with positive and finite energy to exist, λ must be positive and thus the Lagrangian symmetric under $\phi \rightarrow -\phi$. Two solutions now exist. If $\mu^2 > 0$ the potential energy is a minimum at $<\phi>= 0$. In this case the vacuum state is unique. If $\mu^2 < 0$ the potential has two minima:

$$<\phi>= \sqrt{-\frac{\mu^2}{\lambda}} = \pm v \tag{1.45}$$

where v is identified as the vacuum expectation value of the field. The form of the potential for $\mu^2 < 0$ can be seen in Figure 1.4. In this case the vacuum state is not unique but degenerate. By arbitrarily

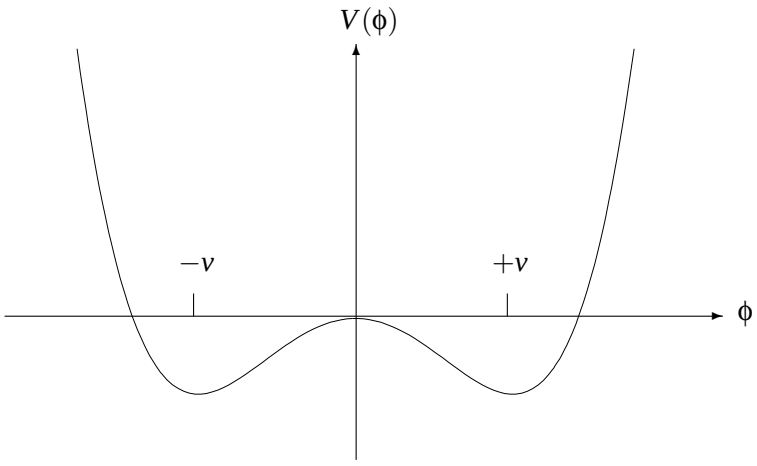

Figure 1.4: *The scalar potential for* $\mu^2 < 0$.

choosing one of the states, say $<\phi>= +v$, to be the ground state the symmetry ($\phi \rightarrow -\phi$) is broken. This process is known as *spontaneous symmetry breaking*. At first, it is not immediately obvious as to how spontaneous symmetry breaking allows for mass terms in the Lagrangian. However, if a new basis for ϕ is chosen:

$$\phi(x) = v + \eta(x) \tag{1.46}$$

where $\eta(x)$ is a field measuring the quantum fluctuations about the vacuum state, then in terms of this new field, the Lagrangian (1.43) becomes:

$$\mathcal{L} = \frac{1}{2}(\partial_\mu \eta)^2 - \left(\lambda v^2 \eta^2 + \lambda v \eta^3 + \frac{1}{4}\lambda \eta^4\right) \tag{1.47}$$

A mass-like term, $-\lambda v^2 \eta^2$, of the correct sign can now be seen, which, identifying with mass terms seen in previous Lagrangians, leads to the result:

$$m_\eta = \sqrt{2\lambda v^2} = \sqrt{-2\mu^2} \tag{1.48}$$

Thus, by considering perturbations about the chosen vacuum state, mass terms can be introduced in a gauge invariant way.

1.1.6.2 The Complex Scalar Field Model

A more interesting case comes when considering a complex scalar field, $\phi = \frac{\phi_1 + i\phi_2}{\sqrt{2}}$. The Lagrangian:

$$\mathcal{L} = (\partial_\mu \phi)^\star (\partial^\mu \phi) - \mu^2 \phi^\star \phi - \lambda (\phi^\star \phi)^2 \tag{1.49}$$

is invariant under U(1) global phase transformations. Following the same procedure as above for a choice of $\lambda > 0$ and $\mu^2 < 0$ the minima of the potential are found to be:

$$\phi_1^2 + \phi_2^2 = v^2 \tag{1.50}$$

Again, they are not unique and instead lie on a circle in the (ϕ_1, ϕ_2) plane (see Figure 1.5). The U(1) symmetry is broken by choosing the vacuum states $<\phi_1> = v$ and $<\phi_2> = 0$. Expanding ϕ about the vacuum state introduces two new fields:

$$\phi(x) = \frac{1}{\sqrt{2}}(v + \eta(x) + i\rho(x)) \tag{1.51}$$

Rewriting the Lagrangian (1.49), in terms of the new fields gives:

$$\mathcal{L} = \frac{1}{2}(\partial_\mu \eta)^2 + \frac{1}{2}(\partial_\mu \rho)^2 - \frac{1}{2}\mu^2 \eta^2 + O(\eta^3) + O(\rho^3) + O(\eta^4) + O(\rho^4) + const \tag{1.52}$$

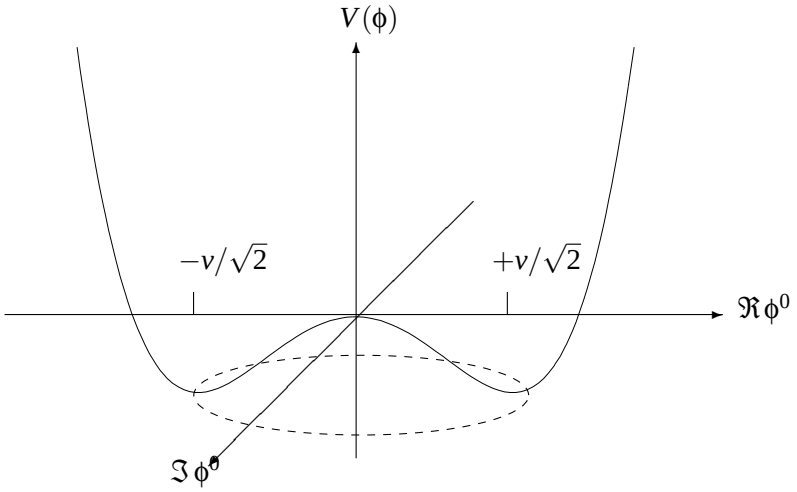

Figure 1.5: *The complex scalar potential for* $\mu^2 < 0$.

Again, the third term looks like a mass term of the form $-\frac{1}{2}m_\eta^2\eta^2$ with:

$$m_\eta = \sqrt{-2\mu^2} \tag{1.53}$$

However, there is also a kinetic energy term for the field ρ, but no associated mass term. In attempt to break the symmetry a new massless boson, known as the *Goldstone boson*, has been introduced. These bosons do not exist or at least have not been observed in nature.

1.1.6.3 The Higgs Mechanism

The difference between the previous complex scalar field model and the Higgs mechanism can be viewed as the requirement that global U(1) gauge invariance must also hold locally. Following the strategy for achieving local U(1) gauge invariance, demonstrated for QED in Section 1.1.3, derivatives ∂_μ are replaced by covariant derivatives $D_\mu = \partial_\mu - ieA_\mu$ to give a gauge invariant Lagrangian:

$$\begin{aligned}\mathcal{L} &= (D_\mu\phi^\star)(D^\mu\phi) - \mu^2\phi^\star\phi - \lambda(\phi^\star\phi)^2 - \frac{1}{4}F_{\mu\nu}F^{\mu\nu} \\ &= (\partial_\mu + ieA_\mu)\phi^\star(\partial^\mu - ieA^\mu)\phi - \mu^2\phi^\star\phi - \lambda(\phi^\star\phi)^2 - \frac{1}{4}F_{\mu\nu}F^{\mu\nu}\end{aligned} \tag{1.54}$$

For $\mu^2 > 0$ this is just the QED Lagrangian for a charged scalar particle of mass μ (with a self interaction term $\lambda(\phi^\star\phi)^2$). However, consistent with the previous models the $\mu^2 < 0$ solution is used to break the symmetry. Naively, it would make sense to chose the same basis for $\phi(x)$ as in the complex scalar model. It turns out that doing so results in gaining an extra degree of freedom in the

form of a Goldstone boson. However by an astute choice of gauge, this extra degree of freedom can be absorbed into the gauge field. The chosen gauge is called the *unitary gauge* and thus the basis chosen for ϕ is:

$$\phi = \frac{1}{\sqrt{2}}(v+\eta(x)+i\rho(x)) \approx \frac{1}{\sqrt{2}}(v+\eta(x))\,e^{i\frac{\rho(x)}{v}} \tag{1.55}$$

where $e^{i\frac{\rho(x)}{v}}$ represents the unitary gauge. The symmetry is broken by choosing $\rho(x) = 0$ and thus rendering $\eta(x)$ real. Inserting this form for ϕ into the Lagrangian (1.54) gives:

$$\mathcal{L} = \frac{1}{2}(\partial_\mu h)^2 - \lambda v^2 h^2 + \frac{1}{2}e^2 v^2 A_\mu A^\mu - \frac{1}{4}F_{\mu\nu}F^{\mu\nu} + \textit{higher order terms} \tag{1.56}$$

where $\eta(x)$ has been replaced by $h(x)$. This Lagrangian represents two interacting massive particles: a vector gauge boson A_μ with mass ev and a scalar, h, with mass $\sqrt{2\lambda}v$ - the Higgs boson.

1.1.6.4 Weinberg's Interpretation of The Higgs Mechanism

In Weinberg's interpretation of the Higgs mechanism, the broken symmetry is the SU(2) symmetry. Weinberg chose to introduce a weak isospin doublet of complex scalar fields with hypercharge $Y = 1$:

$$\phi = \begin{pmatrix} \phi^+ \\ \phi^0 \end{pmatrix} = \frac{1}{\sqrt{2}}\begin{pmatrix} \phi_1 + i\phi_2 \\ \phi_3 + i\phi_4 \end{pmatrix} \tag{1.57}$$

which transforms in the same manner as the electroweak doublet fields under $\mathrm{SU}(2)_L \otimes \mathrm{U}(1)_Y$ transformations (see Equation (1.37)). The upper component of the doublet is electrically charged while the lower component is neutral. The Lagrangian for the field ϕ is given by:

$$\mathcal{L}_{Higgs} = (D_\mu\phi)^\dagger(D^\mu\phi) - \mu^2(\phi^\dagger\phi) - \lambda(\phi^\dagger\phi)^2 \tag{1.58}$$

The introduction of covariant derivatives, Equation (1.38), is used to ensure gauge invariance under local $\mathrm{SU}(2)_L \otimes \mathrm{U}(1)_Y$ transformation. Weinberg broke the symmetry by taking $\mu^2 < 0$, which leads to a degenerate vacuum state, and chose the vacuum state:

$$<\phi> = \frac{1}{\sqrt{2}}\begin{pmatrix} 0 \\ v \end{pmatrix} \tag{1.59}$$

This choice is motivated by the need to keep the ground state electrically neutral which ultimately keeps the photon massless. Perturbations around the ground state are once again considered and

parameterised accordingly:

$$\phi = \frac{1}{\sqrt{2}} \begin{pmatrix} 0 \\ v + h(x) \end{pmatrix} e^{i\rho_a(x)\tau_a/2v} \tag{1.60}$$

where $\rho_1(x)$, $\rho_2(x)$, $\rho_3(x)$ and $h(x)$ are 4 real fields and τ_a are the Pauli spin matrices. By choosing an appropriate gauge such that $\rho_1 = \rho_2 = \rho_3 = 0$ the field ϕ can be written as:

$$\phi = \frac{1}{\sqrt{2}} \begin{pmatrix} 0 \\ v + h(x) \end{pmatrix} \tag{1.61}$$

Substituting ϕ back into the Lagrangian (1.58) reveals how the gauge bosons acquire mass. The mass terms arise from the gauge terms in the covariant derivatives:

$$\begin{aligned} |D_\mu \phi|^2 &= \left| \left(g_w \frac{\tau_a}{2} W_\mu^a + \frac{g'}{2} Y B_\mu \right) \phi \right|^2 \\ &= \frac{1}{4} v^2 g_w^2 W^+ W^- + \frac{1}{8} v^2 \left(g_w^2 + g'^2 \right) Z_\mu Z^\mu + 0 A_\mu A^\mu \end{aligned} \tag{1.62}$$

where the relations in Equations (1.40) and (1.41) have been used. Comparing these terms with the expected form of mass terms for gauge bosons, it can be deduced that:

$$M_W = \frac{v g_w}{2}; \qquad M_Z = \frac{v\sqrt{g_w^2 + g'^2}}{2}; \qquad M_A = 0 \tag{1.63}$$

The mass of the Higgs boson can be obtained by inserting Equation (1.61) into the potential, $V(\phi^\dagger, \phi)$, to give:

$$m_H = \sqrt{\lambda v^2} \tag{1.64}$$

The value of the vacuum expectation, v, has been determined to be 246 GeV from experiments measuring the lifetime of the muon. λ is a free parameter of the model and must be determined experimentally. Thus, the mass of the Higgs boson is not predicted by the the theory.

The Higgs mechanism also allows for lepton and quark mass terms in the Lagrangian. For leptons, the following terms can be added to the Lagrangian in a gauge invariant way:

$$\mathcal{L}_{leptons} = -G_l \left[\overline{\chi}_L^l \phi \psi_R^l + \overline{\psi}_R^l \phi^\dagger \chi_L^l \right] \tag{1.65}$$

The symmetry is then spontaneously broken, the remaining fields are gauged away and upon substi-

tution of the ground state of ϕ the Lagrangian becomes:

$$\mathcal{L}_{leptons} = -\frac{G_l}{\sqrt{2}}v\left(\bar{\psi}_L^l\psi_R^l + \bar{\psi}_R^l\psi_L^l\right) - \frac{G_l}{\sqrt{2}}\left(\bar{\psi}_L^l\psi_R^l + \bar{\psi}_R^l\psi_L^l\right)h \tag{1.66}$$

The first term can be identified as a mass term and choosing G_l such that $m_l = \frac{G_l v}{\sqrt{2}}$ the mass of the lepton is generated in the Lagrangian:

$$\mathcal{L}_{leptons} = -m_l\bar{\psi}^l\psi^l - \frac{m_l}{v}\bar{\psi}^l\psi^l h \tag{1.67}$$

Quarks mass terms of the form (where the index *i* runs over the number of generations):

$$\mathcal{L}_{quarks} = -m_d^i\bar{\psi}_i^d\psi_i^d\left(1+\frac{h}{v}\right) - m_u^i\bar{\psi}_i^u\psi_i^u\left(1+\frac{h}{v}\right) \tag{1.68}$$

can be added in gauge invariant way to the Lagrangian in a similar manner to those for the leptons. For both quarks and leptons, the coupling to the Higgs is proportional to their masses. The actual mass of the fermions is not predicted since they depend on arbitrary couplings G_l and $G_{d,u}$ known as the Yukawa couplings. Additionally, the theory provides no natural answer as to the hierarchy of the fermion masses.

1.1.7 Limits on The Higgs Boson Mass

In the Standard Model the Higgs mass is not predicted and instead is a free parameter defined by its self-coupling $\lambda(Q^2)$. However, theoretical arguments based on the evolution of the coupling can be used to place upper and lower limits on the mass. In addition direct experimental searches and precision measurements of the electroweak parameters allow further limits to be placed.

1.1.7.1 Theoretical Limits

Three main theoretical arguments exist to constrain the Higgs mass range: *unitarity*, *triviality* and vacuum *stability* [17, 18, 19, 20].

Unitarity is the requirement that the scattering amplitude integrated over all possible diagrams for a process does not exceed unity. Considering the scattering amplitude of longitudinally polarised W bosons, allows an upper limit to be placed on the Higgs mass. Without the presence of the Higgs boson, the cross-section of this process, visualised by the Feynman diagrams in Figures 1.6(a) and 1.6(b), increases with the scattering energy and thus would violate unitarity for energies above 1.2 TeV. The Higgs mechanism provides the solution to restore unitarity by introducing another

diagram, seen in Figure 1.6(c), mediated by the Higgs boson. The contributions from this additional process balance out the divergences but imply that Higgs mass must be below $\sim$800 GeV$/c^2$.

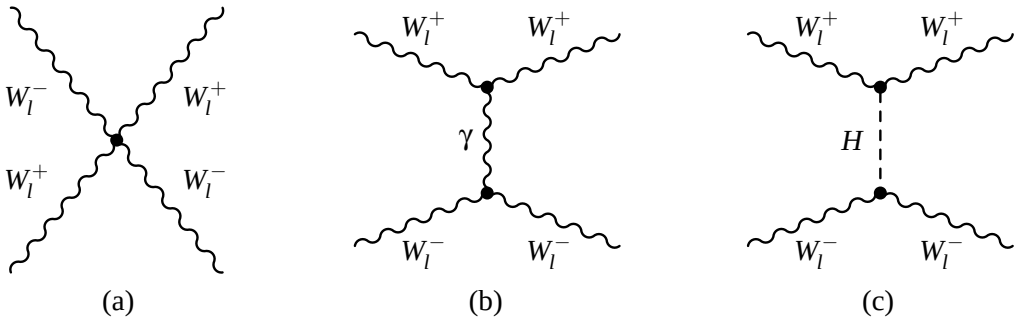

Figure 1.6: *Some of the Feynman diagrams of the scattering of longitudinally polarised W bosons. Without the Higgs mechanism (c) would not exist and thus unitarity would be violated.*

Triviality is the requirement that the self-coupling of the Higgs boson remains finite at some cut-off energy. At tree level there is no constraint on the mass of the Higgs boson. Higher order corrections, such as those in Figure 1.7, lead to the running of the coupling constant, $\lambda(Q^2)$. The self-coupling of the Higgs, $\lambda(v)$, is proportional to the square of the mass of the Higgs boson, m_H. Thus for high mass Higgs bosons, contributions from the quartic self-coupling cause the coupling constant to diverge such that at some energy scale it tends to infinity. A cut-off energy, Λ, is therefore introduced and is defined as the point where new physics enters. For example, if the Standard Model were to be valid up to the Planck energy scale ($\Lambda = 10^{19}$ GeV) then it would follow that the upper limit of the Higgs mass would be $\sim$140 GeV$/c^2$. If new physics might enter at the 10 TeV scale then the upper limit would be $\sim$500 GeV$/c^2$

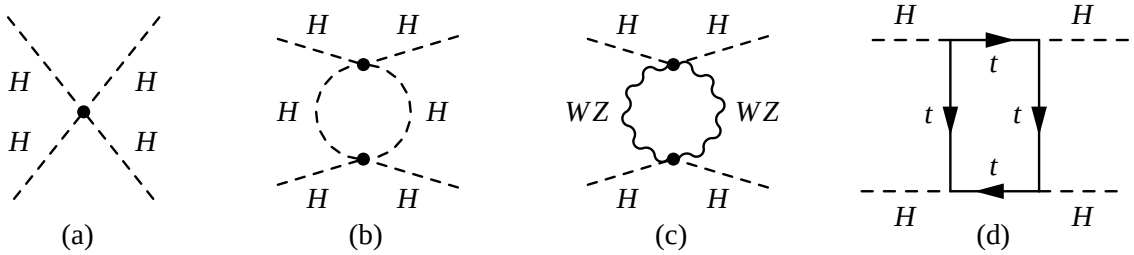

Figure 1.7: *Feynman diagrams of higher order corrections to the Higgs boson self-coupling.*

Higher order corrections also provide an argument for a lower bound to be placed on the Higgs

mass. At low masses the Higgs coupling to the top quark and weak bosons dominates since $m_H << m_t, m_{W/Z}$. To ensure that the coupling $\lambda(Q^2)$ remains positive and thus a stable vacuum, a cut-off energy must be introduced which bounds the Higgs mass from below. For example, assuming a cut-off scale to be of the order of the electroweak unification scale ($\Lambda = 10^3$ GeV) then the mass of the Higgs must be greater than $\sim$70 GeV$/c^2$. Combining the theoretical arguments of triviality and vacuum stability results in defining a Higgs mass window dependent on the scale at which new physics enters (see Figure 1.8).

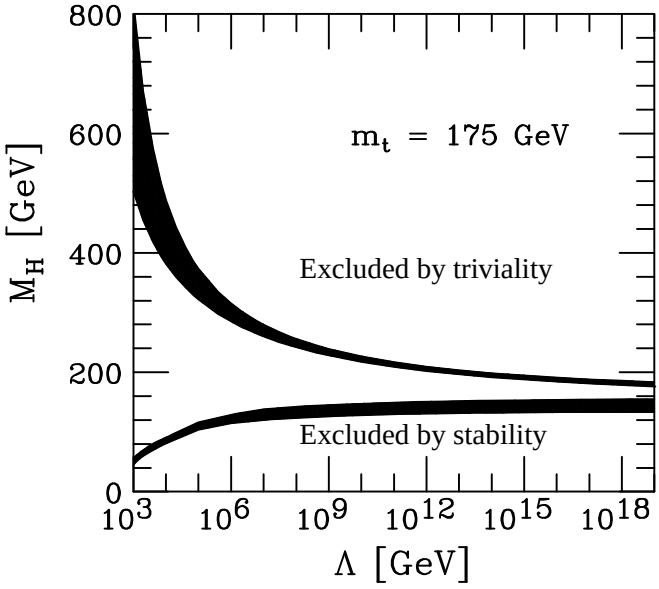

Figure 1.8: *Theoretical allowed mass range of the Higgs boson as a function of the energy scale, Λ. From [21].*

1.1.7.2 Experimental Limits

Experimental limits come from direct searches and indirectly from electroweak precision measurements. The earliest direct measurements come from LEP (Large Electron Positron Collider) which primarily focussed on searches for Higgs boson produced via Higgsstrahlung ($e^+e^- \rightarrow Z^\star \rightarrow ZH$). Whilst searches at LEP did not find conclusive evidence for the Higgs boson, one of the experiments (ALEPH) found an excess of 3σ for a mass around 115 GeV$/c^2$ [22]. Combined results from all experiments at LEP set a lower limit on the Higgs at $m_H = 114.4$ GeV$/c^2$ at 95% confidence level [23].

More recent direct searches have been performed at the CDF and DØ experiments at the $\sqrt{s} =$ 1.96 TeV Tevatron collider. The dominant processes at the Tevatron are the production of a Higgs

boson ($m_H < 135$ GeV$/c^2$) in association with a weak boson and the production via gluon fusion ($m_H > 135$ GeV$/c^2$). Combined results and exclusion limits from both experiments for an integrated luminosity of 5.9 fb^{-1} are shown in Figure 1.9. Whilst the LEP lower limit still remains, the Higgs mass range $158 < m_H < 175$ GeV$/c^2$ has been excluded at 95% confidence level by the Tevatron [24].

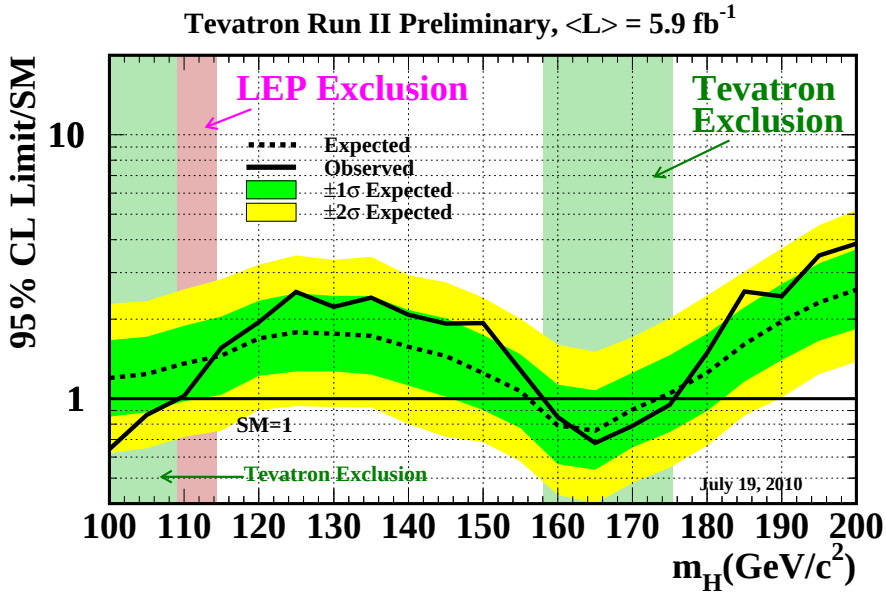

Figure 1.9: *Observed and median expected 95% confidence level upper limit on the cross-section ratio to the SM cross-section, as a function of the Higgs boson mass. The expected upper limit is obtained in the background-only (null) hypothesis. The bands represent regions in which the limits can fluctuate in the absence of signal. Exclusions are made with 5.9 fb^{-1} of data. From [24].*

Indirect constraints can be derived from the precision measurements of the parameters of the electroweak theory. Due to radiative corrections introduced by the Higgs boson, the parameters of the theory are dependent upon its mass. By comparing the theoretical predictions with precision measurements of the electroweak parameters, indirect limits can be set on the mass of the Higgs boson.

Since the Higgs boson couples to other particles proportionally to their mass, it has strong couplings to the top quark and W boson. Therefore, radiative corrections to their mass depend upon the Higgs mass. By accurately measuring the W boson and top quark masses, the mass of the Higgs boson can be constrained. Figure 1.10(a) illustrates the direct constraints on the mass of the top quark and W boson from the Tevatron and LEP2 experiments and also the indirect constraints from LEP1 and SLD. By overlaying the SM relationship between the masses of the top quark and W boson with the Higgs mass, favoured regions are seen. The W mass measurements from the Tevatron seem to

favour a heavier W boson and thus would imply that the Higgs boson is lighter than 114.4 GeV/c^2, in contrast to the direct LEP exclusion limit.

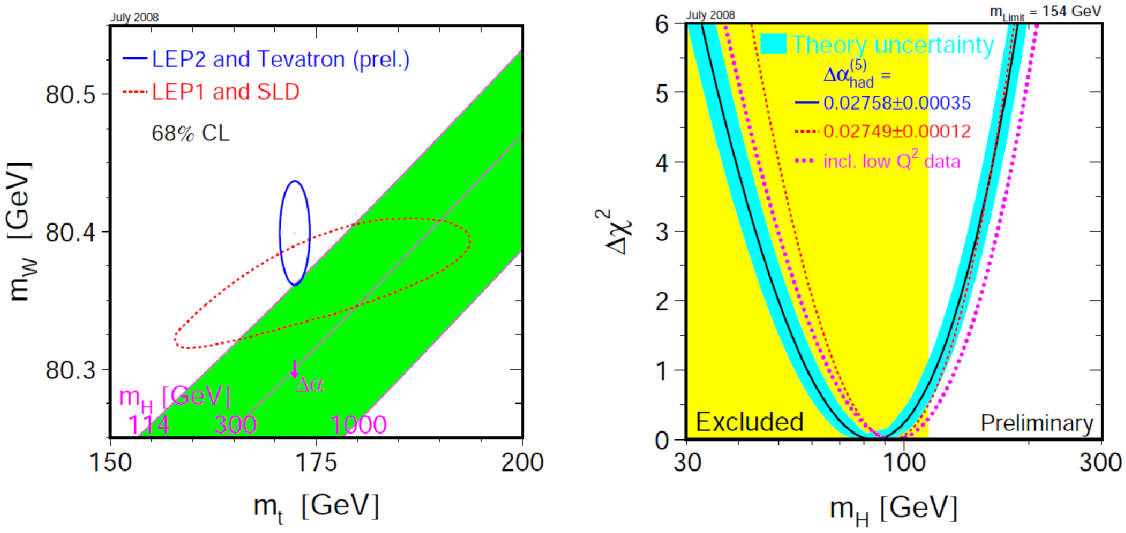

(a) (b)

Figure 1.10: *Indirect and direct measurements of the electroweak parameters constraining the Higgs mass. (a) The 68% confidence level contours in which the top quark and W boson masses are expected to lie. Direct measurements by the Tevatron and LEP2 experiment are indicated by the blue contour and indirect measurements by LEP1 and SLD by the red contour. Overlayed is the SM relationship between the masses of the top quark and W boson with the Higgs boson mass. (b) Global fit of the electroweak parameters as a function of the Higgs boson mass. Regions in yellow have been excluded by the Tevatron and LEP. From [25].*

The Higgs boson mass is also constrained by global fits of the SM electroweak parameters. Figure 1.10(b) shows the global least square fit as a function of the Higgs boson mass. The yellow areas correspond to regions excluded via direct searches by the Tevatron and LEP, although the fit itself does not include the direct search limits. The most probable value is found to be $m_H = 87^{+35}_{-36}$ GeV/c^2 [25]. A more recent treatment including the direct search limits has been performed by the GFitter group giving the result $m_H = 116.4^{+18.3}_{-1.3}$ GeV/c^2 [26].

1.1.8 Higgs Boson Searches at The LHC

At the LHC the Higgs boson will primarily be produced via gluon fusion and vector boson fusion. The cross-sections for the production mechanisms as a function of the Higgs boson mass are shown in Figure 1.11 and the corresponding Feynman diagrams can be seen in Figure 1.12. The dominant production mechanism over the mass range is gluon fusion. However, it can suffer from large higher order QCD corrections and from uncertainties regarding the gluon structure functions. Vector Boson

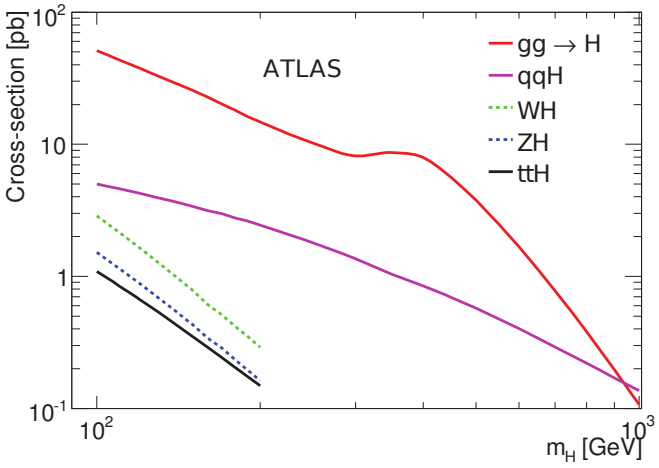

Figure 1.11: *SM Higgs boson production cross-sections for $\sqrt{s} = 14$ TeV. From [27].*

Fusion (VBF) has a cross-section of approximately an order of magnitude lower than that of gluon fusion. It is compensated for by the fact it is associated with two forward quarks which subsequently hadronise into jets. This results in a very clear signature of two forward jets (*tag jets*) in opposite hemispheres, with very or little hadronic activity between them. The remaining production mechanisms are all associated production processes, with lower cross-sections. Whilst on their own they may not have the potential for Higgs boson discovery, they can be used in combination to increase the sensitivity to a low mass Higgs boson.

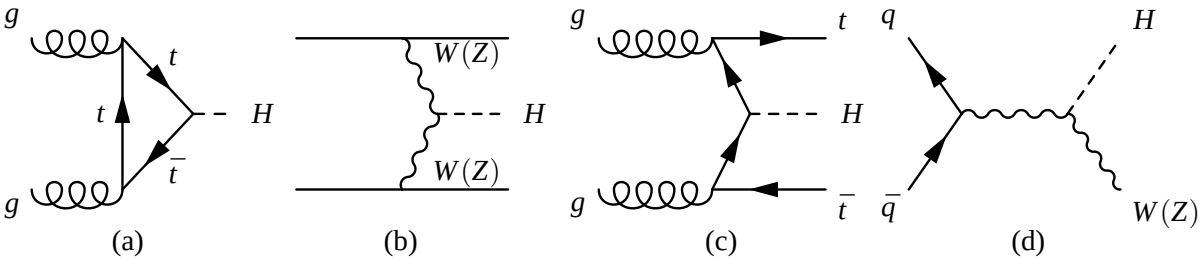

Figure 1.12: *Feynman diagrams of the Higgs boson production at the LHC. (a) gluon fusion, (b) VBF, (c) $t\bar{t}$H, (d) WH/ZH.*

The branching ratios for the different Higgs boson decay channels as a function of the Higgs mass are shown in Figure 1.13. For Higgs masses below 140 GeV$/c^2$, the dominant decay channel is to a pair of b quarks. However, due to the overwhelming QCD background this decay mode is often only used in conjunction with $t\bar{t}$H or WH/ZH, where the emission of leptons can be used to tag the events. In contrast, decays to pairs of photons occur less frequently but are much easier to

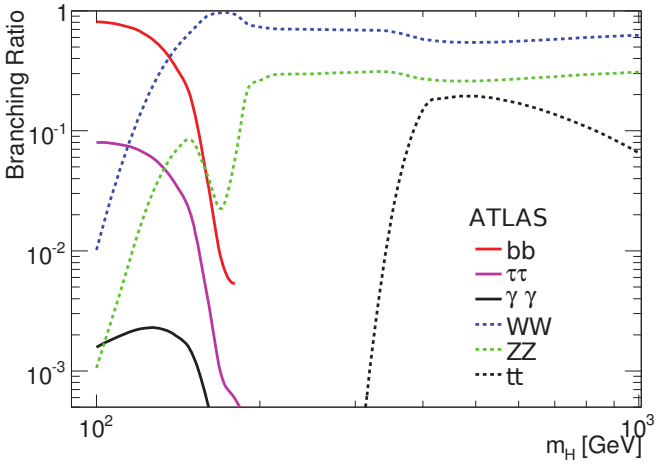

Figure 1.13: *SM Higgs boson branching ratios as a function of the Higgs boson mass, for* $\sqrt{s} =$ 14 *TeV. From [27].*

identify due to excellent invariant mass resolution and photon-jet separation. For Higgs masses above 140 GeV$/c^2$, decays to vector bosons are dominant. In particular the decay to a pair of Z bosons with their subsequent decay to four leptons is known as the “golden channel” due to its very clear signature and its promising discovery potential.

Chapter 2

Fermiophobic Higgs Bosons in Two Higgs Doublet Models

The Standard Model Higgs sector is the simplest possible mechanism allowing particles to acquire mass. However, there is no reason other than simplicity arguments why just one Higgs field is present. Nothing prevents the inclusion of additional Higgs fields in the model and thus increasing the number of expected Higgs bosons. In this fashion the next simplest model is one which contains two complex doublets of Higgs fields. These types of model are called Two Higgs Doublet Models (2HDMs).

Motivation for extending the Higgs sector comes from the lack of an explanation in the Standard Model as to the hierarchy of fermion masses in each generation. In the Standard Model the one Higgs doublet couples to both *u*-type and *d*-type quarks to generate their mass. If however, there were two Higgs doublets, one doublet could exclusively generate *u*-type quark masses whilst the other would generate *d*-type quark masses, therefore providing a mechanism to explain the observed mass hierarchy. Motivation also arises from the desire to introduce Charge-Parity (CP) violation into the Higgs sector although in what follows only CP conserving systems are considered.

The following sections first summarise the formalism of general 2HDMs before focussing on Type-I models in which the lightest CP-even Higgs boson can exhibit a phenomenon called *fermiophobia*. In the fermiophobic limit the coupling between the lightest CP-even Higgs boson and fermions vanishes, such that tree-level decays to fermions are forbidden. In the context of this limit the production at the LHC via gluon-fusion and subsequent decay modes of a fermiophobic Higgs boson are outlined following the work from [28]. Several fermiophobic model benchmarks are proposed, in which the large production cross-section of fermiophobic Higgs boson via gluon-fusion in conjunction with the enhanced decay mode to a pair of photons can be used to probe a substantial

slice of the parameter space. A detailed simulation of the detection prospects of such a signal in the multi-photon channel at the LHC has been performed, and is described in Chapter 7.

2.1 General 2HDMs

The Higgs sector of the Standard Model consists of one Higgs doublet with hypercharge $Y = 1$. Extending this, a second doublet with the same hypercharge is introduced such that:

$$\phi_1 = \begin{pmatrix} \phi_1^+ \\ \phi_1^0 \end{pmatrix} = \frac{1}{\sqrt{2}} \begin{pmatrix} \phi_{1_a} + i\phi_{1_b} \\ \phi_{1_c} + i\phi_{1_d} \end{pmatrix}$$

$$\phi_2 = \begin{pmatrix} \phi_2^+ \\ \phi_2^0 \end{pmatrix} = \frac{1}{\sqrt{2}} \begin{pmatrix} \phi_{2_a} + i\phi_{2_b} \\ \phi_{2_c} + i\phi_{2_d} \end{pmatrix} \tag{2.1}$$

The most general gauge invariant potential under the discrete symmetry $\phi_i \rightarrow -\phi_i$ which describes two complex scalar doublets, can be written in the form [29]:

$$\begin{aligned} V(\phi_1,\phi_2) \;=\; & m_{11}^2\phi_1^\dagger\phi_1 + m_{22}^2\phi_2^\dagger\phi_2 - \left(m_{12}^2\phi_1^\dagger\phi_2 + h.c.\right) + \frac{1}{2}\lambda_1\left(\phi_1^\dagger\phi_1\right)^2 \\ & + \frac{1}{2}\lambda_2\left(\phi_2^\dagger\phi_2\right)^2 + \lambda_3\left(\phi_1^\dagger\phi_1\right)\left(\phi_2^\dagger\phi_2\right) + \lambda_4\left(\phi_1^\dagger\phi_2\right)\left(\phi_2^\dagger\phi_1\right) \\ & + \frac{1}{2}\lambda_5\left[\left(\phi_1^\dagger\phi_2\right)^2 + h.c.\right] \end{aligned} \tag{2.2}$$

where m_{ij} and λ_i are real independent parameters. Whilst the term $m_{12}^2\phi_1^\dagger\phi_2$ corresponds to a violation of the discrete symmetry, the term only violates the symmetry softly and thus can remain [30]. The symmetry is spontaneously broken when the two doublets acquire vacuum expectation values:

$$\langle\phi_1\rangle = \frac{1}{\sqrt{2}}\begin{pmatrix} 0 \\ v_1 \end{pmatrix}, \qquad \langle\phi_2\rangle = \frac{1}{\sqrt{2}}\begin{pmatrix} 0 \\ v_2 \end{pmatrix} \tag{2.3}$$

where the vacuum expectation values have been normalised such that $m_W^2 = \frac{1}{4}g_W^2\left(v_1^2 + v_2^2\right)$. By considering perturbations around the ground states and choosing an appropriate gauge three of the eight degrees of freedom associated with the original doublets are absorbed into the $W^\pm$ and Z bosons. The remaining five degrees of freedom result in five physical Higgs particles: two mass-degenerate charged Higgs bosons ($H^\pm$), one neutral CP-odd scalar (A) and two neutral CP-even scalars (h and H with $m_H \geq m_h$). The mass eigenstates of the Higgs bosons are obtained by a linear transformation of the gauge eigenstates. The angle α is defined as the mixing angle in the CP-even sector and β is

defined as the mixing angle in the CP-odd and charged sector.

The potential in Equation (2.2) has eight independent parameters. Fixing the vacuum expectation values such that $v^2 = v_1^2 + v_2^2$, reduces the number of parameters to seven, which equivalently can be replaced by the masses of the Higgs bosons (m_h, m_H, m_A and $m_{H^\pm}$), $\tan\beta = v_2/v_1$, α and $M^2 = m_{12}^2/(sin\beta cos\beta)$. Here, as M^2 depends on m_{12}^2 it can be thought of as a measure of the discrete symmetry breaking.

The phenomenology of 2HDMs depends greatly on the couplings allowed between the Higgs bosons, gauge bosons and fermions. The Higgs boson couplings to gauge bosons are generated by the covariant derivative in the kinematic part of the Lagrangian. Since this part of the Lagrangian is the same for all 2HDMS the couplings are model independent. Typically these couplings are proportional to either $\cos\delta$ or $\sin\delta$ where $\delta = \alpha - \beta$. In contrast the Higgs boson couplings to fermions depend strongly on the Yukawa sector. Restricting the possible models to only those that prohibit FCNC, there exist four variants of 2HDMS defined by the possible couplings of the Higgs doublets to fermion types. Table 2.1 details the difference between the models, indicating which doublet couples to which fermion type and the coupling associated with lightest CP-even Higgs boson relative to the SM coupling. In Type-I models, only the doublet ϕ_2 couples to all fermions. An interesting

	Type-I		Type-II		Type-III		Type-IV	
	ϕ_i	Coupling	ϕ_i	Coupling	ϕ_i	Coupling	ϕ_i	Coupling
u-type quarks	ϕ_2	$\frac{\cos\alpha}{\sin\beta}$	ϕ_2	$\frac{\cos\alpha}{\sin\beta}$	ϕ_2	$\frac{\cos\alpha}{\sin\beta}$	ϕ_2	$\frac{\cos\alpha}{\sin\beta}$
d-type quarks	ϕ_2	$\frac{\cos\alpha}{\sin\beta}$	ϕ_2	$-\frac{\sin\alpha}{\cos\beta}$	ϕ_1	$-\frac{\sin\alpha}{\cos\beta}$	ϕ_1	$\frac{\cos\alpha}{\sin\beta}$
leptons	ϕ_2	$\frac{\cos\alpha}{\sin\beta}$	ϕ_1	$-\frac{\sin\alpha}{\cos\beta}$	ϕ_1	$\frac{\cos\alpha}{\sin\beta}$	ϕ_2	$-\frac{\sin\alpha}{\cos\beta}$

Table 2.1: *The four distinct structures of the Two Higgs Doublet Models and couplings to the lightest Higgs boson relative to the SM couplings. For each model the table indicates which doublet couples to which fermion type.*

scenario arises when considering the coupling of the lightest Higgs boson (h) to fermions. If the mixing angle $\alpha \to \pi/2$ then the coupling vanishes leaving the heavier CP-even Higgs boson (H) as the sole provider of mass to fermions. In this scenario h is described as *fermiophobic* and couples exclusively to bosons. In Type-II models, the doublet ϕ_1 couples to d-type quarks whilst ϕ_2 couples to u-type quarks and leptons. In Type-III models, ϕ_2 couples to both u-type quarks and leptons whilst ϕ_1 couples to d-type quarks. Finally, in Type-IV models ϕ_2 couples only to quarks and ϕ_1 couples only to leptons. Type-II 2HDMs have received significantly more attention in literature as the Yukawa La-

grangian of this model can be expressed in an invariant form under Supersymmetric transformations. For example, the Minimal Supersymmetric extension of the Standard Model (MSSM) is a constrained version of a Type-II 2HDM [31, 32]. For all of the above models, the coupling of the heavier Higgs boson, H, to fermions is obtained by an interchange $\cos\alpha \leftrightarrow -\sin\alpha$.

As highlighted above, Type-I models can exhibit fermiophobic behaviour in the limit that $\alpha \to \pi/2$. In this limit the coupling of h to fermions vanishes. Additionally, H has Standard Model-like couplings to fermions enhanced by a factor $1/\sin\beta$. Thus, in the fermiophobic limit, the phenomenology of the Standard Model is more closely reproduced by H. It is interesting to note the phenomenology in the limits of $\beta = 0$ or $\pi/2$. If $\beta = 0$ then h acquires Standard model couplings to vector bosons whilst remaining fermiophobic. If $\beta = \pi/2$ then h is not only fermiophobic but also bosophobic and can only couple at tree-level to scalars.

However, the term fermiophobic must be used carefully. This is to say that whilst $\alpha \to \pi/2$ prohibits tree-level decays to fermions it does not exclude the possibility of vector boson mediated decays to fermion pairs via scalar and vector boson loop decays. However, it turns out that the contributions from such decays are negligible compared to tree level decays to gauge bosons [33].

2.2 Fermiophobic Higgs Bosons at the LHC

Experiments both at LEP and the Tevatron have searched directly for evidence of a fermiophobic Higgs boson but as of yet no evidence has been found. With the unprecedented luminosities and collision energies to be provided by the LHC there has never been a better chance of discovering a fermiophobic Higgs boson. Whilst it is noted there are several production mechanisms for fermiophobic Higgs bosons, only the production via gluon-fusion is discussed in the context of this thesis. In particular, discussion will only pertain to a new channel with multiple photons in the final state first proposed in Reference [28].

2.2.1 Fermiophobic Higgs Boson Production via Gluon-Fusion

At the LHC the dominant production mechanism for fermiophobic Higgs bosons is gluon-fusion. Since no tree-level couplings between h and fermions exist, the process $gg \to \mathrm{h}\,X$, where $X = \mathrm{h},\mathrm{H},A$ can only proceed via the diagrams seen in Figure 2.1. Consequently, for the processes $gg \to \mathrm{hh}$ and $gg \to \mathrm{Hh}$ just two diagrams exists per process. Contributions from the Z-boson s-channel exchange have been shown to be negligable [28] and thus the processes $gg \to \mathrm{hh}$ and $gg \to \mathrm{Hh}$ are directly proportional to the scalar couplings g_{Hhh} and g_{HHh} respectively. The third process $gg \to A\mathrm{h}$ has

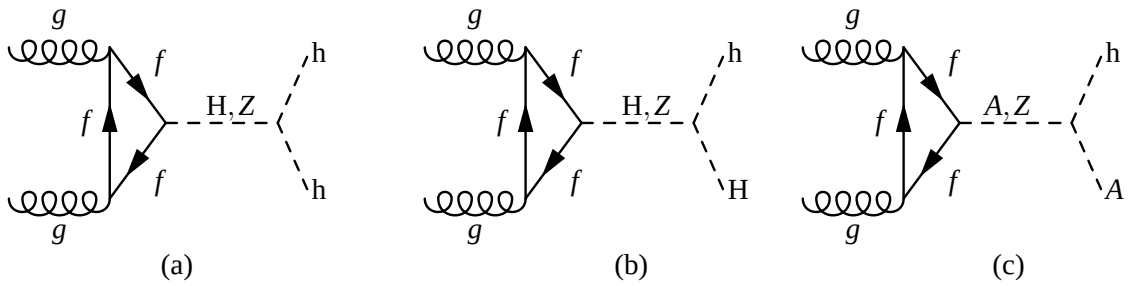

Figure 2.1: *Feynman diagram of fermiophobic Higgs boson production via gluon fusion at the LHC.*

additional contributions from Z-boson s-channel exchange and thus is sensitive to the pure scalar coupling $g_{AA\mathrm{h}}$ along with the gauge coupling $g_{ZA\mathrm{h}}$. However, in the context of this thesis discussion will only pertain to the first two processes and the reader is directed to Reference [28] for further discussion relating to the process $gg \rightarrow A\mathrm{h}$.

The relevant trilinear pure scalar couplings in the fermiophobic limit are as follows [28]:

$$g_{\mathrm{Hhh}} = -\frac{e\lambda_5 v^2 \sin\beta}{4m_W \sin\theta_w} \propto \lambda_5 \frac{\tan\beta}{\sqrt{1+\tan^2\beta}} \tag{2.4}$$

$$g_{\mathrm{HHh}} = \frac{e\lambda_5 v^2 \cos\beta}{4m_W \sin\theta_w} \propto \lambda_5 \frac{1}{\sqrt{1+\tan^2\beta}} \tag{2.5}$$

where $\lambda_5 = M^2/v^2$. Both of the couplings above are directly proportional to λ_5. As M^2 or equivalently here λ_5 is a measure of the discrete symmetry breaking, it is observed that in exact symmetry ($\lambda_5 = 0$) both couplings vanish. Both $gg \rightarrow \mathrm{hh}$ and $gg \rightarrow \mathrm{Hh}$ are mediated by the heavier CP-even Higgs boson which has couplings to fermions $g_{f\bar{f}\mathrm{H}}$ proportional to $1/\sin\beta$. Considering the cross-section for $gg \rightarrow \mathrm{hh}$, it is noted that the β dependence drops out of the cross-section since $\sigma_{gg\rightarrow\mathrm{hh}} \propto g_{f\bar{f}\mathrm{H}} \times g_{\mathrm{Hhh}}$. Therefore, $\sigma_{gg\rightarrow\mathrm{hh}}$ depends only on m_h, m_H and λ_5. For $gg \rightarrow \mathrm{Hh}$ the β dependence in the cross-section remains and for values of $\tan\beta > 1$ the process is suppressed and will not be considered further here.

Additional enhancements to $gg \rightarrow \mathrm{hh}$ production cross-section are observed with increasing values of λ_5 in the theoretically allowed range. Enhancements are also observed for production of a light fermiophobic Higss boson pair on threshold. This observed increase is attributed to the widening of the H width and a non-trivial relationship with λ_5. For light fermiophobic Higgs masses the production cross-section can reach a few hundred picobarn, whilst for masses up to 100 GeV/c^2 the cross-section is still larger than 0.1 picobarn. This would potentially result in thousands of events with just $10\,fb^{-1}$ of data at the LHC [28].

2.2.2 h_f Decay Modes

One of the distinguishing features of a light fermiophobic Higgs is its experimental signature. Due to the absence of tree-level decays to fermions the primary decay mode for a light fermiophobic Higgs is to a pair of photons via gauge boson loops. For a fermiophobic Higgs of mass up to 100 GeV$/c^2$ the branching ratio, BR(h $\rightarrow \gamma\gamma$) $\sim$100%, barring the region around $\lambda_5 = 0$ as seen in Figure 2.2. In

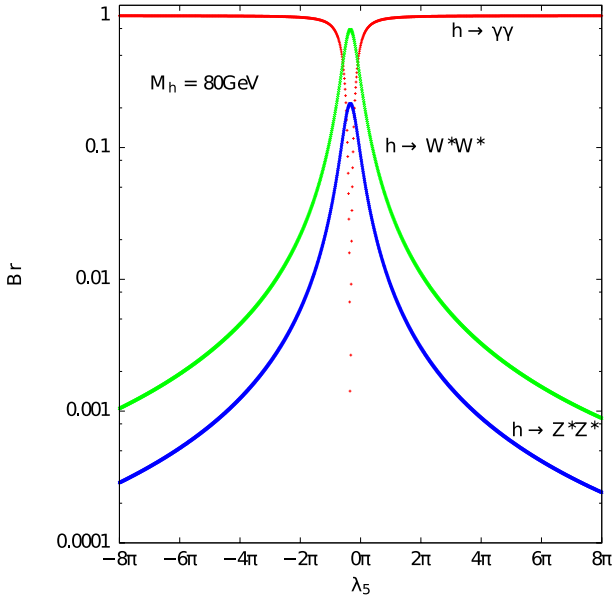

Figure 2.2: *Branching ratios of an 80* GeV$/c^2$ *fermiophobic Higgs boson as a function of* λ_5*, where* $\tan\beta = 10$ *and* $m_H = m_A = m_{H^\pm} = 150$ GeV$/c^2$*. From [28].*

comparison, for a SM Higgs boson mass of 80 GeV$/c^2$ the branching fraction to a pair of photons is of the order of 10^{-3}. Even for $m_h = 140$ GeV$/c^2$ the branching fraction to a pair of photons is of the order of the SM fraction. However, for masses greater than 140 GeV$/c^2$ decays to W boson pairs dominate. Hence, there is a clear enhancement in the fermiophobic model which can be exploited for Higgs boson masses up to $m_h = 140$ GeV$/c^2$. For the process, $gg \rightarrow$ hh, this results in a clean, identifiable signature comprising of four photons with high transverse momentum as seen in Figure 2.3.

2.3 Constraints on Fermiophobic 2HDM Scenarios

Both experimental and theoretical constraints limit the available regions of parameter space in which a fermiophobic Higgs boson may lie. Experimental searches for a fermiophobic Higgs particle have been performed at LEP and the Tevatron. As no evidence for its existence has been found mass

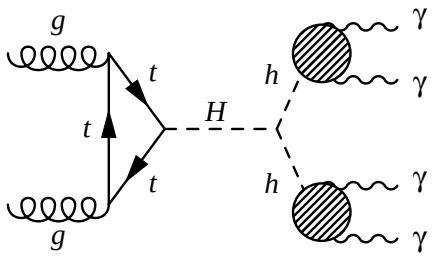

Figure 2.3: *Feynman diagram of the newly proposed fermiophobic Higgs channel.*

limits have been set in the context of a model benchmark. This benchmark assumes that the coupling of h to vector bosons is that of the Standard Model and that no decays to fermions are allowed. LEP, utilising the channel $e^+e^- \rightarrow \mathrm{h}Z$ with $\mathrm{h} \rightarrow \gamma\gamma$, determined that for this model the lower bound on the mass of a fermiophobic Higgs boson is $\mathrm{m_h} = 109.7\ \mathrm{GeV}/c^2$ [34, 35, 36, 37, 38]. Results from the Tevatron experiments utilising the channels $q\bar{q}' \rightarrow V^* \rightarrow \mathrm{h}V$, $p\bar{p} \rightarrow \mathrm{h}V \rightarrow \gamma\gamma + X$ and $p\bar{p} \rightarrow VV \rightarrow \mathrm{h} \rightarrow \gamma\gamma + X$, yield a lower bound of $\mathrm{m_h} = 106\ \mathrm{GeV}/c^2$ [39, 40]. Whilst the lower bounds may seem stringent it is still possible that a light ($\mathrm{m_h} << 100\ \mathrm{GeV}/c^2$) fermiophobic Higgs could have escaped detection. The assumption in the benchmark is that the hVV coupling is as in the Standard Model (i.e. $\beta = 0$) and consequently so is the branching ratio to photon pairs. However, if $\beta \neq 0$, then the coupling to vector bosons is suppressed relative to the SM and the branching ratio to photon pairs is significantly increased. Therefore, it is of interest to consider other possible production mechanisms of light fermiophobic Higgs bosons such as the one presented here.

Additional constraints come from searches at two LEP experiments, OPAL and DELPHI, in the channel $e^+e^- \rightarrow A\mathrm{h}$ [37, 34]. The results excluded the region: $m_A + \mathrm{m_h} < 160\ \mathrm{GeV}/c^2$. Therefore, a light fermiophobic Higgs is still possible providing A is sufficiently heavy.

Indirect searches from measuring the branching ratio of $B \rightarrow X_s\gamma$ impose a lower limit on the charged Higgs mass of $m_{H^\pm} > 316\ \mathrm{GeV}/c^2$ in Type-II models [41]. However, this limit does not affect Type-I models which are only mildly constrained by the LEP lower limit on the mass of the charged Higgs boson, $m_{H^\pm} > 80\ \mathrm{GeV}/c^2$ [42].

The final experimental constraint considered is the one arising from the Higgs sector contributions to the ρ-parameter [43]. The ρ-parameter, which is the relative strength of the neutral current and charged current interaction, is defined as:

$$\rho = \frac{m_W^2}{m_Z^2 \cos\theta_w} \tag{2.6}$$

and is predicted to take a value of 1. However, this parameter is sensitive to radiative corrections arising from the Higgs boson. Current precision measurements have limited $|\Delta\rho| < 10^{-3}$. For the fermiophobic model this implies that only a small splitting in mass is allowed between m_A and $m_{H^\pm}$. Thus, in scenarios considered in this thesis $m_A = m_{H^\pm} = 300$ GeV$/c^2$.

The fermiophobic model is also constrained by theoretical arguments. In the same fashion of the Standard Model the most restrictive constraints come from tree-level unitarity, vacuum stability and triviality. In the context of Type-I 2HDMs, the implication of triviality is such that no Higgs boson can have a mass exceeding 800 GeV$/c^2$. Bounds from perturbative unitarity in the 2HDMs restrict the parameters of the potential to $|\lambda_i| < 8\pi$ [44]. This in turn implies that the mass of the light Higgs boson is constrained by the value of $\tan\beta$ and M^2. Figures 2.4(a) and 2.4(b) show how the theoretical and current experimental limits restrict the parameter-space for the fermiophobic model.

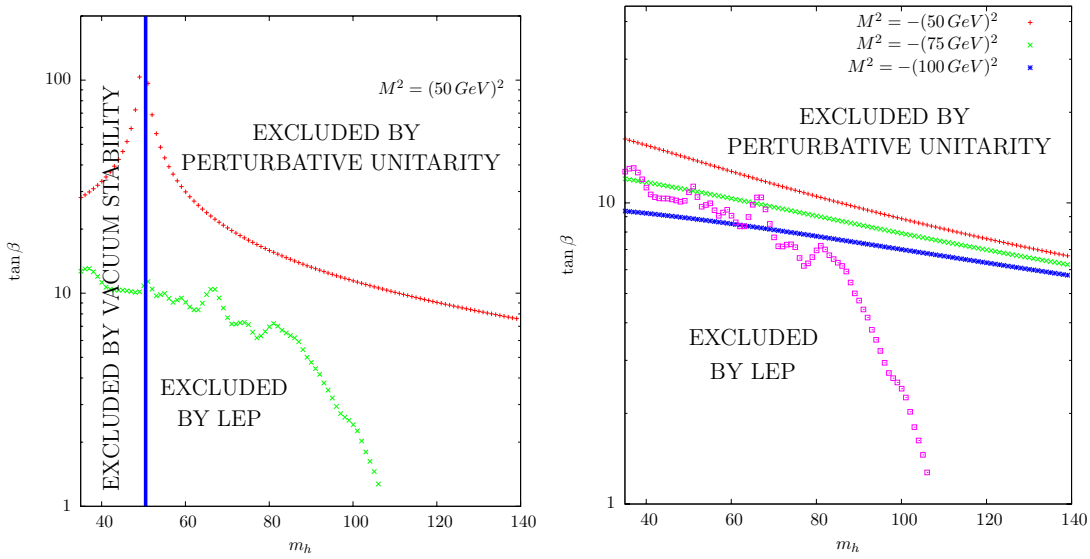

(a) $M^2 > 0$ (b) $M^2 < 0$

Figure 2.4: *Current theoretical and experimental constraints in the fermiophobic model* ($m_h, \tan\beta$) *parameter space. Exclusions are shown for 4 values of* M^2*, (a) one positive value and (b) for three negative values. It has been checked that for any allowed* ($m_h, \tan\beta$) *point that the mass of the heavy Higgs boson may take any value in the range* $2m_h \leq m_H \leq 600$ GeV$/c^2$*. From [45].*

For allowed regions of parameter space m_H can take any value between $2m_h \leq m_H \leq 600$ GeV$/c^2$. The upper limit is derived from the requirement that the channel $H \rightarrow AA$, where m_A has been fixed at 300 GeV$/c^2$, is closed. For positive values of M^2 there are constraints on the light Higgs boson mass arising from vacuum stability requirements. It should be noted that this lower bound is not fixed but varies linearly with M. No such limit is present for negative M^2 values.

In summary, the fermiophobic channel presented here allows large, yet to be excluded regions of

Parameter	**Allowed Range/Value**	**Comments**
m_h	$40 \leq \mathrm{m_h} \leq 140$ GeV$/c^2$	Lower bound depends on M^2 for $M^2 > 0$
m_H	$2m_h \leq \mathrm{m_H} \leq 600$ GeV$/c^2$	
m_A, $m_{H^\pm}$	300 GeV$/c^2$	
α	0	Fermiophobic limit
$\tan\beta$	See Figures 2.4(a) and 2.4(b)	Depends on M^2, $\mathrm{m_h}$
M^2	$M^2 = \pm(25\ \mathrm{GeV})^2, \pm(50\ \mathrm{GeV})^2,$ $\pm(75\ \mathrm{GeV})^2, -(100\ \mathrm{GeV})^2$	

Table 2.2: *Allowed ranges of the fermiophobic model parameters.*

parameter space to be probed. Rather than searching for a fermiophobic Higgs in a fully specified benchmark we consider the set of benchmarks as defined in Table 2.2. The prospects for discovery with this channel are presented in Chapter 7.

Chapter 3

The ATLAS Detector at the LHC

3.1 The Large Hadron Collider

The Large Hadron Collider (LHC) [46, 47] is a $\sqrt{s} = 14\,\text{TeV}$ proton-proton collider, situated at the European Organisation for Nuclear Research (CERN) 100m under the Swiss-Franco border in the old 27km long LEP tunnel. It has been designed to push back the frontiers of particle physics with its unprecedented high energy and luminosity. Protons will travel in opposite directions around the LHC, colliding at four interaction points up to 40 million times per second.

At each interaction point, collisions are recorded by purpose built detectors. There are two general purpose detectors: ATLAS (A Toroidal LHC ApparatuS); and CMS (Compact Muon Solenoid), whose primary focus is the search for new physics beyond the Standard Model along with two more specialised detectors: LHCb (Large Hadron Collider beauty experiment), specialising in b-quark physics; and ALICE (A Large Ion Collider Experiment), optimised to study heavy-ion physics.

Prior to protons being injected in the main LHC ring they must be accelerated using CERN's accelerator complex (see Figure 3.1). 50 MeV protons emanating from a linear particle accelerator, LINAC 2, are boosted to 1.4 GeV by the Proton Synchrotron Booster (PSB). Next, the protons are injected into the Proton Synchrotron (PS) where they are further boosted to an energy of 26 GeV before they are injected into the Super Proton Synchrotron (SPS). The SPS increases their energy to 450 GeV before they are finally injected into the main LHC ring. Here, the proton bunches are accumulated, accelerated (over a period of 20 minutes) to their peak 7 TeV energy. This is achieved by varying the field in the 1,232 superconducting dipole magnets from 0.54 T to 8.4 T. The superconducting dipole magnets keep the beams on a circular path, whilst some of the 392 quadrupole magnets in use throughout the LHC are used to focus the beams at the interaction points.

The LHC technical design [47] has been motivated by the search for rare physics processes. The

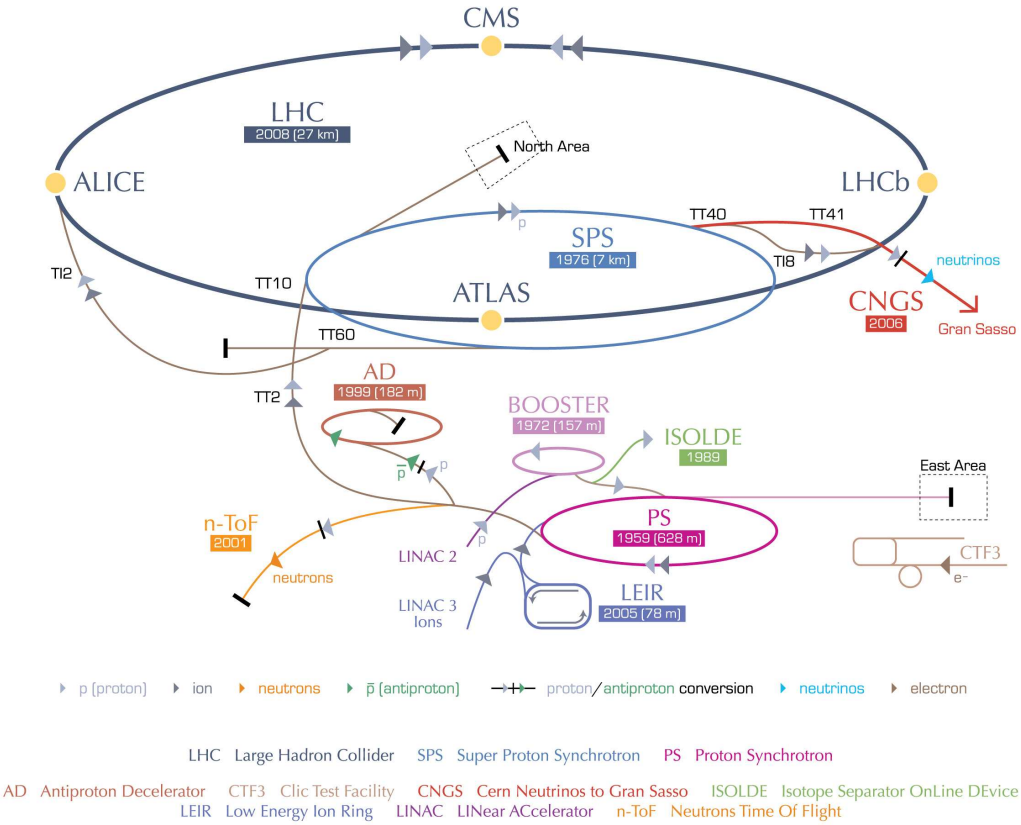

Figure 3.1: *Schematic view of the CERN accelerator complex. From [48]*

rate of collisions for any given process is given by $R = \mathcal{L} \times \sigma$, where $\mathcal{L}$ is the machine's instantaneous luminosity (effectively the flux of particles per unit area, per unit time) and σ is the cross-section of the physics process. The cross-section is purely a physics quantity, which is proportional to the probability for the considered process to occur, whilst the luminosity depends only on machine parameters. To achieve a peak luminosity of $10^{34}\,\mathrm{cm}^{-2}\mathrm{s}^{-1}$ a typical beam will contain 2808 bunches, with each bunch containing $\sim 1.15 \times 10^{11}$ protons. The spacing between consecutive bunches is 25 ns or equivalently 7.5 m. Consequently, the interaction between the two beams is not a continuous flow, but is in fact discrete. Bunches are crossed at a rate of 40 MHz, where an individual bunch crossing is defined as an *event*.

The vast majority of collisions at the LHC will be inelastic proton-proton collisions, which at the nominal LHC energy ($\sqrt{s} = 14$ TeV) have a cross-section of $\sigma = 79\,\mathrm{mb}$ [49]. This cross-section together with an instantaneous luminosity of $10^{34}\,\mathrm{cm}^{-2}\mathrm{s}^{-1}$ means that a rate of nearly 1 GHz is expected for proton-proton collisions, with an average of 25 interactions per bunch-crossing. Most of these interactions, termed *soft*, stem from long-range proton-proton interactions and consequently lit-

tle momentum is transferred between the partons. These soft interactions are therefore superimposed upon on any hard interaction (scattering) and can as such been seen as noise. This effect, known as pile-up, introduces a potentially serious background to any search for new physics and therefore must be well understood.

A landmark was finally reached on the morning of the 10^{th} September 2008, when the first beam was circulated through the LHC collider. Protons were successfully circulated around the beam pipe in stages, one sector at a time. Initially, the beam was circulated in a clockwise direction, followed by a successful circulation of the beam anti-clockwise. However, on the 19^{th} of September 2008, a quench occurred in approximately 100 bending magnets located in sectors 3 and 4, causing a loss of approximately six tonnes of liquid helium. The fault was traced to an electrical connection between a dipole and a quadrupole magnet. The decision was taken to warm up the machine, replace 53 affected magnets and install extra pressure relief valves.

Approximately a year later, the LHC began circulating beams. On the 30^{th} of November 2009, a new world record was set when twin beams were accelerated up to energies of 1.18 TeV, eclipsing the previous record of 0.98 TeV set by the US Fermi National Accelerator Laboratory's Tevatron collider in 2001. Following this milestone, there was an extended data-taking period with collisions at centre-of-mass energies of $\sqrt{s} = 900$ GeV and $\sqrt{s} = 2.36$ TeV providing much anticipated data for the experiments. Before the energies could be increased, a shut-down was required to ensure that the machine protection systems could cope with the increased electrical currents in the magnets. On the 30^{th} of March 2010, the LHC set a record for high energy collisions, by colliding 3.5 TeV beams. The current plan foresees a running period of 18-24 months at a centre-of-mass energy of $\sqrt{s} = 7$ TeV, before a year-long shut-down to prepare for $\sqrt{s} = 14$ TeV collisions.

3.2 The ATLAS Detector

The ATLAS detector [50, 49] is the largest of the four main detectors. It stands at 25m in height, 44m in length and weighs approximately 7000 tonnes. It was designed as a general purpose detector with the ability to detect a broad range of new physics signals.

ATLAS, as seen in Figure 3.2, is comprised of three main sub-detector systems each of which have their own specific role within the whole detector. Working from inside out:

- The inner detector has the role of determining the trajectory of charged particles, finding primary or secondary vertices and measuring the momentum of charged particles thanks to a magnetic field of 2T supplied by the central solenoid.

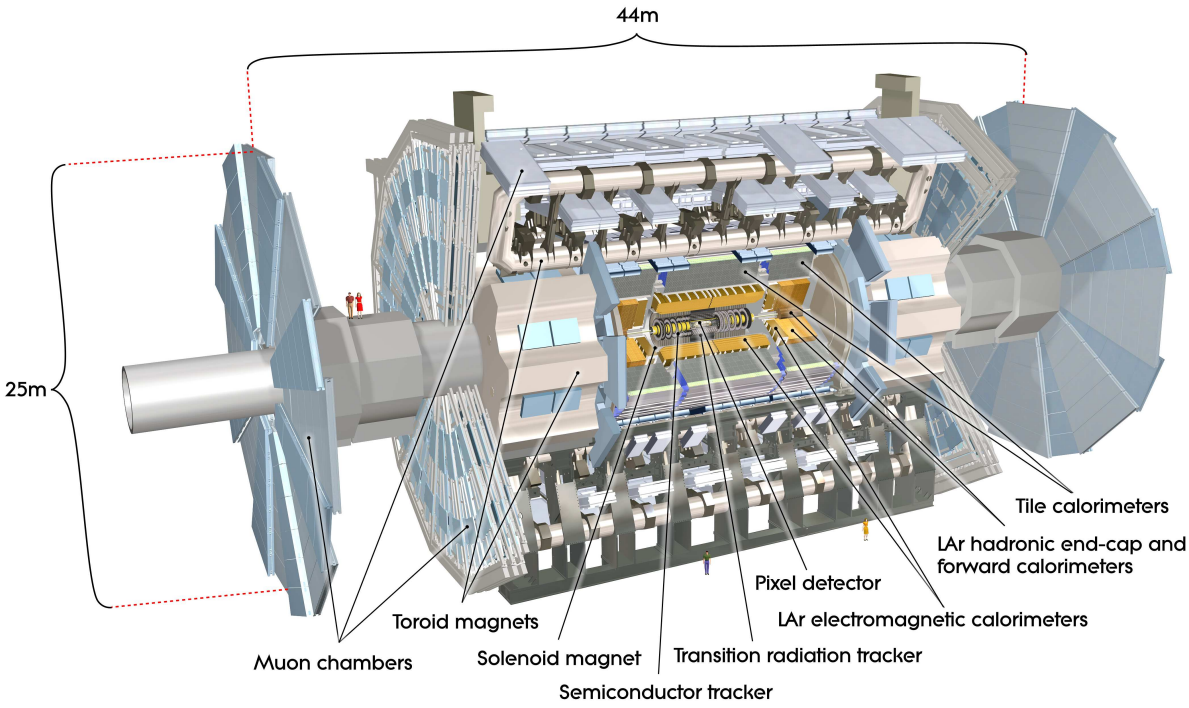

Figure 3.2: *A cut away view of the ATLAS detector. From [49]*

- The electromagnetic, hadronic and forward calorimeter systems have the job of accurately measuring the energy and direction of electrons, photons and jets.

- The muon spectrometer's role is to measure the momentum of muons independently from the inner detector, by using the magnetic field of the toroidal magnets which is orthogonal to the field of the solenoid magnet.

The coordinate system used by ATLAS is defined with the detector centred around the nominal interaction point $(x,y,z) = (0,0,0)$, where the x-axis points towards the centre of the main LHC ring, the y-axis points vertically upwards towards the surface and the z-axis points down the beam line towards LHCb. Since the detector is cylindrical in design it is conventional to define r as the transverse radius from the beam axis, θ as the polar angle as measured from the beam axis and ϕ as the azimuthal angle around the beam axis in the x,y plane. Instead of θ, the polar angle is often denoted in terms of the pseudorapidity η defined as:

$$\eta = -ln\left(tan\left(\frac{\theta}{2}\right)\right). \tag{3.1}$$

This is a dimensionless quantity which is derived from taking the relativistic limit of the rapidity:

$$y = -\frac{1}{2} ln \left(\frac{E + p_z}{E - p_z} \right). \tag{3.2}$$

Differences in rapidity (y_1-y_2) are independent of Lorentz boosts along the z-axis. The reason the pseudo-rapidity is preferred as a spatial coordinate is because it only depends on the trajectory of a particle rather than the energy. Low values of $|\eta|$ are referred to as *central* and high values of $|\eta|$ are referred to as *forward* as they are close to the beam pipe.

Since energy and momentum measurements along the z-axis are not particularly useful[1], energy and momentum are usually quoted in the transverse x, y plane. Transverse energy, E_T, and transverse momentum, p_T, are defined as:

$$E_T = \sqrt{E_x^2 + E_y^2} \tag{3.3a}$$

$$p_T = \sqrt{p_x^2 + p_y^2} \tag{3.3b}$$

where E_{x} and E_{y} are the x and y components of the particle's energy and p_{x} and p_{y} are the x and y components of the particle's 3-momentum vector.

The following sections introduce the main sub-detector systems of the ATLAS detector. The original technical design report (TDR) [50] and a more recent description, including the expected performance of the detector, [49], provide more detailed information.

3.2.1 The Inner Detector

The main task of the ATLAS Inner Detector (ID) is to accurately measure the momentum and position of charged particles throughout its volume. It must be able do this under the most extreme of conditions, with approximately 1000 particles emanating from the interaction point every 25ns [49]. In order to accurately measure the momentum and position of charged particles, three complementary tracking detectors are placed around the beam pipe as seen in Figure 3.3. The ID is immersed in a 2T magnetic field, supplied by the central solenoid, causing charged particles to bend. The direction of curvature reveals the particle's charge and the degree of curvature allows a precise measurement of its momentum.

[1] This is because the exact p_z of a particle is unknown due to longitudinal boosts.

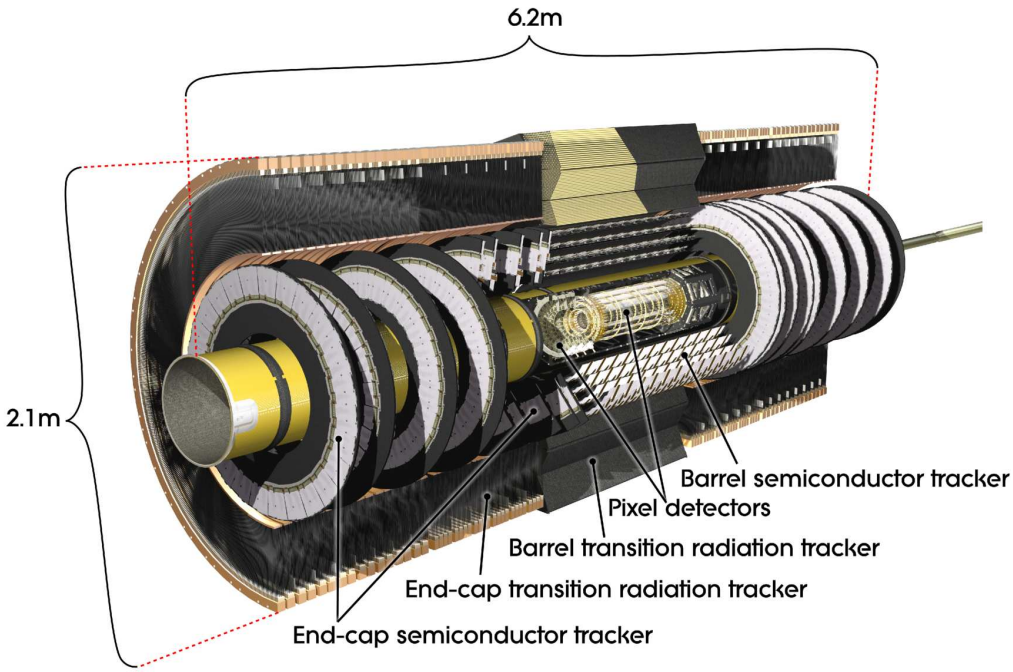

Figure 3.3: *Cut-away view through the barrel of ATLAS inner detector, indicating the main components of the ID. From [49].*

3.2.1.1 The Pixel Detector

The silicon pixel detector provides the most accurate tracking capabilities of the ID, and sits as the closest detector to the beam pipe. Its role is to measure with precision tracks emanating from the interaction point and identify short lived particles via primary and secondary vertices. When a charged particle passes through a silicon pixel, electron-hole pairs are created. These pairs drift under the influence of a bias voltage and a signal is induced on the electrode, which is read as a *hit* by the external electronics.

As seen in Figures 3.4 and 3.5, the barrel of the pixel detector contains three cylindrical silicon layers located at radii of 50.5, 88.5 and 122.5 mm from the beam axis. The first layer is called the B-layer and plays an important role of the identification of *b*-quark decays, and the identification of photon conversions ($\gamma \rightarrow e^+e^-$). The B-layer, due to its proximity to the interaction point, will receive significant amounts of radiation damage. The approximate lifetime of this layer is expected to be three years at high luminosity [49]. Therefore, it has been designed in such a way that it can be replaced easily. In the end-caps of the pixel detector, there are three silicon disk layers located at distances of $z = \pm 495$, ± 580 and ± 650 mm. Therefore, any charged particle passing through the coverage ($|\eta| < 2.5$) of the pixel detector will produce at least three hits.

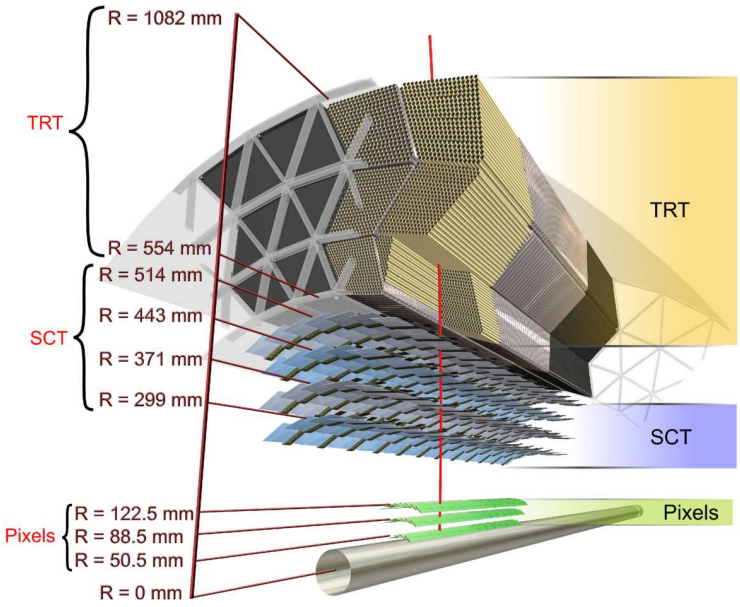

Figure 3.4: *Cross-section of the ATLAS inner detector barrel indicating the radii of the layers of the component sub-detectors. The passage of a charged particle travelling through the inner detector is shown in red.*

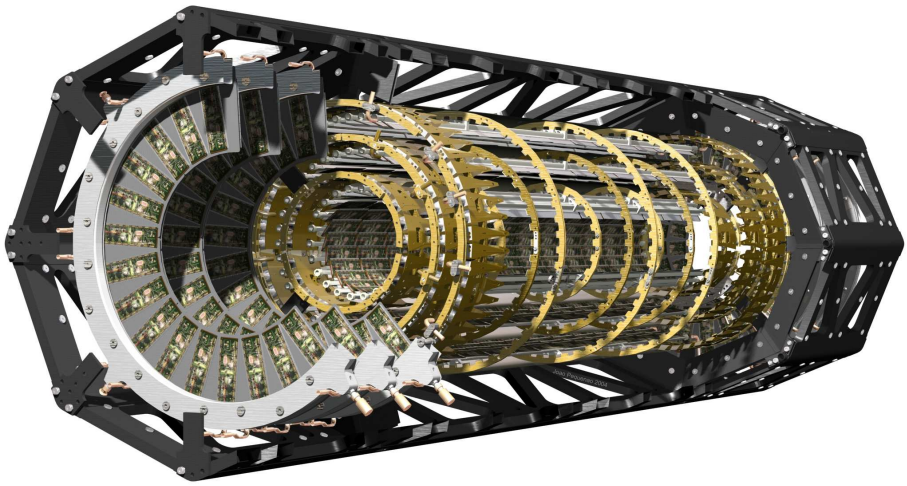

Figure 3.5: *Computer generated cut away view of the ATLAS pixel detector and its support structure. Three cylindrical layers in the barrel can be seen with the three disk layers making up each end-cap.*

The pixel detector contains 1744 pixel sensor modules which are held together with a carbon chassis, which also allows liquid coolant to dissipate the heat from the readout electronics. Modules

in the barrel are arranged in identical staves (or *shells*) and in the end-caps are arranged in identical *sectors*. Each module is a rectangular silicon wafer, 19 mm×63 mm in size with some 47232 pixels on each wafer. However, due to space requirements there are only 46080 readouts from each stave. This equates to approximately 80 million readout pixels in the detector, each just 400 μm×50 μm in size. The modules also overlap each other to ensure a good hermeticy and are inclined at an azimuthal angle of 20 degrees. A configuration like this provides the high granularity that is required for identifying individual particle tracks in high track density environments. The pixel detector has a nominal resolution of 10 μm in the $r\phi$ direction and 115 μm in the z direction. The only reason pixel detector technology is not used more widely throughout the ATLAS detector is due to its high-cost of production.

3.2.1.2 The Semi-Conductor Tracker

The semi-conductor tracker (SCT) or silicon micro-strip tracker is the middle component of the inner detector. It is similar in design and concept to the pixel detector and adds complimentary coverage over the range $|\eta| < 2.5$. It consists of 4088 modules distributed over four layers in the barrel and nine disks in each end cap. Each module consists of four single-sided silicon microstrip sensors. Two sensors are glued back-to-back, with a 40 mrad stereo rotation, thus allowing two-dimensional track reconstruction. Whilst all modules in the SCT are similar in construction, modules used in the barrel differ in geometry to the modules used in the end-caps. All modules in the barrel are identical, but due to the circular geometry of the disks, end-cap modules use wedge shaped sensors. There are three types of end-cap modules: inner, middle and outer. In all, the detector contains 61 m^2 of silicon sensors, with 6.2 million readouts.

A charged particle passing through the SCT will pass through at least eight layers of silicon, creating at least four two-dimensional "space-points" along its trajectory. The SCT has a nominal resolution of 16 μm in the $r\phi$ direction and 580 μm in the z direction.

3.2.1.3 The Transition Radiation Tracker

The transition radiation tracker (TRT) is the outermost detector in the ID and is both a tracker and a transition radiation detector. It contains 73 layers of drift tubes (or straws) in the barrel and 160 in the end-caps. All charged tracks with a $p_T > 0.5$ GeV$/c$ will pass through at least 36 straws, with that number decreasing to at least 22 straws in the barrel-end-cap transition region ($0.8 < |\eta| < 1.0$).

Each drift tube is 4 mm in diameter and is made of two 35 μm thick Kapton multi-layer films bonded back-to-back. A special film coating of aluminium and graphite-polyimide is applied to

achieve good electrical conductivity. A gold plated tungsten wire, with a diameter of 31 μm, is placed in the centre of the tube and the tube is filled with a mixture of gas (70% xenon, 27% CO_2 and 3% O_2). The wire and the drift tube wall act as the anode and cathode. A charged particle passing through the straw will ionize the gas and the resultant cascaded charge collected on the anode. This signal is then interpreted as a "hit" much as in the same way the pixel and SCT detectors interpret hits. The tubes are surrounded with fibres of polypropylene which act as radiators. When relativistic particles cross through the interface between two materials with differing dielectric constants, they emit X-rays known as transition radiation. These transition radiation photons are absorbed by the xenon rich gas, producing additional ionization electrons, which increase the signal collected on the anode. The intensity of the radiation is proportional to the particle's Lorentz factor, $\gamma = E/m$. Therefore, for particles of the same energy, a lighter particle, such as an electron, will on average produce more ionization than a heavier particle, such as a pion. Thus, electrons can be discriminated from pions by the presence of higher-threshold hits.

The barrel of the TRT is divided into three cylindrical layers of 32 modules each. Each layer uses a different type of module, differing in size and number of straws. Each straw is 144cm long and is orientated parallel to the beam axis. The space between the straws is filled with 15 μm diameter polypropylene fibres. The end-caps consist of two sets of independent wheels, with the inner set containing 12 wheels and the outer set containing eight wheels. Each wheel has eight layers, with each layer containing 768 drift tubes, 37 cm in length, arranged radially. The tubes are surrounded with 15 μm thick polypropylene radiator foils separated by a polypropylene net. In all the TRT has around 351,000 read-out channels.

3.2.2 Calorimetry

The calorimeter system, as seen in Figure 3.6, is situated just outside the solenoidal magnet that surrounds the inner detector. It is designed such that incident particles deposit their energy within the high-density calorimeter material, predominantly through the creation of particle showers whose energies are absorbed and measured. There are three main components: an inner electromagnetic calorimeter (ECAL), an outer hadronic calorimeter (HCAL) and the forward calorimeter (FCAL). The ATLAS calorimeter system has been designed to be fully ϕ-symmetric and provide coverage up to $|\eta| < 4.9$. The ECAL is the innermost component of the system and is housed in one barrel and two end-cap cryostats. The barrel cryostat only contains the ECAL barrel, whereas the two end-cap cryostats each contain an ECAL end-cap (EMEC), a HCAL end-cap (HEC) and an FCAL to cover the region closest to the beam.

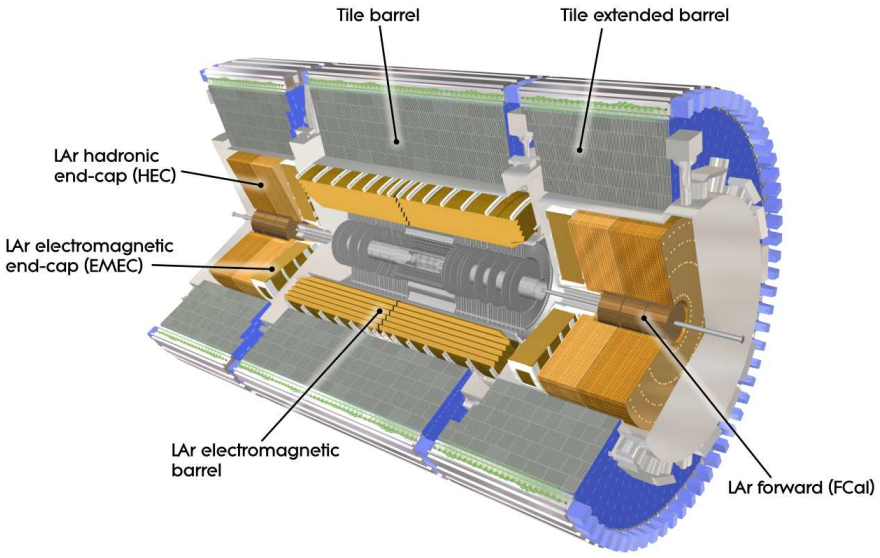

Figure 3.6: *Schematic view of the ATLAS calorimetry system. From [49].*

Since calorimeters use the interaction of the incident particles with material to measure the energy, all particles are detected, including electrically neutral ones with the exception of weakly interacting particles (e.g. neutrinos). Different calorimeter designs are used for particles interacting via electromagnetic (EM) processes and for particles interacting via the strong force. Each calorimeter is typically optimized to measure particles produced by one type of shower.

Electromagnetic showers occur when a high-energy photon, electron or positron (called the primary particle) enters a medium and, via alternating pair-production ($\gamma \rightarrow e^+e^-$) and bremsstrahlung ($e \rightarrow \gamma e$), produce a cascade of electromagnetic particles. The shower will continue until the energy falls below the critical energy, at which point the particles will lose their energy mainly through ionization. The depth of a shower can be described by the relation [51]:

$$X = X_0 \frac{ln\,(E_0/E_c)}{ln\,2}, \tag{3.4}$$

where X_0 is the radiation length, defined as the mean distance over which an electron will lose all but a fraction $1/e$ of its energy by bremsstrahlung (or 7/9 of the mean free path for pair-production by a high-energy photon), E_0 is the initial energy and E_c is the critical energy. Thus the longitudinal length of the shower is proportional to the logarithm of the initial energy. The characteristic radius of the shower, the Moliere radius, is used as a measure of the transverse dimension of the shower. Formally, the Moliere radius is defined as the radius of a cylinder in which 90% of the shower energy will be fully contained and is independent of the energy of the initial particle.

Hadronic showers are produced in a similar way to EM showers, but with different particle interactions involved. Quarks and gluons, produced from a high-energy collision cannot exist individually due to colour confinement. Instead they hadronise, a process whereby they combine with quarks and antiquarks, spontaneously created from the vacuum, to form hadrons. As a result, instead of seeing the individual quarks in detectors, *jets* of many colour-neutral particles (mesons and baryons), clustered together, are observed. When these hadrons enter the dense detector media, they lose energy via inelastic collisions with nuclei, creating secondary strongly interacting particles. This process is repeated and a hadronic shower formed. The depth of a hadronic shower can be characterised by the interaction length, or mean free path, λ, of a material. In comparison with EM showers, for a given material, λ is much greater than X_0 (radiation length). Consequently hadronic showers are generally broader and deeper than EM showers. On average, approximately 1/3 of the particles produced in the first hadronic interaction are electromagnetic, predominately due to the decay of neutral pions ($\pi^0 \rightarrow \gamma\gamma$) [49].

All of ATLAS's calorimeters are sampling calorimeters. The sampling calorimeter works by using one material for shower development, known as a passive medium, and another to measure the shower energy, known as an active medium. Typically, passive media require a high-density material such as lead whereas the active media require a material with the ability to produce a signal, usually via scintillation or ionization. The calorimetry system of the ATLAS detector is based on two different technologies: the ECAL, the FCAL and the HEC use liquid argon (LAr) as the active medium, while the barrel region of the hadronic calorimeter uses scintillating plastic tiles. Reasons for the choices of each type of material are given in the individual calorimeter sections which follow.

The calorimeters must provide good containment for the EM and the hadronic showers to prevent leakage into the encompassing muon system. The ECAL is approximately 22 radiation lengths (X_0) thick in the barrel and approximately 24 X_0 in the end-caps. This thickness, together with the expansive η coverage, ensures a good missing transverse energy measurement which is important for the detection of many physics signatures.

3.2.2.1 The LAr Electromagnetic Calorimeter

The ECAL is a sampling calorimeter made of several layers of lead (passive medium) and liquid argon (active medium). Lead was chosen as the absorber since it has a small radiation length (0.56 cm), causing the shower to evolve quickly, whilst liquid argon is used due to its intrinsic radiation hardness and stability of response over time. The result is good temperature stability and an excellent linear response to photons with energies ranging from a few MeV up to a few GeV.

EM Calorimeter	**Barrel**		**End-cap**	
Coverage	$\|\eta\| < 1.475$		$1.375 < \|\eta\| < 3.200$	
Longitudinal Segmentation	3 Samplings	$\|\eta\| < 1.350$	3 Samplings	$1.500 < \|\eta\| < 2.500$
	2 Samplings	$1.350 < \|\eta\| < 1.475$	2 Samplings	$1.375 < \|\eta\| < 1.500$
			2 Samplings	$2.500 < \|\eta\| < 3.200$
Granularity ($\Delta\eta \times \Delta\phi$)				
1^{st} Layer	0.025/8×0.1	$\|\eta\| < 1.400$	0.050×0.1	$1.375 < \|\eta\| < 1.425$
	0.025×0.025	$1.400 < \|\eta\| < 1.475$	0.025×0.1	$1.425 < \|\eta\| < 1.500$
			0.025/8×0.1	$1.500 < \|\eta\| < 1.800$
			0.025/6×0.1	$1.800 < \|\eta\| < 2.000$
			0.025/4×0.1	$2.000 < \|\eta\| < 2.400$
			0.025×0.1	$2.400 < \|\eta\| < 2.500$
			0.1×0.1	$2.500 < \|\eta\| < 3.200$
2^{nd} Layer	0.025×0.025	$\|\eta\| < 1.400$	0.050×0.025	$1.375 < \|\eta\| < 1.425$
	0.075×0.025	$1.400 < \|\eta\| < 1.475$	0.025×0.025	$1.425 < \|\eta\| < 2.500$
			0.1×0.1	$2.500 < \|\eta\| < 3.200$
3^{rd} Layer	0.050×0.025	$\|\eta\| < 1.350$	0.050×0.025	$1.500 < \|\eta\| < 2.500$
Presampler	**Barrel**		**End-cap**	
Coverage	$\|\eta\| < 1.520$		$1.500 < \|\eta\| < 1.800$	
Granularity ($\Delta\eta \times \Delta\phi$)	0.025×0.1	$\|\eta\| < 1.520$	0.025×0.1	$1.500 < \|\eta\| < 1.800$
Hadronic tile	**Barrel**		**Extended Barrel**	
Coverage	$\|\eta\| < 1.000$		$1.500 < \|\eta\| < 1.800$	
Number of layers	3		3	
Granularity ($\Delta\eta \times \Delta\phi$)	0.1×0.1		0.1×0.1	
Last layer	0.2×0.1		0.2×0.1	
LAr hadronic end-cap			**End-cap**	
Coverage			$1.500 < \|\eta\| < 3.200$	
Number of layers			4	
Granularity ($\Delta\eta \times \Delta\phi$)			0.1×0.1	$1.500 < \|\eta\| < 2.500$
			0.2×0.2	$2.500 < \|\eta\| < 3.200$
LAr forward calorimeter			**Forward**	
Coverage			$3.100 < \|\eta\| < 4.900$	
Number of layers			3	
Granularity ($\Delta\eta \times \Delta\phi$) [cm]				
1^{st} Layer			3.0×2.6	$3.150 < \|\eta\| < 4.300$
			∼four times finer	$3.100 < \|\eta\| < 3.150$
			∼four times finer	$4.300 < \|\eta\| < 4.830$
2^{nd} Layer			3.3×4.2	$3.240 < \|\eta\| < 4.500$
			∼four times finer	$3.200 < \|\eta\| < 3.240$
			∼four times finer	$4.500 < \|\eta\| < 4.810$
3^{rd} Layer			5.4×4.7	$3.320 < \|\eta\| < 4.600$
			∼four times finer	$3.290 < \|\eta\| < 3.320$
			∼four times finer	$4.600 < \|\eta\| < 4.750$

Table 3.1: *Pseudorapidity coverage, transverse granularity and longitudinal segmentation of the ATLAS calorimeters. From [49].*

The ECAL is made of two half-barrels covering the central region, $|\eta| < 1.375$, and two endcaps, themselves made out of a larger external wheel covering the region $1.375 < |\eta| < 1.5$ and a smaller internal wheel covering the region $2.5 < |\eta| < 3.2$. Each wheel contains eight modules and each half barrel contains sixteen modules. The absorbers and electrodes are arranged in an accordion geometry. Using such a geometry has the advantages that a fast response time is achieved, whilst minimising the noise, and total hermeticy in ϕ is provided. The modules are composed of alternating lead absorber plates separated from the copper-Kapton electrodes by 2.1 mm of liquid argon.

The ECAL is segmented into 173312 cells which point towards the nominal interaction point and vary in size according to sampling and pseudorapidity. The segmentation in η is achieved by etched patterns in the copper layers of the readout electrodes and the segmentation in ϕ is achieved by ganging together appropriate numbers of readouts from adjacent layers. The modules are arranged in three distinct sampling layers (inner, middle and outer: see Figure 3.7) over the precision-measurement region ($0 < |\eta| < 2.5$), two in the overlap region ($1.375 < |\eta| < 1.5$) between the barrel and the EMEC, and two in the extended-η region ($2.5 < |\eta| < 3.2$).

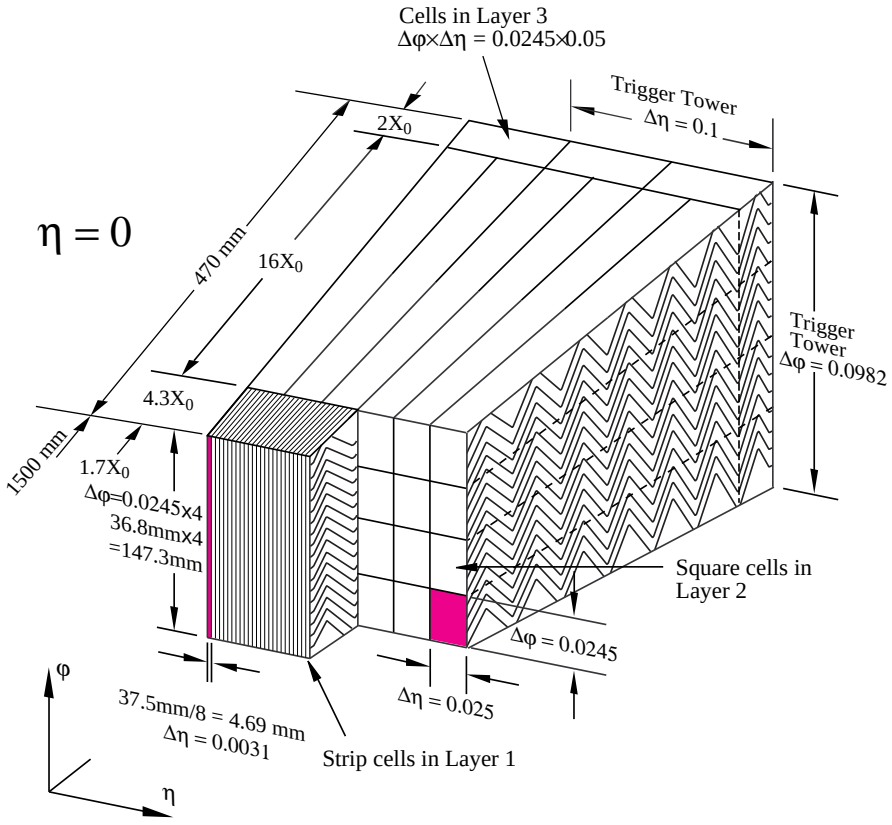

Figure 3.7: *Schematic view of a barrel module at $\eta = 0$. The granularities in η and ϕ are shown for each of the three layers. From [49].*

The first sampling layer has the finest granularity: $\Delta\eta \times \Delta\phi = 0.025/8 \times 0.1$ for $|\eta| < 1.4$. The fine granularity allows precise measurement of the impact point of the primary particle, which is important in the discrimination between spatially close showers as well as discrimination between photons and π^0. Table 3.1 lists the granularities across all the η ranges for all components of the calorimeter system.

The second calorimeter layer is designed to contain the majority of an electromagnetic shower produced by a photon with an energy of 50 GeV (the typical energy of a photon from the decay of a Higgs boson with a mass of 120 GeV$/c^2$). A granularity of $\Delta\eta \times \Delta\phi = 0.025 \times 0.025$ in the second layer allows, in association with the first layer, measurement of the incident angle of a particle in η and thus the determination of the axis of the shower development.

The third sampling layer has a coarser granularity since the majority of an EM shower is absorbed by the second layer. Its role is to estimate the amount of energy escaping from the detector, caused by late showering particles.

Completing the ECAL are presamplers, situated just before the first sampling layer and just after the cryostat. They consist of essentially a thin layer of liquid argon with readout electrodes and are present to correct for the energy lost by a particle in passing through the inner detector, solenoid and cryostat wall.

The region between the barrel and the endcap ($1.37 < |\eta| < 1.52$) is not used for precision physics due to the large amount of material preceding the ECAL. This region is commonly referred to as the *crack* region since particles in this region may not be seen by the detector.

The ECAL performance was studied in a test beam with electrons and positrons of energy between 1 and 250 GeV. The energy resolution was found to be [49]:

$$\frac{\sigma_E}{E} = \frac{10.1\%}{\sqrt{E\,[\,\mathrm{GeV}]}} \oplus 0.2\% \tag{3.5}$$

which is in accordance with the strict design specifications of the ECAL. These specifications required that the ECAL must have sufficient energy resolution to be able to determine the mass of a low mass Higgs boson (m_H = 90-180 GeV$/c^2$), decaying to pairs of photons or Z bosons, to within 1%.

3.2.2.2 The Hadronic Calorimeter

The hadronic calorimeter (HCAL) measures the energies of hadronic jets initiated from quarks and gluons. It consists of two parts: the Tile calorimeter (tile barrel and extended barrel) and the LAr hadronic end-cap (HEC). The HCAL is designed to be thick enough to absorb all the energy of a

hadronic shower, thus keeping the rate of punch-throughs into the muon system to a minimum. On the other hand, the calorimeter must not be too thick otherwise there will be multiple scattering of muons which will degrade the muon resolution in the muon spectrometer. The total thickness of the HCAL is 11λ (including 1.5λ from the outer support structure) at $\eta = 0$, a level at which it has been shown by measurements and simulation to sufficiently reduce the number of particles other than muons (and neutrinos) to a manageable level. The large and complete η coverage guarantees a good missing transverse energy measurement, which is crucial for a broad set of physics signatures.

The Tile Calorimeter

The hadronic tile calorimeter is a sampling calorimeter consisting of 14mm thick steel absorber plates interleaved with 3mm thick plastic scintillating tiles. Hadronic particles entering the calorimeter initiate hadronic showers in the steel plates. As the showers pass through the scintillating tiles, they induce the production of scintillation light. Each tile is read out by two wavelength shifting fibres, which feed the light into photomultiplier tubes.

The tile calorimeter is placed just outside the ECAL and consists of a barrel, covering the region $|\eta| < 1.0$, and an extended barrel, covering the region $0.8 < |\eta| < 1.7$. Both barrels have an internal radius of 2.28 m and an outer radius of 4.25 m. They are segmented azimuthally into 64 modules and longitudinally into three layers with interaction lengths 1.5λ, 4.1λ and 1.8λ in the barrel and 1.5λ, 2.6λ and 3.3λ in the extended barrel. The granularity in the first two layers is $\Delta\eta \times \Delta\phi = 0.1 \times 0.1$ and in the third layer is $\Delta\eta \times \Delta\phi = 0.2 \times 0.1$. The total number of channels is 4672: 2880 in the barrel and 1792 in the extended barrel.

The tile calorimeter performance was studied in a test beam with single pions of energy between 20 and 350 GeV. The energy resolution was found to be [49]:

$$\frac{\sigma_E}{E} = \frac{56.4\%}{\sqrt{E[\,\mathrm{GeV}]}} \oplus 5.5\% \tag{3.6}$$

The LAr Hadronic End-Cap Calorimeter

The hadronic endcap calorimeters (HECs), like the ECAL, are sampling calorimeters using liquid argon as the active medium. However the HECs use copper rather than lead as the absorber. The HECs sit just behind the EMECs in the same cryostat and covers the region $1.5 < |\eta| < 3.2$. Figure 3.8 shows the position of the HEC in the endcap cryostat. They consist of two independent wheels each containing 32 modules. Each wheel has an external radius of 2030 mm and consists of two longitudinal sections. The inner wheel (HEC1) is made of twenty-four 25 mm thick copper plates whilst

the second wheel (HEC2) is made of sixteen 50 mm thick copper plates. The plates are interleaved with a gap of 8.5 mm for the liquid argon to fill.

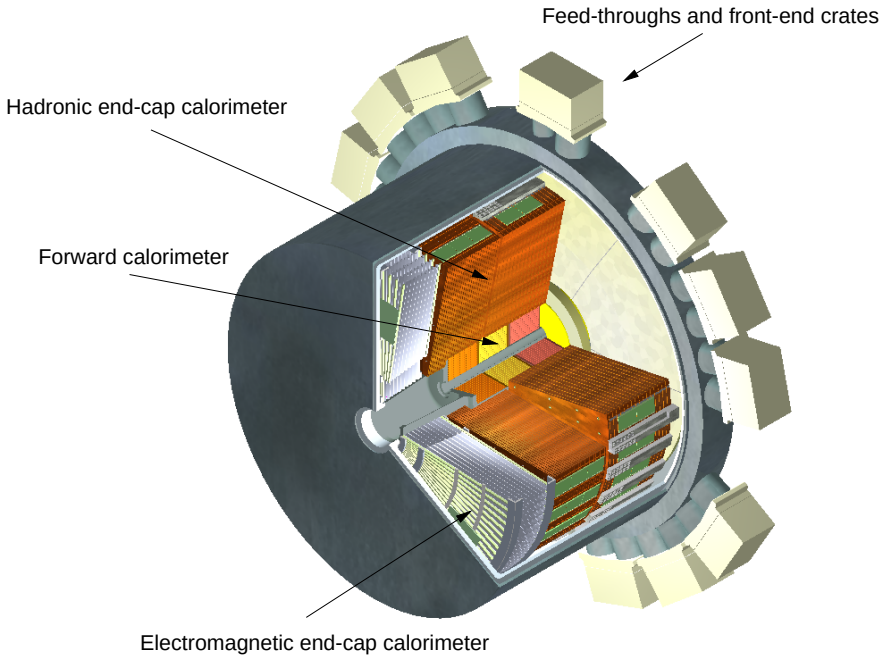

Figure 3.8: *Schematic view of the calorimeter endcap cryostat showing the positions of the hadronic, electromagnetic and forward calorimeters.*

The HEC resolution for single pions of energy from 5 to 200 GeV was measured in a test beam and was found to be [49]:

$$\frac{\sigma_E}{E} = \frac{70.6\%}{\sqrt{E\,[\,\mathrm{GeV}]}} \oplus 5.8\% \tag{3.7}$$

3.2.2.3 The Forward Calorimeter

The forward calorimeter (FCAL) is situated in the same cryostat as the EMEC and HEC and covers the region $3.1 < |\eta| < 4.9$. It is both an electromagnetic and hadronic calorimeter which is designed to measure the energies of forward jets and aid in the calculation of missing transverse energy. It plays an important role in the study of Higgs channels produced via vector-boson fusion, where forward-backward jets are produced and subsequently, can be tagged in order to help identify the signature.

The FCAL has four wheels, the first uses copper/liquid argon technology (EM), whilst the second two use tungsten/liquid argon (hadronic). Tungsten, being a very dense material, can stop high energy jets and reduce leakage into the muon chambers. The fourth wheel has no instrumentation and uniquely, is only there to protect the muon chambers. The FCAL is exposed to high flux of beam

remnants from the interaction point and therefore makes use of radiation hardened materials. It is made of a metal matrix with regularly spaced longitudinal channels. The channels are filled with tubes of a diameter 5.8 mm with a central rod down the middle that acts as the electrode. The tubes are then filled with liquid argon. The layers of liquid argon are smaller than those in the ECAL to prevent the accumulation of ions, allowing a larger density of absorber.

The granularity of the detector is $\Delta\eta \times \Delta\phi = 0.2 \times 0.1$. Results from the test beam using pions with momenta between 10 and 200 GeV/c show that the expected resolution is [49]:

$$\frac{\sigma_E}{E} = \frac{70\%}{\sqrt{E\,[\,\mathrm{GeV}]}} \oplus 3.0\% \tag{3.8}$$

3.2.3 The Magnet System

The ATLAS superconducting magnet system comprises a central solenoid (CS) and three large air-core toroids as seen in Figure 3.9. It has been designed to facilitate the bending of charged particles throughout the detector volume, whilst minimising the amount of material available for particles to interact with.

The central solenoid provides a 2 T axial magnetic field throughout the inner detector which is of sufficient strength to bend charged particles with transverse momenta of up to 100 GeV/c. It is situated just outside of the ID and shares the same cryostat as the the liquid argon electromagnetic calorimeter. Not having its own cryostat eliminates the need for additional vacuum walls, thus reducing the amount of material upstream of the calorimeter and reducing the potential for particles to shower before reaching the calorimeters. The magnetic flux generated is returned in the steel of the hadronic calorimeter and its support structure. It has an inner diameter of 2.46m, an outer diameter 2.56m and is 5.3m in length. In all, the CS only contributes $\sim$0.66 radiation lengths to the material budget.

The air-core toroid system consists of a barrel toroid system and two endcap toroids. It has been designed to provide a tangential magnetic field throughout the muon spectrometer. The barrel toroid comprises eight superconducting coils, spaced symmetrically around and parallel to the beam-axis. The coils of the barrel toroid are of *racetrack* type, each 25 m long, 5 m wide and weighing 100 tonnes. They are grouped in a torus shape and placed in eight separate cryostats. The endcap toroids, also made of eight *racetrack* type superconducting coils, are positioned either side of the central solenoid and inside the barrel toroid. They are housed in dedicated cryostats and are rotated by 22.5° with respect to the barrel toroid to provide radial overlap and optimized bending power in the transition region ($1.4 < |\eta| < 1.6$). In the barrel region ($|\eta| < 1.4$) the bending power is expected to be between

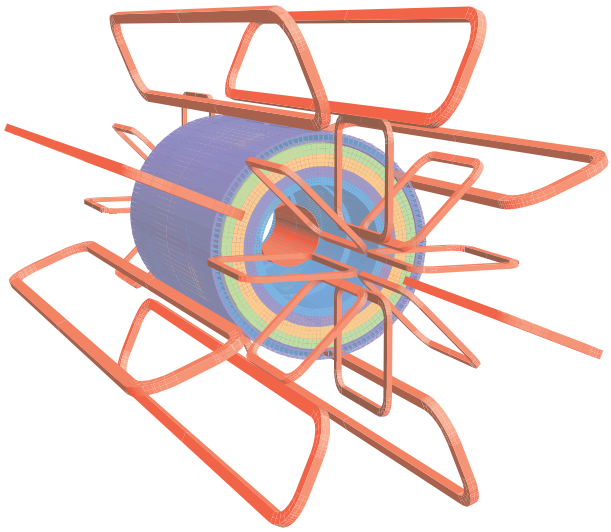

Figure 3.9: *Geometry of the magnet windings. The barrel and endcap toroid windings are shown along with the windings of the central solenoid located inside the calorimeter volume.*

1.5 and 5.5 Tm, whilst in the endcaps it is expected to be between 1 and 7.5 Tm.

3.2.4 The Muon Spectrometer

The muon spectrometer is the outer component of the ATLAS detector and has been designed for the precision measurement of the momentum of muons. The muon system covers the pseudorapidity range $|\eta| < 2.7$ for precision tracking and $|\eta| < 2.4$ for triggering. There are two types of detectors: the precision chambers (MDT and CSC) and the trigger chambers (RPC and TGC). The overall layout of the muon spectrometer is shown in Figure 3.10, which indicates the regions where the different chamber technologies are used.

The muon system consists of barrel, covering the range $|\eta| < 1.0$, and two endcaps, covering the range $1.0 < |\eta| < 2.4$. The barrel contains three layers of chambers, located at radii of 5.0 m, 7.5 m and 10.0 m, and the endcaps contain four layers of chambers, located at $|z|$ of 7.4 m, 10.8 m, 14.0 m and 21.5 m. Therefore, a muon emanating from the interaction point will typically pass through at least three chambers.

3.2.4.1 Precison Chambers

The precision measurements of muons are performed by the Monitored Drift Tubes (MDT) and Cathode Strip Chambers (CSC). The MDTs are used over the full $|\eta| < 2.7$ pseudorapidity region, except for the first layer of the innermost ring of the endcaps ($2.0 < |\eta| < 2.7$). Each MDT chamber is

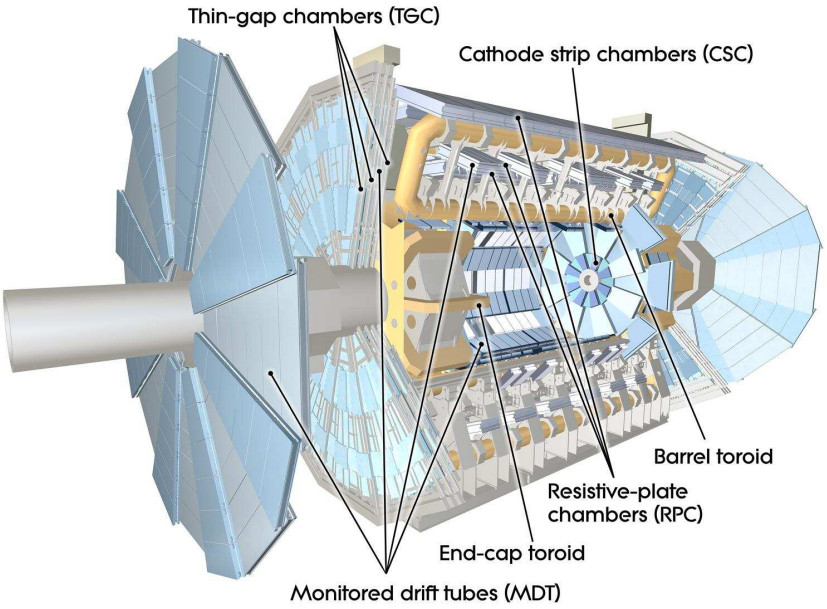

Figure 3.10: *Cut-away view of the ATLAS muon spectrometer. From [49].*

made from layers of 30 mm diameter aluminium tubes, containing a tungsten-rhenium wire running through the centre. The tubes are filled with a mixture of argon and carbon dioxide gas, held at a pressure of 3 bar. A rigid support structure is sandwiched between two 3-4 layer sets of tubes to form a chamber. The MDTs have a spatial resolution of 35 μm per chamber or 80 μm per tube.

CSC chambers are only used in the first layer of the innermost ring of the endcaps since this area is subject to a higher flux of particles. The safe operation limit of MDT chambers is at fluxes of 150 Hz/cm^2 in contrast to the 1000 Hz/cm^2 limit that the CSC chambers provide. CSCs are multi-wire proportional chambers. They consist of several layers of wire anodes, which are aligned radially, and two sets of cathodes which are segmented into strips. One set of cathodes are aligned parallel to the wires and provide the transverse coordinate whilst the other are aligned perpendicular to the wires to provide the precision coordinate. The gas enclosure is filled with a mixture of argon and carbon dioxide gas.

The CSC system is constructed from two disks each containing eight chambers (eight small chambers and eight larger chambers as seen in Figure 3.11). The resolution of a CSC plane is 60 μm in the radial direction and 5mm azimuthally. CSC chambers also have a timing resolution of less than 7 ns compared with 700 ns for MDTs, which makes them ideal for use in areas of high particle flux.

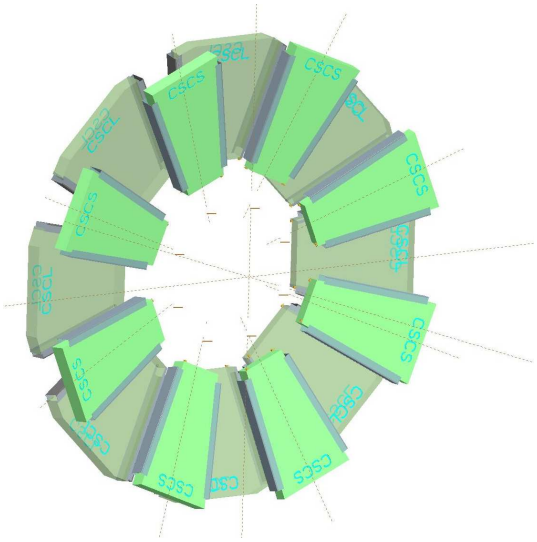

Figure 3.11: *Layout of chambers in a CSC endcap. The disk contains eight small chambers and eight large chambers alternately arranged. From [49].*

3.2.4.2 Trigger Chambers

The trigger chambers consist of a fast trigger system capable of providing tracking information just a few tens of nanoseconds after a particle has passed through. Different chambers are used in the barrel and endcaps due to the fact that the muon momentum, for a given p_T, is strongly η dependent [49]. In the central region ($|\eta| < 1.05$) three layers of RPC chambers are used, whilst in the end cap region ($1.05 < |\eta| < 2.4$) four layers of TGC chambers are used. These chambers are primarily designed to provide a fast response time but they also provide positional information.

The RPC chambers are made out of two parallel graphite-coated plastic (Bakelite) resistive plates separated by a 2 mm gap. The gap is filled with a gaseous mixture of $C_2H_2F_4$, Iso-C_4H_{10} and SF_6. An electric field of 4.9 kV/mm is applied between the plates allowing the primary ionization electrons to avalanche towards the anode. The signal is read out, via capacitance coupling, from metal plates fixed to the surface of the resistive plates.

RPCs are fixed to the same supports as the MDT chambers and are of the same dimensions. Figure 3.12 shows a schematic cross-section through the barrel indicating the location and distribution of the RPC chambers. In the middle layer (pink) RPC1 and RPC2 sandwich their respective MDT partner and RPC3 is installed above its MDT partner. In the outer layers (blue) RPC1 and RPC2 again sandwich their MDT partner but RPC3 is installed below its partner. Therefore a muon emanating from the interaction point will pass through six layers of detector (three MDTs & three RPCs) delivering six measurements in η and ϕ. The spatial resolution of an RPC chamber is around 10 mm with

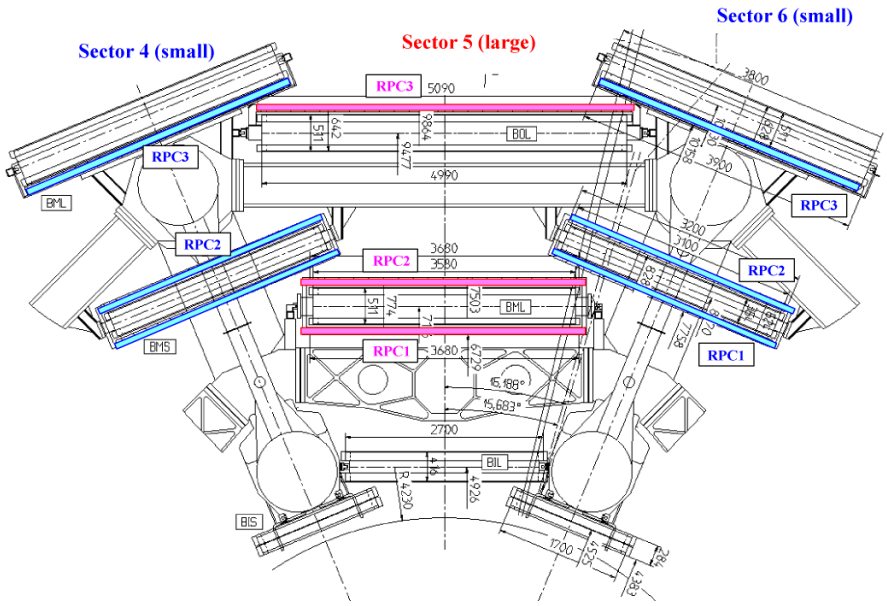

Figure 3.12: *Schematic cross-section through the upper part of the muon spectrometer barrel indicating the distribution of RPC chambers. From [49].*

a timing resolution of 1.5 ns [49].

TGCs are similar in design to the CSCs (in that they are multi-wire proportional chambers) except that they use a smaller wire-to-cathode distance (1.4 mm) than the anode-to-wire distance (1.8 mm). The gas used is a mixture of carbon-dioxide and n-pentane (n-C_5H_{12}). A design such as this means that an excellent maximum time resolution of 25 ns along with an ability to operate in a quasi-saturated mode.

TGCs are constructed in triplets and doublets of chambers, known as units. These units are mounted in concentric circles to form circular disks. An outer disk covers the endcap region ($1.05 < |\eta| < 1.92$) whilst an inner one covers the forward region ($1.92 < |\eta| < 2.4$). Combined, an inner disk and an outer disk form what is termed a big-wheel. At each end of ATLAS there are three wheels constructed out of TGC units, the innermost wheel using the triplet units and the outer two using the doublet units.

3.2.5 The Trigger and Data Acquisition System

At the LHC design luminosity ($\mathcal{L} = 10^{34}\text{cm}^{-2}\text{s}^{-1}$) 40 million proton bunch crossings will occur every second. With each bunch crossing containing multiple pp interactions, the event rate is expected to reach 1 GHz. Due to technological limits the amount of data that can be written to disk is ∼300 Mb/s. With a typical event being 1.5 Mb in size, the maximum rate at which events can be

stored on disk is ∼200 Hz. Therefore, a system is needed to reduce the event rate from 1GHz down to 200 Hz, whilst retaining as many of the "interesting events" as possible. The system utilised is the ATLAS Trigger and Data Acquisition System (TDAQ).

The ATLAS TDAQ system consists of three sequential levels: Level 1 (L1), Level 2 (L2) and Event Filter (EF). L1 is entirely hardware based, while L2 and the EF (collectively called the high-level trigger: HLT) are software based, running on a grid of commercially available computers. The system is programmable which means that as conditions change the trigger is able to adapt.

In this section an overview of the general functionality of the trigger at each level is presented.

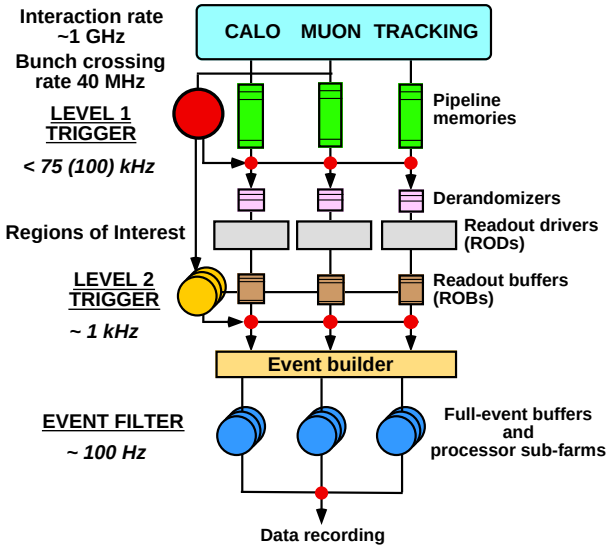

Figure 3.13: *Block diagram of the ATLAS trigger and data acquisition system. From [52].*

3.2.5.1 Level 1

The first trigger level has dedicated access to the data from the muon spectrometer and calorimeters. It uses reduced granularity information from the trigger chambers (TGC & RPC) in the muon spectrometer and from all the calorimeters (EM and hadronic and forward) to identify objects with large transverse energies and events with large missing or total transverse energies. No ID/tracking information is used due to the time involved in reconstructing the large numbers of tracks. L1 must be able to make a decision within 2.5 μs in order to reduce the rate from 40 MHz (or 1 GHz interaction rate) down to 75 kHz. However, as a bunch crossing occurs every 25 ns, a latency is needed in the form of a pipeline memory to give the L1 trigger enough time to process any individual crossing. A schematic overview of the L1 trigger is seen in Figure 3.14.

The calorimeter trigger searches for high-p_T photons, electrons, jets and hadronically decayed

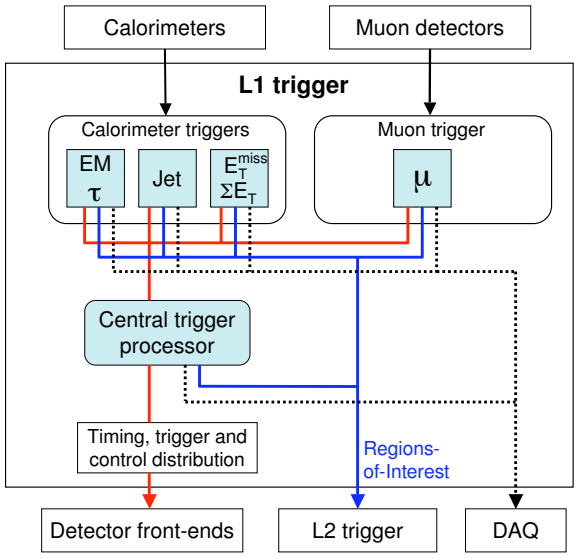

Figure 3.14: *Block diagram of the ATLAS Level 1 trigger. From [49].*

τ-leptons, as well as events with large missing or total transverse energies. These objects are measured by L1 algorithms using information obtained from trigger towers[2]. For electrons, photons and τ/hadrons isolation cones can be applied. For an object to be identified it must pass a pre-defined p_T threshold. There are limited numbers of thresholds that can be defined at any one time for a particular object type.

The L1 muon trigger uses information from the RPC and TGC trigger chambers to measure the trajectories of muons. Coincidence is used between several trigger chambers to reduce the background from cosmic muons. Two stations of chambers are used for low-p_T (6-9 GeV$/c$) thresholds, whilst three are used for high-p_T (9-15 GeV$/c$) thresholds.

Information from the calorimeters and the muon system is then passed to the central trigger processor (CTP). The role of the CTP is to compare this information with pre-defined selection criteria. If the selection criteria are passed then positional and kinematic information about identified objects is passed to the read out buffers in the form of regions of interest (ROIs). The ROIs are held in the buffers until requested for use by the second level of the trigger. The CTP, in conjunction with timing, trigger and control (TTC) system also uniquely identifies any specific bunch-crossing.

Once the bunch-crossing has passed the L1 selection, the detector data currently held in the pipeline memories is passed to the readout buffer input cards (ROBINs), via readout drivers (RODs)

[2] A trigger tower is a 0.1×0.1 granularity in $\Delta\eta \times \Delta\phi$ radial tower through the calorimeter that uses the sum of all the cells in each of the sampling layers.

and derandomisers.[3].

3.2.5.2 Level 2

Level 2 receives the ROIs from L1 and attempts to confirm their validity using the full granularity of their respective detector of origin. Once validated, additional features from the inner detector system can be requested (feature extraction) to further help identification of particles, thus transforming the ROIs into global trigger objects. These trigger objects will eventually become candidate photons, electrons, muons, τs and jets.

The processing is performed by a farm of computers adjacent to the ATLAS cavern. High speed broadband cables link the farm to the the detector front ends. The use of ROIs means that detector data is only requested from specific geometric regions thus limiting the size of data transferral needed to $\sim$2% of the total event size. An individual ROI must pass a set of selection criteria, known as a hypothesis. Any ROI failing the hypothesis is subsequently discarded. The processing time per event is $\sim$10 ms with the rate being reduced from 75 kHz down to 2 kHz.

3.2.5.3 Event Filter

The final level of the trigger system is the Event Filter (EF). Its role is to perform the final selection of events that will be written to disk. Events passing L2 are passed to the Event Builder (EB). Here the data from the ROBINs is combined with the information from L2 and the event is built. The complete event is passed to the EF where it can operate using the full granularity of the detector sub-systems. At this level vertex reconstruction, track fitting and photon conversion searches can be performed. The processing time per event is approximately 4 seconds. This comparatively high latency time means that the EF can reconstruct events using refined offline-like algorithms. Hypotheses similar to those used at L2 are used to refine the L2 trigger objects.

Events passing the EF selections are then directed into different streams according to which trigger has been passed. Events passed to different streams will be written out in different files for reprocessing later. These streams are not exclusive, meaning that if an event passes several triggers then the same event will be written out to several streams.

[3] A derandomiser is a device that averages out a random data flow into a homogeneous one.

Chapter 4

Event Simulation and Reconstruction at ATLAS

The unprecedented experimental conditions at the LHC, along with the complexity of the ATLAS detector, make it necessary to provide accurate simulations of how particles in an event propagate through, and interact with, the detector. To meet these requirements, ATLAS has developed a computing framework called ATHENA [53], which integrates all the necessary elements of Monte-Carlo event generation, detector simulation and the reconstruction of particles and events. In this chapter, the process by which a physics event is generated with Monte-Carlo simulation is detailed, along with how the response of the detector to the particles in the event is simulated. Two distinct methods, termed *full simulation* and *fast simulation*, model the detector response to particles and subsequently convert the detector responses into meaningful representations of particles. A comprehensive description of the ATLAS simulation infrastructure is found in [54].

In what follows, particular attention is given to the ATLAS fast simulation package, ATLFAST-I, as it was used extensively to carry out the work in Chapters 6 and 7. Additionally, the generation of Monte-Carlo events is discussed in more depth as several generator programs are used in Chapter 7.

4.1 Monte-Carlo Event Generators

To model the many complex physics processes that will be present at the LHC, event generators (Monte-Carlo tools) are used. Their use allows physicists to set detector requirements, formulate analysis models and calculate rates of processes at unprecedented energy scales. There are many varying types of generators, from those such as ALPGEN that are designed to study particular processes, to the more general such as MadGraph that cover a broad range of physics. ATLAS, via the

ATHENA framework, provides interfaces to many of the leading event generators, whilst also supplying utility services to enable filtering of events and the handling of the Monte-Carlo truth records.

4.1.1 Tree Level Matrix Element Generators

Matrix element (ME) generators are parton-level generators describing a specific final state to lowest order. Typically, they are based on either the direct calculation of the appropriate Feynman diagrams or on the solutions of the underlying classical field theory. The final states consist of bare quarks and gluons, which are showered/hadronised by specific programs (see Section 4.1.2).

ME generators tend to come in two flavours: those designed for specific processes and those for arbitrary processes. ME generators for specific processes contain code for producing events with a pre-defined list of partonic processes. The MEs relevant to the individual processes are calculated with a ME generation program. The advantage of these is that there are often phase space routines which are optimised for the processes, subsequently allowing the programs to output weighted or un-weighted partonic events. An example of one such specific ME generator is a program called ALPGEN [55]. It is designed for generation of jet-rich final state SM processes in hadronic colliders. It provides 15 "modes", an example of which is: $N\gamma + M$ jets, where the user can request a final state containing any combination of photons and jets that satisfies $N \geq 1$, N+$M \leq 8$ and $M \leq 6$.

General purpose ME generators can be thought of as automatic generators. The user supplies the initial state and final state and the generator calculates the scattering amplitude for all possible Feynman diagrams contributing to the processes. The program then writes out code to sum over all the sub-processes, helicity and colour states before integrating over the phase space to provide the cross-section and (un)weighted partonic events. The programs are able to produce events for any standard model process as well as more recently extended Higgs models and SUSY processes. However, limitations apply due to the complexity of events and limited CPU time. The advantages are that they provide coverage for processes for which there are no dedicated generators, whilst also providing capabilities for users to add in beyond the standard model processes themselves. An example of a generic ME generator is MadEvent/MadGraph [56]. MadGraph uses an innovative web-interface whereby the user can specify an initial and final state and specify machine and model parameters before submitting for calculation. MadGraph enumerates all the possible Feynman diagrams up to a user controllable order, calculates the amplitudes for each diagram and returns a packaged stand-alone code termed a MadEvent. This code can be downloaded and run locally to produce (un)weighted events as well as providing the resultant cross-section. MadGraph is limited to processes containing less than 10,000 diagrams or sub-processes.

Both of the generators, used as examples above, have adopted the standardised Les-Houches [57] output form. The Les-Houches output form is XML-like and thus can just as easily be read by a hadronisation program written in C++ as one written in FORTRAN.

4.1.2 Parton Showering and Hadronisation Programs

Showering and hadronisation programs that use the parton shower-evolution approach, have proved popular amongst the particle physics community. They are general purpose tools that are able to simulate a wide variety of initial and final states. Starting with the leading order hard process, higher order effects are added by *evolving* the event using the parton shower model, which allows partons to split or branch into other pairs of partons. The hard scattering of partons results in the acceleration of colour charge which, in analogy with the way photons are radiated from accelerated electrically charged particles, means that gluons and quarks are radiated from accelerated colour particles. At the parton level scale, perturbative expansion can be used to provide a reliable prediction of QCD radiation.

Figure 4.1 is a graphical representation of the evolution of an event. For example, a quark and anti-quark are respectively resolved from each of two colliding protons. The exact way in which each parton is resolved is determined by a parton distribution function (PDF) which describes the distribution of the momentum fraction x of the partons in a hadron when probed at a scale Q. The quark and anti-quark annihilate, producing an s-channel resonance, which subsequently decays into a pair of quarks. This part of the event is known as the *hard sub-process*. Each of the quarks can split into $q(\bar{q})g$ pairs, whilst any gluons present may branch into $q\bar{q}$ or gg pairs. These resultant partons may themselves branch, resulting in a cascade of partons (*parton shower*). With each branching, the QCD force grows until confinement effects result in the partons grouping together into colour-singlet hadrons, a process known as *hadronisation*. Fortunately, since hadronisation occurs at larger scales than the parton scale, it can be considered independent from the hard scattering. This means that hard scattering can be performed by specific generators, as described in Section 4.1.1, whilst the hadronisation can be performed by separate showering and hadronisation programs.

Showering and hadronisation generators are also able to model the underlying event, i.e. the proton remnants which do not participate in the hard sub-process. However, the remnants are colour connected to the hard sub-process and therefore must be included when hadronisation is performed. Multiple interactions whereby more than one pair of partons from the protons interact, along with pile-up from other proton-proton collisions in the same bunch crossing are also features often included in these types of generators. Probably the two most widely used showering and hadronisation generators

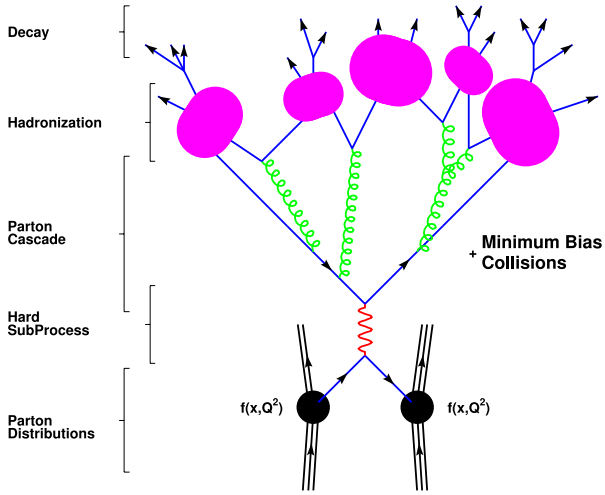

Figure 4.1: *Graphical representation of the evolution of an event. In this figure, time proceeds vertically.*

are PYTHIA [58] and HERWIG/JIMMY [59, 60]. Both generators are able to simulate collisions in lepton-lepton, lepton-hadron and hadron-hadron colliders and contain large libraries for $2 \rightarrow n$ sub-processes at leading order.

ATLAS, via ATHENA, has provided generator interfaces to allow passing of the relevant parameters at run-time to the generator programs without the need for re-compilation. This structure allows integration of common services such as random number seeds and run/event number allocations alongside the event generation. Since each generator has its own output/memory format, events produced must be mapped into a common format that can later be read by simulation software without knowledge of the specific generator used. The format used by ATLAS is HepMC [61]. This is a package of C++ classes that holds the full generated event in a tree like structure and is often referred to as Monte Carlo *truth* or generator-level information.

4.2 Full Simulation

This section describes the procedure used in ATLAS to fully simulate the response of the ATLAS detector and the process by which the detector responses are converted or *reconstructed* into meaningful physics objects. Particles from Monte-Carlo generated events are propagated through a detailed model of the ATLAS detector and their interactions with the media of each sub-detector system are modelled. Any energy deposited in sensitive portions of the detector is collected as so called *hits*. These hits are then converted into *digits* (voltages and currents) in a process called *digitisation*. Digits are formatted in such a way that they are identical to the signals that would have been expected

to be produced by the actual detector. In this manner, simulated and real data can be treated indistinguishably by the trigger and reconstruction algorithms. The flow of both simulated and real data through the ATLAS simulation infrastructure can be seen in Figure 4.2.

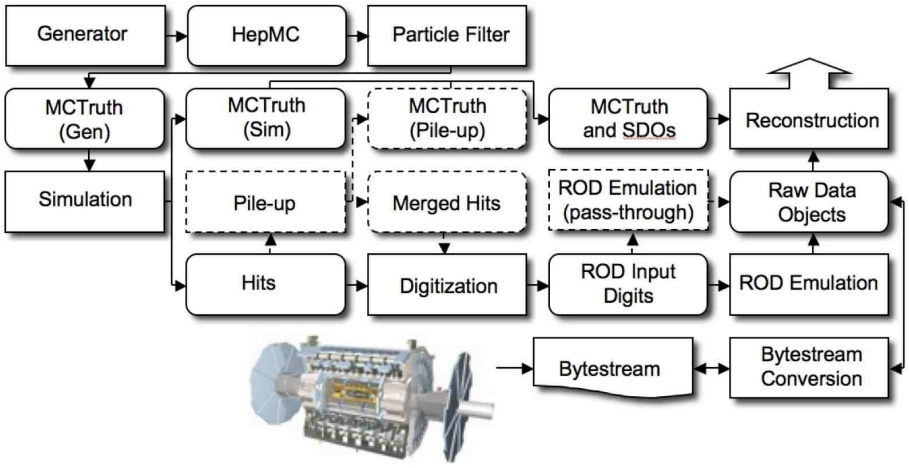

Figure 4.2: *The data flow of the ATLAS simulation infrastructure. From [62].*

4.2.1 Simulation of The ATLAS Detector Response

The standard simulation of the ATLAS detector is performed by the GEANT4 toolkit [63] which models the interactions of particles with the ATLAS detector. The detector is described by use of a package called *GeoModel*, which uses libraries of basic geometric shapes to build a complete detector description including all detector sub-systems, services and dead material. GeoModel is separate from the GEANT4 toolkit. This allows not only simulation jobs to access GeoModel but also digitisation and reconstruction jobs, thereby utilising a consistent description of the detector at all stages. Consequently, the GeoModel is translated into GEANT4 format before simulation takes place.

Generated events in HepMC format provide the input to the simulation step. These events are converted into a GEANT4 format before being propagated through the detector. The way in which particles interact with the detector material is controlled by various physics models [64]. Once the simulation has been performed, events are written to files which contain run configuration information, Monte Carlo truth information and records of 4-vectors of energy depositions (*hits*) from all detector sub-systems. The original Monte Carlo truth record from the generator is still kept and is added to by the GEANT4 simulation. It is impractical to retain all the information produced by GEANT4 and instead only interactions which are of relevance, e.g. photon conversions to e^+e^- pairs, are added to the record.

4.2.2 Digitisation

The digitisation system converts hits produced by the simulation process into real detector responses, such as voltages and currents, and also includes detector noise. This process happens at the level of the sub-detectors, who each have their own digitisation software to model the detector response. The sub-detector software has been tuned to reproduce the detector response as seen in test beams, lab tests and cosmic runs. Dead channels and noise rates from particular runs are recorded in databases which the digitisation process can use to reproduce the conditions of the run.

Digits provide the input to the ReadOut Drivers (RODs) in the detector electronics. The ROD functionality is then emulated with the final outputs of the digitisation process being Raw Data Objects (RDOs). As real data from the detector is delivered in a bytestream format, converters are supplied to convert from RDO to bytestream and vice-versa, allowing for direct comparisons between real and simulated data to be made. As the first level of the ATLAS trigger system is hardware based, it is simulated in pass-through mode which allows all events to be retained whilst evaluating all implemented trigger hypotheses.

4.2.3 Pile-up

Typically, for each bunch crossing there will be multiple inelastic proton-proton interactions in addition to the hard scattering. Collectively known as pile-up, the effects of the additional interactions along with the effects of beam gas and halo interactions must be accounted for in the simulation process. Therefore, pile-up events are generated and simulated separately from the hard scattering. During the digitisation process, hits from pile-up events are overlaid with those from the hard-process at a specific rate. This approach can also be used to overlay real pile-up events, collected from the *zero-bias* trigger, with simulated hard scattering events.

4.2.4 Particle Reconstruction

Before any analysis of detector information can begin, the responses of the detector must be interpreted into recognisable objects. This process, known as *reconstruction*, condenses and calibrates all raw signals from the detector sub-systems and uses them to identify individual particles and event level quantities. The result is that only individual particle *objects*, overall event variables, such as missing or total transverse energy, and specific detector information, such as particle tracks and calorimeter cells/clusters are kept. This reduces the overall event size from around $1.5\,MB$ to $100\,kB$.

Reconstructed objects, are then, representations of signals consistent with the interaction of a par-

ticle with the detector. The types of reconstructed object include: electron, photons, muons, hadronic taus and jets. Each reconstructed object may itself be derived from tracks in the ID and muon spectrometer along with energy deposits in the calorimeters. Typically, for each particle type a set of selection criteria are used to classify and define reconstructed objects further. The selection criteria used for the reconstruction of photons and converted photons are detailed in Chapter 5. For detailed information regarding the reconstruction of other particle types and jets the reader is directed to References [50, 49, 27].

In principle the reconstruction process should result in a one-to-one correspondence between generator-level particles and reconstructed objects. However, due to several reasons this is not always possible as there may not always be a corresponding reconstructed object. Firstly, the particle may be of too small an energy to be recorded by the detector. Additionally, the particle might deposit its energy in an insensitive region of the detector and thus escape detection. The reconstruction software itself is not perfect and sometimes will misidentify a particle as another particle type. In these cases the particles are termed *fakes*. The reconstruction efficiency is defined as the probability that a given (truth) particle will be reconstructed as that particle. For example, the reconstruction efficiency for photons, ε_γ is defined as:

$$\varepsilon_\gamma = \mathrm{P}(\text{object is reconstructed as a photon} \,|\, \text{object is a photon}) \tag{4.1}$$

The reconstruction efficiency then may depend on factors such as the location of the particle in the detector and/or the transverse momentum of the particle.

It should be noted that exactly the same reconstruction algorithms are used for simulated and real data. In this way selection criteria tuned using Monte-Carlo simulations should produce similar results when used with real data. This will be one of the earliest commissioning studies undertaken when real data arrives.

4.3 Fast Simulation

The full simulation process is a very CPU intensive and time consuming procedure[1] due to the complicated GEANT4 simulation and detailed detector description. Consequently, due to limited resources, quotas exist on the number of full simulation events that can be produced. Typically, each working group has an assigned quota on the amount of simulated data it can request, with the distribution of

[1] A typical full simulation event takes approximately 10-20 minutes to simulate, depending upon the complexity of the physics involved.

the quota to specific signals/backgrounds decided upon by the group. Therefore, studies that require large statistics need a different simulation approach. Fast simulation strategies aim to provide a faster processing time by parameterising components of the full simulation process or by providing less detailed information.

A number of fast simulation options now exist within the ATHENA framework. The GEANT4 fast simulation [65] aims to speed up the slowest part of the full simulation process, namely the time taken simulating electromagnetic particles traversing the calorimeters. The strategy is to replace low energy electromagnetic particles with showers from a pre-simulated library. The result is a reduction in the CPU time by a factor of two with minimal impact on the resultant physics reproduction.

ATLFAST-I, detailed in Section 4.3.1, is the original fast simulation package of ATLAS. Its primary design goal is to massively reduce the simulation computation time, allowing rapid production of large numbers of events that do not require the level of detail provided by full simulation. ATLFAST-I makes no use of the GEANT4 package but instead uses detector resolution functions to create physics objects similar to full simulation ones. This compromise reduces the computation time by a factor of 1000 in comparison to full simulation.

ATLFAST-II is a relatively new simulation package that aims to fill the void between full simulation and ATLFAST-I. The idea is to be able to simulate events as fast as possible whilst retaining the ability to use the same ATLAS reconstruction packages as full simulation. ATLFAST-II makes use of two components which can speed up the simulation of particles in the various sub-detectors. The first component known as Fatras (fast ATLAS tracking simulation), uses a slimmed down detector description, only keeping full details in sensitive regions of the detector to reduce simulation time in the inner detector and muon system. The second component, referred to as FastCaloSim, uses parameterisations of lateral and longitudinal energy profiles of single particle showers to replace the simulation of particle interactions with detector material. ATLFAST-II retains the ability to simulate any sub-detector with GEANT4 in conjunction with either of the two components. The default mode of ATLFAST-II is to use GEANT4 for the inner detector and muon system and FastCaloSim for the calorimeters. Optionally, the user can switch to a mode called ATLFAST-IIF that uses FastCaloSim for the calorimeters and Fatras for inner detector and muon system. The default mode of ATLFAST-II reduces computation time by a factor of $\sim$10 compared with full simulation, whilst ATLFAST-IIF reduces it by a factor of $\sim$100.

4.3.1 ATLFAST-I

The ATLFAST-I fast simulation package has been designed in order to simulate large samples of signal and background events for physics studies, especially those that require very high statistics. Due to the CPU requirements of full simulation, fast simulation is an essential tool, allowing the rapid production of simulated events on scales that would be impossible to achieve using full simulation alone. As shown in Figure 4.3, ATLFAST-I replaces the full detector simulation and reconstruction steps by smearing the Monte-Carlo truth information of particles with parameterised resolutions measured from full simulation studies. Since no detailed simulations of any particle interactions with the detector media are performed, CPU usage is minimised. Consequently, this makes ATLFAST-I the ideal tool for obtaining quick estimates of systematic uncertainties arising from the use of different generators and performing parameter scans.

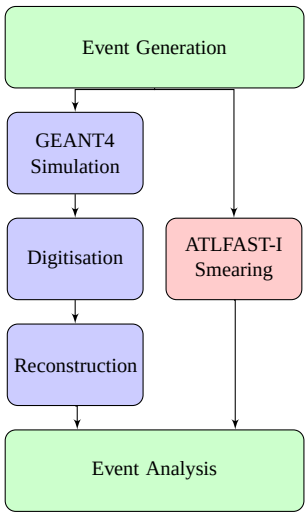

Figure 4.3: *Full simulation steps versus ATLFAST-I simulation. Adapted from [66].*

Generated events, stored in HepMC format, provide the input to ATLFAST-I. These events can either be created on the fly by an event generator and then processed by ATLFAST-I one by one or they can be read in from files containing previously generated events. ATLFAST-I algorithms performing specific tasks, such as isolation or clustering, can then be scheduled and their properties configured to suit the users requirements.

The following section gives a brief description of the ATLFAST-I simulation package included in ATHENA release 12.0.6.

4.3.1.1 Simulation

Contrary to full simulation, ATLFAST-I employs a very basic detector description which can be classified into three main components:

- **Primary Interaction Vertex**: This is defined to be in the geometric centre of the detector and collision points do not vary either laterally or longitudinally from event to event.
- **Inner Detector**: Defined as an empty volume with a homogeneous magnetic field extending up to $|\eta| < 2.5$. It is only used to simulate the effect of the magnetic field on the path of a particle before it strikes the calorimeter. As the ID model is void of material no particle interactions with detector media are simulated and hence no hits or tracks are recorded.
- **Calorimeter**: Divided into a central ($|\eta| < 3.2$) and forward ($3.2 < |\eta| < 5.0$) region with $\Delta\eta \times \Delta\phi$ cell sizes of 0.1×0.1 and 0.2×0.2 in each region respectively. No separation between the electromagnetic and hadronic compartments exists in the standard version of ATLFAST-I although an extension can provide that functionality.

ATLFAST-I only selects stable final state particles from the HepMC record for further processing. These particles are then tracked through the magnetic field using a helix model and the impact point on the calorimeter surface is calculated. In the calculation of this point no interactions of the particle with the detector media, i.e. no multiple scattering, energy loss or nuclear interactions are taken into account. In particular, this implies that no electron energy is lost due to bremsstrahlung and photons do not convert. Track parameters are calculated from the four-momentum and the starting point of stable particles, which is taken from the generator information.

When an electron, photon or hadron strikes the calorimeter surface all of its energy is deposited in the hit calorimeter cell. The response of the calorimeter is assumed to be uniform over the full detector region and no lateral or longitudinal shower development is simulated. At this stage no smearing, i.e. no energy resolution function, is applied.

4.3.1.2 Reconstruction

At present ATLFAST-I has no reconstruction layer based on simulated detector information and thus reconstruction of the physics objects relies heavily on the Monte Carlo truth information. Consequently, the way in which physics objects are classified is dependent upon the true particles and can be summarised below:

- **Clusters**: A cluster reconstruction algorithm is carried out based on the energy deposits in the calorimeter cell map. A cone algorithm, using cones of size $\Delta R = \sqrt{\Delta\eta^2 + \Delta\varphi^2} = 0.4$ is used to create clusters of cells. Cones can only be initialised by seed cells with energies above 1.5 GeV. The algorithm is applied to the seed cells in decreasing order of p_T. Once a cluster has been associated to a seed cell (only one cluster can be associated to any particular seed cell) the sum of the energy within it is calculated. The cluster energy must pass a threshold which is typically set to be 5 GeV. At a later point, clusters are associated to truth particles and once a cluster has been associated it is removed from the list of available clusters.

- **Electrons and Photons**: For each stable final state true electron or photon, a calorimeter cluster is searched for that can be matched to the particle. A match is accepted if the separation between the cluster and true particle is found to be less than $\Delta R = 0.15$. Isolation can be applied at this stage if required and is defined as: the sum of the energy deposited in cells contained in a cone of $\Delta R = 0.2$ around the particle direction, minus the energy of the true particle itself, must be less than a pre-defined threshold (typically 10 GeV). In addition to the particle isolation, cluster isolation is also applied requiring that there must be no other clusters within a distance $\Delta R = 0.4$ around the particle direction.

  Reconstructed electrons are obtained by *smearing* the true energy using resolution functions derived from test beam studies with calorimeter modules [50]. Reconstructed photons are obtained by using almost the same energy resolution functions [67], the only difference being in the sampling term which accounts for the fact that photons are unaffected by energy losses due to bremsstrahlung in the inner detector. Additionally, for photons the η direction is smeared. No distinction between converted and unconverted photons is made. For a particle to be recorded in the list of reconstructed objects, the smeared transverse energy must be at least 5 GeV and it must lie within the pseudorapidity range $|\eta| < 2.5$.

- **Muons**: For each true muon with $p_T > 0.5$ GeV$/c$, a Gaussian resolution function which depends on p_T, η and ϕ is used to smear the momentum. More details on the muon resolution function can be found in reference [68]. Only muons with $p_T > 5$ GeV$/c$ and within a pseudorapidity range $|\eta| < 2.5$ are recorded as reconstructed objects. Muons are classified as either isolated or non-isolated by a similar algorithm to that of the electron/photon isolation algorithm with the exception that energy isolation is performed using a larger cone size of $\Delta R = 0.4$.

- **Jets**: Any cluster that has not already been associated to an electron or photon is treated as a candidate jet. In addition, if any muon is within $\Delta R = 0.4$ of the jet direction then it is absorbed

into the jet with the jet momentum adjusted accordingly. The jet energy, taken from the sum of the cluster energy and any additional muons, is then smeared according to the jet resolutions found in Reference [50] and the jet direction is taken from the cluster. For the jet to be reconstructed it must have transverse energy greater than 10 GeV and lie within $|\eta| < 5$. Subsequently, jets are labelled according to the closest matching *b*-quark, *c*-quark or hadronically decaying τ. For the case of $b(c)$ quarks with $p_T > 5$ GeV/c a jet is searched for that can be matched within $\Delta R = 0.2$. Similarly, τ leptons with $p_T > 10$ GeV/c are matched to jets within $\Delta R = 0.3$. If a jet is found within the specified cone, then it is labelled accordingly. Parameterisations of the identification efficiencies are then used to determine whether the labelled jet becomes a tagged jet. Any un-labelled jet is classified as a light jet.

- **Missing transverse momentum**: is calculated from the vector sum of the momentum of reconstructed objects (electrons, photons. muons, taus and jets) and any remaining unassociated clusters and cells.

- **Tracks**: ATLFAST-I takes charged particle tracks straight from the generator record. To be considered reconstructed, tracks must have $p_T > 500\,\text{MeV}/c$ and lie within $|\eta| < 2.5$. Five track parameters[2] are then associated to each track. The parameters are calculated from the track properties by applying parameterised resolution functions, taken from full simulation events, which account for energy loss, multiple scattering, measurement precision and hadronic interactions in the inner detector. The non-Gaussian tails caused by hadronic interactions are taken into account by applying a double-Gaussian correlated smearing to the track parameters of hadrons [67, 69]. ATLFAST-I distinguishes between three types of charges particles: hadrons, electrons and muons. As high-p_T electrons suffer energy losses via bremsstrahlung they are treated separately with an additional energy loss correction applied. Tracks in ATLFAST-I are predominately used for B-physics studies and are not used for lepton identification or b-tagging.

By design, ATLFAST-I is assumed to have a uniform response to all particle types. Apart from the parameterised identification efficiencies used for muons and tagging no reconstruction/identification efficiencies are applied.

Performance related discussions and further details of the ATLFAST-I simulation package can be found in [69].

[2] The five parameters are ϕ, longitudinal impact parameter z_0, transverse impact parameter d_O, θ and the ratio of charge to momentum.

Chapter 5

Photon Reconstruction and Identification

The efficient reconstruction of photons is vital for any search requiring photons in the final state, such as H$\rightarrow \gamma\gamma$. One of the greatest challenges is the ability to separate isolated photons from the large background of jets. Information from the finely segmented electromagnetic calorimeter, hadronic calorimeter and inner detector can be used to derive powerful discriminating variables. The efficiency of detection of high-mass photon final states can be greatly enhanced by the recovery and reconstruction of photon conversions in the inner detector since as many as 40% of photons will convert before reaching the calorimeter [49]. Reconstructed vertices from converted photons also provide an insight into the material budget of the detector and provide opportunities for commissioning with early data.

In this chapter, only information specific to the reconstruction of photons and photon conversions is detailed. Information regarding the reconstruction of electrons, jets, muons, taus, tagged-jets and missing transverse energy can be found in References [50, 49, 27].

5.1 Reconstruction of Tracks and Photon Conversions

The ATLAS detector will have the ability to detect photons with energies above 1 GeV. Before these photons reach the calorimeter, they must pass through the material in the inner detector. At photon energies above 1 GeV, a high proportion of photons will interact with the detector material producing electron-positron pairs in a process known as conversion ($\gamma \rightarrow e^+e^-$). This is by far the most dominant process and is dependent on the presence of material for the conversion to satisfy energy and momentum conservation. Consequently, the more material in front of the calorimeter the higher the chance that a photon will convert before reaching calorimeter. Figure 5.1 shows the amount of material, in terms of radiation lengths, in the inner detector as a function of $|\eta|$. Thus, in the precision physics range ($|\eta| < 2.5$) more conversions occur in the crack region due to the large

amount of material located in this region.

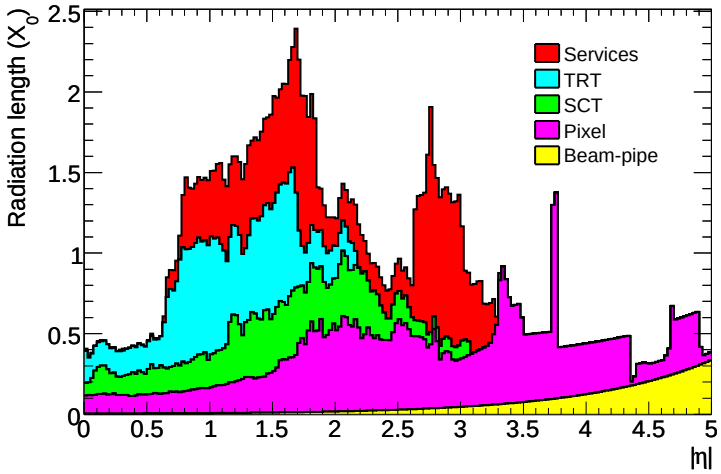

Figure 5.1: *Material in the inner detector as a function of* $|\eta|$*, averaged over* ϕ*. From [49].*

For photon energies of 1 GeV and above, the cross section for the conversion process is almost completely independent of the energy of the incident photon [70]. Additionally, the differential conversion cross-section implies that the energy of the photon is not always shared equally between the resultant electron and positron. This results in a fraction of conversions being highly asymmetric, with either the electron or positron being of low energy. If the energy is too small, then it may not leave a reconstructible track, resulting in the presence of just one visible track. These cases are known as *single-track conversions* and are hard to distinguish from single electrons or positrons. This effect is energy dependent, with an increase in single-track conversions from lower energy photons [70].

To reconstruct converted photons, tracks left by charged particles in the inner detector must be identified and reconstructed. Tracks from converted photons are required to pass basic quality cuts. Pairs of opposite charge tracks that can be reconstructed into a massless conversion vertex are collected and associated to a conversion candidate. Finally, the reconstruction of single-track conversions is performed, before all conversions candidates are written to a separate container for later classification through matching with electromagnetic clusters (see Section 5.2).

5.1.1 Track Reconstruction

Track reconstruction is performed by two main algorithms: *inside-out*, for reconstruction of charged particle tracks emanating from interaction region and *outside-in*, for reconstructing tracks originating later in the detector. Both algorithms reconstruct tracks with Silicon (Si) and transition radiation tracker (TRT) hits, placing them in separate containers. Additionally, any tracks which are recon-

structed using only TRT hits are stored in a separate container. All three containers are scanned for any double counting before being merged into a final track collection. For a track to be reconstructed it must have $p_T > 0.5$ GeV$/c$. Further details on the track reconstruction algorithms can be found in reference [49].

Since only a fraction of reconstructed tracks come from converted photons, it is important to remove tracks not associated with conversions as early as possible before the CPU intensive task of track-pairing begins. Cuts on the track's transverse momentum, perigee impact and longitudinal parameters are first applied. Tracks associated to electrons are then selected using the ratio of high-threshold TRT hits to the total number of TRT hits.

After the track quality selections have been applied, the track collection is separated into two groups containing tracks of opposite charge. Three types of opposite charge pairs are formed:

- Both tracks in the pair with Si hits;
- One track in the pair with TRT only hits;
- Both tracks in the pair with TRT only hits.

An initial pre-selection, applied to pairs of tracks, is performed to help reduce the combinatorial background. The two tracks in a pair are required to have a small initial polar angle difference and the distance of minimum approach between the two tracks must be small. To reduce the load on the vertex fitting routine an initial estimate of the vertex position is also provided. The aforementioned cuts have been developed and tuned to provide at least two orders of magnitude rejection power on the combinatorial background.

5.1.2 Vertex Fitting

For all tracks, the original perigee parameter assigned during reconstruction is set at the interaction point. For converted photons this is a poor assumption, since conversions occur at significant distances from the interaction point. Therefore, the perigee is redefined using the initial estimate of the vertex position described previously. After this process, the new vertex position along with an error matrix and χ^2 value for the fit are computed using a fitter based on the fast-Kalman filtering method [71]. The fit is always successful for correct track pairs, but often fails if the pairing is incorrect. Selections based on the χ^2 value, reconstructed photon p_T and invariant mass can be applied to further reduce wrong pairings. Finally, all identified conversion vertices are stored along with their associated track parameters and can be retrieved when required for further classification through matching with electromagnetic (EM) clusters.

5.1.3 Inner Detector Conversion Reconstruction

Conversions are only reconstructed up to 800 mm away from the interaction point, as the reconstruction efficiency falls off above this point. Additionally, there is a drop in reconstruction efficiency for conversions occurring at radial distances above 400 mm due to the lack of measurements from the pixel detector and reduced measurements in the SCT (see Figure 5.2). The reconstruction of late high-p_T conversions also poses a problem, since the resultant electron tracks are highly boosted, meaning that the TRT is unable to resolve the two tracks. Consequently, there is a bias towards reconstructing electrons rather than converted photons which can be resolved by the use of recovery algorithms which make use of ECAL information and track extrapolation methods.

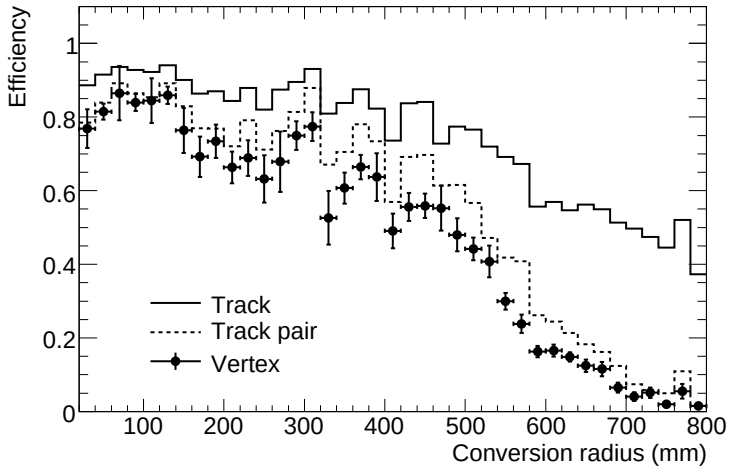

Figure 5.2: *The efficiency, found from Monte-Carlo* $H \rightarrow \gamma\gamma$ *events, to reconstruct conversions of photons with* p_T*=20* GeV$/c$ *and* $|\eta|$ *<2.1, as a function of the conversion radius. Shown are the Monte-Carlo efficiencies to reconstruct single tracks from conversions, the pair of tracks from the conversion and the conversion vertex using inner detector information only. From [49].*

5.2 Photon Reconstruction

Sliding window algorithms, which locate the local E_T maximum in a $\Delta\eta \times \Delta\phi$ window, are used to identify EM clusters. At this stage a window size of 5×5 cells in the middle sampling layer of the ECAL is used. For each cluster, a reconstructed track is then searched for that can be matched to a cluster within a $\Delta\eta \times \Delta\phi$ window of 0.05×0.10, and which satisfies the requirement that the ratio of the energy of the cluster (E) to the track momentum (p) must be less than 10 ($E/p < 10$). If such a track is found, the presence of an associated reconstructed converted photon vertex (see Section 5.1) from the inner detector is searched for. If no conversion vertex can be found then an electron candidate

is produced. Otherwise, a photon candidate is produced, with converted photon candidates defined by the association of a track and conversion vertex and unconverted photon candidates defined by the absence of a track. An early classification of particle type at this stage allows for different corrections to be applied at later stage.

The EM cluster is then rebuilt depending on the candidate type and calorimeter region. In the barrel, the cluster is resized to 3×7 for electron candidates, 3×5 for unconverted photon candidates and 5×5 for converted photons. The cluster size for electrons and converted photons is larger in ϕ in order to help minimise contributions from pile-up and contain as much energy as possible in the case of hard Bremsstrahlung. In the end-caps the cluster is rebuilt and resized to 5×5 for all candidates.

The η and ϕ position of the cluster is calculated as the energy-weighted barycentre of the cluster. Corrections are applied to account for the amount of material upstream and the calorimeter segmentation. The energy of the cluster is computed as the sum of the energies deposited in the presampler and each subsequent layer in the ECAL. Energy dependent corrections are applied to correct for energy lost upstream and lateral and longitudinal leakage.

5.2.1 Photon Identification

Photons are much harder to identify than electrons due to large backgrounds from jets with leading neutral pions. In order to separate photons from jets, variables based on calorimeter and inner detector information have been developed to maintain high photon identification efficiencies whilst providing strong jet rejection power. The variables used are briefly outlined in the order of their application below.

Hadronic Leakage:

Since photons deposit most of their energy in the second (middle) layer of the ECAL a very small amount, typically less than 2%, leaks into the hadronic calorimeter. Conversely, jets have a significant hadronic component which can be detected by the HCAL. The hadronic leakage, R_{had}, is defined as the ratio of the transverse energy in a $\Delta\eta\times\Delta\phi$=0.2$\times$0.2 in the first layer of the HCAL to the transverse energy of the EM cluster.

Second layer ECAL:

Since photons deposit most of their energy in this layer, several shower shape variables are used:

- $R_{\eta}(37)$, the ratio of the energy contained in a 3×7 window to the energy contained in a 7×7

window.

- $R_\phi(33)$, the ratio of the energy contained in a 3×3 window to the energy contained in a 3×7 window.

- ω_{η^2}, the lateral width of a shower calculated using the energy-weighted sum over all cells in a 3×5 window.

First layer ECAL:

Jets containing leading π^0s are the main source of fake photons at this stage. Due to the fine granularity of the first (strip) layer of the ECAL, information about the sub-structure of an EM shower can be extracted to distinguish between isolated π^0s and photons.

- As neutral pions decay to pairs of photons they are typically associated with two maxima. Windows of size $\Delta\eta \times \Delta\phi$=0.125×0.2 are constructed around the cell with the highest transverse energy. If another maximum exists within the window then the following variables from the second maximum are constructed:

  - $\Delta E_s = E_{max2} - E_{min}$, the difference between the energy of the second maximum and the lowest energy cell located between the primary and secondary maxima.

  - $\tilde{E}_{max2}$, the ratio of the corrected energy of the second maximum to the transverse energy of the cluster.

- F_{side}, the fraction of energy deposited outside the shower core of three central strips.

- $\omega_{3strips}$, the shower width using three strips around the one with the maximal energy deposit.

Since the above calorimeter variables are η and E_T dependent, the cut values are tuned separately in several intervals:

- E_T: <30 GeV, 30-40 GeV, 40-50 GeV, >50 GeV.

- $|\eta|$: 0-0.8, 0.8-1.37, 1.52-1.8, 1.8-2.0 and 2.0-2.37.

The intervals in η are motivated by the varying granularity of the detector and amount of material preceding the ECAL. No coverage is provided in the region above $|\eta|$ >2.40 or in the crack region, 1.37< $|\eta|$ <1.52, as there is no finely granulated strip layer in these regions. Additionally, the intervals allowing tuning of the cuts to provide ∼80% efficiency independent of η.

For the cuts using calorimeter information, converted photons are treated the in same manner as unconverted photons. However, studies indicate that there may be a possible benefit in developing an independent set of cuts for converted photons [72].

Inner Detector:

After the application of all of the above cuts, the remaining background is dominated by jets containing high-p_T neutral pions. Calorimeter information alone is not enough to reduce the background from mainly very asymmetric pion decays or decays with small opening angles. Associated with these decays is a non-negligible amount of hadronic activity around the cluster which can be identified by extrapolated tracks from the inner detector. Track isolation, defined as the sum of the p_T of all tracks, with $p_T > 1$ GeV$/c$, within a ΔR$<$0.3 cone centred on the cluster, is used to increase the rejection power. In order not to include tracks from photon conversions in this calculation, any track within ΔR$<$0.1 is subject to the following requirements:

- The impact parameter, d_0, must be less than 0.01cm.
- Track p_T $<$15 GeV$/c$, to remove asymmetric conversion tracks.
- Nearest opposite charged track in $|\cot(\theta)|$ must not have a partner forming a conversion.

Full details of the selection cuts outlined above, including the calorimeter cut values in each η, E_T interval can be found in [27, 73].

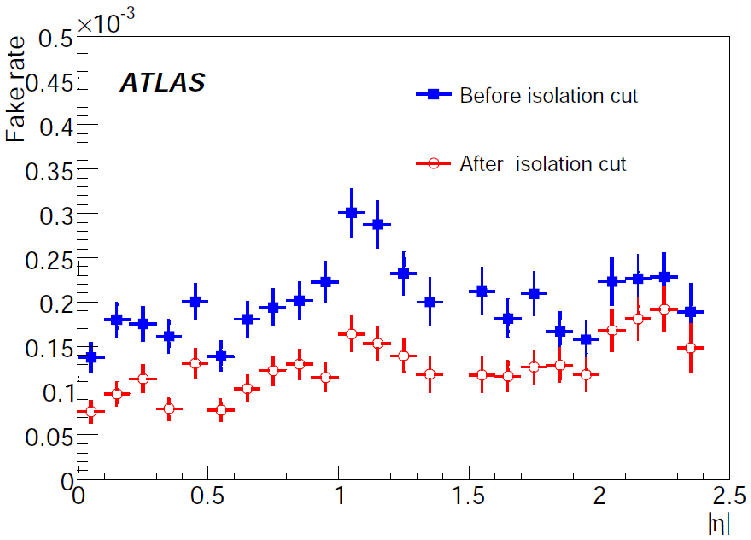

Figure 5.3: *Monte-Carlo fake-photon rate as a function of pseudorapidity for jets with $E_T > 25$ GeV. From [27].*

Using the aforementioned selection criteria the average reconstruction efficiency for a photon with transverse energy greater than 25 GeV has been found to be 84.3% $\pm$ 0.2% [27]. For this value of the reconstruction efficiency, the expected fake rate (or inverse of the jet rejection power) is shown as a function of $|\eta|$ in Figure 5.3 for jets with $E_T > 25$ GeV. Converted photons up to 800 mm from the interaction point are reconstructed with only a slightly lower average efficiency of almost 80% compared with unconverted photons. As mentioned at the beginning of this chapter, the recovery and reconstruction of converted photons plays a crucial role in searches for physics processes in which photons are the primary decay product. In particular, they can be used to be increase the signal statistics for the SM H $\rightarrow \gamma\gamma$ search and be used to accurately point back to the mother Higgs particle which aids identification of such events.

Chapter 6

Photon Identification Efficiencies for Fast Simulation

ATLFAST-I, detailed in Section 4.3.1, provides a fast simulation of the ATLAS detector response. Since ATLFAST-I does not model the interactions of particles with detector materials no reconstruction efficiencies or particle mis-identifications are provided. Instead, it is left for the user to provide their own efficiencies at the analysis stage. Typically, a user might correct for the lack of realistic efficiencies by applying a flat particle reconstruction efficiency for the objects of interest. Whilst this approach may be acceptable in low particle multiplicity scenarios, when multi-particle final states are required, any deviations from the flat efficiency are multiplied. Such deviations occur in the crack region of the detector and at higher pseudorapidities. To avoid these shortcomings, a tool has been developed called *AtlfastC*, which aims to accurately parameterise particle reconstruction and mis-identification efficiencies from full simulation and apply them to reconstructed objects in ATLFAST-I.

This chapter concentrates on the improvement of the photon identification efficiency parameterisations within AtlfastC. The motivation for doing so is that powerful photon identification and jet rejection is needed for the Standard Model $H \rightarrow \gamma\gamma$ search. As quotas are placed on the number of full simulation events that can be processed, background rejections can often be limited due to a lack of available events. If it can be demonstrated that ATLFAST-I in conjunction with AtlfastC can be used to obtain results comparable to those from full simulation, then large scale production of fast-simulated background samples can be produced without the restriction of quotas.

The chapter is arranged as follows. Firstly, the details of the AtlfastC algorithm are outlined and results from the default photon reconstruction efficiency parameterisations are discussed. Whilst

the default parameterisations are a significant improvement upon an application of a flat efficiency, there are several shortcomings that motivate the need for improvement. The derivation of new set of paramtrisations along with their subsequent validation is then presented. The validation of the new parameterisation reveals the need to treat converted and unconverted photons separately. Since approximately a third of all photons within the precision physics range will convert in the presence of the material preceding the calorimeter, two new separate parameterisations are presented: one for converted photons and one for unconverted photons. These new parameterisations are then shown to reproduce the desired efficiencies for isolated photons from several physics samples. It is observed that the parameterisations do not perform to the same degree in samples containing significant numbers of non-isolated photons. The reason for the discrepancy is identified and a potential solution is outlined.

6.1 AtlfastC Overview

AtlfastC [74] is an algorithm, run within ATLFAST I, that applies reconstruction efficiencies and mis-identifications for particles (electrons, muons, photons) and jets. A summary of all the efficiencies can be included in one efficiency matrix as seen in Table 6.1. Each of the above elements in the matrix is

Truth \ **Reconstructed**	**Electron**	**Photon**	**Muon**	**Jet**
Electron	$\varepsilon(e_{tr}, e_{rec})$	$C(e_{tr}, \gamma_{rec})$	$C(e_{tr}, \mu_{rec})$	$C(e_{tr}, jet_{rec})$
Photon	$C(\gamma_{tr}, e_{rec})$	$\varepsilon(\gamma_{tr}, \gamma_{rec})$	$C(\gamma_{tr}, \mu_{rec})$	$C(\gamma_{tr}, jet_{rec})$
Muon	$C(\mu_{tr}, e_{rec})$	$C(\mu_{tr}, \gamma_{rec})$	$\varepsilon(\mu_{tr}, \mu_{rec})$	$C(\mu_{tr}, jet_{rec})$
Jet	$C(jet_{tr}, e_{rec})$	$C(jet_{tr}, \gamma_{rec})$	$C(jet_{tr}, \mu_{rec})$	$\varepsilon(jet_{tr}, jet_{rec})$

Table 6.1: *AtlfastC efficiencies for particle identification and mis-identifications. Elements along the leading diagonal, e.g.* $\varepsilon(e_{tr}, e_{rec})$ *represent the reconstruction efficiency. Off-diagonal elements, e.g.* $C(e_{tr}, \gamma_{rec})$ *represent the mis-identification efficiencies*

a separate two-dimensional (in p_T and η) parameterisation. The parameterisations of reconstruction efficiencies run along the leading diagonal in the table. For example, $\varepsilon(e_{tr}, e_{rec})$ is the parameterisation of the efficiency for reconstructing an electron as an electron, where e_{tr} is a true electron and e_{rec} is a reconstructed electron. Off-diagonal elements in the table represent the mis-identification efficiencies, e.g. $C(\gamma_{tr}, jet_{rec})$ is the efficiency for a photon to be reconstructed as a jet. The individual parameterisations contain values of the reconstruction/mis-identification efficiency in each bin of p_T

and η and are stored in plain datafiles. The efficiencies in AtlfastC are obtained from studies with full simulation events. For example, the reconstruction and mis-identification efficiencies of electrons are obtained from fully simulated samples of $Z \rightarrow e^+e^-$.

Particles reconstructed by ATLFAST-I are stored by their type in data structures known as particle containers. To apply particle reconstruction efficiencies AtlfastC takes each particle from the container, retrieves the appropriate efficiency value from the datafile based on the particle's p_T and η and compares that value to a randomly generated number between 0 and 1. If the random number is less than the efficiency value then the particle is deemed to be reconstructed and is recorded into the appropriate AtlfastC particle container. If the random number is greater than the efficiency value then the particle is simply not recorded into the AtlfastC container. The application of mis-identification efficiencies works in much the same manner except that the mis-identified particle is recorded into the appropriate AtlfastC particle container. For example, if an ATLFAST-I photon is adjudged to be mis-identified as a jet then it is recorded into the AtlfastC jet container. No new particles are created in this process, instead the particle is just recorded into another container with the same p_T and η. If reconstruction and mis-identification efficiencies are both desired then the reconstruction efficiencies are applied first and the mis-identification efficiencies are applied only to those particles that have not been deemed reconstructed by the AtlfastC routine.

6.1.1 Original AtlfastC Photon Efficiency parameterisations

Prior to the development of the photon reconstruction efficiency parameterisations in the present work, the original AtlfastC parameterisations were derived from a study with full simulation gg→H(120)→ $\gamma\gamma$ events (where the notation has been adopted in which the Higgs boson mass in units of GeV/c^2 is given in parenthesis next to the "H") in release 12.0.6 of Athena. The parameterisations were divided into:

- 50 bins between $0 < |\eta| \leq 5$,
- 5 bins between $5 < p_T \leq 55$ GeV$/c$ and 1 bin for $p_T > 55$ GeV$/c$.

Figure 6.1 shows the reconstruction efficiency for photons from gg→H(120)→ $\gamma\gamma$ events as a function of p_T and $|\eta|$ for full simulation, ATLFAST-I and ATLFAST-I with the parameterisations applied (often just referred to as AtlfastC). The reconstruction efficiency for ATLFAST-I is seen to be almost constant at 100% with small deviations arising from photons not being reconstructed due to the acceptance range of ATLFAST-I. The effect of the AtlfastC parameterisations can be viewed as the change from the ATLFAST-I to AtlfastC efficiency distribution. The aim of using the AtlfastC

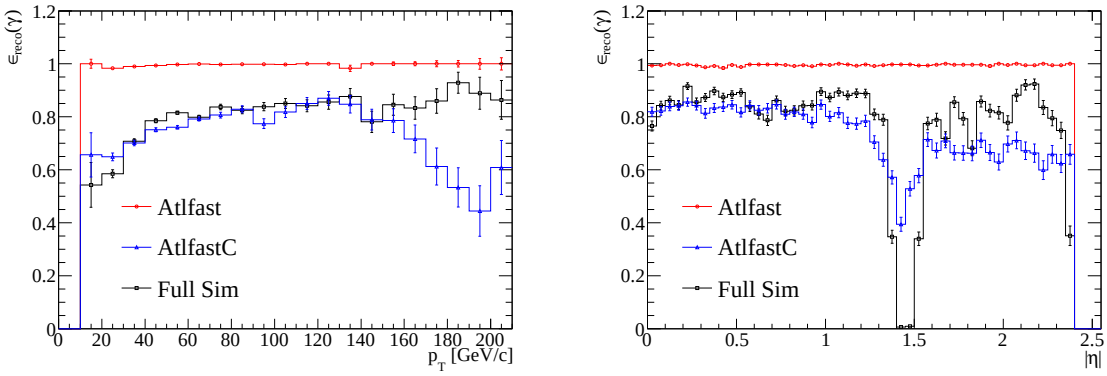

(a) p_T (b) $|\eta|$

Figure 6.1: *Photon reconstruction efficiency from $gg \rightarrow H(120) \rightarrow \gamma\gamma$ events as a function of p_T and $|\eta|$ for full simulation (black), ATLFAST-I (red) and ATLFAST-I with AtlfastC (blue), using the original photon reconstruction efficiency parameterisations.*

parameterisation is to reproduce the reconstruction efficiency of full simulation. However, in these distributions the AtlfastC photon reconstruction efficiency parameterisation does not accurately reproduce the full simulation reconstruction efficiency with the largest discrepancies seen in the crack region of the detector, $1.37 < |\eta| < 1.52$, and the high-p_T ($p_T > 160$ GeV$/c$) region. These effects can be explained by inadequate binning of the parameterisation in those regions and thus not accurately sampling the full simulation reconstruction efficiency. To correct for these deficiencies, a new set of parameterisations have been created which aim to improve upon the original parameterisations by using a finer bin granularity in $|\eta|$ and extending the range in p_T beyond 55 GeV$/c$.

6.2 Derivation of New parameterisations

To create a new set of photon reconstruction parameterisations to replace the original AtlfastC parameterisations, a detailed study with full simulation events has been performed. Since ATLFAST-I is not able to reliably simulate photons with $p_T < 10$ GeV$/c$ or $|\eta| > 2.5$ these regions have not be included in the new parameterisation. However, this does not impose any real restrictions as the precision physics range of the detector only extends upto $|\eta| = 2.5$ and, in general, any physics analysis would require photons above 10 GeV$/c$.

The sections that follow describe the process undertaken to create a new set of photon reconstruction efficiency parameterisations.

6.2.1 Strategy for Extracting parameterisations

Photon reconstruction efficiencies must be extracted from full simulation events, parameterised and then implemented, via AtlfastC, into the ATLFAST-I simulation. To ensure maximum coverage over the parameterisation range, $|\eta| < 2.5$ and $p_T > 10$ GeV$/c$, a range of fully simulated samples, detailed in Table 6.2.1, have been chosen as the sources for the parameterisations. All H$\rightarrow \gamma\gamma$ events in

Process	Number Of Events
$(gg+VBF) \rightarrow H(120) \rightarrow \gamma\gamma$	50,000
$gg \rightarrow H(120) \rightarrow \gamma\gamma$	10,000
$gg \rightarrow H(200) \rightarrow \gamma\gamma$	10,000
Single γ $(7 < E_T < 80$ GeV)	50,000

Table 6.2: *Fully simulated physics samples used as the sources for the photon reconstruction efficiency parameterisations.*

the source samples have been generated with a filter applied which rejects events where either there were less than two photons or one of the two photons transverse momentum was less that 20 GeV$/c$. To cover parameterisations in the $10 < p_T < 20$ GeV$/c$ range, a single photon sample containing photons with $7 < E_T < 80$ GeV has also been used.

Here, reconstruction efficiency is defined as the fraction of Monte-Carlo truth photons that have a reconstructed photon matched to them, divided by the total number of truth photons. Defining it in such a manner ensures that all possible losses, such as fiducial, kinematic and detector effects can be included. This can all be summed up in an equation to give the reconstruction efficiency:

$$\varepsilon_\gamma(p_T, |\eta|) = \frac{n_\gamma^{matched}(p_T, |\eta|)}{n_\gamma^{truth}(p_T, |\eta|)} \tag{6.1}$$

where the $n_\gamma^{matched}$ is the number of truth photons that are matched to reconstructed ones, n_γ^{truth} is the total number of truth photons, and ε_γ is the reconstruction efficiency. Since the parameterisation will be two dimensional the reconstruction efficiency is a function of both p_T and $|\eta|$.

The reconstruction efficiency is somewhat dependent upon the configuration of the algorithm used to reconstruct photons. There are several differing configurations used throughout ATLAS, each of which depends on the requirements of physics groups. The configuration used here is a tuned version of the standard reconstruction algorithm, described in Section 5.2.1, and is widely used throughout

ATLAS [75]. It was originally developed for the H$\rightarrow \gamma\gamma$ search to enhance the jet rejection power whilst maintaining a reconstruction efficiency of 84%. The algorithm will attempt to reconstruct photons as long as they are in the fiducial range $0 < |\eta| < 1.37$, $1.52 < |\eta| < 2.37$ and have a transverse momentum greater than 10 GeV$/c$. Thus, it follows that this will effectively limit the parameterisation scope to these ranges.

An important aspect in obtaining the reconstruction efficiency is the method by which truth photons are *matched* to reconstructed photons. The matching is performed by means of a ΔR requirement, where $\Delta R = \sqrt{\Delta\eta^2 + \Delta\phi^2}$. For each final state truth photon with $p_T > 10$ GeV$/c$ and within $|\eta| < 2.5$, the ΔR value to the nearest reconstructed photon is recorded. An example distribution of the ΔR between truth and nearest reconstructed photon using photons from the parameterisation source samples can be seen in Figure 6.2. Based on the distribution, a match is only accepted if the

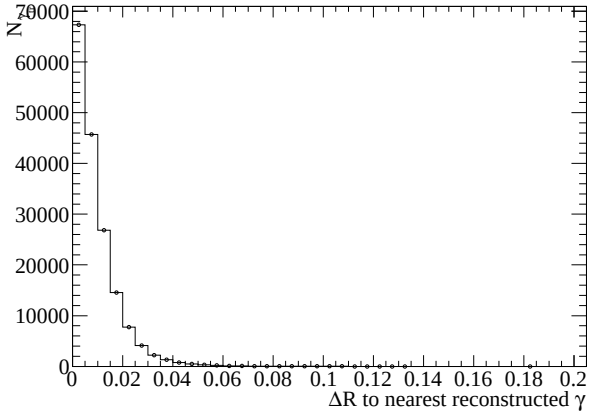

Figure 6.2: *Distribution of the minimum ΔR value (defined in the text) between reconstructed photons and truth level photons from the fully simulated event samples in Table 6.2.1.*

nearest reconstructed photon is inside of a cone of $\Delta R = 0.1$ around the truth photon. To check the quality of matching, differences in p_T and η between truth photons and their respective matched reconstructed photon are plotted. Any large deviations from zero would be evidence that the matching is not performing well. A Gaussian distribution would be expected since if the matching process has found the correct pairing then the only differences in p_T and η would be down to the reconstruction process itself, i.e. the detector resolution. More often than not the reconstruction process underestimates the true energy of the photon. This is primarily due to leakage of the electromagnetic shower and the performance of the clustering algorithms. Therefore, it would be expected that the difference between the p_T of truth photons and reconstructed ones should have a positive tail arising from the underestimation. Figure 6.3 shows the matching process performing as expected and indicates that

for photons the ATLAS detector has a p_T resolution of $\sim$1 GeV$/c$ whilst in η the resolution is $\sim$0.01.

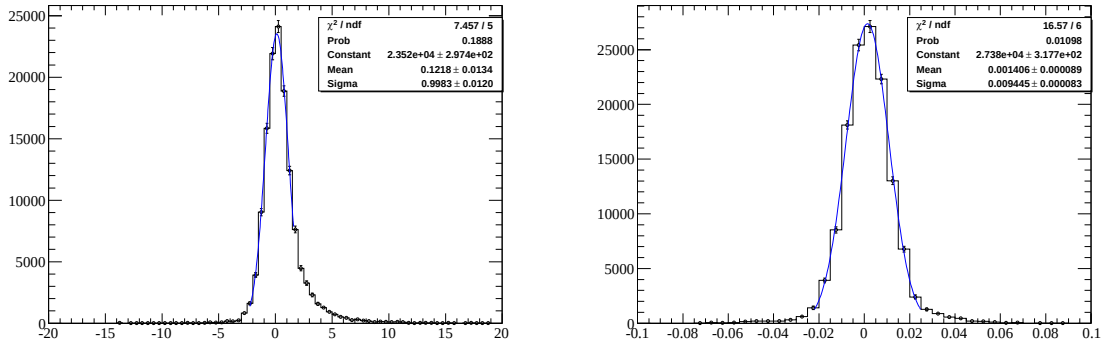

(a) p_T(*truth*)-p_T(*reconstructed*) (b) η(*truth*)-η(*reconstructed*)

Figure 6.3: *Truth to reconstructed photon matching performance distributions indicating simulated detector resolutions for the p_T and η of photons from the parameterisation source event samples contained in Table 6.2.1.*

To illustrate the effect of the detector simulation and of the reconstruction process, distributions showing the p_T and $|\eta|$ of truth photons and truth photons that have been matched to a reconstructed photon (subsequently referred to as matched truth photons), are shown in Figure 6.4. The matched

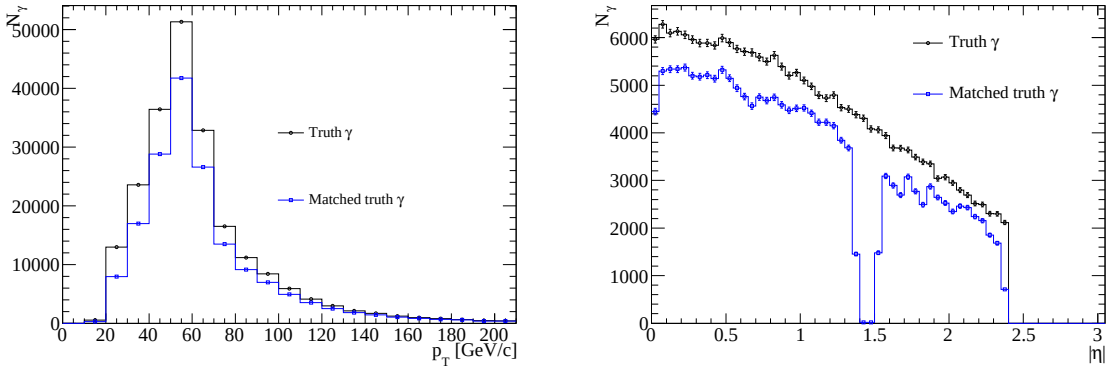

(a) p_T (b) $|\eta|$

Figure 6.4: *Distributions of matched truth photons (a) p_T and (b) $|\eta|$ for photons from the parameterisation source event samples contained in Table 6.2.1. Each figure shows the distribution for all truth photons (black) and the distribution of truth photons matched with a reconstructed photon (blue).*

truth photon distributions give a detector slant to the truth. For example, the effect of the detector simulation and reconstruction can be viewed as the difference between the distribution of truth photons and the distribution of matched truth photons. Following the definition of reconstruction efficiency

in Equation 6.1, dividing the distribution of matched truth photons by the respective truth photon distributions yields the reconstruction efficiency as a function of p_T and $|\eta|$, as seen in Figure 6.5.

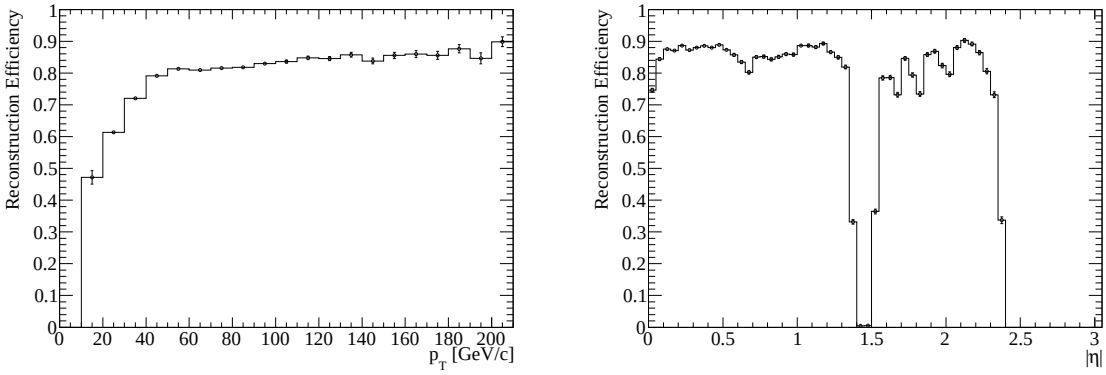

(a) p_T (b) $|\eta|$

Figure 6.5: *Photon reconstruction efficiency as a function of (a) p_T and (b) $|\eta|$ for photons from the parameterisation source event samples contained in Table 6.2.1.*

Since the parameterisation will be two-dimensional (p_T and $|\eta|$) the granularity must be set. As established above the original parameterisations suffered from a lack of detail arising from too coarse a granularity. Ideally, a fine granularity would be used but this requires a large number of events containing photons in order to populate all the bins. Therefore, a middle ground is needed, whereby each bin of the parameterisation has enough statistics to be reliable, and that the granularity is fine enough such that it accurately samples the reconstruction efficiency. The scheme that has been chosen is as below:

- 12 p_T regions: 10-20 GeV$/c$, 20-30 GeV$/c$,..., 110-120 GeV$/c$, 120+ GeV$/c$;
- 50 bins in $|\eta|$: 0.00-0.05, 0.05-0.10,..., 2.40-2.45, 2.45-2.50

For each p_T region there is a corresponding 50 bin $|\eta|$ distribution. Practically, this is achieved by grouping photons with p_T in a certain range, e.g. $10 < p_T < 20$ GeV$/c$, and calculating the reconstruction efficiency as a function of $|\eta|$ for these photons. There are 12 histograms displaying the reconstruction efficiency as a function of η. For regions not covered by the scope of the parameterisations they are manually set to have 0% efficiency. For each histogram the value of the reconstruction efficiency in each bin is read-out and stored in a datafile. The datafile is formatted such that when requested it can be read-in by the AtlfastC algorithm.

6.2.2 Validation of Initial parameterisations

In the creation of the parameterisation only half of the full simulation events in any one Monte-Carlo sample were used. This was done so that the event generator record of the remaining half could be passed to the ATLFAST-I simulation to create a fast simulation sample. The AtlfastC algorithm with the new parameterisations was then applied to the fast simulation sample. This ensures that independent events are used in the creation of the parameterisations to those used for testing the parameterisations, whilst guaranteeing that the Monte-Carlo generation between samples is consistent.

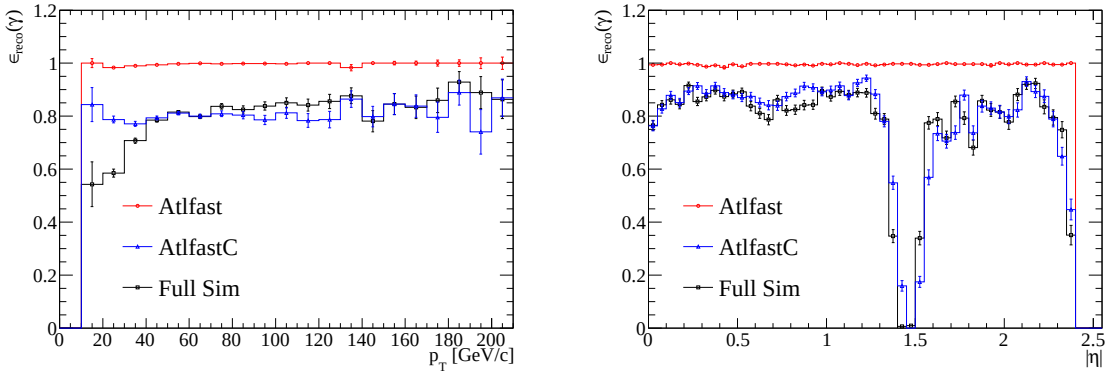

(a) p_T (b) $|\eta|$

Figure 6.6: *Photon reconstruction efficiency from gg→ H(120) → γγ events as a function of (a) p_T and (b) $|\eta|$ for full simulation (black), ATLFAST-I (red) and ATLFAST-I with AtlfastC (blue) using the new photon reconstruction efficiency parameterisations.*

Figure 6.6(b) shows the photon reconstruction efficiency in gg→H(120)→ γγ events as a function of p_T and $|\eta|$ for full simulation, ATLFAST-I and AtlfastC using the newly created photon reconstruction efficiency parameterisations. Whilst the new parameterisations have addressed the issues of the original parameterisations (see Section 6.1.1), one particular feature is still seen not to agree well between AtlfastC and full simulation efficiencies. AtlfastC photons with $10 < p_T < 40$ GeV$/c$ are seen to have a much larger reconstruction efficiency than those from full simulation. To investigate the reason for the low-p_T discrepancy, truth photons with $10 < p_T < 40$ GeV$/c$ that are not matched to full simulation reconstructed photons were checked as to whether they converted. A truth tool [76], part of the H→ γγ working group's analysis package, was used to scan the GEANT4 Monte-Carlo truth record for the presence of converted photons. If a photon was found to convert to an electron and positron pair then it was flagged by the tool. Figure 6.7 shows the fraction of converted and unconverted photons with $10 < p_T < 40$ GeV$/c$ from fully simulated events used to create the new parameterisations, firstly for for all truth photons, secondly for matched truth photons

and finally for unmatched truth photons. Figure 6.7(a) indicates that at truth level ∼35% of pho-

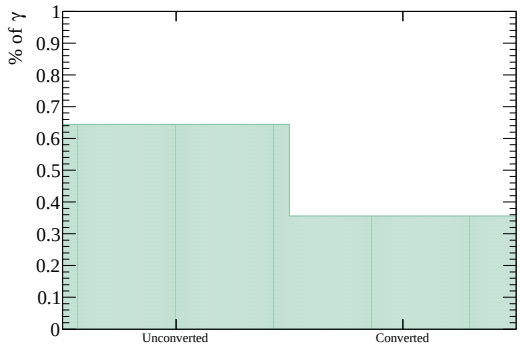

(a) Truth γ

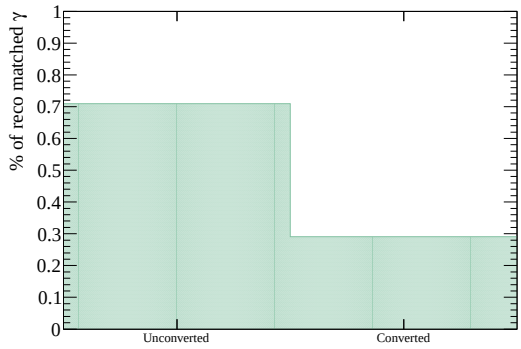

(b) Matched truth γ

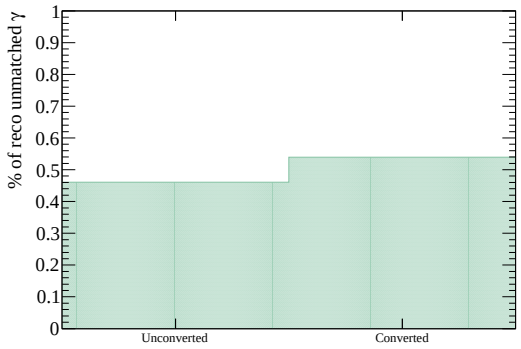

(c) Unmatched truth γ

Figure 6.7: *Fraction of converted and unconverted (a) truth photons, (b) matched truth photons and (c) unmatched truth photons. Distributions are from fully simulated events used to create the parameterisations, where truth photons have* p_T *in the range 10*$< p_T <$*40* GeV$/c$.

tons convert. If converted and unconverted photons are reconstructed with the same efficiency the ratio of converted-to-unconverted should remain the same regardless of whether they have a reconstructed photon matched to them. However, Figure 6.7(c) shows that a much larger fraction, ∼54%, of unmatched truth photons are converted photons. This leads to the conclusion that converted and unconverted photons are reconstructed with differing efficiencies and hence should be treated separately. Therefore, the parameterised photon reconstruction efficiency obtained above is actually a convolution of ∼35% of the converted photon reconstruction efficiency and ∼65% of the unconverted photon reconstruction efficiency. Effectively, this ratio has been hard-coded into the parameterisations, thus if the parameterisations are used in conjunction with ATLFAST-I on a sample with a different ratio of converted-to-unconverted photons then converted photons in that sample may be reconstructed with the wrong efficiency. This effect is the cause of the discrepancy seen in Figure 6.6(a). To address this

issue the parameterisation strategy has evolved to create separate parameterisations for converted and unconverted photon reconstruction efficiencies.

6.2.3 Treatment of Converted Photons

As outlined above converted and unconverted photons have differing reconstruction efficiencies and in full simulation are reconstructed with different algorithms (see Chapter 5). Typically, converted photons have a lower reconstruction efficiency as they are harder to identify than unconverted photons. This is partly because the probability that a photon will convert is proportional to the amount of material it traverses and therefore more conversions happen in the crack region of the detector. Additionally, as tracks from low-p_T conversions are more affected by bremsstrahlung the efficiency for reconstruction of low-p_T converted photons is degraded. These effects can be seen when comparing the reconstruction efficiencies of converted and unconverted photons in Figure 6.8. The dip

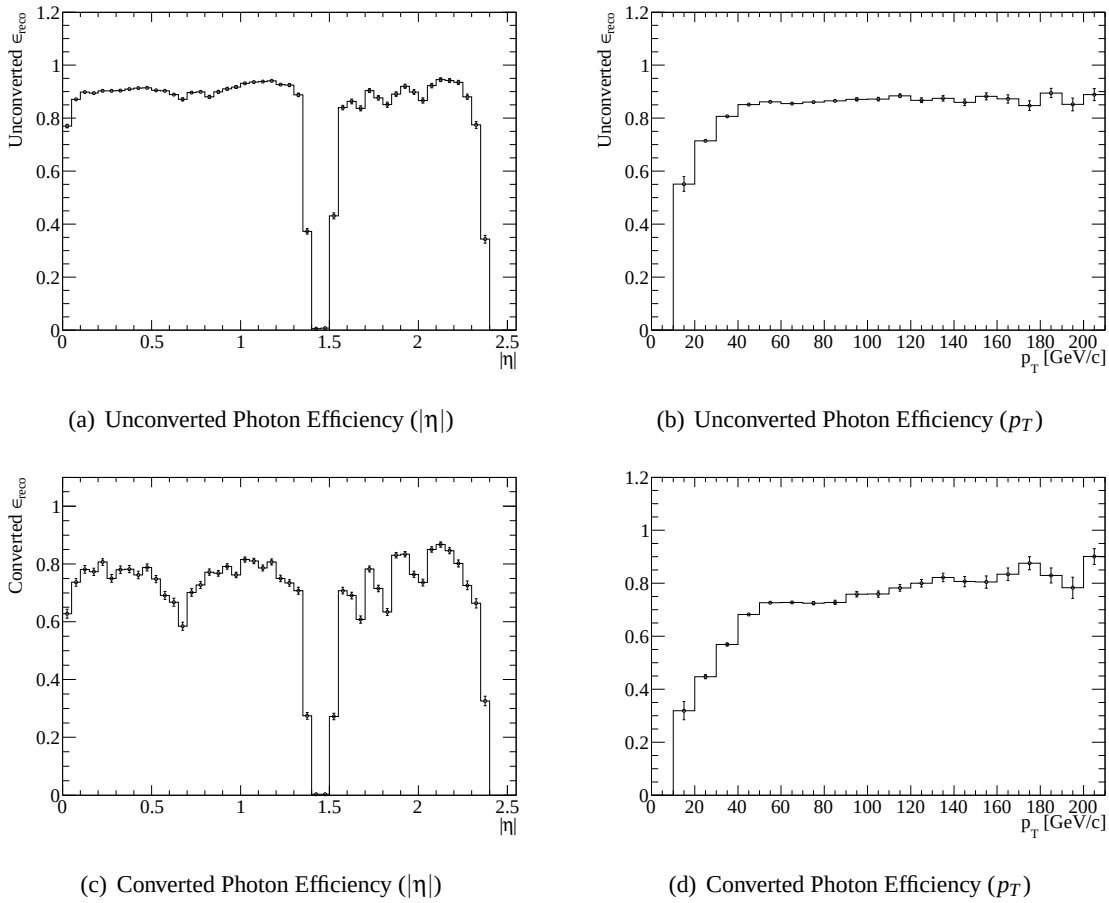

(a) Unconverted Photon Efficiency ($|\eta|$)

(b) Unconverted Photon Efficiency (p_T)

(c) Converted Photon Efficiency ($|\eta|$)

(d) Converted Photon Efficiency (p_T)

Figure 6.8: *Photon reconstruction efficiency as a function of p_T and $|\eta|$ for converted and unconverted photons from the parameterisation source event samples contained in Table 6.2.1.*

in converted photon reconstruction efficiency at $|\eta|$=0.7 is due to track reconstruction inefficiencies in the gap region between the TRT barrel and end-cap. The modulation in the pseudorapidity range after the crack region is caused by material effects and the use of the TRT end-cap in track reconstruction. Efficiency for both unconverted and converted photons tails off above $|\eta|$ =2.1 due to the pseudorapidity limit of the TRT.

The need for separate parameterisations is clear. This was achieved by using the aforementioned conversion flagging tool to separate, at truth level, full simulation converted photons from unconverted photons. The same parameterisation strategy, described in Section 6.2.1, was used to create separate parameterisations for converted and unconverted photons. However, the AtlfastC algorithm had originally been written to include just one photon reconstruction efficiency parameterisation. In order for AtlfastC to apply the correct parameterisation, ATLFAST-I photons need to have been flagged as converted or unconverted. Since ATLFAST-I, contrary to the full simulation process, does not simulate (GEANT4) particle interactions with the detector media, no conversion information exists and the conversion flagging tool cannot be used. To provide this information in the ATLFAST-I simulation, the probability that a given photon will convert, or not, has been found from full simulation events and included into the ATLFAST-I simulation. The probability of conversion is defined as:

$$P_{conv} = \frac{n_{\gamma}^{converted}}{n_{\gamma}} \tag{6.2}$$

where $n_{\gamma}^{converted}$ is the number of full simulation converted truth photons and n_{γ} is the total number of truth photons. Figure 6.9 shows the probability of conversion as a function of $|\eta|$, $|\phi|$ and p_T for full simulation photons from the parameterisation source samples. The probability of conversion is seen to only depend on $|\eta|$. This is unsurprising since the probability of conversion is dependent upon the amount of material that the photon passes through (see Figure 5.2). It is also sensible that the probability of conversion is flat as a function of ϕ since the detector, to first approximation, is symmetric in ϕ. Notably, the probability that a photon will convert is not intrinsically linked with the photon's transverse momentum [77]. Therefore, the probability of conversion can be approximately parameterised as just a function of $|\eta|$ as seen in Figure 6.9(a). Here, the parameterisation uses the same $|\eta|$ granularity of 50 bins in $0< |\eta| \leq 2.5$ as the reconstruction efficiency parameterisations. Since the AtlfastC datafile format expects the parameterisation to be two-dimensional, a dummy p_T bin is used in the conversion probability parameterisation datafile to remove the need to create separate datafile interpreter routines in the AtlfastC algorithm.

Figure 6.10 is a flowchart to demonstrate how the additional conversion probability and recon-

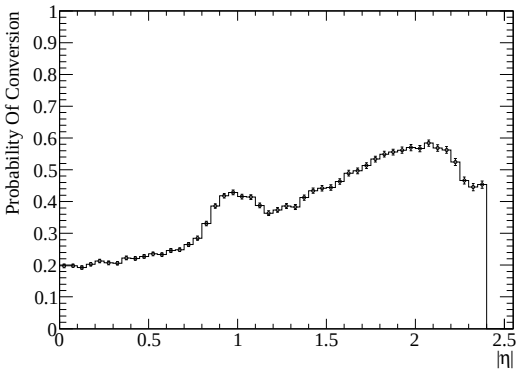

(a) Probability of conversion vs $|\eta|$

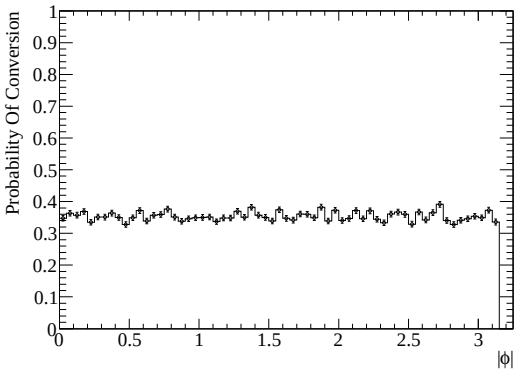

(b) Probability of conversion vs $|\phi|$

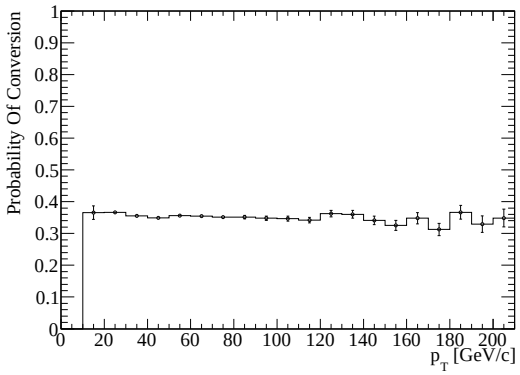

(c) Probability of conversion vs p_T

Figure 6.9: *Probability of conversion as a function of (a) $|\eta|$, (b) $|\phi|$ and (c) p_T for truth photons from the parameterisation source event samples contained in Table 6.2.1.*

struction efficiency parameterisations are integrated into the existing AtlfastC algorithm. In the original parameterisations AtlfastC passed ATLFAST-I reconstructed photons to the single photon efficiency parameterisation routine, where, based upon the reconstructed photon's p_T and $|\eta|$, it was decided whether to record the photon in the AtlfastC photon container or not. In Figure 6.10 this process has been indicated by the red arrow. With the new scheme, which accounts for converted photons, a decision is made as to whether reconstructed ATLFAST-I photons would have converted or not. Since the parameterisation of the probability of conversion was based on full simulation truth conversion information, the original (or *associated*) truth photon, from which ATLFAST-I creates the reconstructed photon, is retrieved from the Monte-Carlo record. The associated truth photon is then passed to the probability of conversion routine which is used to decide whether the photon would have converted or not. If the associated truth photon is deemed as a conversion then the reconstructed ATLFAST-I photon is passed to the converted photon reconstruction efficiency parameterisation rou-

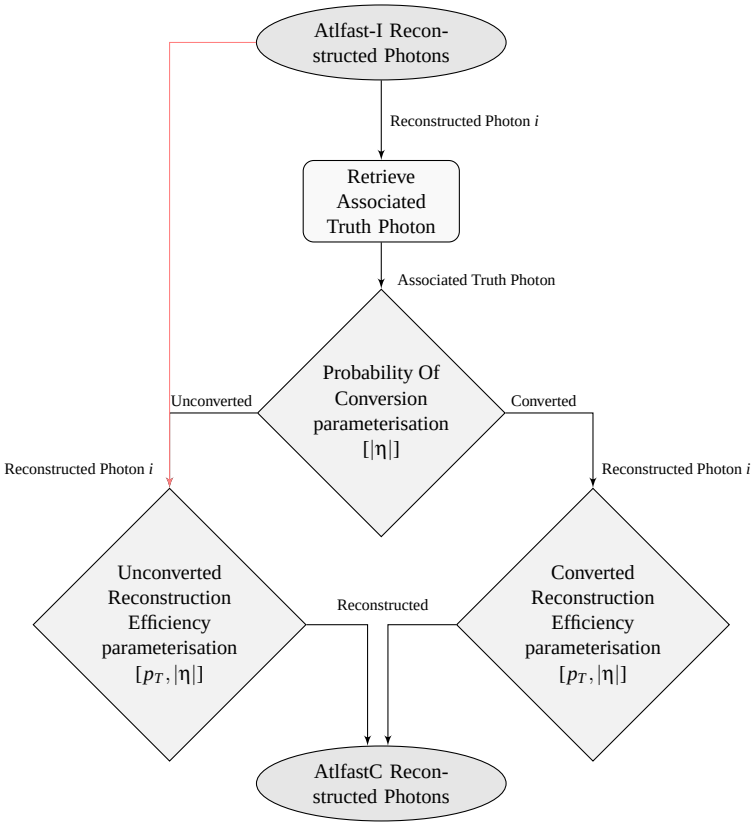

Figure 6.10: *Flow diagram showing how the new converted photon parameterisations are implemented. For reference the red path indicates the route that the original AtlfastC parameterisations took.*

tine, where a decision is made to either reconstruct and record the photon in the AtlfastC photon container or discard it. Equivalently, if the associated truth photon is deemed not to have converted then the unconverted photon reconstruction efficiency parameterisation is applied. Currently, the decision as to whether a photon converts is not stored as a property of an ATLFAST-I photon, and is only used in the photon-by-photon determination of which efficiency parameterisation to apply. It is feasible that future versions of the ATLFAST-I simulation could incorporate the conversion probability routine.

6.2.4 Final parameterisations

The full set of the new AtlfastC photon reconstruction efficiency parameterisations can be found in Appendix A. Figure 6.11 shows a one-dimensional view of the parameterisations versus p_T, where the average value of the reconstruction efficiency and error on it have been calculated from the corresponding $|\eta|$ distributions. The parameterisations assume that photons with p_T greater than

120 GeV/c are reconstructed with the same efficiency. parameterisation bin sizes and the use of large numbers of events in the creation of the parameterisations ensures that the parameterisations can be reliable and accurate.

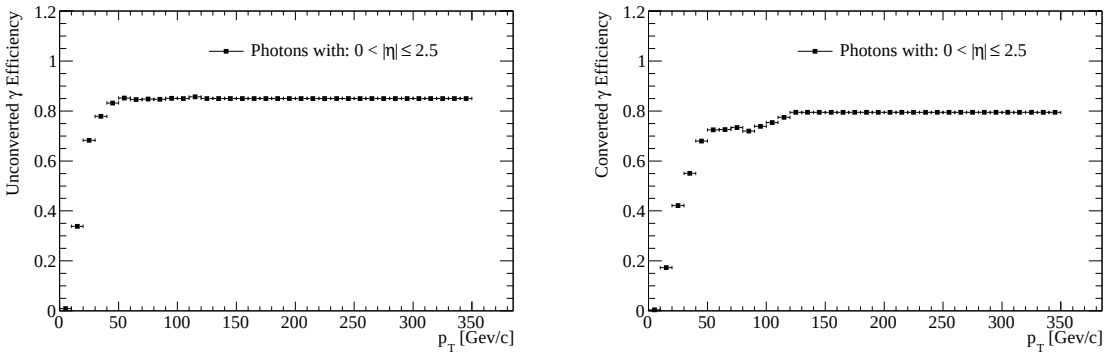

(a) unconverted photons (b) converted photons

Figure 6.11: *parameterisations of the photon reconstruction efficiency as a function of p_T, averaged over the whole $|\eta| < 2.5$ range, for (a) unconverted photons and (b) converted photons.*

6.3 Validation of Final parameterisations

The new parameterisation for converted and unconverted photons have been validated using the same technique as detailed in Section 6.2.2. Several samples are used in order to validate the parameterisations (see Table 6.3). Since certain samples, e.g. $gg \rightarrow \mathrm{H}(120) \rightarrow \gamma\gamma$, were used in the creation of the parameterisations they represent the best case scenario in terms of ascertaining the validity of the parameterisations. It should be noted that care has been taken in the validation of such samples to use independent events so as to ensure no biases are introduced. Additionally, the parameterisations have been tested with a non-resonant production of $gg(q\overline{q}) \rightarrow \gamma\gamma$ (a main background to the H$\rightarrow \gamma\gamma$ search) sample. This sample is ideal for testing the performance of the parameterisations as it was not used in their creation and the sample also contains photons of a similar p_T range. Finally, the parameterisations are tested with $t\overline{t}(\mathrm{H}\rightarrow \gamma\gamma)$. This sample provides a new challenge for the parameterisations compared to the last two samples since this sample is associated with an increase in hadronic activity in the hard process itself.

6.3.1 Validation with $gg \rightarrow$H$\rightarrow \gamma\gamma$ Signal Events

The idea of the validation is to compare the reconstruction efficiencies along with distributions of reconstructed photons obtained from full simulation and AtlfastC. As highlighted earlier only the first

Process	Number Of Events
$gg \rightarrow H(120) \rightarrow \gamma\gamma$	10,000
$gg(q\bar{q} \rightarrow \gamma\gamma$	125,000
$t\bar{t}(H(120) \rightarrow \gamma\gamma)$	13,000

Table 6.3: *Numbers of events in three simulated physics samples used in the validation of the new photon reconstruction efficiency parameterisations.*

half of the full simulation events in any of the source samples are used to create the parameterisations. The remaining half can be used to create a fast simulation (ATLFAST-I) sample, which in turn can be used to create the AtlfastC sample containing the new reconstruction efficiency parameterisations. To check whether it is indeed the same process albeit with independent events being compared, truth photon distributions are shown from the fast simulation and full simulation samples in Figure 6.12.

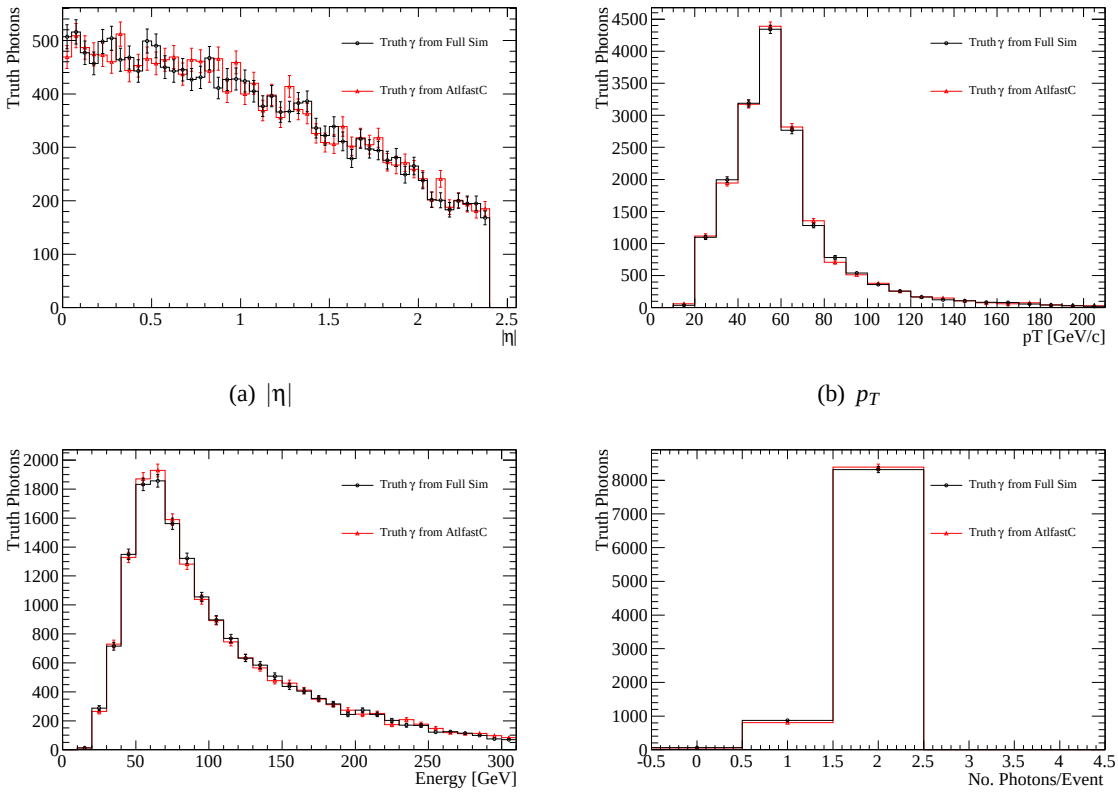

(a) $|\eta|$ (b) p_T

(c) energy (d) Photon multiplicity

Figure 6.12: *Distributions showing (a) $|\eta|$, (b) p_T, (c) energy and (d) multiplicity of truth photons from $gg \rightarrow H(120) \rightarrow \gamma\gamma$ full simulation (black) and fast simulation (red) events.*

The results of the validation are shown in Figure 6.13 which shows the $|\eta|$, p_T, energy and multiplicity distributions of reconstructed photons from full simulation and fast simulation with (AtlfastC) and without (standard ATLFAST-I) the parameterisations applied. Good agreement is seen between full simulation and AtlfastC photon distributions, indicating that the application of the parameterisations enable fast simulation photons to resemble full simulation photons. The distributions also demonstrate the usefulness of the parameterisations, since without them the standard ATLFAST-I simulation greatly overestimates the number of photons present, compared with full simulation, and does not reproduce any of the features seen in the $|\eta|$ distribution.

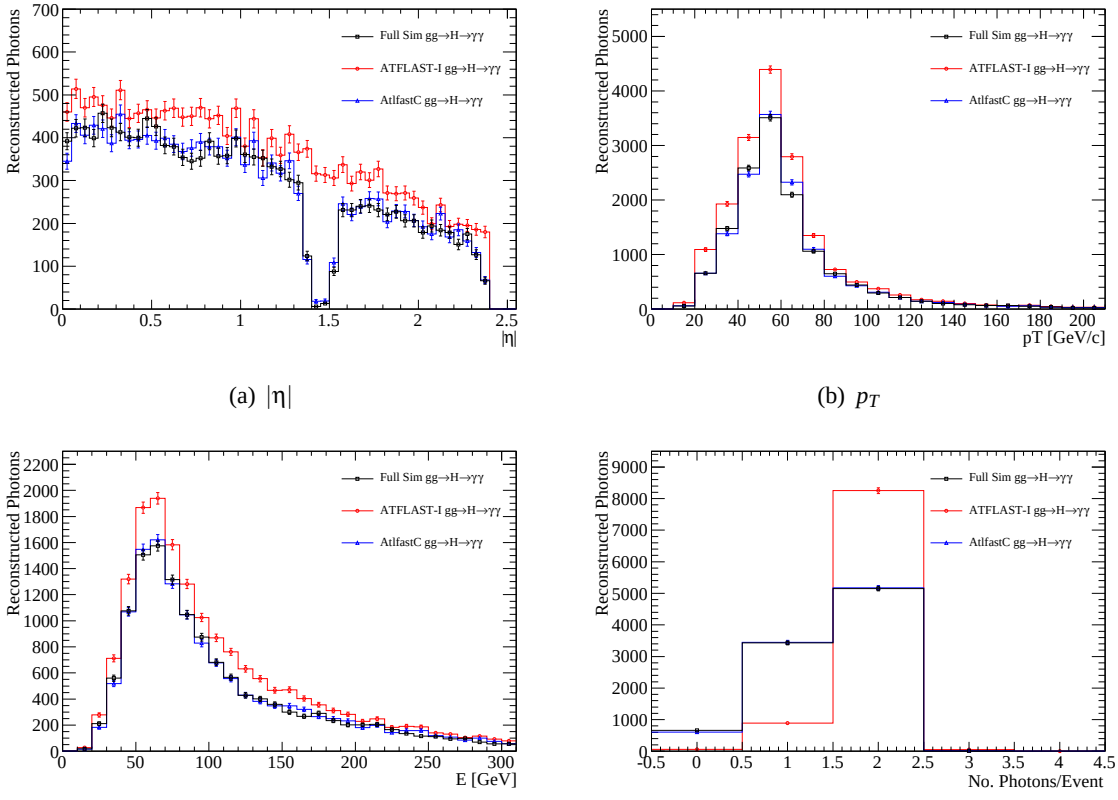

(a) $|\eta|$ (b) p_T

(c) energy (d) Photon Multiplicity

Figure 6.13: *Results of the validation with $gg \rightarrow H(120) \rightarrow \gamma\gamma$ events. Reconstructed photon distributions are shown as a function of (a) $|\eta|$, (b) p_T, (c) energy and (d) multiplicity for full simulation (black), ATLFAST-I (red) and AtlfastC with the new parameterisations (blue).*

The performance of the parameterisations can also be seen by viewing the photon reconstruction efficiencies. The comparison of the reconstruction efficiency as a function of $|\eta|$ and p_T from full simulation and fast simulation with (AtlfastC) and without (standard ATLFAST-I) the parameterisations is shown in Figure 6.14. The standard ATLFAST-I reconstruction efficiency is, by default, almost constant at 100% since no losses are accounted for. However, with the AtlfastC parameter-

isations derived in this work, the reconstruction efficiency for both p_T and $|\eta|$ compares well with the full simulation. Additionally Table 6.4 indicates that the mean photon reconstruction efficiency for $gg \rightarrow \mathrm{H}(120) \rightarrow \gamma\gamma$ events is in statistical agreement between full simulation and the AtlfastC parameterisations.

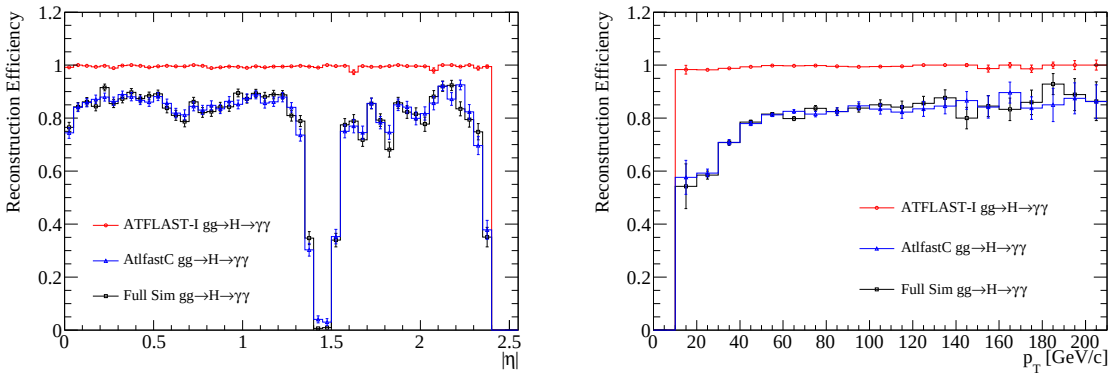

(a) $\varepsilon(|\eta|)$ (b) $\varepsilon(p_T)$

Figure 6.14: *Results of the validation with $gg \rightarrow H(120) \rightarrow \gamma\gamma$ events. Photon reconstruction efficiency distributions are shown as a function of (a) $|\eta|$ and (b) p_T for full simulation (black), ATLFAST-I (red) and AtlfastC with the new parameterisations (blue).*

Simulation	Reconstruction Efficiency(%)
Full Simulation	78.56±0.31
AtlfastC Simulation	78.63±0.31
ATLFAST-I Simulation	99.49±0.05

Table 6.4: *Average photon reconstruction efficiency in $gg \rightarrow H(120) \rightarrow \gamma\gamma$ events for each of the simulations.*

6.3.2 Validation with Di-Photon Background Events

As might have been expected the parameterisations perform well with events from a process that was used in the derivation of the parameterisations. To fully test the parameterisations they have been validated with events from a $gg(q\bar{q}) \rightarrow \gamma\gamma$ process which were not used in the creation of the parameterisations. This process is one of the major backgrounds to the search for a Standard Model Higgs decaying to a pair of photons and therefore represents a useful test case. The results of the validation can be seen in Figures 6.15 and 6.16 which, following the same format as the above validation using $gg \rightarrow \mathrm{H}(120) \rightarrow \gamma\gamma$ events, show the distributions of reconstructed photons and photon reconstruction

efficiencies for full simulation and AtlfastC. Again, good agreement is seen between full simulation photon distribution and those from the AtlfastC parameterisations. Table 6.5 also indicates that the mean value of the photon reconstruction efficiency as obtained from the full simulation sample is in agreement with the one obtained from the AtlfastC sample. The primary advantage of the parameterisations derived in this work, is that they can be used in conjunction with fast simulation to rapidly create large samples of this background process. Additionally, the photons in these samples would replicate the behaviour of photons seen in fully simulated events.

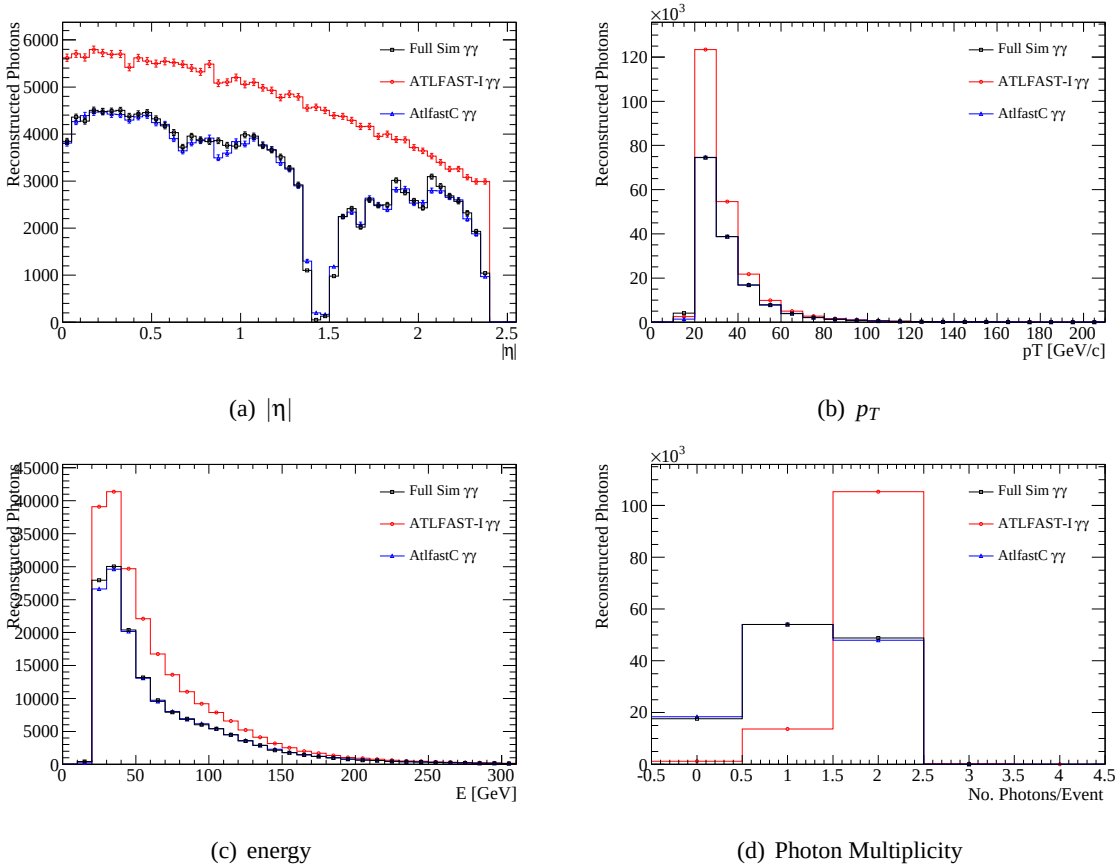

(a) $|\eta|$ (b) p_T

(c) energy (d) Photon Multiplicity

Figure 6.15: *Results of the validation with $gg(q\bar{q}) \rightarrow \gamma\gamma$ events. Reconstructed photon distributions are shown as a function of (a) $|\eta|$, (b) p_T, (c) energy and (d) multiplicity for full simulation (black), ATLFAST-I (red) and AtlfastC with the new parameterisations (blue).*

6.3.3 Validation with $t\bar{t}(\mathbf{H}\rightarrow\gamma\gamma)$ Signal Events

The above validations using two different processes demonstrate the performance of the parameterisations in *clean* environments. Here, a *clean* environment is one which is characterised by a relative lack of hadronic activity from the hard process itself, and as a consequence means that a very high proportion of photons in the $gg \rightarrow \mathrm{H}(120) \rightarrow \gamma\gamma$ and in the $gg(q\bar{q}) \rightarrow \gamma\gamma$ sample are isolated. How-

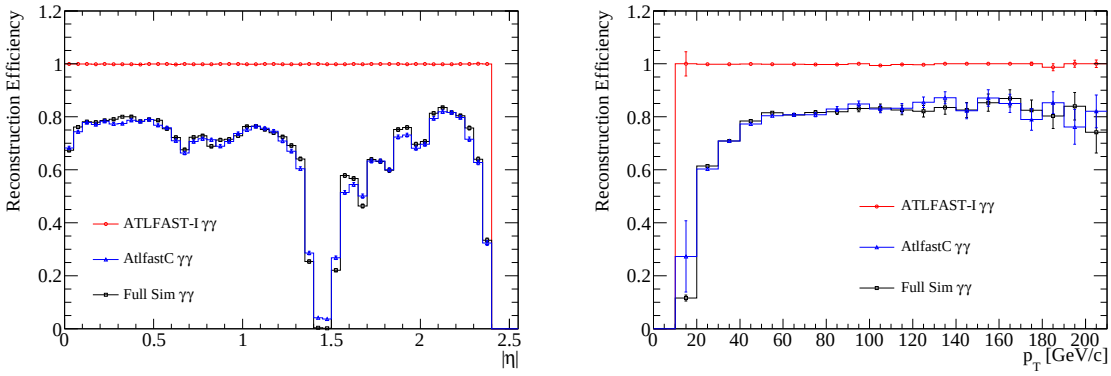

(a) $\varepsilon(|\eta|)$ (b) $\varepsilon(p_T)$

Figure 6.16: *Results of the validation with $gg(q\bar{q}) \rightarrow \gamma\gamma$ events. Photon reconstruction efficiency distributions as are shown as a function of (a) $|\eta|$ and (b) p_T for full simulation (black), ATLFAST-I (red) and AtlfastC with the new parameterisations (blue).*

Simulation	Reconstruction Efficiency(%)
Full Simulation	67.40±0.15
AtlfastC Simulation	67.28±0.15
ATLFAST-I Simulation	99.89±0.01

Table 6.5: *Mean photon reconstruction efficiency in $gg(q\bar{q}) \rightarrow \gamma\gamma$ background events for each of the simulations.*

ever, not all processes involving photons in the final state can be characterised as clean environments. For example, the Higgs boson may also be produced in association with a $t\bar{t}$ pair, a process which is associated with a higher amount of hadronic activity. Upon closer inspection of the Feynman diagrams for Higgs production via gluon fusion and in association with a $t\bar{t}$ pair in Figure 6.17, the difference in terms of hadronic activity in the hard process between the two becomes apparent. The $t\bar{t}(\mathrm{H}\rightarrow\gamma\gamma)$ channel is associated with the production of two free t-quarks, which subsequently decay into a b-quark and $\mathrm{W}^{\pm}$. In turn the $\mathrm{W}^{\pm}$ may decay either leptonically or hadronically. This is the reason for the increase in hadronic activity compared with the $gg \rightarrow \mathrm{H}\rightarrow\gamma\gamma$ channel. Experimentally, the increase in activity is seen as an increase in the multiplicity of jets and tracks. The isolation of full simulation photons is determined by the requirement that the sum of the p_T of all tracks inside of a fixed $\Delta\mathrm{R} = 0.3$ cone centred on the photon must be less than 4 GeV$/c$. Consequently, the increase in hadronic activity results in an increase in track multiplicity which in turn means that a smaller proportion of isolated photons are found in the $t\bar{t}(\mathrm{H}\rightarrow\gamma\gamma)$ channel.

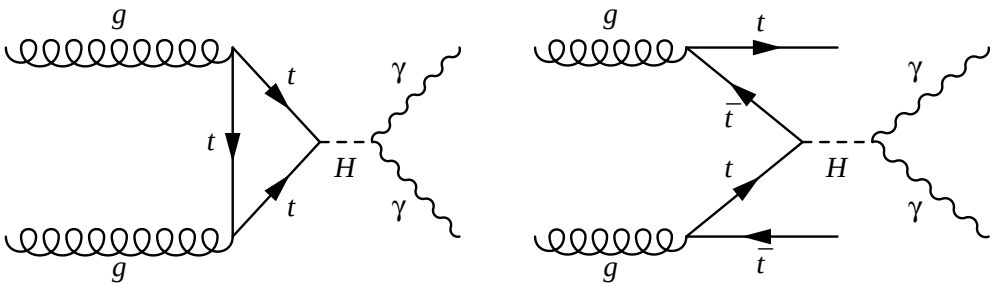

(a) $gg \rightarrow \mathrm{H} \rightarrow \gamma\gamma$ (b) $t\bar{t}(\mathrm{H} \rightarrow \gamma\gamma)$

Figure 6.17: *Feynman diagrams of Higgs production via gluon fusion (left) and in association with a $t\bar{t}$ pair (right) with subsequent decay to photons.*

The results of the validation with a $t\bar{t}(\mathrm{H}(120) \rightarrow \gamma\gamma)$ sample are presented in Figures 6.18 and 6.19. It is evident from these Figures that the AtlfastC overestimates the reconstruction efficiency

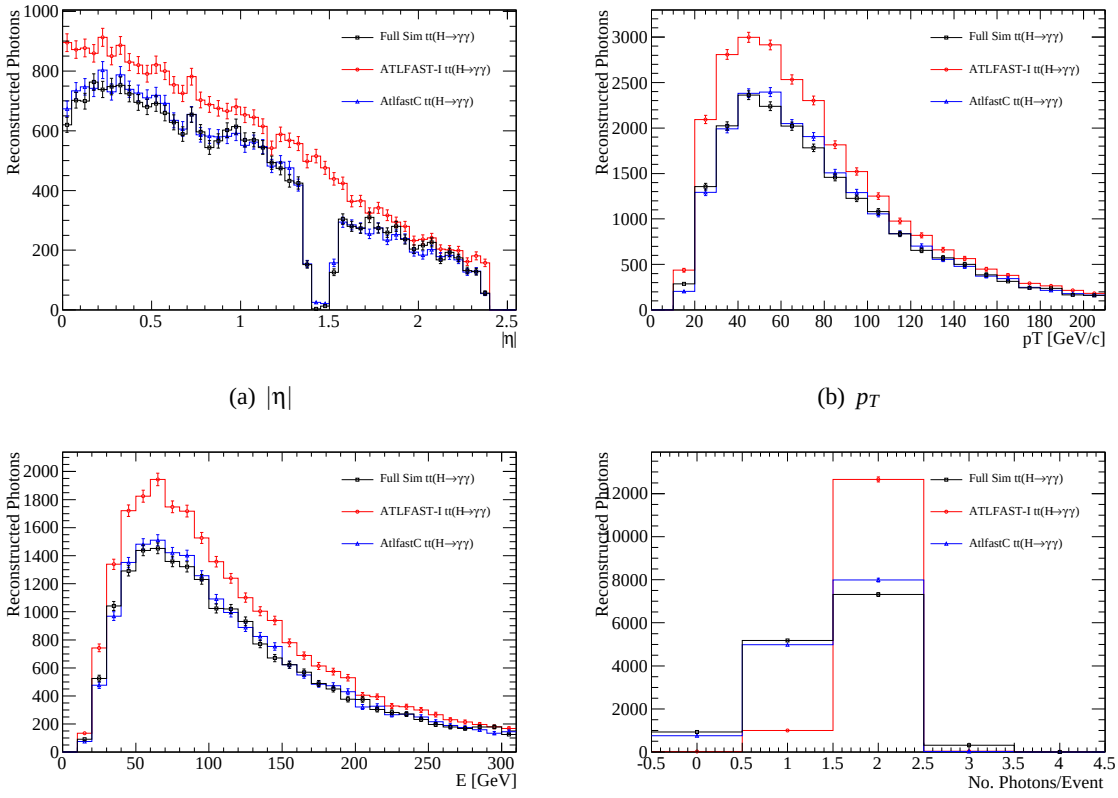

(a) $|\eta|$ (b) p_T

(c) energy (d) Photon Multiplicity

Figure 6.18: *Results of the validation with $t\bar{t}(H(120) \rightarrow \gamma\gamma)$ events. Reconstructed photon distributions are shown as a function of (a) $|\eta|$, (b) p_T, (c) energy and (d) multiplicity for full simulation (black), ATLFAST-I (red) and AtlfastC with the new parameterisations (blue).*

compared to the full simulation efficiency. From the mean photon reconstruction efficiencies for

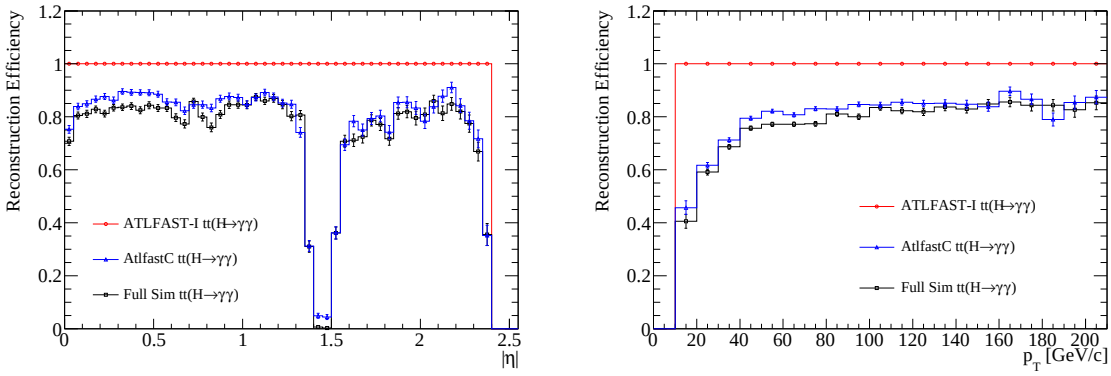

(a) $\varepsilon(|\eta|)$ (b) $\varepsilon(p_T)$

Figure 6.19: *Results of the validation with $t\bar{t}(H(120) \rightarrow \gamma\gamma)$ events. Photon reconstruction efficiency distributions are shown as a function of (a)$|\eta|$ and (b)p_T for full simulation (black), ATLFAST-I (red) and AtlfastC with the new parameterisations (blue).*

Simulation	Reconstruction Efficiency (%)
Full Simulation	77.52±0.25
AtlfastC Simulation	79.47±0.25
ATLFAST-I Simulation	99.92±0.02

Table 6.6: *Mean photon reconstruction efficiency in $t\bar{t}(H(120) \rightarrow \gamma\gamma)$ events for each of the simulations.*

each simulation, contained in Table 6.6, it is seen that the AtlfastC parameterisations overestimate the efficiency by ∼2.5% relative to the full simulation efficiency. To understand why the AtlfastC parameterisations have overestimated the reconstruction efficiency, a study comparing distributions of photons from fully simulated $t\bar{t}(\mathrm{H}(120) \rightarrow \gamma\gamma)$ and $gg \rightarrow \mathrm{H}(120) \rightarrow \gamma\gamma$ events was carried out and is detailed in the next section.

6.3.4 Investigation of Photons in Events with High Levels of Hadronic Activity

One of the underlying assumptions made when creating the parameterisations is that, for photons defined as isolated by the full simulation reconstruction software, the reconstruction efficiency has no dependence on the degree of isolation but just on the photon's p_T and η. To ascertain the validity of this assumption the reconstruction efficiency must be obtained as a function of the degree of isolation. For reconstructed photons in full simulation, the isolation variable is defined as: the sum of the p_T of all tracks above 0.5 GeV$/c$ which lie inside of a cone $\Delta\mathrm{R} = 0.3$ centred on the photon candidate.

This variable is commonly referred to as *ptCone30*. For fully simulated reconstructed photons to be deemed isolated, the value of ptCone30 must be less than 10 GeV/c. However, for truth photons, which are needed in the calculation of the reconstruction efficiency, the ptCone30 variable is not available (since no detailed tracking information is available at truth level). Instead, the degree of isolation of a truth photon will be defined by the distance, ΔR, from the truth photon to the nearest other *truth jet*, where the truth jet must have a transverse momentum of at least 10 GeV/c. Truth jets are obtained by running the same jet finding algorithm as used in the reconstruction process, but instead of the inputs being calorimeter clusters, the inputs are all final state truth particles (excluding muons, neutrinos and non-interacting particles). In what follows the truth jets have been created using a seeded cone algorithm with a cone size, $\Delta R = 0.4$.

Figure 6.20 shows the photon reconstruction efficiency as a function of the ΔR value between truth photons and the nearest truth jet with $p_T > 10$ GeV/c, in $gg \rightarrow H(120) \rightarrow \gamma\gamma$ and $t\bar{t}(H(120) \rightarrow \gamma\gamma)$ full simulation events. Above a value of $\Delta R \sim 0.5$ the efficiency for both samples is seen to be, to

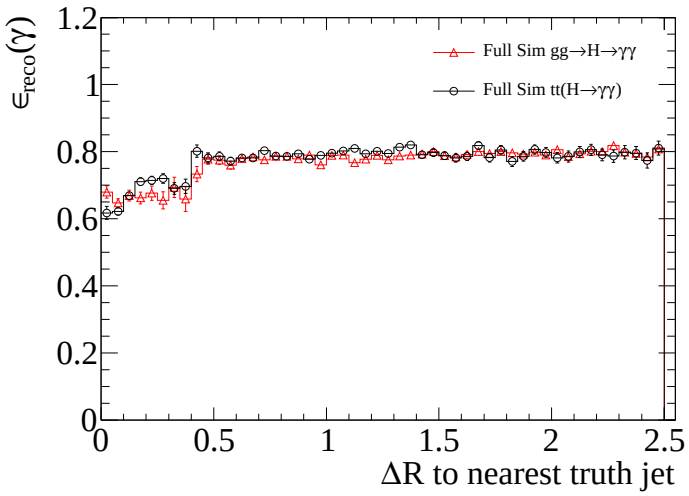

Figure 6.20: *Photon reconstruction efficiency as a function of the ΔR value between the truth photon and the nearest truth jet (with $p_T > 10$ GeV/c) in $gg \rightarrow H(120) \rightarrow \gamma\gamma$ (black) and $t\bar{t}(H(120) \rightarrow \gamma\gamma)$ events (red).*

first approximation, consistently flat at ~80%. This is as expected since photons with no energetic particles or jets nearby are more likely be be isolated. Therefore, the reconstruction efficiency of an individual photon should not depend on a particle or jet being present at a distance $\Delta R \gtrsim 0.5$ from the photon. The reconstruction efficiency for photons which have a truth jet outside of a $\Delta R \geq 0.5$ in $gg \rightarrow H(120) \rightarrow \gamma\gamma$ and $t\bar{t}(H(120) \rightarrow \gamma\gamma)$ events is shown in Figure 6.21. Good agreement in the reconstruction efficiency as a function of p_T and $|\eta|$ can be seen. This is due to selecting photons

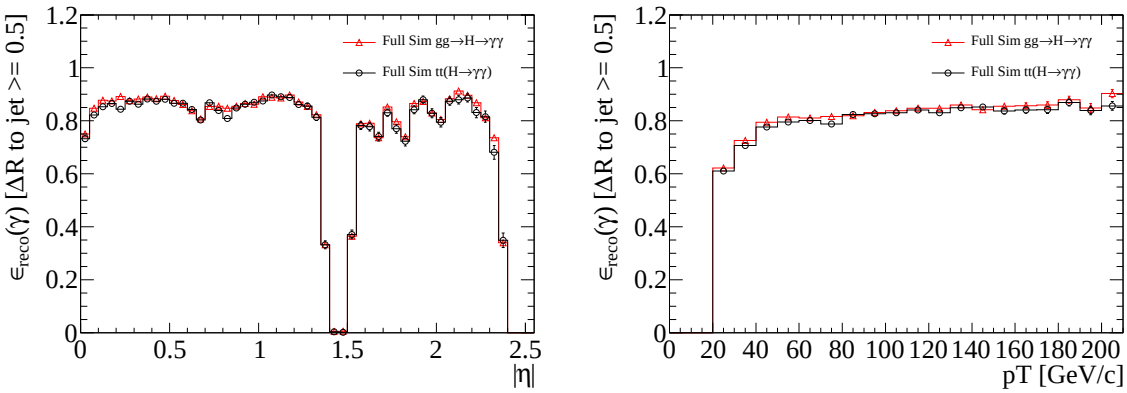

(a) γ reconstruction efficiency ($|\eta|$) (b) γ reconstruction efficiency (p_T)

Figure 6.21: *Distributions of the photon reconstruction efficiency as a function of (a) $|\eta|$ and (b) p_T, where there is no truth jet (with $p_T > 10$ GeV$/c$) inside of a cone $\Delta R = 0.5$ around the truth photon, in $gg \rightarrow H(120) \rightarrow \gamma\gamma$ (black) and $t\bar{t}(H(120) \rightarrow \gamma\gamma)$ events (red).*

with no energetic particle or jets in close proximity. The conclusion reached is that reconstruction efficiency only depends on the p_T and η of these photons and is independent of the physics process being investigated. Table 6.7 compares the fraction of isolated photons in each sample. A very

Process	Isolated ($\Delta R \geq 0.5$)	Non-Isolated ($\Delta R < 0.5$)
$gg \rightarrow H(120) \rightarrow \gamma\gamma$	97.24±0.04%	2.76±0.04%
$gg(q\bar{q}) \rightarrow \gamma\gamma$	98.24±0.03%	1.76±0.03%
$t\bar{t}(H(120) \rightarrow \gamma\gamma)$	81.23±0.24%	18.77±0.24%

Table 6.7: *Fraction of isolated photons in $gg \rightarrow H(120) \rightarrow \gamma\gamma$, $gg(q\bar{q}) \rightarrow \gamma\gamma$ and $t\bar{t}(H(120) \rightarrow \gamma\gamma)$ events.*

high fraction, 97.24%, of photons in the $gg \rightarrow H(120) \rightarrow \gamma\gamma$ sample and 98.24% in the $gg(q\bar{q}) \rightarrow \gamma\gamma$ sample are deemed isolated by the requirement that there must be no truth jet, with a $p_T > 10$ GeV$/c$, within a cone of $\Delta R = 0.5$. Since the parameterisations were extracted from samples with very small fractions of non-isolated photons, excellent agreement between the AtlfastC parameterisations and full simulation reconstruction efficiencies in $gg \rightarrow H(120) \rightarrow \gamma\gamma$ and $gg(q\bar{q}) \rightarrow \gamma\gamma$ events is explained.

Figure 6.22 shows the reconstruction efficiency for photons that have a truth jet inside a cone of $\Delta R = 0.5$, in $gg \rightarrow H(120) \rightarrow \gamma\gamma$ and $t\bar{t}(H(120) \rightarrow \gamma\gamma)$ events. Comparing these efficiencies with those in Figure 6.21, it is seen that there is a drop in efficiency in both samples for reconstructing photons with energetic particles/jets within a cone $\Delta R = 0.5$. The average relative drop in efficiency for $gg \rightarrow H(120) \rightarrow \gamma\gamma$ and $t\bar{t}(H(120) \rightarrow \gamma\gamma)$ events, detailed in Table 6.8, is $\sim$13%. However, the

Process	Reconstruction Efficiency ($\Delta R \geq 0.5$)	Reconstruction Efficiency ($\Delta R < 0.5$)
$gg \rightarrow H(120) \rightarrow \gamma\gamma$	79.49±0.09%	68.24±0.60%
$gg(q\bar{q}) \rightarrow \gamma\gamma$	67.52±0.10%	60.14±0.78%
$t\bar{t}(H(120) \rightarrow \gamma\gamma)$	78.98±0.28%	67.50±0.67%

Table 6.8: *Average photon reconstruction efficiency for isolated and non-isolated photons in $gg \rightarrow H(120) \rightarrow \gamma\gamma$, $gg(q\bar{q}) \rightarrow \gamma\gamma$ and $t\bar{t}(H(120) \rightarrow \gamma\gamma)$ events.*

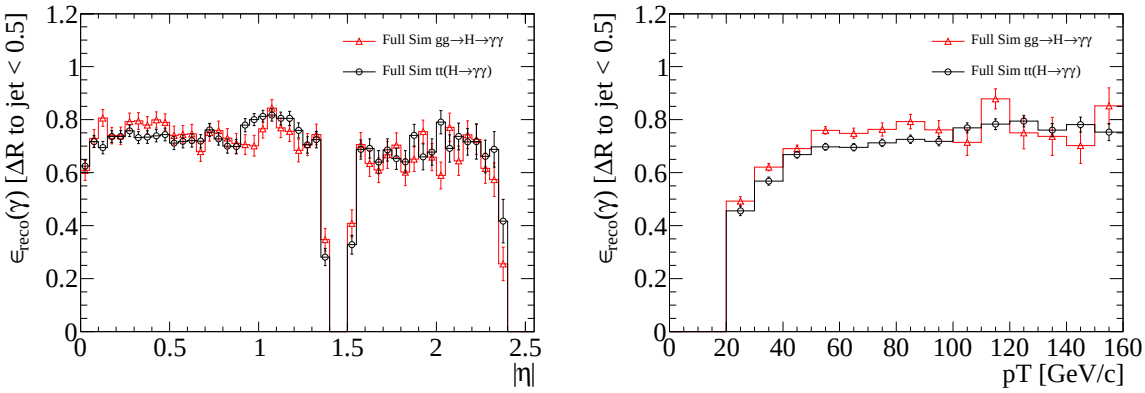

(a) γ reconstruction efficiency ($|\eta|$) (b) γ reconstruction efficiency (p_T)

Figure 6.22: *Distributions of the photon reconstruction efficiency as a function of (a) $|\eta|$ and (b) p_T, where the nearest truth jet (with $p_T > 10$ GeV$/c$) lies inside of a cone $\Delta R = 0.5$ around the truth photon, in $gg \rightarrow H(120) \rightarrow \gamma\gamma$ (black) and $t\bar{t}(H(120) \rightarrow \gamma\gamma)$ events (red).*

AtlfastC parameterisations assume that photons are reconstructed with the same efficiency regardless of the proximity of an energetic particle/jet. Clearly, this assumption is not valid for events containing a significant fraction of photons with energetic particles/jets nearby. From Table 6.7, 18.77% of photons in $t\bar{t}(H(120) \rightarrow \gamma\gamma)$ events have a particle/jet, with a $p_T > 10$ GeV$/c$, within a cone $\Delta R = 0.5$, whilst the equivalent fraction in $gg \rightarrow H(120) \rightarrow \gamma\gamma$ events is only 2.76% . This explains why the parameterisations have overestimated the efficiency for reconstructing photons in $t\bar{t}(H(120) \rightarrow \gamma\gamma)$ events and why the same effect is not observed in $gg \rightarrow H(120) \rightarrow \gamma\gamma$ events.

Figure 6.22 demonstrates that the efficiency for reconstructing photons with energetic particles or jets nearby differs between $t\bar{t}(H(120) \rightarrow \gamma\gamma)$ and $gg \rightarrow H(120) \rightarrow \gamma\gamma$ events. However, the efficiency for reconstructing a photon from one sample should be the same as the efficiency to reconstruct an identical photon from another sample. For photons with energetic particles or jets nearby it simply is not good enough to parameterise the reconstruction efficiency with just the $|\eta|$ and p_T of photons.

This indicates that there is an additional dependence on another variable(s).

As the degree of isolation is affected by the presence of energetic particles or jets nearby Figure 6.23(a) shows the reconstruction efficiency in both samples as a function of the transverse energy of the nearest truth jet. Two distinct regions are apparent, with the reconstruction efficiency for photons

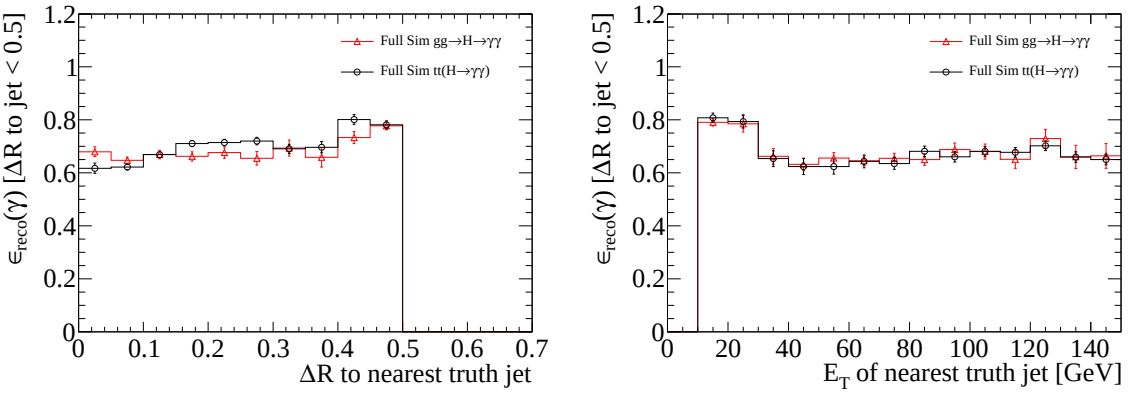

(a) γ reconstruction efficiency vs ΔR to nearest truth jet

(b) γ reconstruction efficiency vs E_T of nearest truth jet

Figure 6.23: *Distributions of the photon reconstruction efficiency as a function of (a) the cone size ΔR and (b) the E_T of the nearest truth jet, where the truth jet (with $p_T > 10$ GeV/c) lies inside of cone ΔR = 0.5 around the photon. Distributions are shown for both $gg \rightarrow H(120) \rightarrow \gamma\gamma$ (black) and $t\bar{t}(H(120) \rightarrow \gamma\gamma)$ events (red).*

with a truth jet of $E_T \geq 30$ GeV within a cone of ΔR = 0.5 approximately 10% lower than that for photons with a truth jet of $10 \leq E_T < 30$ GeV within a cone of ΔR = 0.5. Whilst the efficiency is different in these regions it is consistent between the two samples. Additionally, the comparison of the reconstruction efficiencies as a function of p_T and η for the two regions is shown in Figure 6.24. Whilst the efficiencies for the $10 < E_T \leq 30$ GeV region suffer from low statistics, it can be seen that for both regions the efficiencies agree to a good extent between the two processes. This result indicates that photons with truth jets nearby can be split into two groups, whereby photons of the same $|\eta|$ and p_T in each group are reconstructed with the same efficiency.

Based on the findings above, a scheme is proposed below that would further improve upon the photon reconstruction efficiency parameterisations by incorporating the treatment of non-isolated photons:

- A 2D parameterisation in p_T and $|\eta|$, as detailed in Section 6.2.1, would be used for photons which either had a truth jet (with $p_T > 10$ GeV/c) at a distance greater than or equal to ΔR = 0.5, or had no truth jet nearby.

- A 3D parameterisation in p_T, $|\eta|$ and E_T of the nearest truth jet, providing that the truth jet

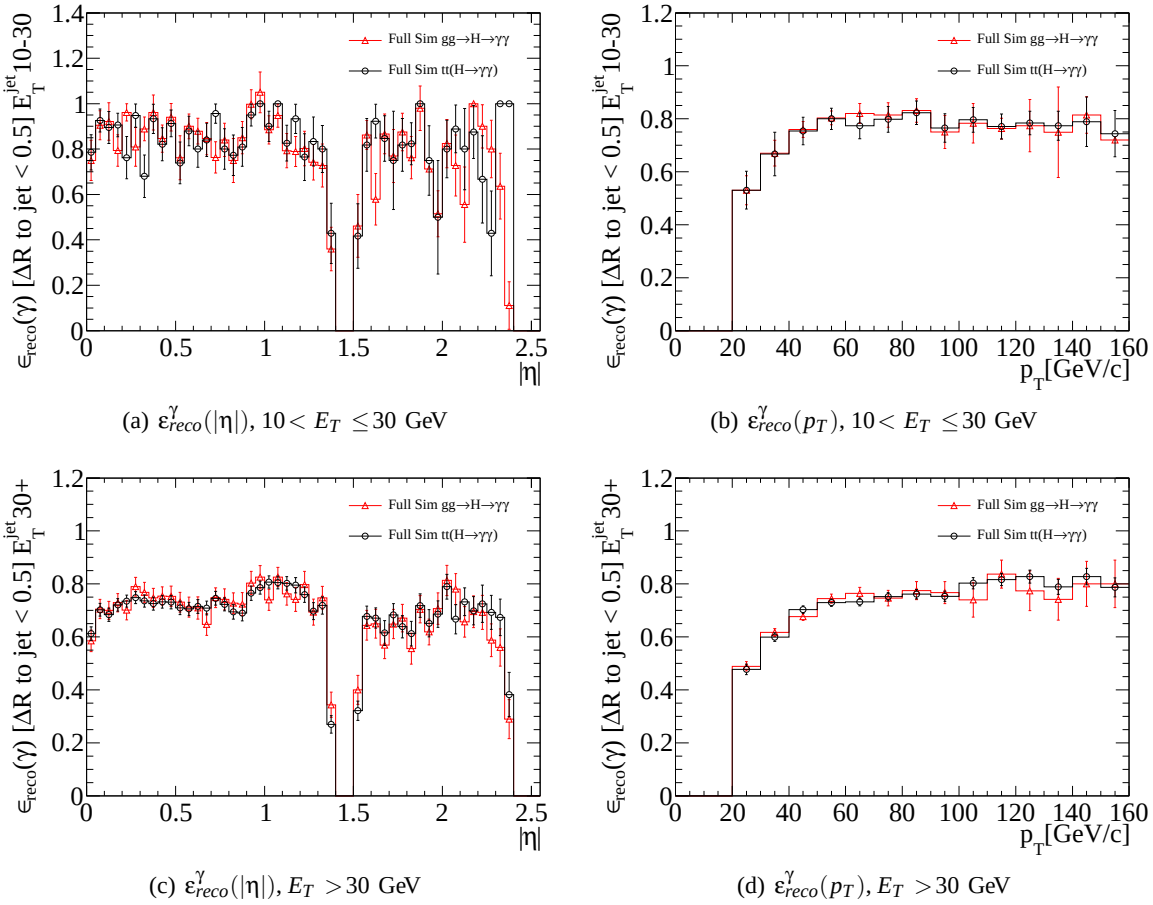

(a) $\varepsilon^{\gamma}_{reco}(|\eta|)$, $10 < E_T \leq 30$ GeV

(b) $\varepsilon^{\gamma}_{reco}(p_T)$, $10 < E_T \leq 30$ GeV

(c) $\varepsilon^{\gamma}_{reco}(|\eta|)$, $E_T > 30$ GeV

(d) $\varepsilon^{\gamma}_{reco}(p_T)$, $E_T > 30$ GeV

Figure 6.24: *Distributions of the photon reconstruction efficiency as a function of* η *and* p_T *for the two regions in* E_T *of the nearest truth jet, where the nearest truth jet (with* $p_T > 10$ GeV$/c$*) lies inside a cone of* $\Delta R = 0.5$*. Distributions are shown for both* $gg \rightarrow H(120) \rightarrow \gamma\gamma$ *(black) and* $t\bar{t}(H(120) \rightarrow \gamma\gamma)$ *(red) events.*

is within a distance of $\Delta R = 0.5$ of the photon and has $p_T > 10$ GeV$/c$. The parameterisation would have the same granularity in p_T and $|\eta|$ as the 2D parameterisations, whilst in E_T it would be sub-divided into 2 bins: $10 < E_T \leq 30$, $E_T \geq 30$ GeV.

The separate treatment of converted and unconverted photons would also still be adhered to.

It has been demonstrated that it would be possible to create such a set of parameterisations that could describe the photon reconstruction efficiency in events with a high fraction of isolated photons and at the same time in $t\bar{t}(\mathrm{H}(120) \rightarrow \gamma\gamma)$. To provide a fully physics independent parameterisation studies with other samples containing non-isolated photons would need to be performed. The reason that these options have not be pursued further is down to several factors. At the time of creation of the parameterisations not enough large Monte-Carlo samples of suitable events were available to extract a 3D parameterisation accurately. However, this could potentially be resolved by introducing variable

bin sizes in the $|\eta|$ dimension, with finer granularity around the crack region and coarser granularity in regions of constant efficiency. Development of the ATLFAST-I package was foreseen to change the isolation algorithm, bringing it into line with that of full simulation. This would also enable studies comparing isolation effects in fast simulation and full simulation to become more straight forward. The AtlfastC algorithm was, in later releases of the ATHENA software (version 14 onwards), incorporated into a package called *AtlfastCorrectors* which limited the ability to incorporate 3D parameterisations. For these reasons a decision was made to wait for the forthcoming changes to the fast simulation package before pursuing further. At the present time, the proposed changes to the fast simulation isolation algorithm have been implemented but not yet validated.

6.4 Conclusions

In this chapter, a strategy for extracting parameterised reconstruction efficiencies from full simulation and the subsequent application of them to fast simulation photons, has been presented. The parameterisations were obtained and validated extensively using independent simulated event samples covering a range of physics processes. The parameterisations, described in Section 6.2.1, have been incorporated into the AtlfastC package from version 12.0.6 onwards of the ATHENA software. The have also been included in the extended *AtlfastCorrectors* package available from version 14.2.0 onwards. The parameterisations presented in this work are valid for any sample containing a high fraction of isolated photons (converted or unconverted). Excellent results have been demonstrated in the $gg \rightarrow \mathrm{H}(120) \rightarrow \gamma\gamma$ and $gg(q\bar{q}) \rightarrow \gamma\gamma$ processes which together represent the main signal and background processes for the Standard Model $\mathrm{H} \rightarrow \gamma\gamma$ search.

Whilst the parameterisations can be used for other physics samples, the user should be aware that the efficiency and multiplicity of reconstructed photons will be slightly overestimated, i.e. 2.5% relative increase in reconstruction efficiency is seen in $t\bar{t}(\mathrm{H}(120) \rightarrow \gamma\gamma)$ events. The overestimation has been shown to arise from photons with energetic particles or jets in close proximity. A method was proposed to correct for this effect by taking into account the differing reconstruction efficiencies for isolated and non-isolated photons. In any case, the overestimation for events with a significant fraction of non-isolated photons is moderate when compared to the results obtained with the default ATLFAST-I simulation, since without the parameterisations the photon reconstruction efficiency of ATLFAST-I is 100%.

Chapter 7

Search For a Light Fermiophobic Higgs Signal

This chapter presents the search for a light fermiophobic Higgs boson decaying to photons at a centre-of-mass of $\sqrt{s} = 14\,\text{TeV}$ in pp collisions at the LHC. Fermiophobic models are discussed in Chapter 2. A light fermiophobic Higgs, h, can be pair produced via its coupling to a (non-fermiophobic) heavy Higgs, H, provided m_H is at least $2m_h$ (where m_h and m_H are, respectively, the masses of the light and heavy CP-even Higgs bosons). For a light fermiophobic Higgs boson the primary decay mode is to a pair of photons. Thus, for the channel of interest, $gg \rightarrow \text{H} \rightarrow \text{hh} \rightarrow 4\gamma$, shown in the Feynman diagram in Figure 7.1, an identifiable signal of four high-p_T photons is expected. This

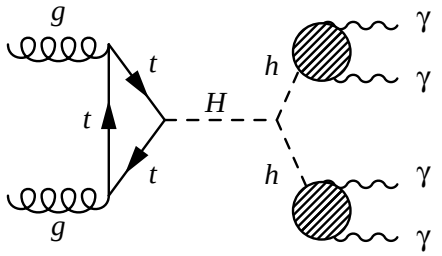

Figure 7.1: *Feynman diagram of the newly proposed fermiophobic Higgs channel.*

signal can have a large rate due to the exploitation of the enhanced branching fraction to photon pairs of a fermiophobic Higgs boson and the large production cross-section of a heavy Higgs boson via gluon-fusion. Additionally, it will be shown that there is little background to a signature of four high-p_T photons. These factors allows us to look for a fermiophobic Higgs with mass up to 140 GeV/c^2. Above this value the decay to a pair of W bosons dominates and in the context of this thesis is not

investigated.

This chapter is structured as follows: the generation of simulated fermiophobic Higgs signals and major background events is first discussed in Section 7.1. The generator-level analysis model and its development is then dealt with in Section 7.2 along with the strategy used in order to extract the signal from the background. Section 7.3 presents the selection efficiencies for both signal and background events. From the results of the analysis, Section 7.4 presents the sensitivity of the search in the context of several fermiophobic benchmarks, which were outlined in Section 2.3. Finally, in addition to the generator-level analysis, Section 7.5 presents the results of performing the same analysis but with detector-level information rather than generator-level information. In this section, the photon reconstruction efficiency parameterisations, the subject of Chapter 6, are applied to fast simulated detector-level photons in order to provide realistic reconstruction efficiencies in a multi-photon final state.

7.1 Simulated Event Generation

7.1.1 Signal Samples

Samples of simulated signal events have been generated at several (m_h, m_H) mass points so as to cover all of the allowed search regions, described in Section 2.3. Signal samples, each with 100,000 $gg \rightarrow H \rightarrow hh \rightarrow 4\gamma$ events, were generated at m_h values from 40 GeV/c^2 to 140 GeV/c^2 in 10 GeV/c^2 steps and at allowed m_H values that are multiples of 50 GeV/c^2 in the range $2m_h \leq m_H \leq 600$ GeV/c^2. Additionally, for each m_h value samples were generated on the kinematic threshold diagonal $m_H = 2m_h$ and on the diagonal $m_H = 2m_h + 20$ GeV/c^2. All generated mass points are represented as dots in the (m_h, m_H) plane in Figure 7.2.

Signal events have been generated with PYTHIA version 6.4.2.1 [58], using an LHC style underlying event tuning, at a centre of mass energy of 14 TeV. Additionally, PHOTOS[1] [78], which is run on top of PYTHIA, has been used to add radiated photons to the decay tree. For the generation of signal samples, QCD and electroweak parameters have been fixed to appropriate values in PYTHIA as seen in Table 7.1.

[1] PHOTOS is a MC algorithm that simulates QED photon emissions in decays, by calculating $O(\alpha)$ radiative corrections for charged particles using a leading log collinear approximation.

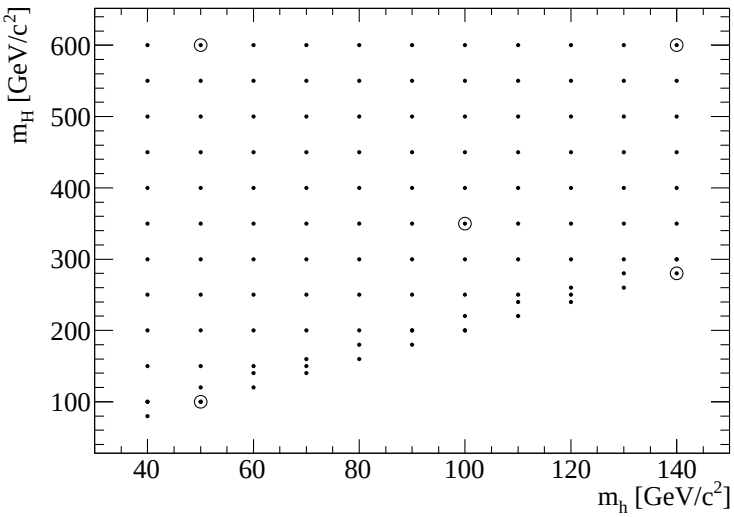

Figure 7.2: *Each point in the grid represents a 10,000 event signal sample generated at specific light (m_h) and heavy Higgs boson (m_H) mass. Points highlighted with a circle indicate samples that will be used later on as signals representative of the different parts of the mass plane.*

Parameter	PYTHIA value
PDF	CTEQ6L1
$[\alpha_s(m_z)]_{n_{loop}}$	$[0.130]_1$
$\alpha_{em}(Q^2)$	runs
Q^2	$\widehat{s}$
$\sin^2\theta_W$	0.2222
m_W	80.403
m_Z	91.188

Table 7.1: *QCD and electroweak parameters used in the generation of signal events with the PYTHIA generator.*

7.1.2 Background Samples

Background processes can be split into two main groups: backgrounds arising from the production of four isolated photons, which are usually referred to as irreducible, and reducible backgrounds arising from events with at least one fake photon. Fake photons are primarily due to the presence of π^0s resulting from the fragmentation of gluons and quarks. Consequently, the primary source of fake photons are jets. As a typical rate for jets faking photons at the LHC is around $1/2000$, final states of photons and jets are of particular interest to this study.

To this end, ALPGEN [55] was chosen as the generator to calculate the cross-sections and gener-

ate the background events. ALPGEN is a leading order matrix element generator (see Section 4.1.1) whose primary use is in the study of multi-parton hard processes in hadronic collisions. The generator calculates the exact matrix elements for a large set of parton-level processes, one of which is of particular interest to this study, Nγ + M$jets$. Final states can be generated with M$\geq$ 0 jets and N$\geq$ 1 real photons with $N + M \leq 8$. The backgrounds considered for further investigation are those where

Process	$\sigma_{Alpgen}(fb)$	$\sigma_{Madgraph}(fb)$	Events On Disk
$pp \rightarrow 4\gamma$	3.27×10^{-1}	3.54×10^{-1}	485,000
$pp \rightarrow 4\gamma + 1j$	6.89×10^{-1}	6.89×10^{-1}	494,000
$pp \rightarrow 3\gamma + 1j$	3.55×10^{2}	3.41×10^{2}	500,000
$pp \rightarrow 3\gamma + 2j$	4.61×10^{2}	4.93×10^{2}	518,000
$pp \rightarrow 2\gamma + 2j$	3.27×10^{5}	3.34×10^{5}	500,000
$pp \rightarrow 2\gamma + 3j$	1.71×10^{5}	Not Available	530,000

Table 7.2: *Backgrounds considered for the fermiophobic signal search. Cross-sections are obtained, after the application of the generator cuts defined in the text, from ALPGEN and are compared with the corresponding MadGraph cross-sections. The QCD and electroweak parameters are fixed to the same values in both ALPGEN and MadGraph (see in Table 7.3).*

there is a possibility of obtaining four photons, whether they are real or fake (jets).

Simulated samples of all backgrounds in Table 7.2 have been generated with ALPGEN using the following loose generator level cuts:

- Transverse momentum of photons and jets must be greater than 10 GeV$/c$;
- Pseudorapidity of photons and jets must be within $|\eta| < 3.0$;
- The distance in terms of ΔR must be greater than 0.4 between any pair of photons or jets and between any photon and any jet.

The cross-sections, shown in Table 7.2, are obtained from ALPGEN after the application of the aforementioned cuts. Additionally, the ALPGEN cross-sections have been verified[2] with MadGraph [56] using the same set of generation cuts and the same QCD and electroweak parameters as used by ALPGEN. The exact values of the parameters used in the generation is shown in Table 7.3. Generated background events from ALPGEN have been subsequently hadronised with HERWIG/JIMMY [59, 60] using an appropriate LHC-style underlying event tune. As per the generation of the signal, PHOTOS was run on top of HERWIG/JIMMY to add soft radiated photons to the decay tree.

[2]MadGraph is unable to calculate the cross-section for the process $pp \rightarrow 2\gamma + 3j$, due to the very high number of diagrams associated with it.

Parameter	ALPGEN/MadGraph Value
PDF	CTEQ6L1
$[\alpha_s(m_z)]_{n_{loop}}$	$[0.130]_1$
$\alpha_{em}(m_z)$	1/132.5
Q^2	$\Sigma p_{T\gamma}^2 + \Sigma p_{Tj}^2$
$\sin^2\theta_W$	0.2222
g	0.6532
G_F	1.16639×10^{-5}
m_W	80.403
m_Z	91.188

Table 7.3: *Values of the QCD and electroweak parameters used in the calculation of the cross-sections for the background processes at the LHC. More details can be found in the ALPGEN and MadGraph documentation [55, 56].*

7.2 Generator-Level Analysis Model and Development

7.2.1 Object definitions

Only prompt truth photons are selected for use in the analysis. Here, a prompt photon is defined as a photon direct from the hard process. For the signal, this would be a photon from the decay of a light Higgs boson. For the background, consider one of the possible Feynman diagrams in Figure 7.3, for the process $pp \rightarrow 4\gamma$. In this example of a $pp \rightarrow 4\gamma$ background event, a prompt photon would

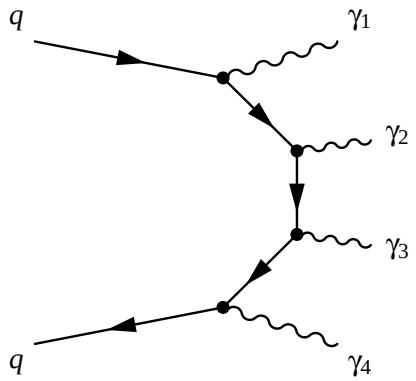

Figure 7.3: *An example Feynman diagram for the process $pp \rightarrow 4\gamma$. In this example of a $pp \rightarrow 4\gamma$ background event, a prompt photon would be defined as one of the four labelled photons.*

be defined as one of the four labelled photons $\gamma_{1,2,3,4}$. Defining photons in such a manner allows us to collect up all other interacting particles, including radiated soft photons, into *truth jets*. Truth

jets are obtained by running the same jet finding algorithm as used in the reconstruction process, but instead of the inputs being calorimeter clusters the inputs are all final state truth particles (excluding muons, neutrinos and non-interacting particles). In what follows the truth jets have been created using a seeded cone algorithm with a cone size $\Delta R = 0.4$. However, since truth jets are seeded from all final state truth particles, including prompt photons, overlap between the prompt photons and the truth jets exists. Figure 7.4 shows an example distribution of the ΔR between truth jets and the

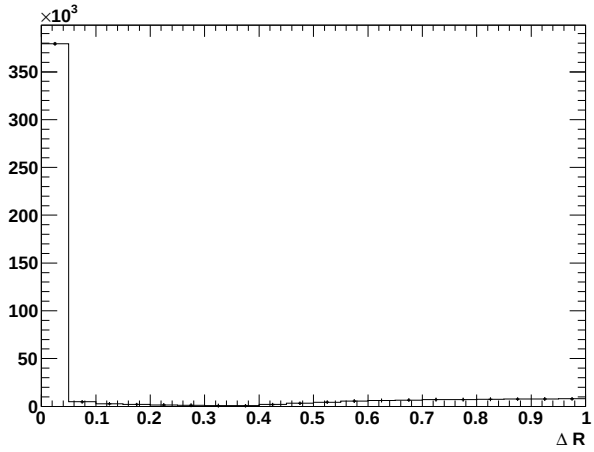

Figure 7.4: *ΔR value between truth jets and the nearest prompt truth photon in* $(m_h, m_H) = (100, 350)$ GeV$/c$ *events.*

nearest prompt truth photon in a $(m_h, m_H) = (100, 350)$ GeV$/c^2$ signal samples (where the notation $(100, 350)$ GeV$/c^2$ has been adopted for $gg \rightarrow H(350) \rightarrow hh(100) \rightarrow 4\gamma$). The overlap is removed by requiring that no truth jet can have a prompt truth photon within a distance of $\Delta R = 0.05$ from the truth jet.

7.2.2 Pre-Selection of Prompt Truth Photons and Truth Jets

As will be detailed in Section 7.2.3 truth jets will be considered as candidates for faking photons. Therefore, in what follows they will be treated indistinguishably from photons. Truth objects (prompt photons and truth jets) defined above must pass the following pre-selection requirements for them to be considered further. Firstly, objects must be visible to the detector. For example, the ATLAS detector at the LHC is able to identify photons with transverse momentum greater than 1 GeV$/c$ [49]. Secondly, objects must lie within the precision physics range, $|\eta| < 2.5$ of the ATLAS detector. This is motivated by the coverage of the inner detector which plays a crucial role in the reconstruction of photons and the separation from jets. In what follows, the previous two requirements are referred to

as *acceptance* cuts. Finally, objects must be isolated. Here, a simplistic isolation is used that requires that the distance in ΔR between any pair of photons, any pair of jets or between any photon and jet must be greater than 0.4. A summary of the pre-selection cuts is included in Table 7.4.

Pre-selection Cut		**Cut Value**
Acceptance	Kinematic (visible)	$p_{T\gamma} > 1$ GeV$/c$; $p_{Tj} > 1$ GeV$/c$
	Fiducial (precision range)	$\lvert\eta_\gamma\rvert < 2.5$; $\lvert\eta_j\rvert < 2.5$
Isolation		$\Delta R_{\gamma\gamma}, \Delta R_{\gamma j}, \Delta R_{jj} > 0.4$

Table 7.4: *Pre-selection cuts used for truth prompt photons and truth jets in the analysis. The index j is used to represent truth jets, while the index γ is used to represent prompt truth photons.*

The effect of the pre-selection cuts on the multiplicity of prompt truth photons and truth jets is shown in Figure 7.5 for an example $(m_h, m_H) = (100, 350)$ GeV$/c^2$ signal process, and in Figure 7.6 for an example background ($pp \rightarrow 4\gamma + 1j$) process.

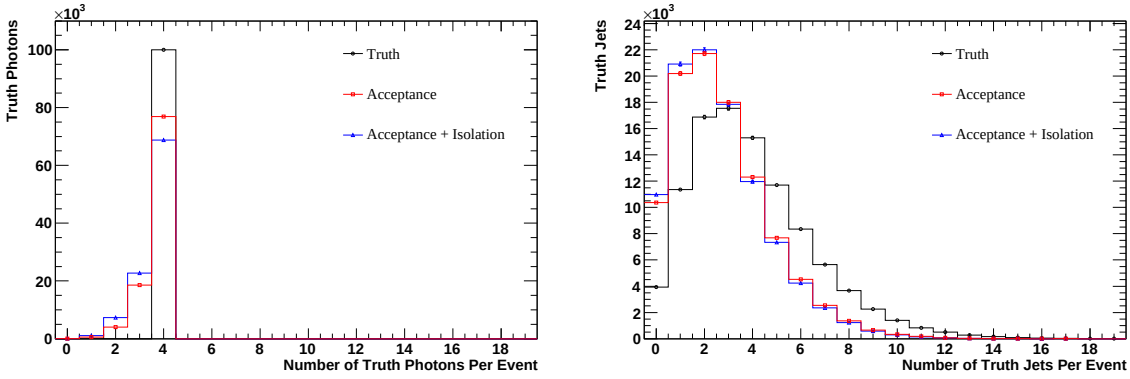

(a) Multiplicity per event of truth photons

(b) Multiplicity per event of truth jets

Figure 7.5: *Multiplicities per event of (a) prompt truth photons and (b) truth jets in a $(m_h, m_H) = (100, 350)$ GeV$/c^2$ sample, after the application of each of the pre-selection cuts listed in Table 7.4.*

7.2.3 Analysis Model and Treatment of Fake Photons

As stated previously, the primary source of fake (misidentified) photons is from the decays of leading neutral pions, $\pi^0 \rightarrow \gamma\gamma$, in hadronic jets. In what follows, the rate at which jets fake photons has been set at 1/2000. This fake rate can be compared to the fake rates in Figure 5.3 which, for a photon efficiency of 84%, indicate that 1/2000 is actually a conservative estimate. There are of course other contributions to the fake rate besides misidentification of jets as photons, but this is by far the most

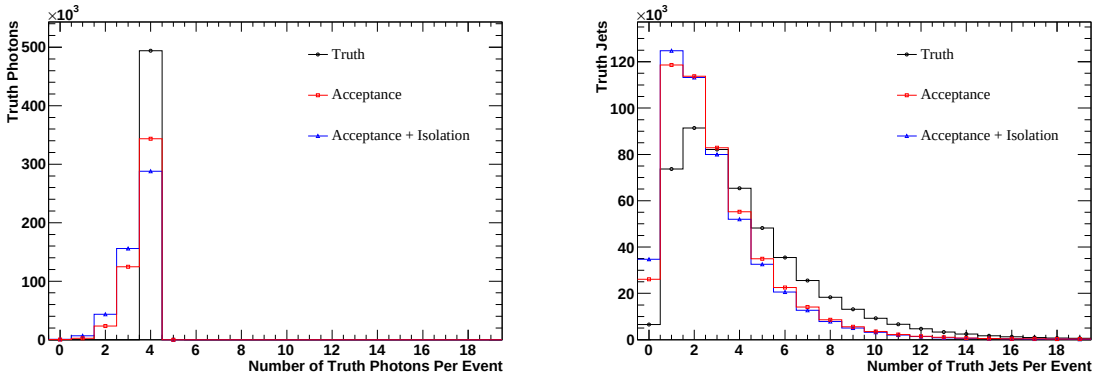

(a) Multiplicity per event of truth photons

(b) Multiplicity per event of truth jets

Figure 7.6: *Multiplicities per event of (a) prompt truth photons and (b) truth jets in* $pp \rightarrow 4\gamma + 1j$ *events, after the application of each of the pre-selection cuts listed in Table 7.4.*

dominant contribution [27]. To deal with fakes, the analysis could have adopted the approach where every 2000 events a truth jet is treated as a photon. This approach however, would have required tens of millions of events for each background process to have been generated in order to accurately determine the selection efficiency. Instead, the analysis presented here has adopted the approach whereby in every event, truth jets are treated as photons. When the selection efficiency is calculated at the end, the fake rate (depending on the numbers of truth jets faking photons per event) is then applied. Therefore, much fewer events than might otherwise have been needed have been generated.

Figure 7.7 shows the multiplicity of pre-selected truth photons per event for an example signal mass point, with a light Higgs mass of 100 GeV/c^2 and a heavy Higgs mass of 350 GeV/c^2. It is

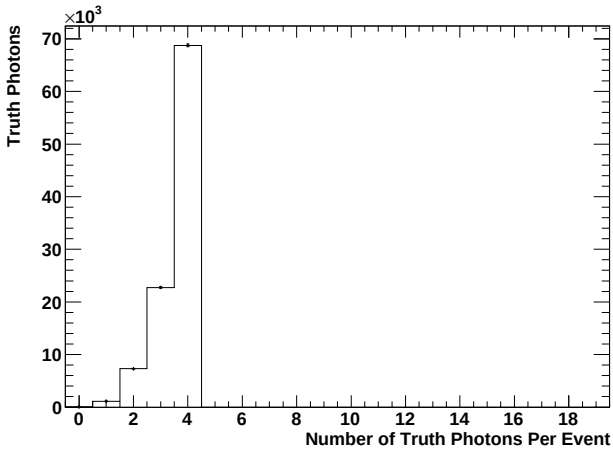

Figure 7.7: *Multiplicity per event of pre-selected prompt truth photons from a* $(m_h, m_H) = (100, 350)$ GeV/c^2 *signal sample.*

observed that the majority of events contain four pre-selected prompt truth photons per event. This distribution is representative of all signal mass points. Therefore, the first requirement that is imposed is that any event must have at least four photons per event. For the equivalent background distributions seen in Figure 7.8, it is observed that the maximum number of pre-selected truth photons for any process is never larger than the generated number of prompt photons. In general, for a background process such as $pp \rightarrow$Nγ+Mj (where j is used to represent truth jet(s)), no event contains more than N prompt truth photons. Therefore, for background events where the number of pre-selected photons, N, is less than four, (4-N) fake photons (truth jets) are required for the event to pass the requirement that any event must have at least four photons (real or fake) per event. However, each additional fake photon (truth jet) required would carry a weight of 1/2000 (the fake rate). Using this information, Table 7.5 shows, for each background process, the maximum number of events expected for a luminosity of $1\,fb^{-1}$ at the LHC, under the assumption that all events contain N photons and M jets such that $N+M=4$. For example, consider the process, $pp \rightarrow\ 3\gamma+1j$ which has a cross-

Process	$\sigma_{\mathbf{ALPGEN}}$	**Maximum Number Of Expected Events For 1 fb^{-1}**				
	[**fb**]	**4γ+0j**	**3γ+1j**	**2γ+2j**	**1γ+3j**	**0γ+4j**
$pp \rightarrow\ 4\gamma$	3.27×10^{-1}	3.27×10^{-1}	1.64×10^{-4}	8.19×10^{-8}	4.09×10^{-11}	2.05×10^{-14}
$pp \rightarrow\ 4\gamma+1j$	6.89×10^{-1}	6.89×10^{-1}	3.44×10^{-4}	1.72×10^{-7}	8.61×10^{-11}	4.30×10^{-14}
$pp \rightarrow\ 3\gamma+1j$	3.55×10^{2}	0	1.78×10^{-1}	8.88×10^{-5}	4.44×10^{-8}	2.22×10^{-11}
$pp \rightarrow\ 3\gamma+2j$	4.61×10^{2}	0	2.31×10^{-1}	1.15×10^{-4}	5.76×10^{-8}	2.88×10^{-11}
$pp \rightarrow\ 2\gamma+2j$	3.27×10^{5}	0	0	8.18×10^{-2}	4.09×10^{-5}	2.04×10^{-8}
$pp \rightarrow\ 2\gamma+3j$	1.71×10^{5}	0	0	4.28×10^{-2}	2.14×10^{-5}	1.07×10^{-8}

Table 7.5: *The maximum number of events expected for each set of allowed values of Nγ+Mj in the background processes in the background processes. For each set of values of N and M, it is assumed that all events in the sample contain exactly Nγ+Mj. Based on this assumption the corresponding maximum number of expected events for 1 fb^{-1} is calculated. For events with $M>0$ jets, a factor of $\left(\frac{1}{2000}\right)^{M}$ is applied to the expected number of events.*

section, obtained from ALPGEN, of $3.55\times10^{2}\,fb$. From Figure 7.8(c) it is seen that there are no events containing four prompt truth photons. Therefore, the maximum number of events available of this type is zero. However, there are events containing three photons. To pass the requirement that there must be at least four pre-selected photons in any event, a truth jet must fake a photon. These types of events are denoted 3γ+1j in Table above. If it is assumed that all events in the process are of this type then the maximum number of events expected for a luminosity of $1\,fb^{-1}$ would be the

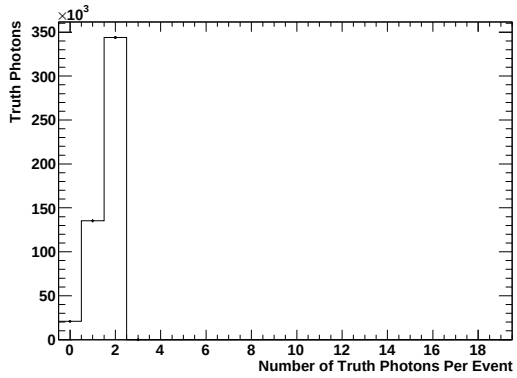

(a) $pp \rightarrow 2\gamma + 2j$

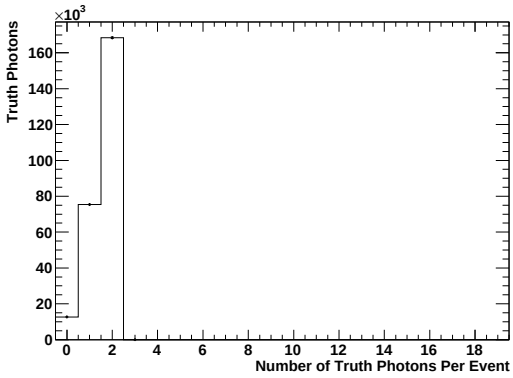

(b) $pp \rightarrow 2\gamma + 3j$

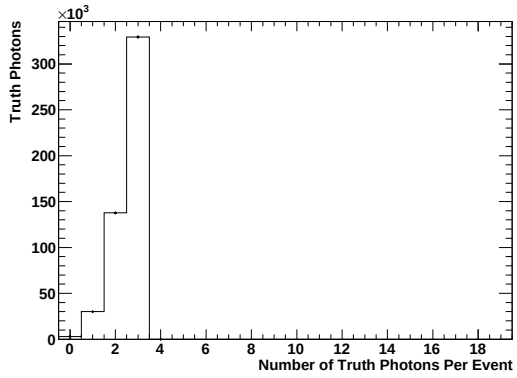

(c) $pp \rightarrow 3\gamma + 1j$

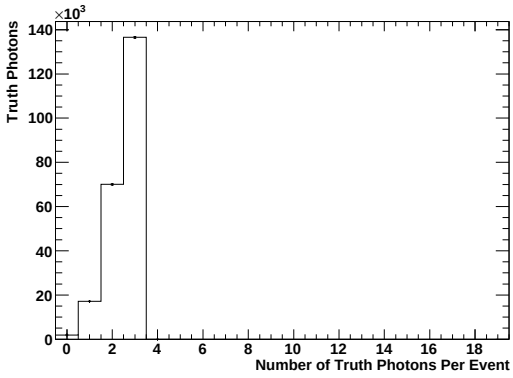

(d) $pp \rightarrow 3\gamma + 2j$

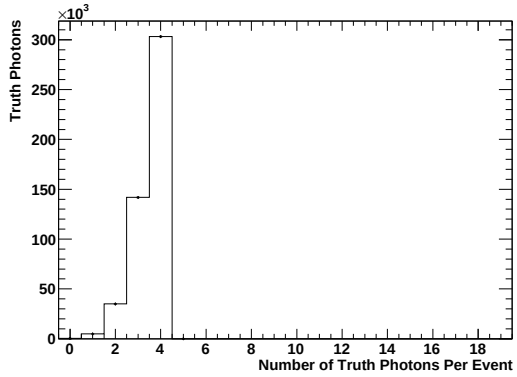

(e) $pp \rightarrow 4\gamma$

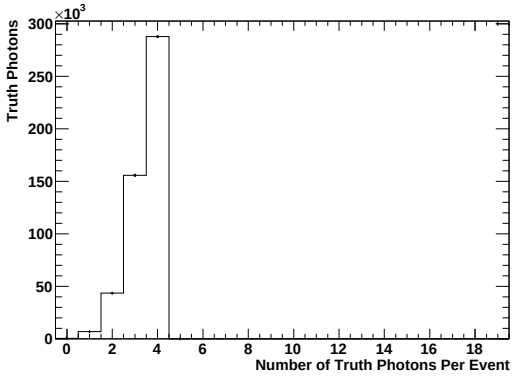

(f) $pp \rightarrow 4\gamma + 1j$

Figure 7.8: *Multiplicity per event of pre-selected prompt truth photons for all of the background processes.*

cross-section (in fb) times the fake rate. For the columns where more than 1 jet is required to fake a photon, the fake rate is applied for each jet. Generalising, if all events are of the type Nγ+Mj such

that $N+M=4$ then the maximum number of background events expected for a luminosity $\mathcal{L}$ is:

$$\chi(N) = \sigma \cdot \mathcal{L} \cdot R_{fake}^{(4-N)} \tag{7.1}$$

where $R_{fake}^{(4-N)} = (1/2000)^{(4-N)}$ and is the rate for jets faking photons to the power of the number of jets required.

In Table 7.5 it assumed all events are of one Nγ+Mj type. From Figures 7.8 however, the fraction of events of each particular Nγ+Mj type is known for every background process. Thus, the fractional number of expected events for each type can be calculated using the formula:

$$\chi(N)_{true} = \sigma \cdot \mathcal{L} \cdot R_{fake}^{(4-N)} \cdot \frac{n_N}{n_{total}} \tag{7.2}$$

where $\chi(N)_{true}$ is the fractional number of expected events for a particular Nγ+Mj type, n_N is the number of events containing N pre-selected photons, as seen from Figure 7.8 and n_{total} is the total number of events in the sample. The $\chi(N)_{true}$ values for each type and for each background process are summarised in Table 7.6. Light shading in cells in the bottom left corner of the table indicates

Process	$\sigma_{\mathbf{ALPGEN}}$ [**fb**]	**Number Of Expected Events For 1 fb^{-1}**				
		4γ+0j	**3γ+1j**	**2γ+2j**	**1γ+3j**	**0γ+4j**
$pp \rightarrow 4\gamma$	3.27×10^{-1}	7.43×10^{-2}	6.41×10^{-5}	2.19×10^{-8}	3.88×10^{-12}	2.95×10^{-16}
$pp \rightarrow 4\gamma+1j$	6.89×10^{-1}	1.25×10^{-1}	1.29×10^{-4}	5.23×10^{-8}	9.76×10^{-12}	6.97×10^{-16}
$pp \rightarrow 3\gamma+1j$	3.55×10^{2}	0	4.15×10^{-2}	3.73×10^{-5}	1.31×10^{-8}	1.33×10^{-12}
$pp \rightarrow 3\gamma+2j$	4.61×10^{2}	0	4.39×10^{-2}	4.70×10^{-5}	1.74×10^{-8}	2.43×10^{-12}
$pp \rightarrow 2\gamma+2j$	3.27×10^{5}	0	0	2.24×10^{-2}	1.96×10^{-5}	4.99×10^{-9}
$pp \rightarrow 2\gamma+3j$	1.71×10^{5}	0	0	1.20×10^{-2}	1.02×10^{-5}	2.58×10^{-9}

Table 7.6: *Table showing the relative number of events expected for each set of allowed values of Nγ+Mj in the background processes. Light shading in the bottom left corner indicates that no events with Nγ+Mj are observed. Heavy shading in the top right of the table indicates that whilst events with Nγ+Mj are observed, the maximum number of events of this type is too low when compared to the dominant contribution, indicated by no shading.*

that no events with Nγ+Mj are observed for the process. Heavy shading in the top right of the table indicates that the fractional number of expected events for a specific Nγ+Mj type is too small when compared to the dominant contribution (no shading). This is based upon the assumption that the remaining event selection, described in the next section, has the same efficiency for all Nγ+Mj types.

The conclusion from the table above is that for a process such as $pp \rightarrow$Nγ+Mj, the main contribution to the background to the signal would come from events which contain N pre-selected prompt truth photons and at least (M = 4-N) pre-selected jets. Therefore, the event is rejected if the above conditions are not met. It should be noted that if there are more than the required number of pre-selected truth jets then all permutations of photons and jets, satisfying the criteria above, are cycled through and tested to see if they pass all event selection cuts. If a permutation is found to have passed all the cuts, then the event is selected. If no permutation exists that passes all cuts, then the event is rejected. The only difference for the signal is that only events containing exactly 4 pre-selected prompt truth photons, and thus no fakes, are considered further.

To illustrate the analysis model a flowchart of the implementation of the analysis can be seen in Figure 7.9.

7.2.4 Event Selection

In this section the development of the event selection is detailed. For each cut, distributions are shown after the application of previous cuts, to motivate the present cut. A summary of all the cuts used is shown in Table 7.7.

Emulation of photon trigger

The first cut implemented is the requirement that the event must pass a photon "trigger". In this analysis it is not possible to implement a real trigger as only truth information is used. Instead, an approximation of the ATLAS primary photon triggers for a centre-of-mass energy of 14 TeV is used as follows:

- **g60**: The event must contain at least one photon with transverse momentum greater than 60 GeV$/c$;
- **2g20**: The event must contain at least two photons, both with transverse momentum greater than 20 GeV$/c$.

For this analysis, events must pass either the g60 or 2g20 trigger.

Photon Transverse Momentum

As described in Section 7.2.3, events are required to have at least four photons (real or fake). Figure 7.10 shows the transverse momentum of the 4 highest (by p_T) photons in events from all background processes and a select group of signal samples. The signal samples used in this figure, have been

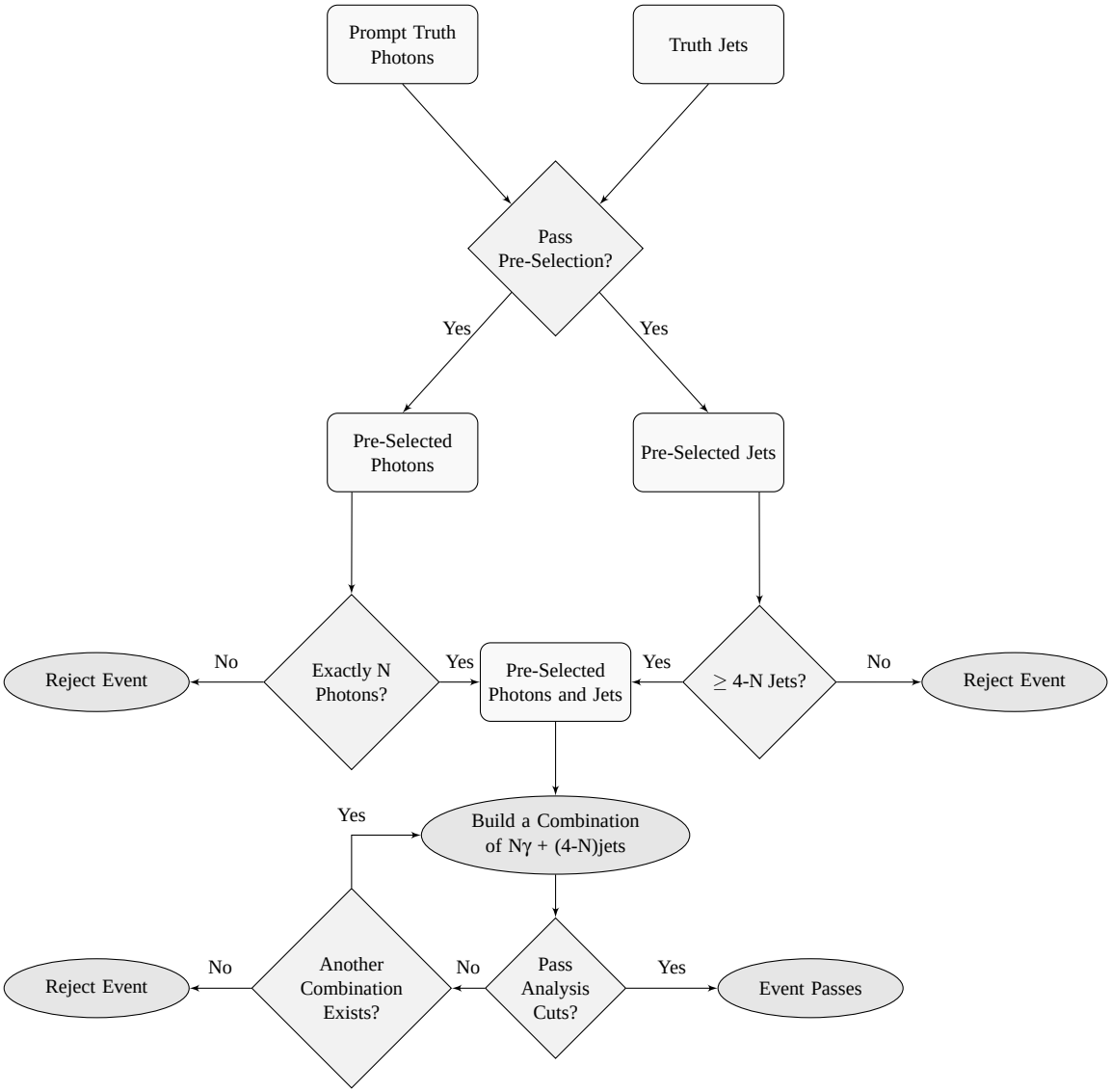

Figure 7.9: *Flow diagram demonstrating the analysis model for an individual event. Here, the value "N" is the required number of prompt truth photons per event. For example, in the* $pp\rightarrow\ 3\gamma + 1j$ *sample N=3, whereas for the signal N=4 and no truth jets are required to fake photons.*

selected in such a manner that they represent differing regions in the (m_h, m_H) mass plane (see Figure 7.2). Additionally, the transverse momentum distributions seen in Figure 7.10 have all been normalised to unit area. For signal samples where $m_h > 100$ GeV$/c^2$ or where $m_H >> m_h$ it can be seen that separation from the background could be achieved by requiring that either the leading photon must have $p_T \gtrsim 60$ GeV$/c$ or that the sub-leading photon has $p_T \gtrsim 50$ GeV$/c$. The second requirement is equivalent to requiring that there must be two photons in the event both with $p_T \gtrsim 50$ GeV$/c$. However, for low mass samples close to the $m_H = 2m_h$ threshold, these requirements lead to losing significant numbers of signal events. Since this search does not presume knowledge of preferred re-

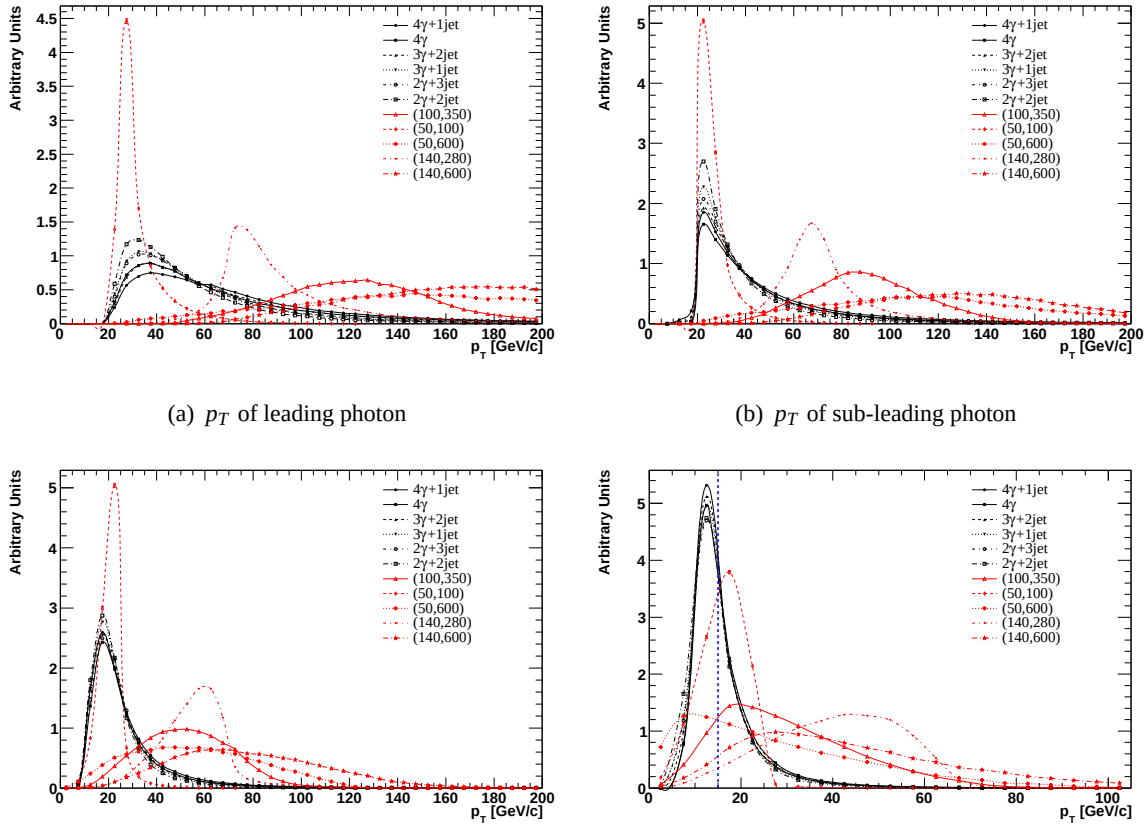

(a) p_T of leading photon

(b) p_T of sub-leading photon

(c) p_T of third photon (by p_T)

(d) p_T of fourth photon (by p_T)

Figure 7.10: *Comparisons of the p_T of the four highest p_T truth photons (real) or truth jets (fake) from all background and selected signal samples. Distributions have been normalised to unit area and all events are required to have passed the trigger cut. The dashed blue line in (d) indicates the cut placed at 15 GeV$/c$ on the transverse momentum of the fourth photon.*

gions in the (m_h, m_H) plane, the most generic (to all mass points) selection has been implemented. The requirement used here, as indicated by the vertical blue line in Figure 7.10(d), is to select events where there are four photons all with $p_T > 15$ GeV$/c$.

Figure 7.11 shows the transverse momentum of the three highest (by p_T) photons after the application of the aforementioned p_T cut. Again, for these distributions, advantage for high Higgs mass signals over the background could be obtained by requiring that the leading $p_T > 50$ GeV$/c$ or the sub-leading $p_T > 40$ GeV$/c$. However, as with the previous set of distributions this will reduce the selection efficiency for signals with low m_h, close to the $m_H = 2m_h$ threshold. Therefore, no cut has been applied to these distributions.

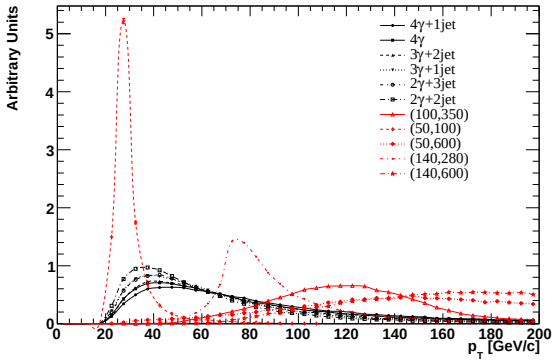

(a) p_T of leading photon

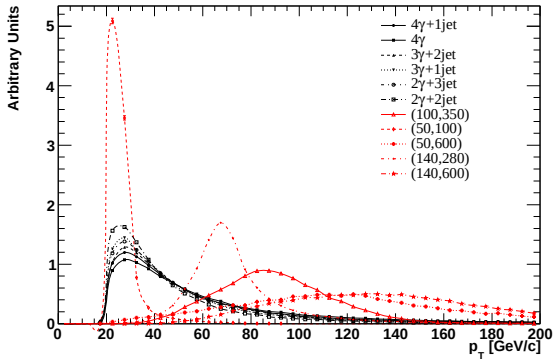

(b) p_T of sub-leading photon

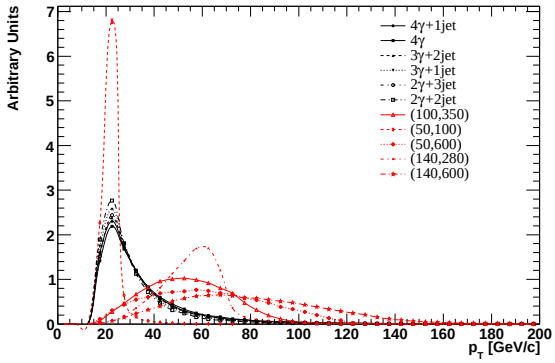

(c) p_T of third highest photon (by p_T)

Figure 7.11: *Comparision of the p_T of the three highest p_T truth photons (real) or truth jets (fake) in signal and background events. Distributions have been normalised to unit area and all events are required to have passed the trigger and contain four photons with $p_T > 15$ GeV$/c$.*

Invariant Mass of Photon Pairs - 1

As we are working with a range of m_h and m_H values it is not possible to select events on the basis that the invariant mass of a photon pair should correspond to a specific m_h value. However, it is possible to require that the invariant mass of any pair of photons cannot be greater than half the value of the invariant mass of all four photons in the event. For each event, it has already been required that there are four photons. These can only be arranged in three independent combinations of photon pairs. The number of combinations which satisfy, $m_{ij} < m_4/2$ and $m_{kl} < m_4/2$, is shown in Figure 7.12 for all backgrounds and in Figure 7.13 for the selected signal samples. In this notation, m_4 is the invariant mass of all four photons and m_{ij}, m_{kl} are the invariant masses of the independent photon pairs, where the indices i, j, k, l are integers in the range 1-4 and obey the relation $i \neq j \neq k \neq l$ for any one combination.

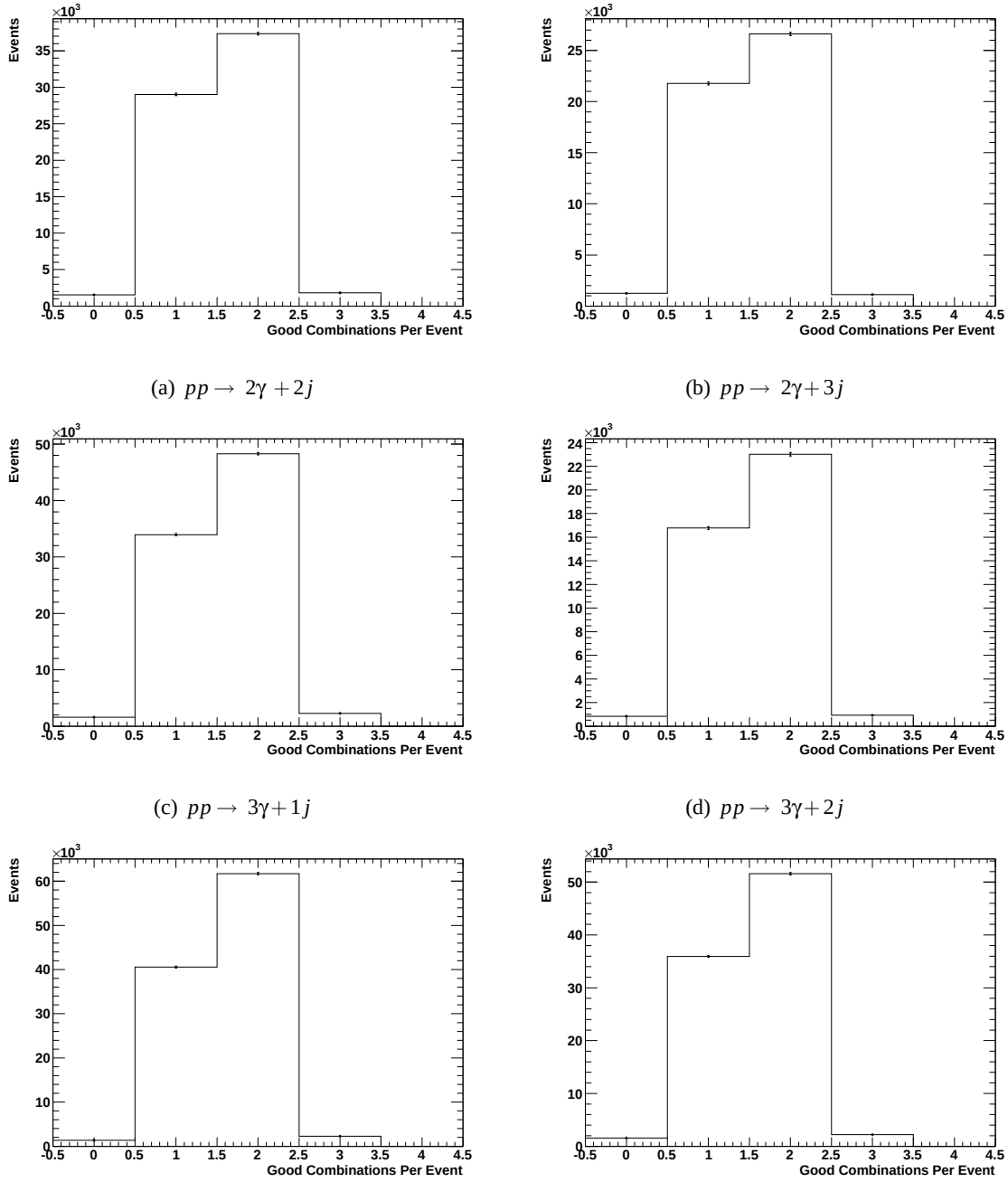

(a) $pp \rightarrow 2\gamma + 2j$

(b) $pp \rightarrow 2\gamma + 3j$

(c) $pp \rightarrow 3\gamma + 1j$

(d) $pp \rightarrow 3\gamma + 2j$

(e) $pp \rightarrow 4\gamma$

(f) $pp \rightarrow 4\gamma + 1j$

Figure 7.12: *Number of combinations in each background sample satisfying* $m_{ij} < m_4/2$ *and* $m_{kl} < m_4/2$. *Distributions shown only contain events which have passed all previous cuts described in the text.*

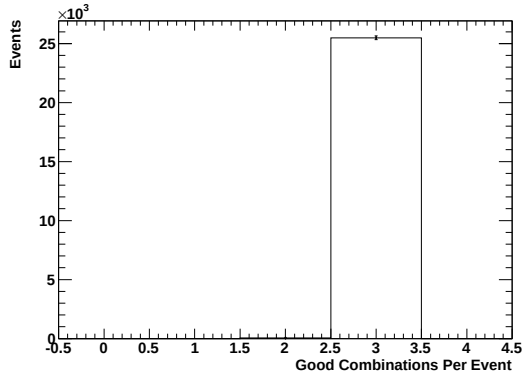

(a) $(m_h, m_H) = (50, 100)$ GeV/c^2

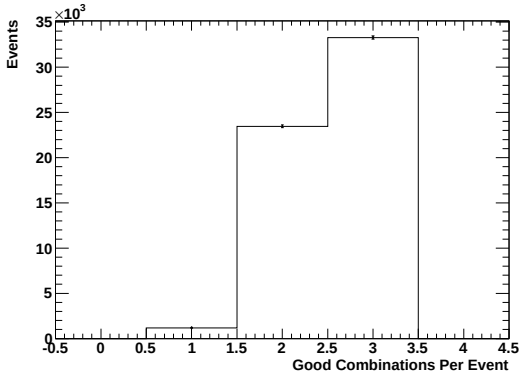

(b) $(m_h, m_H) = (140, 280)$ GeV/c^2

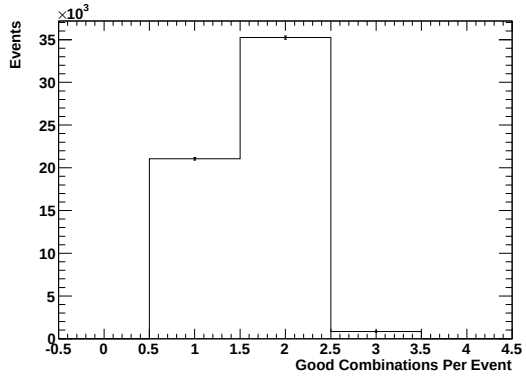

(c) $(m_h, m_H) = (100, 350)$ GeV/c^2

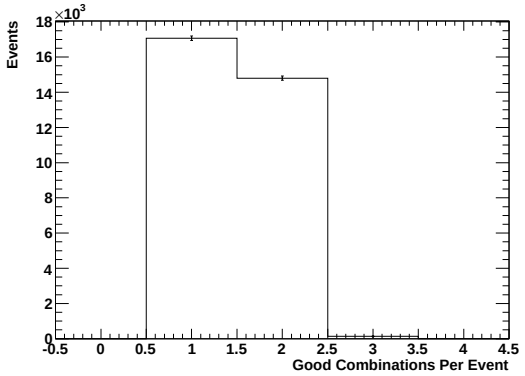

(d) $(m_h, m_H) = (50, 600)$ GeV/c^2

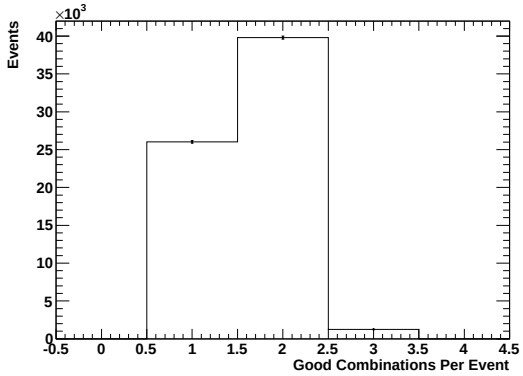

(e) $(m_h, m_H) = (140, 600)$ GeV/c^2

Figure 7.13: *Number of combinations in each of the select signal samples satisfying* $m_{ij} < m_4/2$ *and* $m_{kl} < m_4/2$*. Distributions shown only contain events which have passed all previous cuts described in the text.*

The distributions for all of the backgrounds are similar in shape. For the signal however, interesting differences between different mass points are observed. Whilst all signals away from the $m_h = 2m_H$ threshold have similar distributions, it is noted that the two signals on threshold $(m_h, m_H) = (50, 100)$ GeV/c^2 and $(m_h, m_H) = (140, 280)$ GeV/c^2, are different. First consider the $(m_h, m_H) = (50, 100)$ GeV/c^2 signal. For a 100 GeV/c^2 heavy Higgs boson, the intrinsic width is very narrow (see Figure 7.14(a)) and therefore, is almost exclusively produced with an invariant mass of 100 GeV/c^2. In the centre-of-mass frame of the heavy Higgs, the two light Higgs bosons are produced at rest with invariant masses of 50 GeV/c^2 each. Subsequently, each light Higgs boson decays to a pair of back-to-back photons. The invariant mass of a pair of photons is:

$$m_{ij}^2 = 4E_iE_j \sin^2 \theta_{ij}/2 \tag{7.3}$$

where for back-to-back photons $\theta_{ij} = \pi$ and $m_{ij}^2 = 4E_iE_j$. Therefore, it can be deduced that for the $(m_h, m_H) = (50, 100)$ GeV/c^2 case, $E_i = E_j = E_k = E_l$. For the correct pairing m_{ij} is a maximum of 50 GeV/c^2, whereas for an incorrect pairing this value is lower. Therefore, for any combination of photon pairs $m_{ij} < m_4/2$ and $m_{kl} < m_4/2$ is always true, and is consistent with the distribution in Figure 7.13(a). In contrast to the $(m_h, m_H) = (50, 100)$ GeV/c^2) signal, the other on-threshold signal $(m_h, m_H) = (140, 280)$ GeV/c^2 does not always contain three combinations of photon pairs that satisfy $m_{ij} < m_4/2$ and $m_{kl} < m_4/2$ (see Figure 7.13(b)). This difference is attributed to the intrinsic width of the heavy Higgs, which for a heavy Higgs approaching 300 GeV/c^2 is significantly broader than the width for one of 100 GeV/c^2 (see Figure 7.14(a)). The result is that the heavy Higgs is produced with a minimum invariant mass of 280 GeV/c^2. Therefore, if the heavy Higgs is produced with a mass greater than 280 GeV/c^2, the two 140 GeV/c^2 light Higgs bosons receive a small boost. Therefore, energy is no longer shared equally between pairs of photons from the decay of the light Higgs. Thus, in some combinations of the wrong photon pairs, the condition that $m_{ij} < m_4/2$ and $m_{kl} < m_4/2$ will no longer hold. However, for the combination with the right pairing of photons the condition will still be true. This last statement is true for all signals considered in this analysis.

Taking into account all of the distributions, the analysis requires that at least one combination satisfying $m_{ij} < m_4/2$ and $m_{kl} < m_4/2$ must be present in the event.

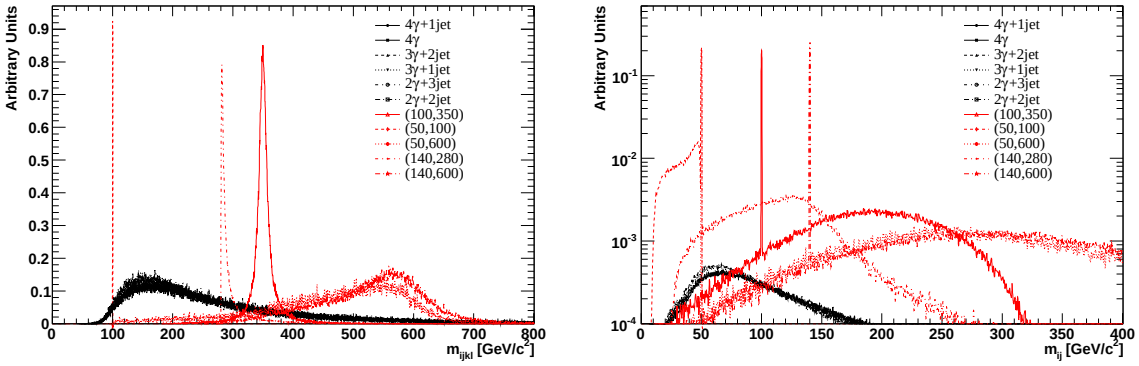

(a) m_4 (b) m_{ij}

Figure 7.14: *Invariant mass distributions for signal and background events: (a) invariant mass of all four photons, (b) invariant mass of all three combinations of pairs of photons.*

Invariant Mass of Photon Pairs - 2

The invariant mass relation between the two light Higgs bosons has also been exploited to separate signal events from background. Figure 7.15 shows the signal and background distribution of $|m_{ij} - m_{kl}|$ for all three combinations in each event. As indicated by the blue line, the analysis requires at least one combination of photons i, j, k, l that satisfies $|m_{ij} - m_{kl}| < 5$ GeV$/c^2$.

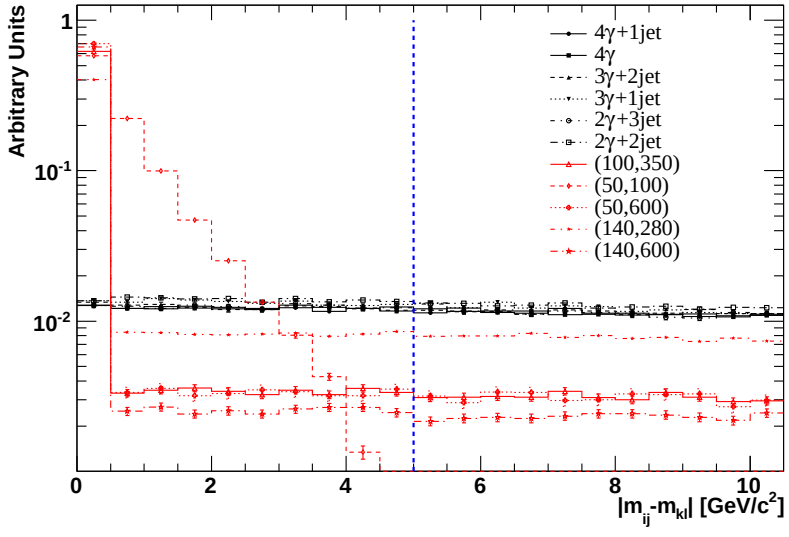

Figure 7.15: *Absolute difference between the invariant mass of photon pairs for all three combinations in each event. Both signal and background distributions are shown and they have been normalised to unit area.*

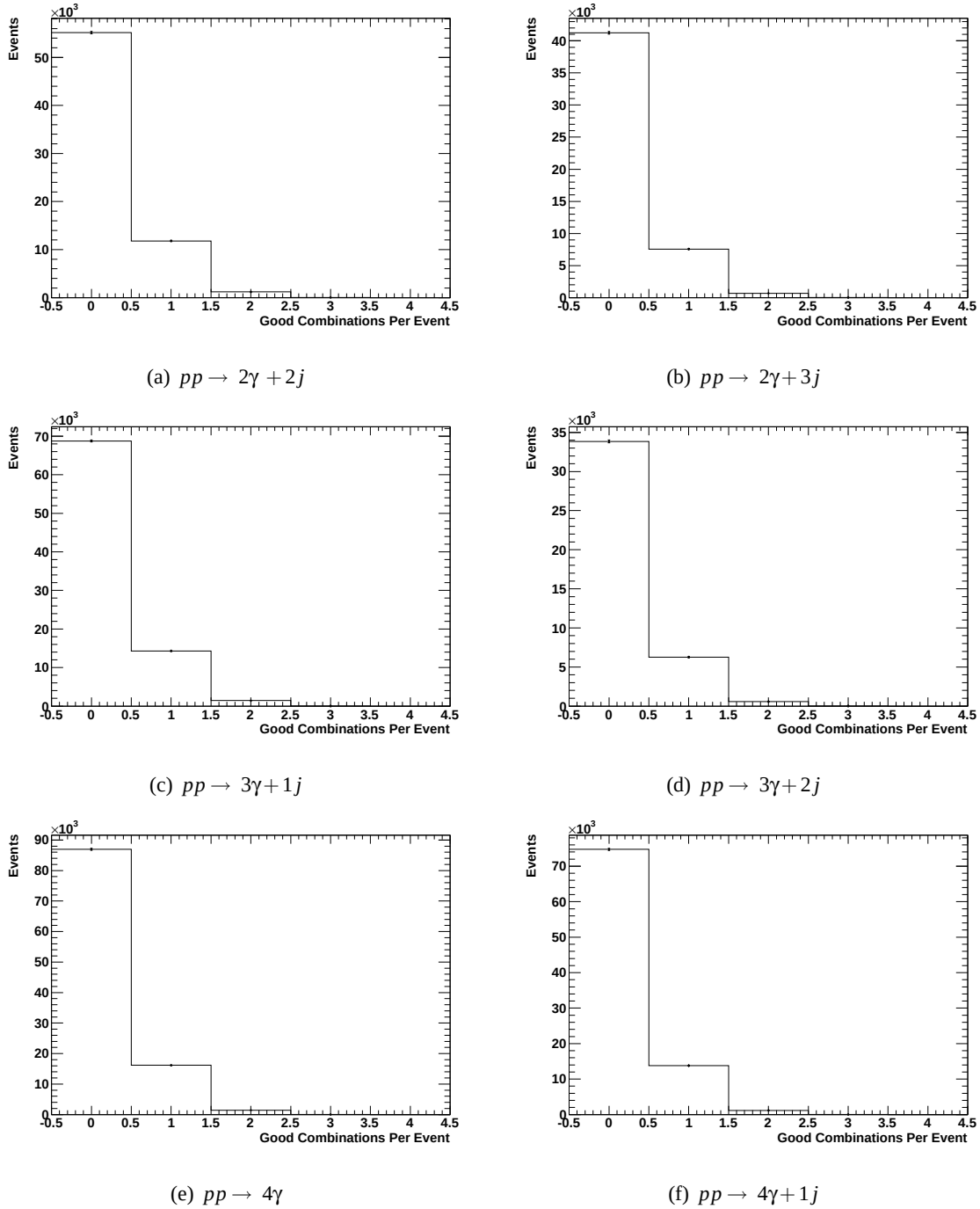

(a) $pp \rightarrow 2\gamma + 2j$

(b) $pp \rightarrow 2\gamma + 3j$

(c) $pp \rightarrow 3\gamma + 1j$

(d) $pp \rightarrow 3\gamma + 2j$

(e) $pp \rightarrow 4\gamma$

(f) $pp \rightarrow 4\gamma + 1j$

Figure 7.16: *Number of combinations in each background sample satisfying* $|m_{ij} - m_{kl}| < 5$ GeV$/c^2$. *Distributions shown only contain events which have passed all previous cuts described in the text.*

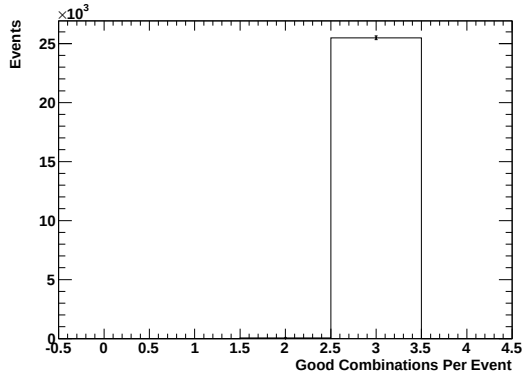

(a) $(m_h, m_H) = (50, 100)$ GeV/c^2

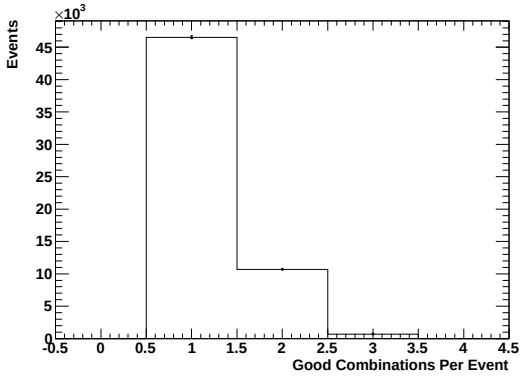

(b) $(m_h, m_H) = (140, 280)$ GeV/c^2

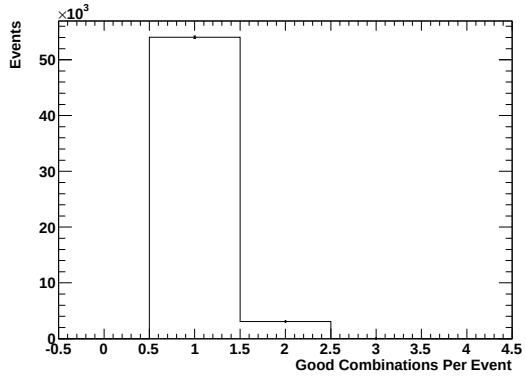

(c) $(m_h, m_H) = (350, 100)$ GeV/c^2

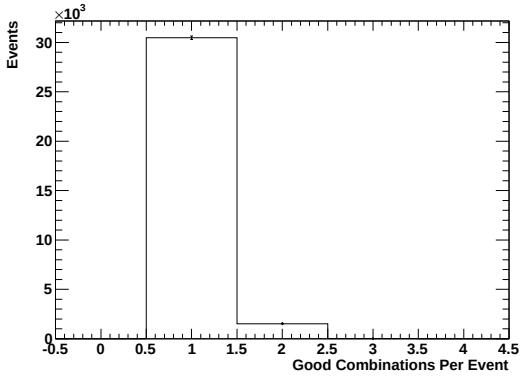

(d) $(m_h, m_H) = (50, 600)$ GeV/c^2

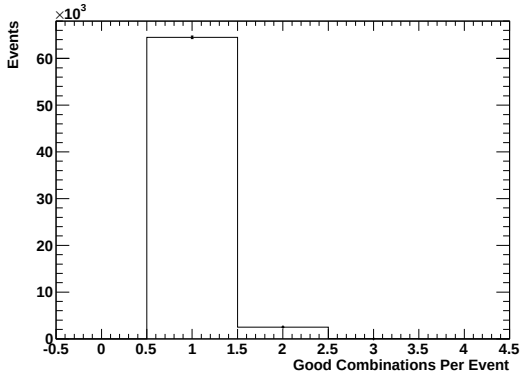

(e) $(m_h, m_H) = (140, 600)$ GeV/c^2

Figure 7.17: *Number of combinations in each of the select signal samples satisfying* $|m_{ij} - m_{kl}| < 5$ GeV/c^2. *Distributions shown only contain events which have passed all previous cuts described in the text.*

The number of combinations meeting this requirement is shown in Figure 7.16 for the background and in Figure 7.16 for the selected signal samples. For the signal, there is always a minimum of one combination per event where $|m_{ij} - m_{kl}| < 5$ GeV$/c^2$. However, for the background samples, a significant number of events do not contain a combination of photon pairs that do not satisfy $|m_{ij} - m_{kl}| < 5$ GeV$/c^2$. Therefore, in this analysis, events are required to have at least one combination where $|m_{ij} - m_{kl}| < 5$ GeV$/c^2$.

(m_h, m_H) Search Range

Since the search is restricted to the allowed ranges of m_h and m_H, two additional requirements can be used. Firstly, the invariant mass of photon pairs, m_{ij}, m_{kl}, must lie in the range $35 < m_h < 145$ GeV$/c^2$, where the upper and lower bound of the range have been extended by an additional 5 GeV$/c^2$ over the nominal search range to account for any mass resolution effects. Secondly, the invariant mass of all four photons in the event, m_4, must lie in the range $70 < m_H < 610$ GeV$/c^2$.

Heavy Higgs Decay

Both the heavy Higgs boson and light Higgs boson are scalars. For decays involving scalars, the quantity $|\cos\theta^\star|$, defined as the magnitude of the daughter particle's decay angle in the parent's rest frame with respect to the parent's flight direction in the laboratory frame, should be uniform. The distribution of $|\cos\theta^\star|$ - in this case the parent is the heavy Higgs and the daughter is one of the light Higgs bosons - is shown in Figure 7.18. For the signal, the distributions are approximately uniform, but they are seen to decrease as $|\cos\theta^\star_H| \to 1$. This effect is due to acceptance and kinematic cuts which tend to suppress $|\cos\theta^\star_H|$ values towards one, where the light Higgs bosons are collinear with the flight direction of the heavy Higgs. Background distributions are seen to have the opposite behaviour as $|\cos\theta^\star| \to 1$. Consequently, events are required to have values of $|\cos\theta^\star_H| < 0.9$, as indicated by the blue line. A summary of the full event selection used in this analysis can be seen in Table 7.7.

Cut Number	Cut Name	Details
0a	Nγ	Exactly N prompt truth photons in the event
0b	Mj	At least M truth jets in the event
1	Trigger	At least two photons with $p_T > 20$ GeV$/c$ or one photon with $p_T > 60$ GeV$/c$ in the event
2	Kinematic 1	At least four photons with $p_T > 15$ GeV$/c$ in the event
3	Invariant Mass Pairs 1	At least one independent combination of photon pairs satisfying $m_{ij} < m_4/2$ and $m_{kl} < m_4/2$
4	Invariant Mass Pairs 2	At least one independent combination of photon pairs satisfying $\lvert m_{ij} - m_{kl}\rvert < 5$ GeV$/c^2$
5	Light Higgs Boson Mass Range	The invariant mass of any pair of photons must lie within $35 < m_h < 145$ GeV$/c^2$
6	Heavy Higgs Boson Mass Range	The invariant mass of all four photons must lie within $70 < m_H < 610$ GeV$/c^2$
7	Heavy Higgs $\lvert\cos\theta^\star_H\rvert$	$\lvert\cos\theta^\star_H\rvert < 0.9$

Table 7.7: *Listing of all event selection cuts used in the analysis. Each individual cut is defined in the text of the current section, apart from cuts 0a and 0b which are requirement stemming from Section 7.2.3. The horizontal line after cut 0b indicates at what point in the analysis truth jets are treated indistinguishably from truth prompt photons.*

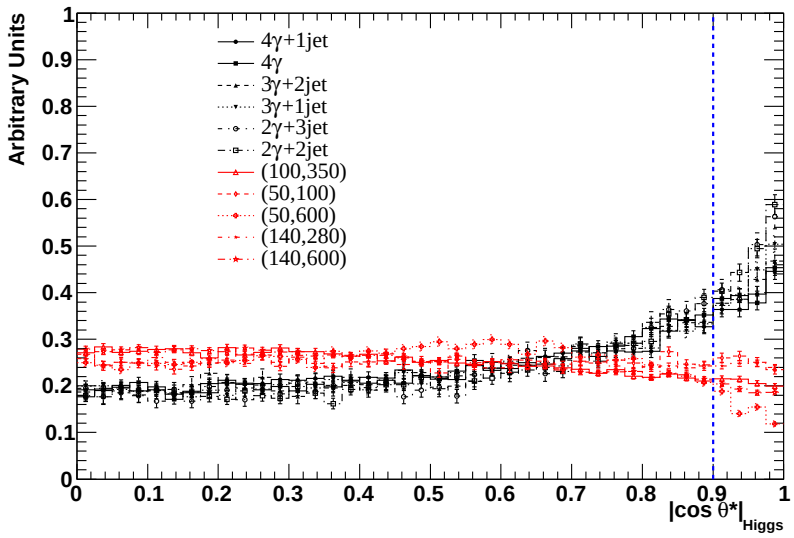

Figure 7.18: *Distribution of* $|\cos\theta^{\star}_{\mathrm{H}}|$*, defined in the text, for the heavy Higgs boson. Distributions are shown for selected signal samples and all background samples. Distributions are normalised to unit area.*

7.3 Event Selection Efficiencies

Event selection efficiencies for both signal and background events are calculated using the following formula:

$$\varepsilon_i = \frac{n_i}{n_{total}} \tag{7.4}$$

where ε_i is the selection efficiency after cut i has been applied, n_i is the number of events passing cut i and n_{total} is the total number of events in the sample. After all cuts have been applied an additional factor is applied based on whether the event contains fake photons or not. The final selection efficiency (after all cuts) is obtained by the formula:

$$\varepsilon(N) = \varepsilon_7 \cdot R_{fake}^{(4-N)} \tag{7.5}$$

where $\varepsilon(N)$ is the final selection efficiency, ε_7 is the efficiency after cut 7 has been applied and $R_{fake}^{(4-N)}$ is the jet-photon fake rate to the power of the number, $M = 4-N$, of jet(s) in the event. Only signal events with exactly four prompt truth photons are considered, thus $N = 4$ and $M = 0$ which means $R_{fake} = 1$ and for the signal $\varepsilon(N) \equiv \varepsilon_7$. The following section present the selection efficiencies for signal and all background samples.

7.3.0.1 Signal Efficiencies

The selection efficiencies for signal events are shown for fixed values of m_h in Figure 7.19(a) and for all of the signal mass points in the (m_h, m_H) plane in Figure 7.19(b). The efficiency, for a fixed value of m_h is seen to rise with m_H. Equally, for fixed values of m_H the efficiency increases with m_h. Signal efficiencies after the application of each cut, listed in Table 7.7, are shown in Table 7.8 for a select group of mass points. For signal events, the dominant cut in the analysis is the requirement that the event must contain exactly four photons.

Cut	**Signal (m_h,m_H) Efficiency (%) After Cut**				
Efficiency	(50,100)	(140,280)	(100,350)	(50,600)	(140,600)
ε_{0a}	48.1(2)	60.0(2)	66.8(1)	47.3(2)	71.5(1)
ε_{0b}	48.1(2)	60.0(2)	66.8(1)	47.3(2)	71.5(1)
ε_1	42.3(2)	60.0(2)	66.8(1)	47.3(2)	71.5(1)
ε_2	25.5(1)	57.9(2)	57.1(2)	32.0(1)	67.1(1)
ε_3	25.5(1)	57.9(2)	57.1(2)	32.0(1)	67.1(1)
ε_4	25.5(1)	57.9(2)	57.1(2)	32.0(1)	67.1(1)
ε_5	25.5(1)	57.9(2)	57.1(2)	32.0(1)	67.1(1)
ε_6	25.5(1)	57.9(2)	57.1(2)	32.0(1)	67.1(1)
ε_7	23.0(1)	52.3(2)	52.3(2)	30.1(1)	61.9(2)

Table 7.8: *Signal efficiencies in percent after the application of each cut (see Table 7.7) for a selected group of*(m_h, m_H) *mass points, where the masses are quoted in units of* GeV/c^2. *The uncertainty on the last digit of the efficiency is indicated in parenthesis.*

7.3.0.2 Background Efficiencies

Selection efficiencies for all of the background processes, are shown, in terms of the ALPGEN cross-section for the process, in Table 7.9. After all cuts have been applied, the total cross-section for the background is $4.28\times10^{-2}\ fb$. Thus, for a luminosity of $1\ fb^{-1}$ 0.0428 events are expected. If instead the MadGraph[3] cross-section obtained for each background is used then the total cross-section for the background is 4.39×10^{-2}. Comparing the total background cross-sections obtained from using either the ALPGEN or MadGraph cross-sections for each process, it is seen that the total background cross-section agrees within 4%.

[3]Note that MadGraph is unable to calculate a cross-section for the process $pp \rightarrow 2\gamma + 1j$. In what follows here the ALPGEN cross-section is used for this process.

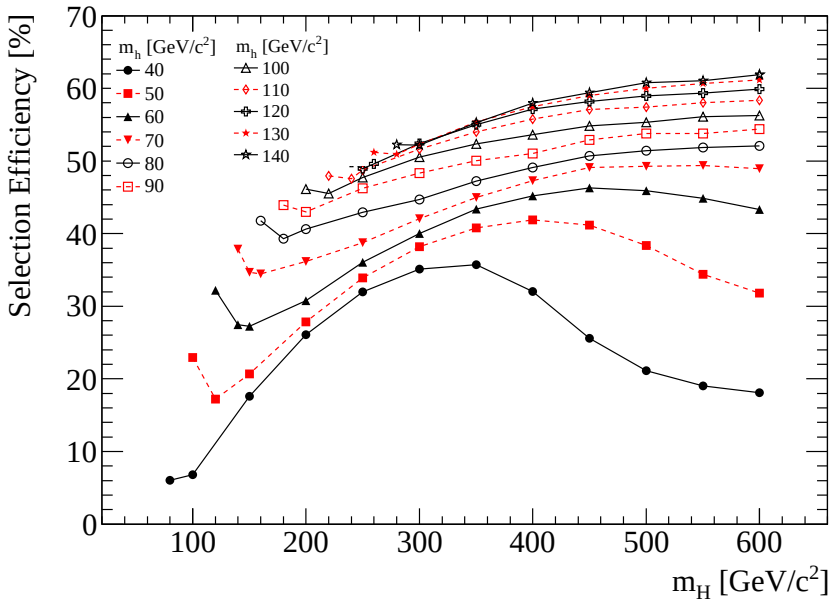

(a)

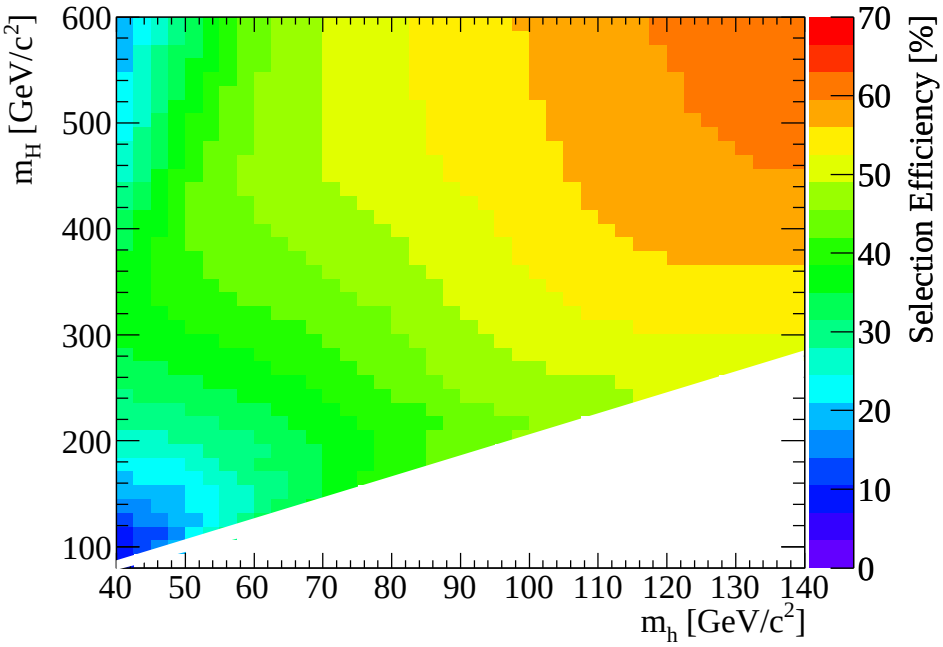

(b)

Figure 7.19: *Signal selection efficiencies for events passing all cuts listed in Table 7.7. Efficiencies are shown for (a) fixed values of* m_h *and (b) across the* (m_h, m_H) *plane.*

Cross-Section	Background Cross-Section [**fb**] After Cut					
After Cut	**pp** $\rightarrow$ **4**γ	**pp** $\rightarrow$ **4**γ+**1j**	**pp** $\rightarrow$ **3**γ+**1j**	**pp** $\rightarrow$ **3**γ+**2j**	**pp** $\rightarrow$ **2**γ+**2j**	**pp** $\rightarrow$ **2**γ+**3j**
σ_{total}	3.27×10^{-1}	6.89×10^{-1}	3.55×10^{2}	4.61×10^{2}	3.27×10^{5}	1.71×10^{5}
$\sigma_{total}\times\varepsilon_{0a}$	2.05×10^{-1}	4.01×10^{-1}	2.34×10^{2}	2.79×10^{2}	2.25×10^{5}	1.12×10^{5}
$\sigma_{total}\times\varepsilon_{0b}$	2.05×10^{-1}	4.01×10^{-1}	2.20×10^{2}	2.75×10^{2}	1.95×10^{5}	1.07×10^{5}
$\sigma_{total}\times\varepsilon_{1}$	1.68×10^{-1}	3.28×10^{-1}	1.39×10^{2}	1.69×10^{2}	8.01×10^{4}	4.72×10^{4}
$\sigma_{total}\times\varepsilon_{2}$	7.15×10^{-2}	1.27×10^{-1}	2.75×10^{1}	3.52×10^{1}	2.03×10^{4}	1.43×10^{4}
$\sigma_{total}\times\varepsilon_{3}$	7.06×10^{-2}	1.25×10^{-1}	2.72×10^{1}	3.48×10^{1}	2.00×10^{4}	1.42×10^{4}
$\sigma_{total}\times\varepsilon_{4}$	1.19×10^{-2}	2.09×10^{-2}	1.25×10^{1}	2.00×10^{1}	1.20×10^{4}	1.00×10^{4}
$\sigma_{total}\times\varepsilon_{5}$	1.19×10^{-2}	2.09×10^{-2}	1.25×10^{1}	1.99×10^{1}	1.20×10^{4}	1.00×10^{4}
$\sigma_{total}\times\varepsilon_{6}$	9.83×10^{-3}	1.73×10^{-2}	1.19×10^{1}	1.93×10^{1}	1.16×10^{4}	9.83×10^{3}
$\sigma_{total}\times\varepsilon_{7}$	8.10×10^{-3}	1.44×10^{-2}	1.13×10^{1}	1.87×10^{1}	1.13×10^{4}	9.66×10^{3}
$\sigma_{total}\times\varepsilon(N)$	8.10×10^{-3}	1.44×10^{-2}	5.67×10^{-3}	9.36×10^{-3}	2.82×10^{-3}	2.42×10^{-3}
Total Background Cross-Section: 4.28×10^{-2} fb						

Table 7.9: *Effective cross-section (from ALPGEN) in fb for all background samples after the application of each cut listed in Table 7.7.*

7.4 Search Sensitivity

Results are presented in two sections: Section 7.4.3 presents the experimental sensitivity across the (m_h, m_H) mass plane, whilst Section 7.4.4 presents the exclusion limits at 95% confidence level in each of the benchmark models defined in Section 2.3. Under the assumption that no signal events are seen, the upper limit on the signal cross-section at 95% confidence level has been calculated for each mass point in the (m_h, m_H) mass plane. Additionally, for each benchmark the upper limit on the signal cross-section is compared to the theoretical cross-section at $\sqrt{s} = 14$ TeV for all allowed mass points. In what follows two integrated luminosity scenarios are considered: 1 fb^{-1} and 10 fb^{-1}.

7.4.1 Confidence Limit Calculations

The upper limit on the signal cross-section at 95% is calculated using the well known CLs Method [1, 2]. The CLs value is defined as:

$$CLs = \frac{CL_{s+b}}{CL_b} = \frac{P_{H_1}(N_{obs}|N_s + N_b)}{P_{H_0}(N_{obs}|N_b)} \tag{7.6}$$

where P_{H_1} is the probability of the signal plus background hypothesis, P_{H_0} is the probability of the background only (null) hypothesis and N_{obs}, N_s, N_b are respectively the number of observed events and expected number of signal events and background events. In the absence of a signal N_{obs} would follow a Poisson distribution with mean $\mu = N_b$. To set an upper limit at the 95% confidence level on N_s, or equivalently on the signal cross-section $\sigma_s^{up} = N_s^{up}/(\mathcal{L} \times \varepsilon_s)$ (where $epsilon_s$ is the signal efficiency after all cuts), the value of N_s is found such that the CLs value converges to 0.05. From this, the upper limit on the cross-section can be obtained for a given N_{obs}. For each one of 10,000 values of N_{obs}, the CLs value is calculated and the mean CLs value is obtained. At each (m_h, m_H) mass point, N_{obs} is obtained for 10,000 background-only toy Monte-Carlo experiments, the corresponding CLs upper limits at 95% confidence level on the cross-section are calculated and the mean value is determined.

The total background cross-section has been obtained in the previous section, and was found to be $4.28 \times 10^{-2}\, fb$ after event selection. Thus, for calculating the 95% CLs upper limit on the cross-section for an integrated luminosity of 1 fb^{-1}, the number of expected background events is $N_b = 0.0428$, where additionally we have assumed a systematic error on this value of $\pm 10\%$ (see the following Section).

7.4.2 Background Uncertainties

To ascertain an estimate of the systematic uncertainty on the total effective background cross-section, the uncertainties relating to the factorisation and renormalisation scale (Q^2) and parton density function (PDF) have been calculated for the dominant backgrounds. Together, the backgrounds $pp \rightarrow 4\gamma$, $pp \rightarrow 4\gamma + 1j$ and $pp \rightarrow 3\gamma + 2j$ contribute approximately 75% to the total effective background cross-section. Therefore, systematics associated with these samples will dominate.

In Alpgen, the factorisation and renormalisation scale has been varied by a factor, $0.25Q_0^2 < Q^2 < 4Q_0^2$, where Q^2 is the effective scale and Q_0^2 is the scale choice, which for all backgrounds has been chosen to be $Q_0^2 = \Sigma {p_T}_\gamma^2 + \Sigma {p_T}_j^2$. The nominal leading order PDF used in this analysis is CTEQ6L1. To estimate the systematic uncertainty related to the PDF, the effective background cross-section is found using another leading order PDF: MRST2002LO. A summary of the systematics found before the event selection has been applied is detailed in Table 7.10. A similar table is shown in Table 7.11 for

Background	$\sigma(Q_0^2)$ [fb]	$\sigma(0.25Q_0^2)$ [fb]	$\sigma(4Q_0^2)$ [fb]	σ(MRST2001LO) [fb]
pp $\rightarrow$ **4**γ	3.27×10^{-1}	2.93×10^{-1} (-10.3%)	3.60×10^{-1} (+10.3%)	3.12×10^{-1} (-4.5%)
pp $\rightarrow$ **4**γ**+1j**	6.89×10^{-1}	7.31×10^{-1} (+6.1%)	6.42×10^{-1} (-6.7%)	6.66×10^{-1} (-3.4%)
pp $\rightarrow$ **3**γ**+2j**	4.61×10^{2}	4.91×10^{2} (+6.4%)	4.30×10^{2} (-6.6%)	4.45×10^{2} (-3.6%)

Table 7.10: *Summary of systematic QCD uncertainties in the dominant backgrounds before event selection. Here $\sigma(Q_0^2)$ represents the background cross-section (fb) obtained from Alpgen when using a factorisation and renormalisation scale $Q_0^2 = \Sigma {p_T}_\gamma^2 + \Sigma {p_T}_j^2$ and PDF: CTEQ6L1. The third and fourth columns contain the Alpgen cross-section when varying the scale by a factor 0.25 and 4 respectively. The last column contains the Alpgen cross-section when the scale $Q_0^2 = \Sigma {p_T}_\gamma^2 + \Sigma {p_T}_j^2$ is fixed and the PDF is changed from CTEQ6L1 to MRST2002LO. Numbers in parentheses indicate the relative differences (in percent) of the background cross-section from the nominal $\sigma(Q_0^2)$ case.*

the effective cross-section after the event selection has been applied. For each of the samples listed in Table 7.11, the systematic uncertainty related to varying the factorisation and renormalisation scale is symmetrised and combined in quadrature with the uncertainty relating to the PDF. Taking the average value, a systematic uncertainty of $\pm$7.1%. To account for other source of systematics not considered here, a conservative value of $\pm$10% has been chosen to represent the systematic uncertainty on the effective background cross-section.

Background	$\sigma_{eff}(Q_0^2)$ [fb]	$\sigma_{eff}(0.25Q_0^2)$ [fb]	$\sigma_{eff}(4Q_0^2)$ [fb]	σ_{eff}(MRST2001LO) [fb]
pp $\rightarrow$ **4**γ	8.10×10^{-3}	7.51×10^{-3} (-7.2%)	8.66×10^{-3} (+6.9%)	7.58×10^{-3} (-6.4%)
pp $\rightarrow$ **4**γ+**1j**	1.44×10^{-2}	1.52×10^{-2} (+5.5%)	1.37×10^{-2} (-4.7%)	1.38×10^{-2} (-4.3%)
pp $\rightarrow$ **3**γ+**2j**	9.36×10^{-3}	9.59×10^{-3} (+2.5%)	9.10×10^{-3} (-2.8%)	8.95×10^{-3} (-4.4%)

Table 7.11: *Summary of systematic QCD uncertainties in the dominant backgrounds after event selection. Here $\sigma_{eff}(Q_0^2)$ represents the effective background cross-section (after the event selection has been applied) when using a factorisation and renormalisation scale $Q_0^2 = \Sigma p_{T\gamma}^2 + \Sigma p_{Tj}^2$ and PDF: CTEQ6L1. The third and fourth columns contain the effective background cross-sections when varying the scale by a factor 0.25 and 4 respectively. The last column contains the effective background cross-section when the scale $Q_0^2 = \Sigma p_{T\gamma}^2 + \Sigma p_{Tj}^2$ is fixed and the PDF is changed from CTEQ6L1 to MRST2002LO. Numbers in parentheses indicate the relative differences (in percent) of the effective background cross-section from the nominal $\sigma(Q_0^2)$ case.*

7.4.3 Experimental Sensitivity

In this section the experimental sensitivity in terms of the upper limit on the signal cross-section, σ_s^{up}, is presented. For each (m_h, m_H) mass point the 95% confidence level upper limit on the signal cross-section has been calculated using the CLs method, as described in Section 7.4.1. The upper limit for each (m_h, m_H) mass point is shown in Figure 7.20 for an integrated luminosity of 1 fb^{-1}. Using one particular mass point as an example, it is seen that the upper limit on the cross-section for the (60,200) signal is $\sim$10 fb. Thus, in the absence of any detected signal events and with a background of 0.0428 events at 1 fb^{-1}, if the theoretical cross-section for a (60,200) signal is greater than the upper limit, then the signal hypothesis is excluded at the 95% confidence level or higher.

For the mass plane as a whole, the search presented here is experimentally more sensitive to high m_h and m_H values. This is wholly driven by the event selection and thus the selection efficiencies for background and signal. Improving the background rejection or tuning the selection cuts for lower m_h and m_H masses would lower the upper limit on the cross-section for these signals, but might impact upon the sensitivity for higher m_h and m_H mass signals.

7.4.4 Sensitivity to Fermiophobic Model Benchmarks

In this section the exclusion limits are presented for each benchmark defined in Section 2.3. Theoretical cross-sections for (m_h, m_H) mass points in the sensitive regions of each benchmark have been provided [45, 79], in accordance with Reference [28]. The cross-section for a given (m_h, m_H) signal depends on the unknown parameter tan β. In order to present conservative results, we have used the

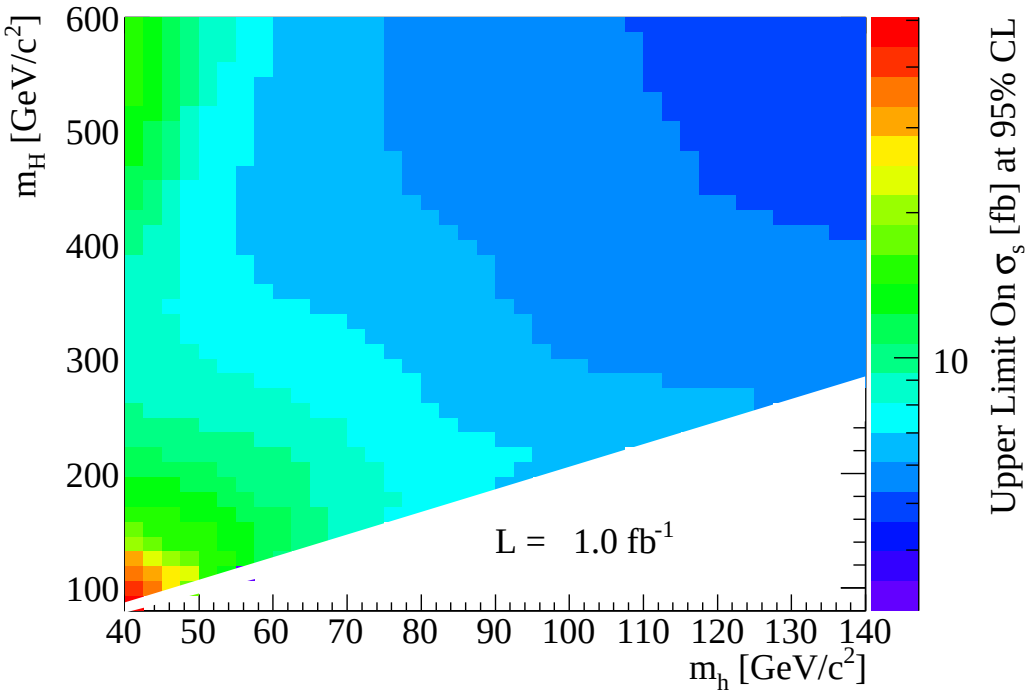

Figure 7.20: *Upper limit on the signal cross-section at 95% confidence level as a function of* (m_h, m_H) *for an integrated Luminosity of 1* fb^{-1}*. The upper limit is calculated via the CLs method, as described in the text. The limit on cross-section is set in the absence of a signal, where for 1* fb^{-1}*, there are 0.0428 expected background events with a* $\pm 10\%$ *systematic error assigned.*

minimum predicted cross-section $\sigma_{th}^{min}(m_h, m_H)$, determined from a scan of all allowed tan β values in each benchmark. For each signal, the ratio of the minimum theoretical cross-section to the 95% confidence level upper limit on the cross-section, is defined as:

$$R_{excl}(m_h, m_H) = \frac{\sigma_{th}^{min}(m_h, m_H)}{\sigma_s^{up}(m_h, m_H)} \tag{7.7}$$

Therefore, for a (m_h, m_H) signal, if R_{excl} is greater than or equal to unity then the signal is excluded at least at the 95% confidence level. Conversely, if $R_{excl} < 1$ then the signal is not excluded at the 95% confidence level.

The excluded region where $R_{excl} > 1$ is shown for an integrated luminosity of 1 fb^{-1} in the four fermiophobic benchmarks with negative values of M^2 in Figure 7.21 and in the three fermiophobic benchmarks with positive values of M^2 in Figure 7.22. Additionally, dependent upon the model, regions of parameter space excluded either by theoretical arguments or experimental limits are indicated where appropriate. It is observed that the region of exclusion increases with increasing values

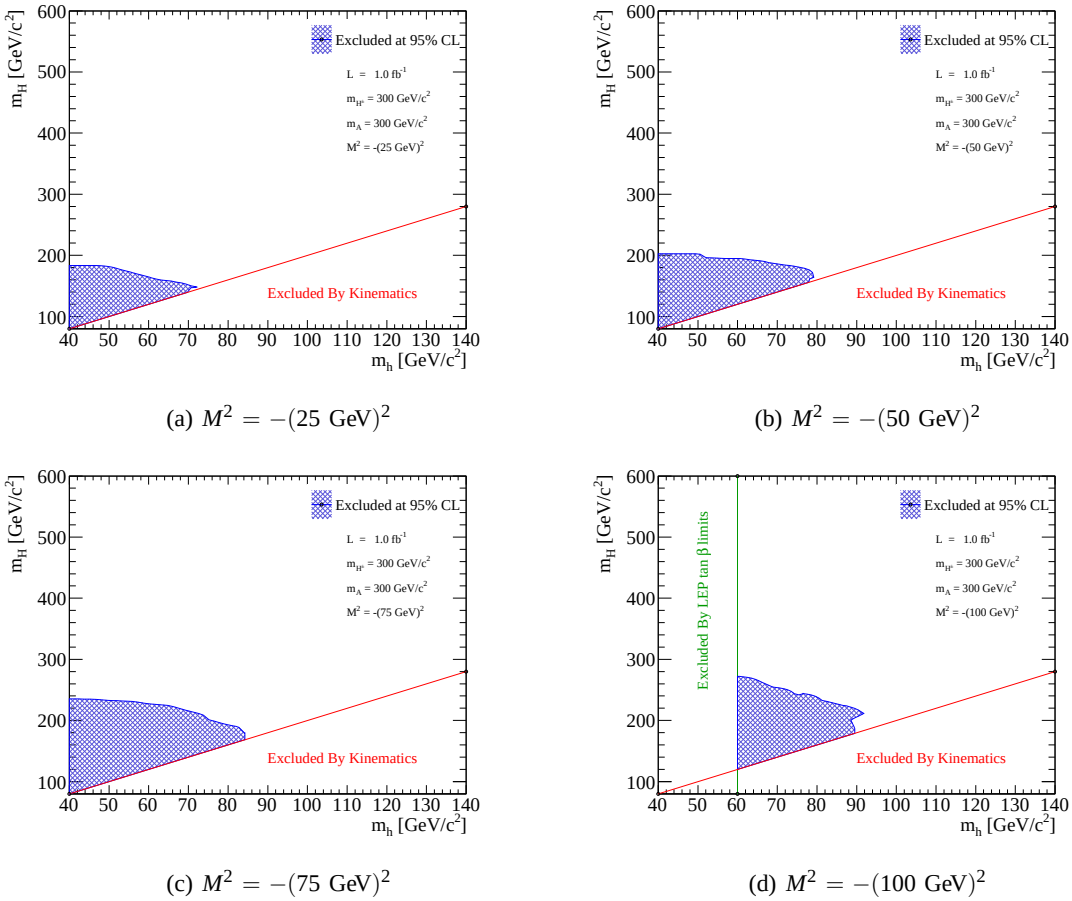

(a) $M^2 = -(25\ \text{GeV})^2$ (b) $M^2 = -(50\ \text{GeV})^2$

(c) $M^2 = -(75\ \text{GeV})^2$ (d) $M^2 = -(100\ \text{GeV})^2$

Figure 7.21: *Exclusion limits, calculated using the generator-level analysis, for the four fermiophobic benchmarks with negative values of M^2. 95% confidence level exclusion contours are shown for 1 fb^{-1}.*

of negative M^2, whilst the exclusion regions shrink with increasing values of positive M^2, such that for the $M^2 = (75\ \text{GeV})^2$ benchmark no exclusion limit can be placed.

The exclusion limits for each fermiophobic benchmark are also shown, for an integrated luminosity of 10 fb^{-1} in the four benchmarks with negative values of M^2 in Figure 7.23 and in the three benchmarks with positive values of M^2 in Figure 7.24. Comparing the exclusions with those from the 1 fb^{-1} scenario, it is observed that the exclusion regions only increase by a fraction for benchmarks with small values of either positive or negative values of M^2. For the benchmarks with larger values of either positive or negative values of M^2, the exclusion region is seen to approximately double in size. However, as per the exclusions with 1 fb^{-1}, no exclusion limit can be placed in the $M^2 = (75\ \text{GeV})^2$ benchmark due to small signal cross-sections.

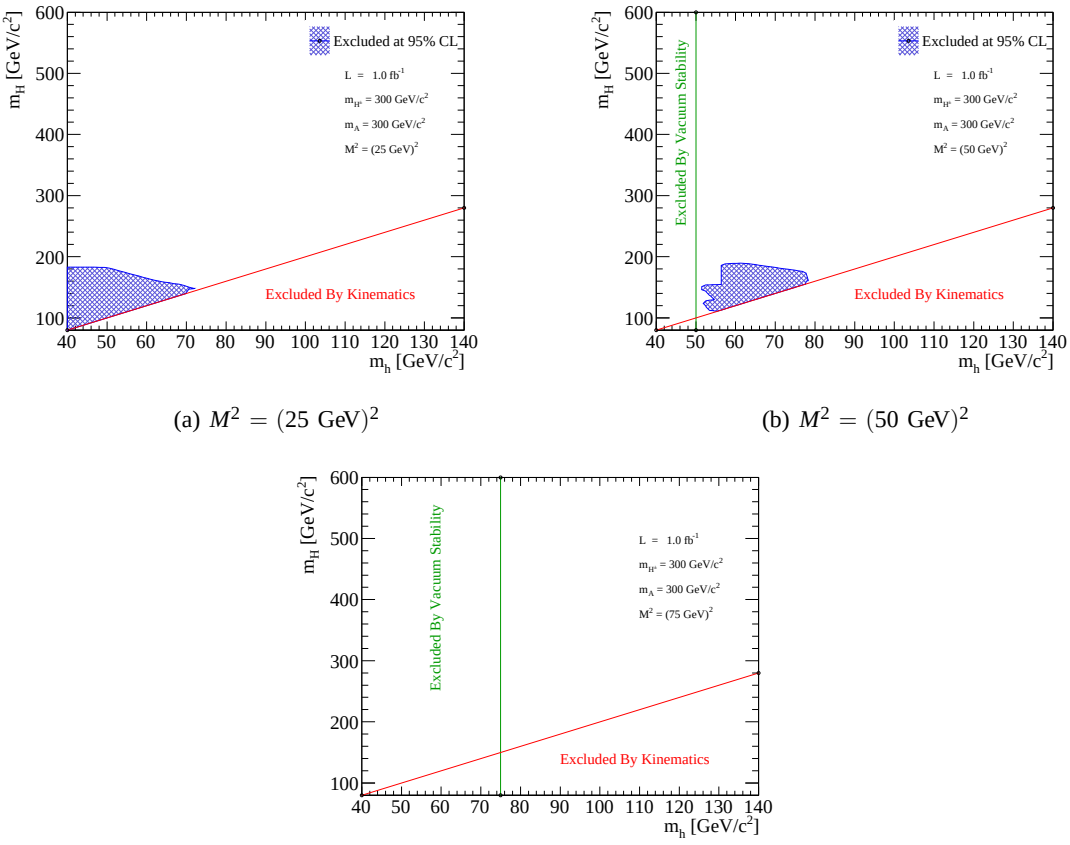

(a) $M^2 = (25\ \text{GeV})^2$

(b) $M^2 = (50\ \text{GeV})^2$

(c) $M^2 = (75\ \text{GeV})^2$

Figure 7.22: *Exclusion limits, calculated using the generator-level analysis, for the four fermiophobic benchmarks with positive values of M^2. 95% confidence level exclusion contours are shown for 1 fb^{-1}. Whilst a figure is shown for $M^2 = (75\ \text{GeV})^2$, it should be noted that no exclusion limit can be placed in this benchmark.*

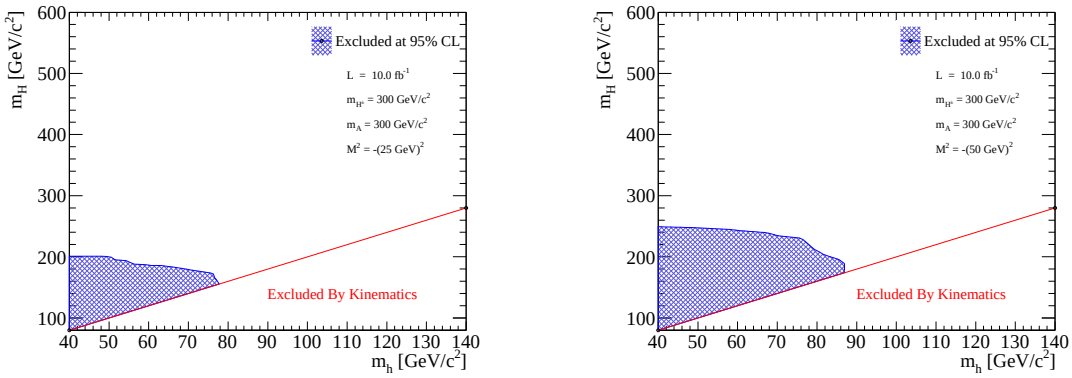

(a) $M^2 = -(25\ \text{GeV})^2$

(b) $M^2 = -(50\ \text{GeV})^2$

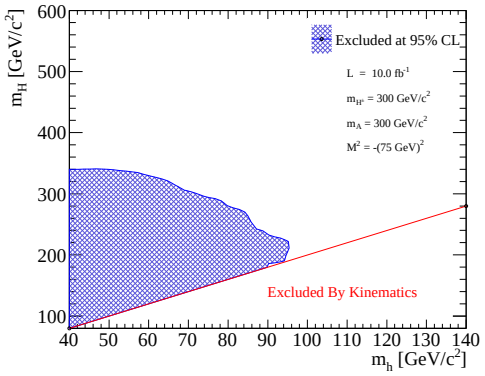

(c) $M^2 = -(75\ \text{GeV})^2$

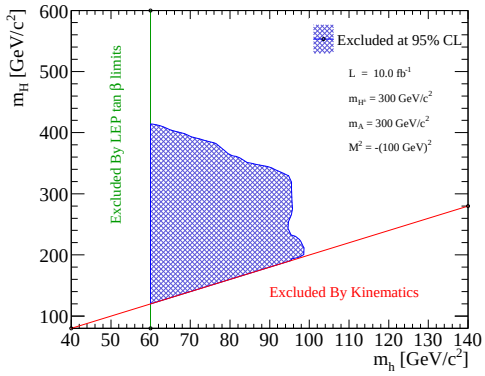

(d) $M^2 = -(100\ \text{GeV})^2$

Figure 7.23: *Exclusion limits, calculated using the generator-level analysis, for the four fermiophobic benchmarks with negative values of M^2. 95% confidence level exclusion contours are shown for 10 fb^{-1}.*

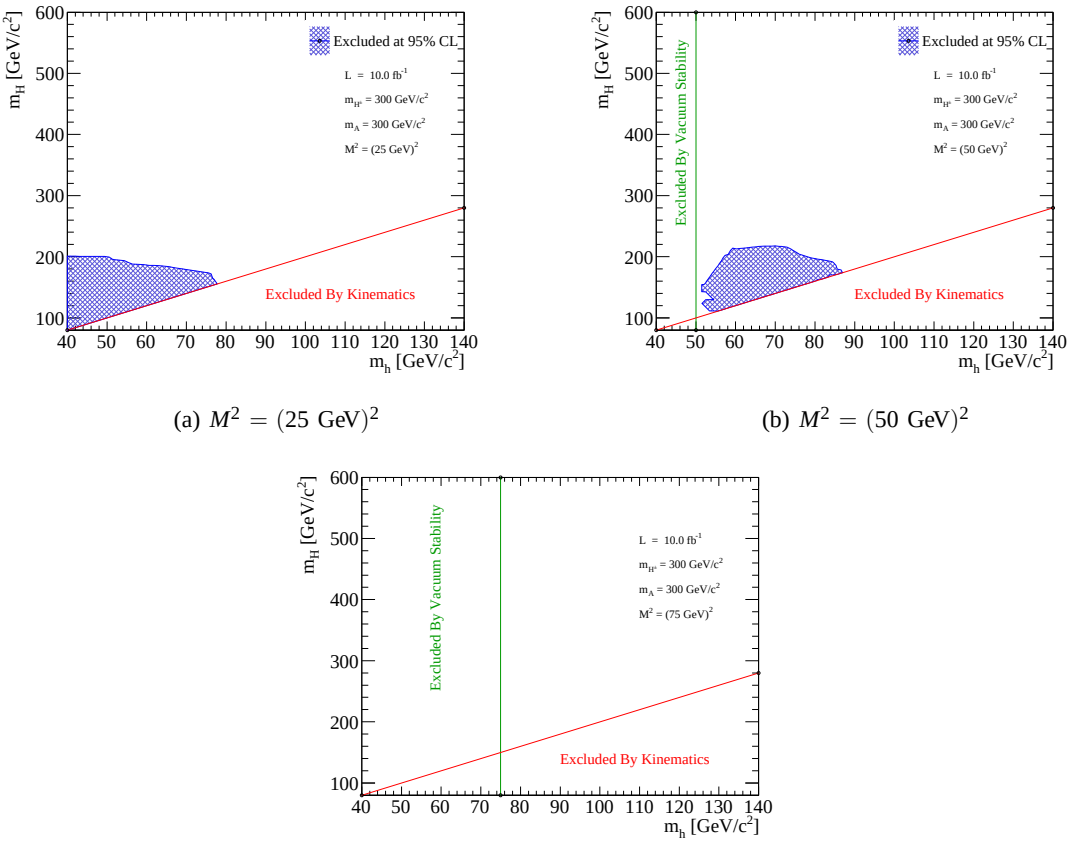

(a) $M^2 = (25\ \text{GeV})^2$

(b) $M^2 = (50\ \text{GeV})^2$

(c) $M^2 = (75\ \text{GeV})^2$

Figure 7.24: *Exclusion limits, calculated using the generator-level analysis, for the four fermiophobic benchmarks with positive values of M^2. 95% confidence level exclusion contours are shown for 10 fb^{-1}. Whilst a figure is shown for $M^2 = (75\ \text{GeV})^2$, it should be noted that no exclusion limit can be placed in this benchmark.*

7.5 Detector-Level Analysis and Results

In what has been presented so far, no detector effects barring acceptance requirements, have been investigated. To give an idea of how a detector such as the ATLAS detector might affect the results of the search, the analysis has been repeated to include detector effects, using the ATLAS fast simulation. Additionally, the photon reconstruction efficiency parameterisations, described in Chapter 6, have been applied to fast simulation reconstructed photons in order to provide realistic reconstruction efficiencies of photons.

In this section the key differences between the generator-level analysis, presented above, and the fast simulation analysis are described. The search sensitivities have also been re-calculated and are compared with those derived from using only generator-level information.

7.5.1 Simulation of Detector-Level Event Samples

To model the effects of the ATLAS detector, the fast simulation program ATLFAST-I has been used. The program itself is described in Section 4.3.1. ATLFAST-I takes as input the generator-level information of an event and simulates the response of the ATLAS detector. In this fashion, corresponding detector-level samples of all the signal and background generator-level samples, used above, have been created. It should be noted that exactly the same events were used in the generator-level samples and in the detector-level samples. The key difference is that the detector-level samples now contain both truth objects and reconstructed objects.

In addition, the photon reconstruction efficiency parameterisations, the subject of Chapter 6, are applied to reconstructed photons in all detector-level samples. This is done to ensure realistic reconstruction efficiencies are present, especially as a multi-photon final state is being investigated.

7.5.2 Analysis Model and Event Selection

The analysis model and event selection, used for the generator-level analysis in Section 7.2, remains unchanged for the purposes of this reconstructed analysis. However, there is a key difference between the two analyses. Truth prompt photons are now replaced by ATLFAST-I reconstructed photons, which have the photon reconstruction efficiency parameterisations applied. For both the signal and background, it is expected that a reduction in the selection efficiency will be seen, characterised by $\sim$80% (the average reconstruction efficiency) per photon required in the final state. Since the signal and two of the backgrounds require four photons in the final state, the selection efficiency can be expected to drop to approximately $(80\%)^4 = 41\%$ of its previous value. However, for photons

with low transverse momentum ($p_T < 50$ GeV$/c$), the average reconstruction efficiency is more like $60-70\%$. Therefore, for signals with low light Higgs boson masses and consequently lower p_T photons, it is expected that the selection efficiency will drop to values less than 41% of previous values.

Whilst for the reconstructed analysis there may be some benefit in optimising the event selection, for the purposes of a direct comparison with the generator-level analysis, no optimisation has been performed and the event selection remains the same.

7.5.3 Selection Efficiencies

Selection efficiencies are presented for the reconstructed analysis for signal and background events. The selection efficiencies are calculated in the same manner as in Section 7.3.

7.5.3.1 Signal

The selection efficiencies for simulated detector-level signal events are shown for fixed values of m_h in Figure 7.25(a) and for all of the signal mass points in the (m_h, m_H) plane in Figure 7.25(b). Signal efficiencies after the application of each cut, listed in Table 7.7, are also shown in Table 7.12 for a selected group of mass points. Compared to the selection efficiencies in the generator-level analysis (see Figure 7.19(b) and Table 7.8) it is seen that as expected all (m_h, m_H) mass signals decrease in efficiency due to the application of the photon reconstruction efficiency parameterisations. For high (m_h, m_H) mass signals the efficiency on average drops to approximately 40% of the corresponding generator-level efficiency. This is in agreement with the expectation outlined earlier. For lower (m_h, m_H) mass signals the efficiency drops to 10-20% of the corresponding generator-level efficiency. Again this in agreement with the expectation that the efficiency would fall by the fourth power of the average photon reconstruction efficiency for a low-p_T photon: $(70\%)^4 \approx 25\%$.

7.5.3.2 Background

Detector-level selection efficiencies for all of the background processes, are shown, in terms of the ALPGEN cross-section for the process, in Table 7.13. After all cuts have been applied, the total cross-section for the background is $7.82\times10^{-3}\,fb$. Thus, for a luminosity of $1\,fb^{-1}$ 0.0078 events

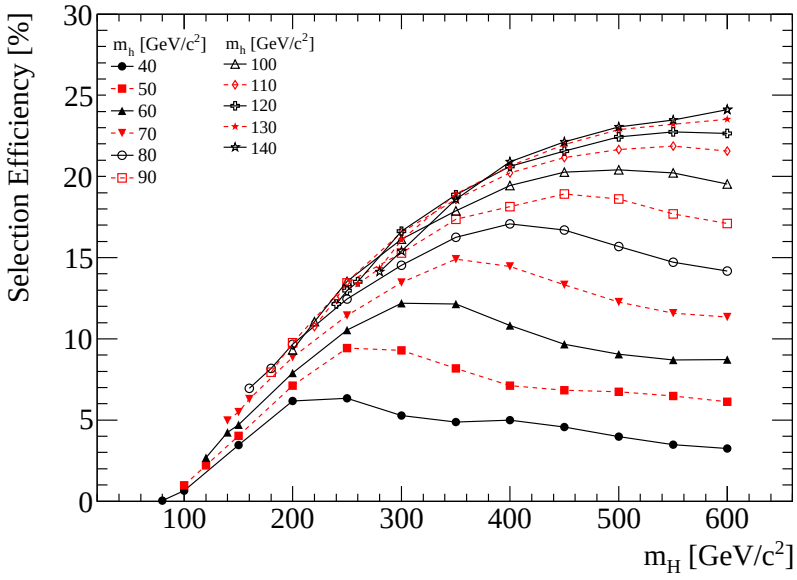

(a)

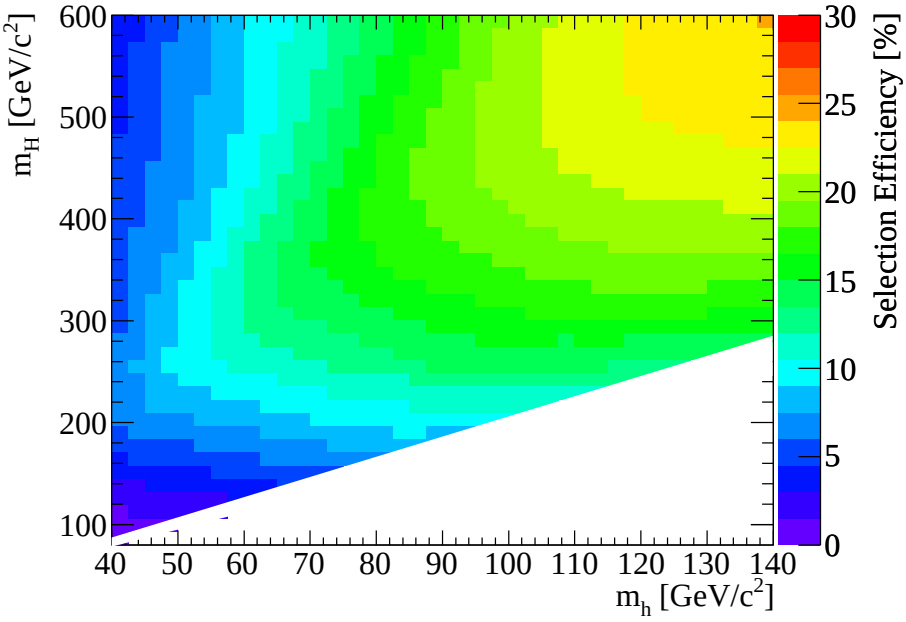

(b)

Figure 7.25: *Signal selection efficiencies for detector-level events passing all cuts listed in Table 7.7. Efficiencies are shown for (a) fixed values of* m_h *and (b) across the* (m_h, m_H) *plane.*

Cut	**Signal (m_h,m_H) Efficiency (%) After Cut**				
Efficiency	(50,100)	(140,280)	(100,350)	(50,600)	(140,600)
ε_{0a}	4.04(6)	18.2(1)	22.0(1)	8.64(9)	28.3(1)
ε_{0b}	4.04(6)	18.2(1)	22.0(1)	8.64(9)	28.3(1)
ε_1	3.70(6)	18.2(1)	22.0(1)	8.64(9)	28.3(1)
ε_2	2.37(5)	17.4(1)	19.6(1)	6.55(7)	26.8(1)
ε_3	2.37(5)	17.4(1)	19.6(1)	6.55(7)	26.8(1)
ε_4	2.37(5)	15.7(1)	19.4(1)	6.54(7)	26.2(1)
ε_5	2.37(5)	15.7(1)	19.4(1)	6.54(7)	26.2(1)
ε_6	1.10(3)	15.6(1)	19.2(1)	6.50(7)	25.9(1)
ε_7	0.97(3)	14.1(1)	17.8(1)	6.12(7)	24.1(1)

Table 7.12: *Signal efficiencies (in percent) in detector-level events after the application of each cut (see Table 7.7), for a selected group of (m_h, m_H) mass points, where masses are quoted in units of* GeV/c^2. *The uncertainty on the last digit of the efficiency is indicated in parenthesis.*

are expected. If instead the MadGraph[4] cross-section obtained for each background is used, then the total cross-section for the background is 8.03×10^{-3}. Comparing this value with the total background cross-section in the generator-level analysis, it is observed that for the fast simulation analysis the total background cross-section falls to about $\sim$20% of the generator-level analysis value. Again this is as expected, since background events contain mainly low-p_T photons, for which the average photon reconstruction efficiency is $\sim$60-70%.

7.6 Search Sensitivity

Results for the detector-level analysis are presented in two sections: Section 7.6.1 presents the experimental sensitivity across the (m_h, m_H) mass plane, whilst Section 7.6.2 presents the exclusion limits at 95% confidence level in each of the fermiophobic benchmarks defined in Section 2.3.

[4]Note that MadGraph is unable to calculate a cross-section for the process $pp \rightarrow 2\gamma + 1j$. In what follows here the ALPGEN cross-section is used.

Cross-Section	Background Cross-Section [**fb**] After Cut					
After Cut	**pp** $\rightarrow$ **4**γ	**pp** $\rightarrow$ **4**γ+**1j**	**pp** $\rightarrow$ **3**γ+**1j**	**pp** $\rightarrow$ **3**γ+**2j**	**pp** $\rightarrow$ **2**γ+**2j**	**pp** $\rightarrow$ **2**γ+**3j**
σ_{total}	3.27×10^{-1}	6.89×10^{-1}	3.55×10^{2}	4.61×10^{2}	3.27×10^{5}	1.71×10^{5}
$\sigma_{total}\times\varepsilon_{0a}$	2.81×10^{-2}	5.25×10^{-2}	4.58×10^{1}	5.21×10^{1}	6.65×10^{4}	3.49×10^{4}
$\sigma_{total}\times\varepsilon_{0b}$	2.81×10^{-2}	5.25×10^{-2}	3.48×10^{1}	4.65×10^{1}	3.68×10^{4}	2.56×10^{4}
$\sigma_{total}\times\varepsilon_{1}$	2.61×10^{-2}	4.82×10^{-2}	2.81×10^{1}	3.66×10^{1}	2.35×10^{4}	1.68×10^{4}
$\sigma_{total}\times\varepsilon_{2}$	1.40×10^{-2}	4.82×10^{-2}	9.38×10^{0}	1.20×10^{1}	7.43×10^{3}	5.71×10^{3}
$\sigma_{total}\times\varepsilon_{3}$	1.38×10^{-2}	2.37×10^{-2}	9.25×10^{0}	1.19×10^{1}	7.32×10^{3}	5.64×10^{3}
$\sigma_{total}\times\varepsilon_{4}$	2.05×10^{-3}	2.34×10^{-2}	2.55×10^{0}	4.08×10^{0}	2.70×10^{3}	2.38×10^{3}
$\sigma_{total}\times\varepsilon_{5}$	2.05×10^{-3}	3.48×10^{-3}	2.54×10^{0}	4.07×10^{0}	2.70×10^{3}	2.38×10^{3}
$\sigma_{total}\times\varepsilon_{6}$	1.68×10^{-3}	2.91×10^{-3}	2.33×10^{0}	3.81×10^{0}	2.49×10^{3}	2.24×10^{3}
$\sigma_{total}\times\varepsilon_{7}$	1.41×10^{-3}	2.46×10^{-3}	2.13×10^{0}	3.55×10^{0}	2.31×10^{3}	2.13×10^{3}
$\sigma_{total}\times\varepsilon(N)$	1.41×10^{-3}	2.46×10^{-3}	1.06×10^{-3}	1.77×10^{-3}	5.76×10^{-4}	5.31×10^{-4}
Total Background Cross-Section: 7.82×10^{-3} fb						

Table 7.13: *Effective cross-section (from ALPGEN) in fb for all simulated detector-level background samples after the application of each cut listed in Table 7.7.*

7.6.1 Experimental Sensitivity

In this section the experimental sensitivity in terms of the upper limit on the signal cross-section, σ_s^{up}, at 95% confidence level is presented for the fast simulation analysis. For each (m_h, m_H) mass point, the 95% confidence level upper limit on the signal cross-section has been calculated using the CLs method, as described in Section 7.4.1. The upper limit for each (m_h, m_H) mass point is shown in Figure 7.26 for an integrated luminosity of 1 fb^{-1}. Compared with the generator-level upper limits

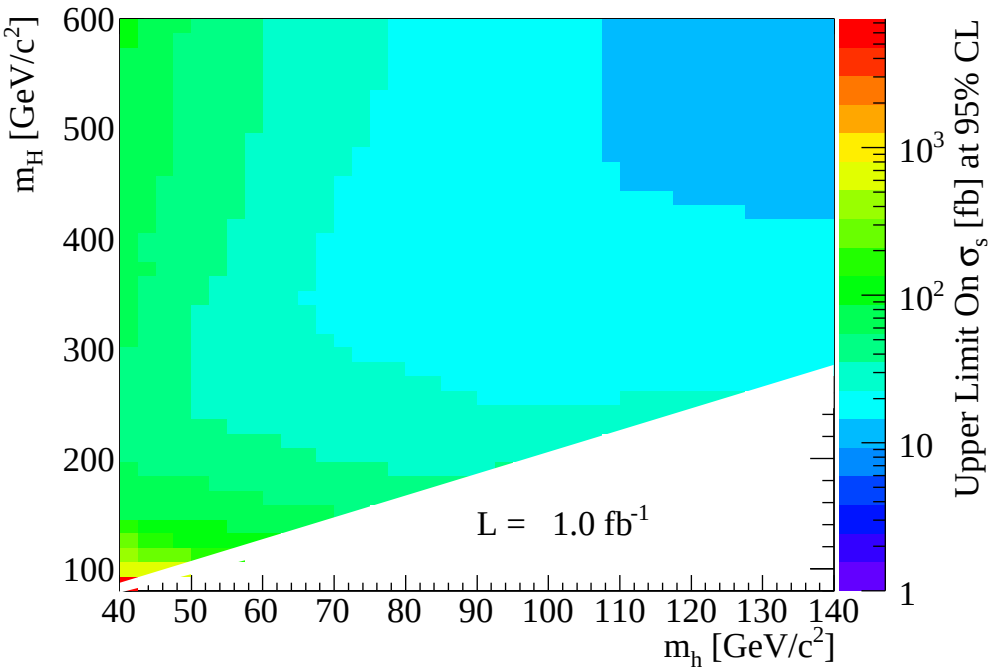

Figure 7.26: *Upper limit on the signal cross-section at 95% confidence level as a function of* (m_h, m_H) *for an integrated luminosity of 1* fb^{-1}. *The upper limit is calculated using the CLs method, as described in the text. The limit on cross-section is set in the absence of a signal, where for 1* fb^{-1}, *there are 0.0078 expected background events, with an assumed uncertainty of* $\pm 10\%$. *A Log scale has been used due to the variation in* σ_s^{up}.

on the cross-section (see Figure 7.20) it is seen that for high (m_h, m_H) mass signals that the upper limit on the cross-section increases by a factor of approximately 3. For low (m_h, m_H) mass signals the upper limit increases by a factor of approximately 5. Consequently, the power to exclude signals is reduced in detector-level analysis.

7.6.2 Sensitivity to Fermiophobic Model Benchmarks

Exclusion limits, calculated using the results of the detector-level analysis, in all fermiophobic benchmarks for integrated luminosities of 1 fb^{-1} and 10 fb^{-1} are presented below.

Exclusion Limits for 1 fb^{-1}

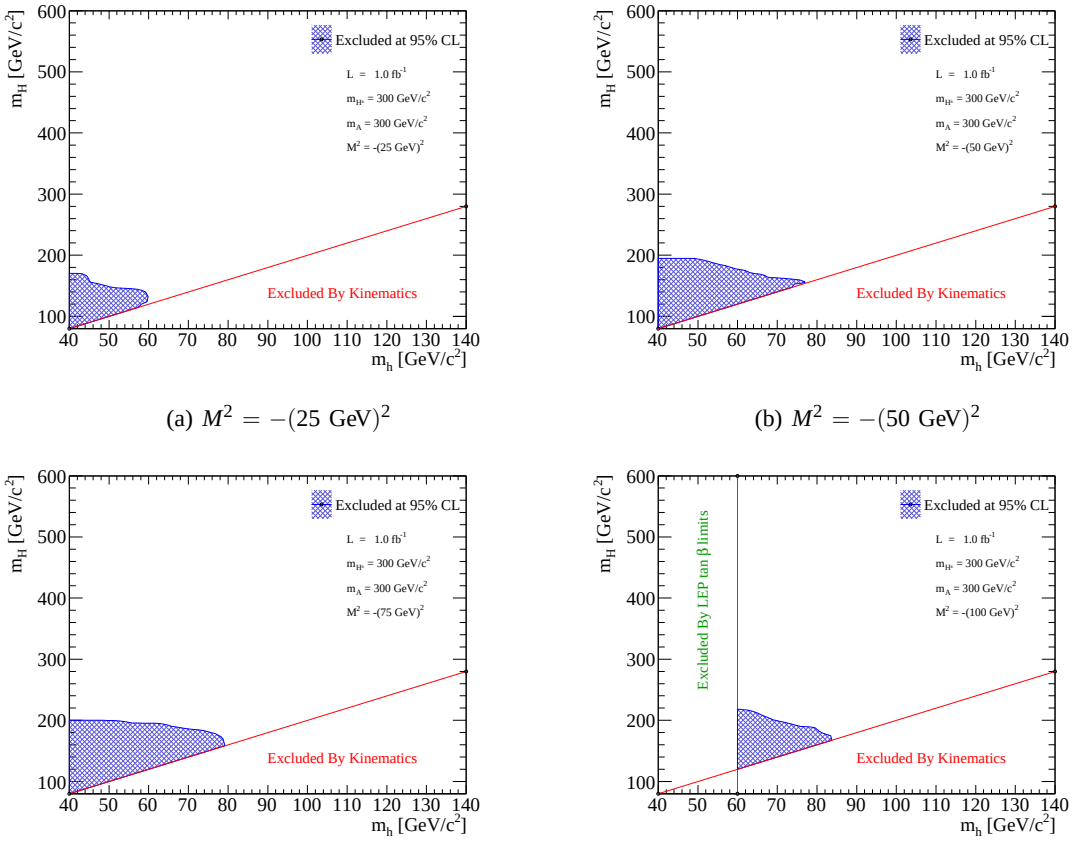

(a) $M^2 = -(25\ \text{GeV})^2$ (b) $M^2 = -(50\ \text{GeV})^2$

(c) $M^2 = -(75\ \text{GeV})^2$ (d) $M^2 = -(100\ \text{GeV})^2$

Figure 7.27: *Exclusion limits, calculated using the detector-level analysis, for the four benchmarks with negative values of M^2. 95% confidence level exclusion contours are shown for 1 fb^{-1}.*

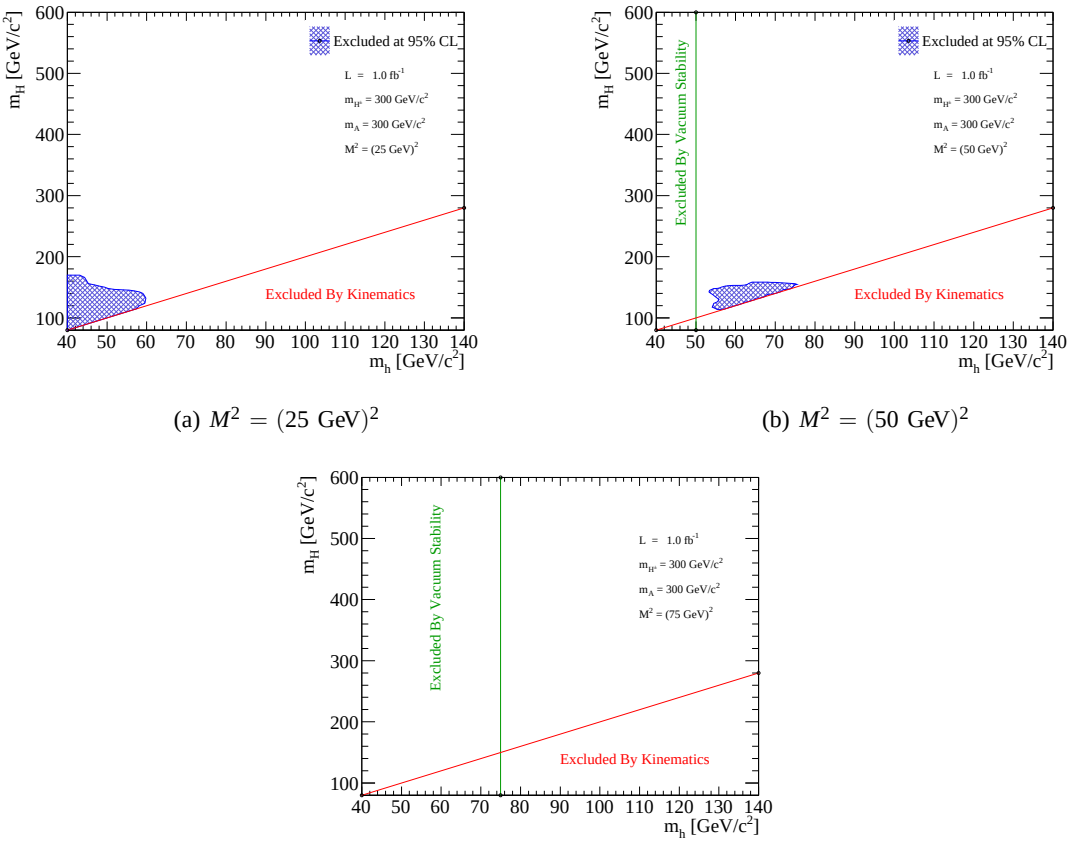

(a) $M^2 = (25\ \text{GeV})^2$

(b) $M^2 = (50\ \text{GeV})^2$

(c) $M^2 = (75\ \text{GeV})^2$

Figure 7.28: *Exclusion limits, calculated using the detector-level analysis, for the four benchmarks with positive values of M^2. 95% confidence level exclusion contours are shown for 1 fb^{-1}. Whilst a figure is shown for $M^2 = (75\ \text{GeV})^2$, it should be noted that no exclusion limit can be placed in this benchmark.*

Exclusion Limits for 10 fb^{-1}

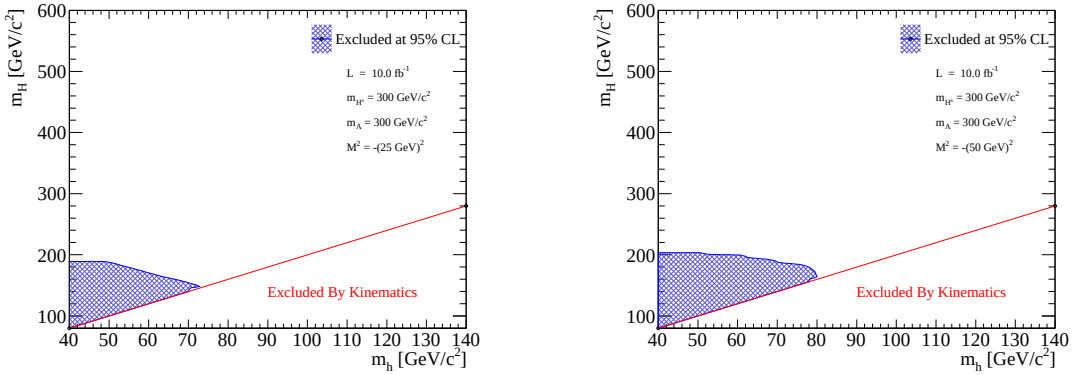

(a) $M^2 = -(25\ \text{GeV})^2$

(b) $M^2 = -(50\ \text{GeV})^2$

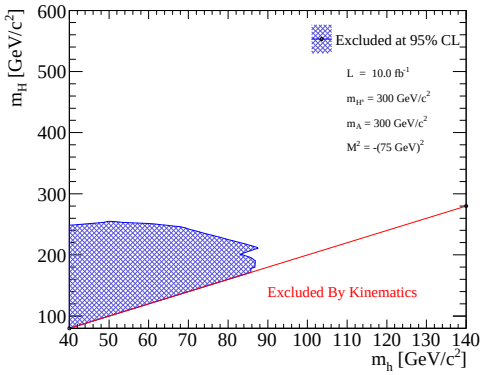

(c) $M^2 = -(75\ \text{GeV})^2$

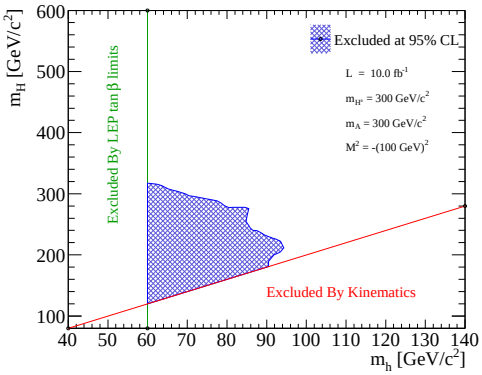

(d) $M^2 = -(100\ \text{GeV})^2$

Figure 7.29: *Exclusion limits, calculated using the detector-level analysis, for the four benchmarks with negative values of M^2. 95% confidence level exclusion contours are shown for 10 fb^{-1}.*

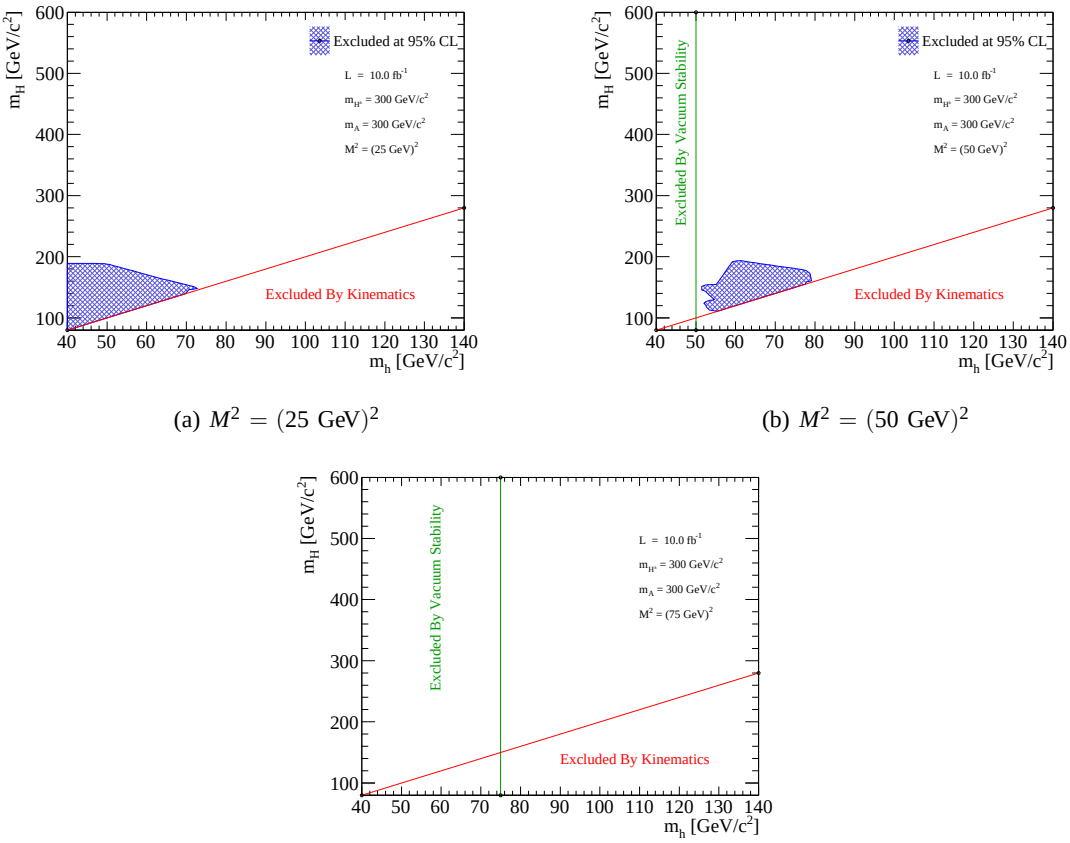

(a) $M^2 = (25\ \text{GeV})^2$

(b) $M^2 = (50\ \text{GeV})^2$

(c) $M^2 = (75\ \text{GeV})^2$

Figure 7.30: *Exclusion limits, calculated using the detector-level analysis, for the four benchmarks with positive values of M^2. 95% confidence level exclusion contours are shown for 10 fb^{-1}. Whilst a figure is shown for $M^2 = (75\ \text{GeV})^2$, it should be noted that no exclusion limit can be placed in this benchmark.*

7.7 Comparison of Generator-Level and Detector-Level Exclusions

The exclusion limits, calculated using the results from detector-level analysis, for two fermiophobic benchmarks are compared with the exclusions, calculated in the generator-level analysis for the same benchmarks. Firstly, the exclusion limits (at 1 fb^{-1}) for each analysis in the $M^2 = -(50\ \text{GeV})^2$ benchmark are shown in Figure 7.31. As expected, the exclusion region at detector-level is smaller,

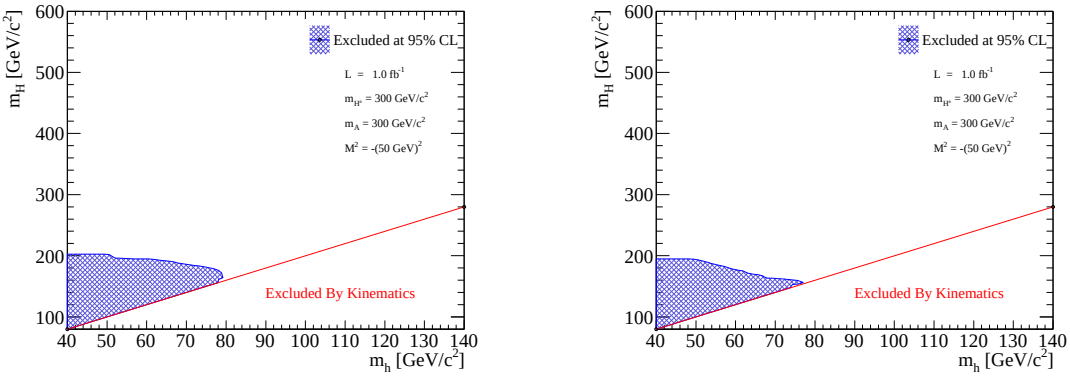

(a) Generator-level (b) Detector-level

Figure 7.31: *Comparison of the exclusion limits (for 1 fb^{-1}) from the (a) generator-level and (b) detector-level analyses for the $M^2 = -(50\ \text{GeV})^2$ benchmark.*

but only by a small fraction. This small reduction in the exclusion region is somewhat typical of all negative M^2 benchmarks considered in this thesis (see Figures 7.27 and 7.29 for exclusion limits in all negative M^2 benchmarks at 1 fb^{-1} and 10 fb^{-1} respectively).

Figure 7.32 compares the exclusion limits (at 1 fb^{-1}) for each analysis in the $M^2 = (50\ \text{GeV})^2$

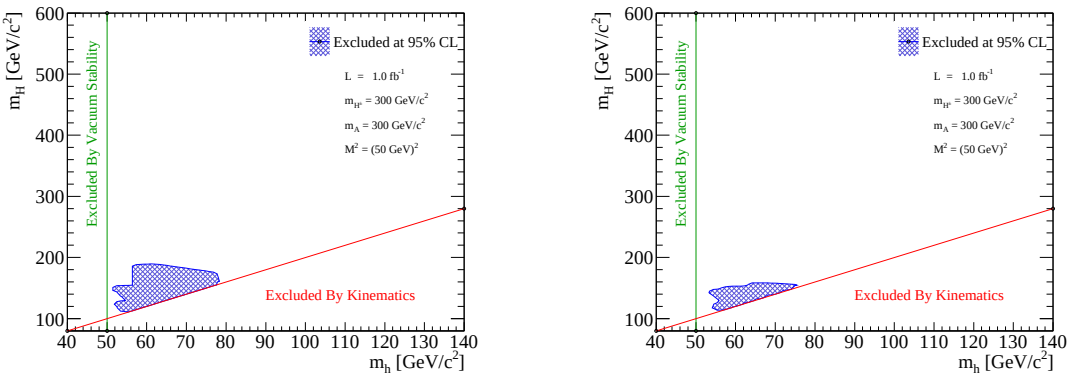

(a) Generator-level (b) Detector-level

Figure 7.32: *Comparison of the exclusion limits (for 1 fb^{-1}) from the (a) generator-level and (b) detector-level analyses for the $M^2 = (50\ \text{GeV})^2$ benchmark.*

benchmark. In this benchmark it is noted that the detector-level exclusion limit is reduced by approximately half with respect to the generator-level exclusion. Whilst the exclusion limits are reduced in the detector-level analysis all benchmarks barring $M^2 = (75\ \text{GeV})^2$ still have regions of parameter space that can be probed with just 1 fb^{-1} of LHC data.

Chapter 8

Conclusions and Outlook

The Standard Model of particle physics has proven to be one of the most successful fundamental theories to date. Indeed several particles predicted by the theory have subsequently been discovered in particle physics experiments. However, there still remains one fundamental particle predicted by the Standard Model that has not been observed in nature. This particle is the Higgs boson, which arises from the need to introduce the Higgs (doublet) field into the Standard Model. There is, however, no reason why just one Higgs field is needed. Nothing stops the inclusion of more fields into the theory and thus increase the number of physical Higgs particles. The simplest extension is to add two doublets of fields. These models, known as Two Higgs Doublet Models (2HDMS), are described in Chapter 2. In 2HDMs the number of physical Higgs particles increases to five. 2HDMs are sub-divided into four Types depending as to how the Higgs fields interact with fermions. In Type-I 2HMDs a phenomenon called fermiophobia is observed where the coupling of the light Higgs boson to fermions vanishes. In the fermiophobic limit a light Higgs boson decays almost exclusively to a pair of photons. Thus, not only is the decay of the Higgs boson to a pair of photons an important channel in the Standard Model search for the Higgs but it is also of importance in 2HDMs searches. The efficient reconstruction and identification of photons by the ATLAS detector is, therefore, of great importance in Higgs searches.

Whilst it is always preferential to study physics channels with fully simulated Monte-Carlo events, this is not always possible as CPU time for simulation is a limited resource. One way around this limitation is to simulate events with the ATLAS fast simulation package, ATLFAST-I, which can reduce the CPU processing time per event by a factor of 1000. However, since there is no modelling of interactions between particles and the detector media in ATLFAST-I, particles are reconstructed with 100% efficiency. To incorporate realistic efficiencies into ATLFAST-I, a set of photon reconstruction efficiency parameterisations have been derived from detailed studies of full simulation events.

The parameterisations, described in Chapter 6, additionally take into account the observation that converted and unconverted photons have differing reconstruction efficiencies. It is demonstrated that it is possible to accurately parameterise the reconstruction efficiency for isolated photons with just the transverse momentum and pseudorapidity of photons. The parameterisations have been validated with several samples with photons in the final state. For samples containing isolated photons in the final state, it is demonstrated that when the parameterisations are applied to ATLFAST-I photons the reconstruction efficiency profile of full simulation photons is accurately reproduced. However, it is observed that in samples that contain a significant fraction of non-isolated photons the parameterisations overestimate the full simulation reconstruction efficiency by approximately 2.5%. This overestimation of the reconstruction efficiency, however, is still far better than the default behaviour of ATLFAST-I. To correct the overestimation, a method is proposed in which the reconstruction efficiency of non-isolated photons is parameterised in terms of (p_T, $|\eta|$) and the transverse energy of the nearest jet, whilst the reconstruction efficiency for isolated photons uses the newly derived set of parameterisations described above.

In Chapter 7, the search for a light fermiophobic Higgs signal was presented. The search centres on a newly proposed 2HDM channel, $gg \rightarrow \mathrm{H} \rightarrow \mathrm{hh} \rightarrow 4\gamma$, which was described in Chapter 2. The signal is characterised by four isolated high-p_T photons in the final state. In this search a scan across the allowed range of light and heavy Higgs boson masses in signals was performed and event samples at each mass point were generated with PYTHIA. The backgrounds to signal characterised by four isolated photons in the final state were identified as: backgrounds arising from the production of four isolated photons and backgrounds arising from events with at least one fake photon. At the LHC, the primary source of fake photons will be from jets containing neutral pions. Therefore, backgrounds involving photons and at least one jet were of main interest to this study. All event samples of background processes were generated with the ALPGEN generator. To separate out the signal events from the background events, a generator-level analysis model and event selection was derived. Selection efficiencies were presented for both signal and background events and for an integrated luminosity of 1 fb^{-1}, 0.0428 background events are expected. In the absence of detection of signal events the upper limit on the signal cross-section is set at 95% confidence level for all mass points. For the seven benchmark models described in Chapter 7 the theoretical cross-section was compared to the upper limit on the signal cross-section and exclusion regions in the $(\mathrm{m_h}, \mathrm{m_H})$ plane were defined. It was observed that for an integrated luminosity of 1 fb^{-1} exclusion regions exist for all benchmarks barring the $M^2 = (75\ \mathrm{GeV})^2$ benchmark. For an integrated luminosity of 10 fb^{-1}, the exclusion region was also seen to grow, and in some fermiophobic model benchmarks was seen

to double in reach.

In addition to the generator-level analysis, a detector-level analysis, using ATLFAST-I simulated events, was performed. The analysis model and event selection used in the detector-level analysis were the same as the ones used in the generator-level analysis. The key difference was the use of reconstructed photons from ATLFAST-I to which the photon reconstruction parameterisations of Chapter 6 were applied. This was the perfect scenario in which to use the parameterisations, since multiple isolated photons were required in the final state. As expected selection efficiencies for both signal and background events decreased compared to the corresponding values in the generator-level analysis. However, exclusion regions in the benchmark models were seen to remain, albeit with a moderate reduction in reach.

The LHC is now fully operational and collecting data at a centre-of-mass of $\sqrt{s} = 7\,\text{TeV}$. The current plan foresees the LHC running until the end of the year 2011, before a year-long shut-down and upgrade in order to prepare for the designed 14 TeV collisions. By the end of 2011 it is estimated that $1\,fb^{-1}$ of data will have been collected. If this indeed is the case, then it might be possible to exclude regions of parameter space in the two Higgs doublet models with the analysis presented in this thesis.

Appendix A

Full Photon Reonstruction Efficiency Parameterisations

In this appendix the full set of reconstruction efficiency parametrisations for AtlfastC are shown. Full details of their derivation and validation can be found in Chapter 6. Photon reconstruction efficiencies as a function of $|\eta|$ for all 12 p_T ranges defined in Chapter 6 are seen, for unconverted photons in Figures A.1, A.2 and A.3, and for converted photons in Figures A.4, A.5 and A.6. Unconverted (converted) photons with $p_T > 120$ GeV$/c$ are assumed to be reconstructed with the same efficiency as in Figure A.3(d) (Figure A.6(d)). All regions not covered by the parametrisations are defined to have 0% efficiency since they represent ranges commonly not used in general analyses.

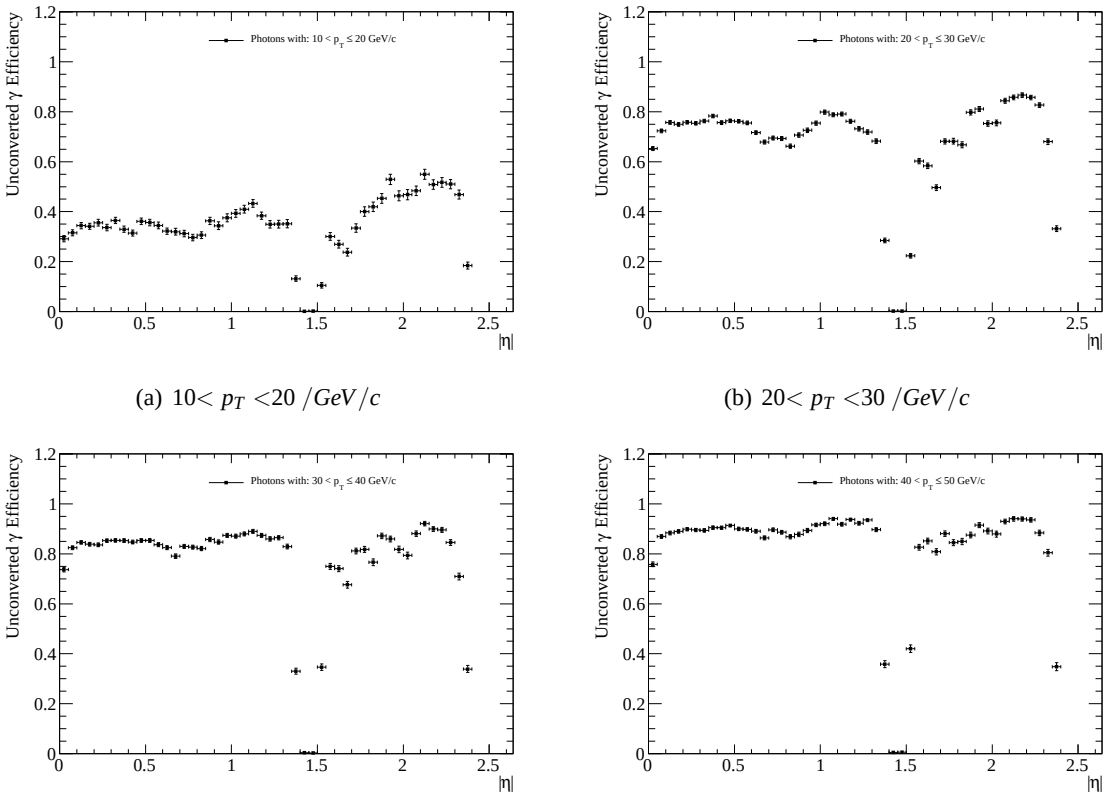

(a) $10 < p_T < 20\ /GeV/c$

(b) $20 < p_T < 30\ /GeV/c$

(c) $30 < p_T < 40\ /GeV/c$

(d) $40 < p_T < 50\ /GeV/c$

Figure A.1: *Full set of unconverted photon reconstruction efficiency parameterisations showing $|\eta|$ distribution for the first 4 p_T ranges.*

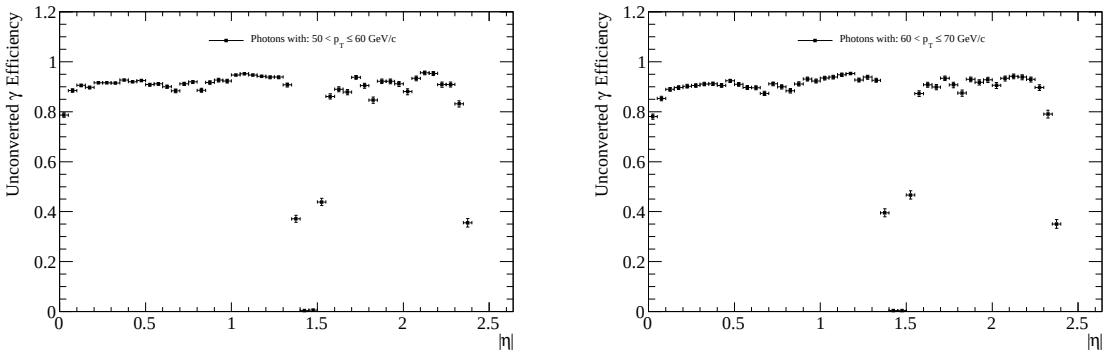

(a) $50 < p_T < 60\ /GeV/c$

(b) $60 < p_T < 70\ /GeV/c$

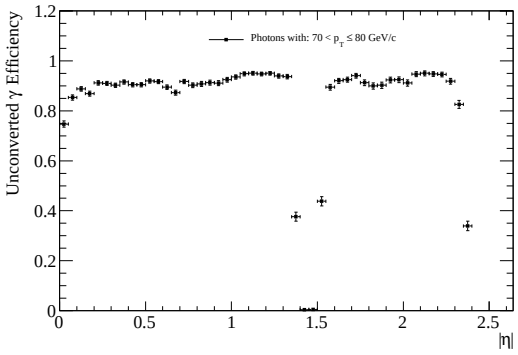

(c) $70 < p_T < 80\ /GeV/c$

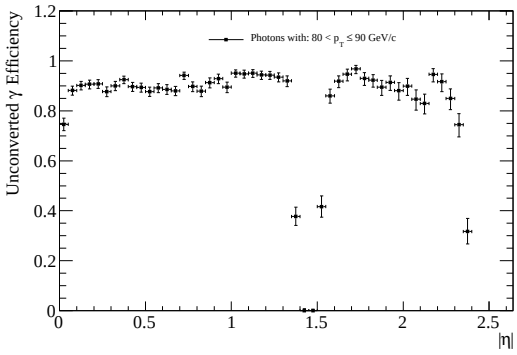

(d) $80 < p_T < 90\ /GeV/c$

Figure A.2: *Full set of unconverted photon reconstruction efficiency parameterisations showing $|\eta|$ distribution for the second 4 p_T ranges.*

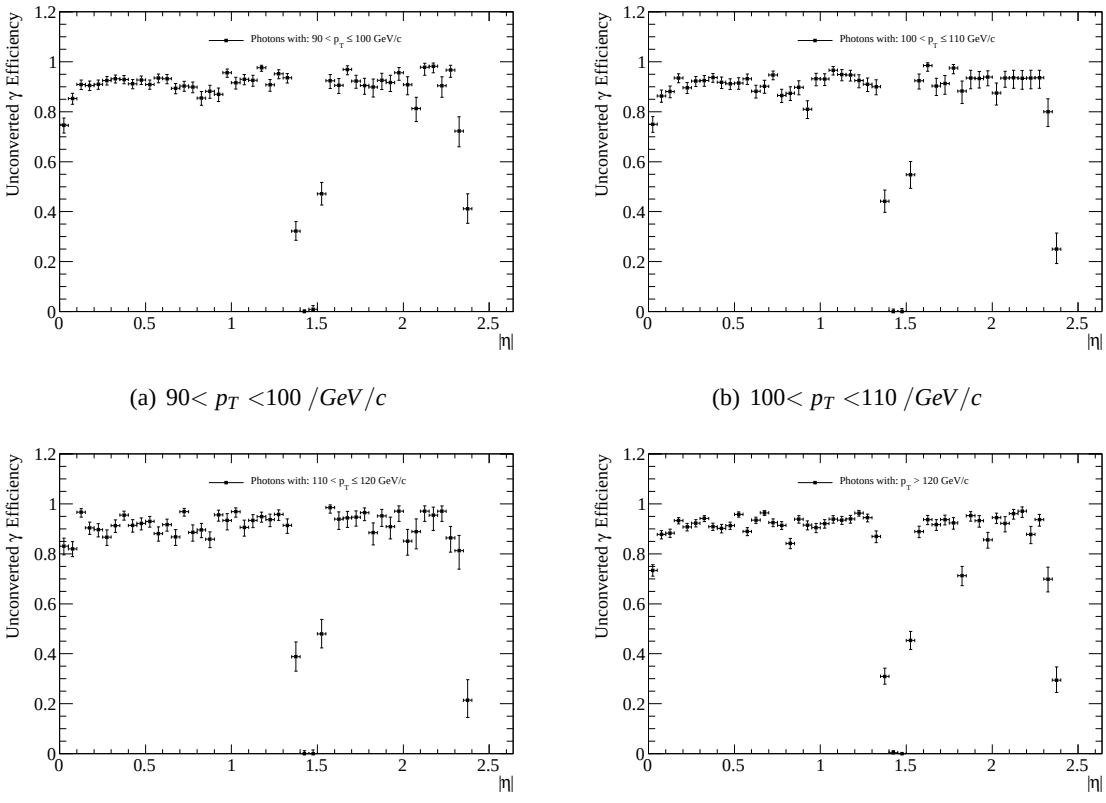

(a) $90 < p_T < 100\ /GeV/c$

(b) $100 < p_T < 110\ /GeV/c$

(c) $110 < p_T < 120\ /GeV/c$

(d) $p_T > 120\ /GeV/c$

Figure A.3: *Full set of unconverted photon reconstruction efficiency parameterisations showing $|\eta|$ distribution for the final 4 p_T ranges.*

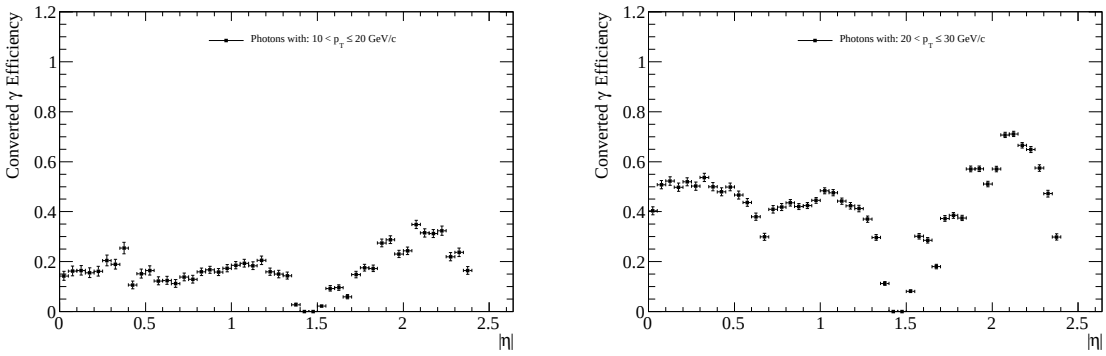

(a) $10 < p_T < 20\ /GeV/c$

(b) $20 < p_T < 30\ /GeV/c$

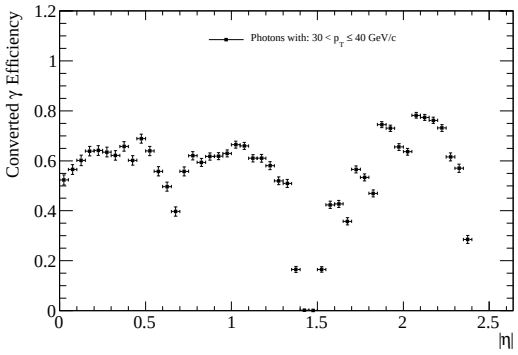

(c) $30 < p_T < 40\ /GeV/c$

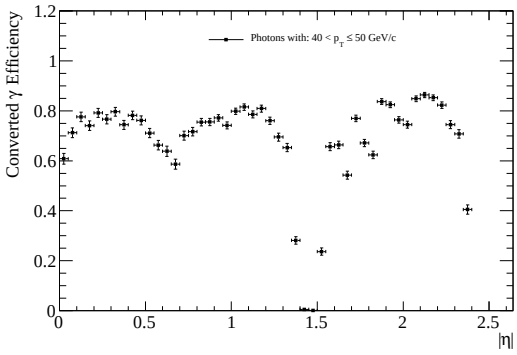

(d) $40 < p_T < 50\ /GeV/c$

Figure A.4: *Full set of converted photon reconstruction efficiency parameterisations showing* $|\eta|$ *distribution for the first 4* p_T *ranges.*

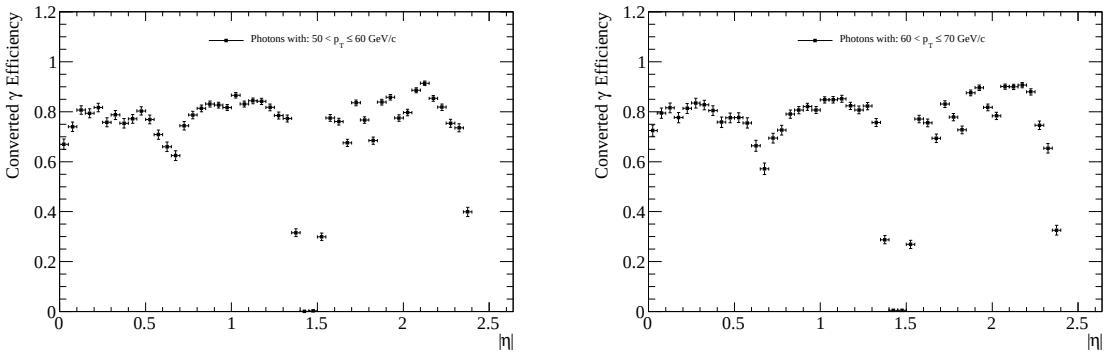

(a) $50 < p_T < 60\ /GeV/c$

(b) $60 < p_T < 70\ /GeV/c$

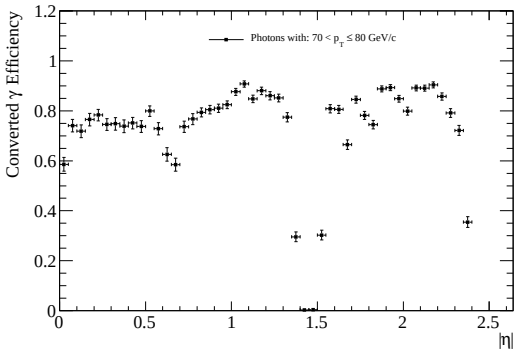

(c) $70 < p_T < 80\ /GeV/c$

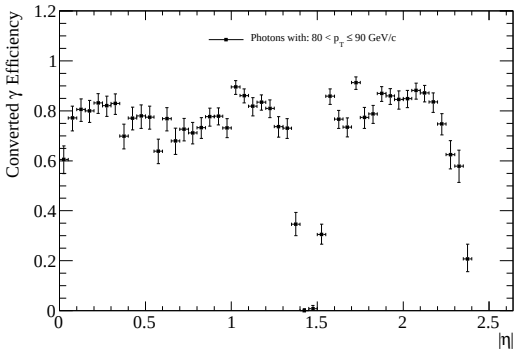

(d) $80 < p_T < 90\ /GeV/c$

Figure A.5: *Full set of converted photon reconstruction efficiency parameterisations showing $|\eta|$ distribution for the second 4 p_T ranges.*

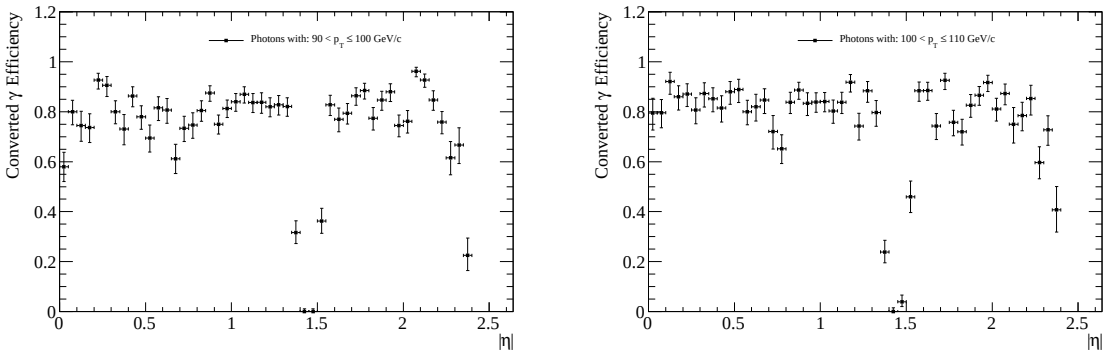

(a) $90 < p_T < 100\ /GeV/c$ (b) $100 < p_T < 110\ /GeV/c$

(c) $110 < p_T < 120\ /GeV/c$ (d) $p_T > 120\ /GeV/c$

Figure A.6: *Full set of converted photon reconstruction efficiency parameterisations showing $|\eta|$ distribution for the final 4 p_T ranges.*

Appendix B

The Search For a Light Fermiophobic Higgs Signal

This appendix contains supplemental information for Chapter 7.

Efficiency Tables For All Signal Mass Points

The table below contains the selection efficiencies, calculated in the generator-level and detector-level analyses, for all (m_h, m_H) mass signal mass points defined in Chapter 7. The efficiencies shown are after all event selection cuts have been applied. Efficiencies at generator-level are contained in the columns titled ε_{gen}, whilst efficiencies at detector-level are contained in the column titled ε_{det}.

Event selection efficiencies for signal											
(m_h, m_H)	ε_{gen}	ε_{det}	(m_h, m_H)	ε_{gen}	ε_{det}	(m_h, m_H)	ε_{gen}	ε_{det}	(m_h, m_H)	ε_{gen}	ε_{det}
(40,80)	6.04	0.03	(70,140)	37.84	4.98	(100,200)	46.15	9.31	(130,260)	51.21	13.37
(40,100)	6.83	0.66	(70,150)	34.69	5.5	(100,220)	45.50	11.05	(130,280)	50.91	14.34
(40,150)	17.62	3.46	(70,160)	34.44	6.28	(100,250)	47.70	13.54	(130,300)	52.27	16.09
(40,200)	26.10	6.18	(70,200)	36.15	8.86	(100,300)	50.54	16.13	(130,350)	55.37	18.92
(40,250)	31.95	6.35	(70,250)	38.73	11.43	(100,350)	52.38	17.87	(130,400)	57.46	20.64
(40,300)	35.12	5.27	(70,300)	42.06	13.47	(100,400)	53.61	19.43	(130,450)	59.02	21.97
(40,350)	35.70	4.88	(70,350)	44.99	14.9	(100,450)	54.84	20.26	(130,500)	60.00	22.89
(40,400)	32.00	4.99	(70,400)	47.29	14.46	(100,500)	55.34	20.41	(130,550)	60.69	23.21
(40,450)	25.58	4.58	(70,450)	49.13	13.32	(100,550)	56.08	20.21	(130,600)	61.18	23.51
(40,500)	21.13	3.97	(70,500)	49.25	12.27	(100,600)	56.26	19.53			
(40,550)	19.03	3.49	(70,550)	49.38	11.57						
(40,600)	18.08	3.24	(70,600)	48.92	11.35						
(50,100)	22.96	0.98	(80,160)	41.78	6.96	(110,220)	47.94	10.76	(140,280)	52.26	14.13
(50,120)	17.21	2.20	(80,180)	39.30	8.17	(110,240)	47.56	12.47	(140,300)	52.16	15.40
(50,150)	20.66	4.02	(80,200)	40.62	9.67	(110,250)	48.75	13.51	(140,350)	55.28	18.58
(50,200)	27.82	7.12	(80,250)	42.94	12.44	(110,300)	51.64	16.56	(140,400)	57.95	20.91
(50,250)	33.93	9.42	(80,300)	44.70	14.52	(110,350)	53.99	18.58	(140,450)	59.37	22.13
(50,300)	38.18	9.29	(80,350)	47.22	16.25	(110,400)	55.74	20.21	(140,500)	60.76	23.04
(50,350)	40.81	8.17	(80,400)	49.08	17.07	(110,450)	57.06	21.17	(140,550)	61.08	23.47
(50,400)	41.91	7.12	(80,450)	50.71	16.71	(110,500)	57.41	21.65	(140,600)	61.90	24.10
(50,450)	41.15	6.84	(80,500)	51.42	15.69	(110,550)	58.02	21.86			
(50,500)	38.33	6.74	(80,550)	51.87	14.71	(110,600)	58.36	21.57			
(50,550)	34.42	6.49	(80,600)	52.09	14.18						
(50,600)	31.83	6.13									
(60,120)	32.19	2.68	(90,180)	43.91	7.95	(120,240)	49.81	12.15			
(60,140)	27.44	4.24	(90,200)	42.99	9.77	(120,250)	48.92	12.97			
(60,150)	27.22	4.71	(90,250)	46.22	13.44	(120,260)	49.57	13.51			
(60,200)	30.76	7.89	(90,300)	48.35	15.29	(120,300)	52.43	16.62			
(60,250)	36.07	10.53	(90,350)	50.02	17.36	(120,350)	55.00	18.87			
(60,300)	40.01	12.20	(90,400)	51.02	18.15	(120,400)	57.16	20.62			
(60,350)	43.36	12.15	(90,450)	52.92	18.92	(120,450)	58.19	21.57			
(60,400)	45.19	10.83	(90,500)	53.80	18.62	(120,500)	58.98	22.43			
(60,450)	46.29	9.67	(90,550)	53.79	17.69	(120,550)	59.36	22.74			
(60,500)	45.90	9.06	(90,600)	54.37	17.09	(120,600)	59.89	22.64			
(60,550)	44.85	8.69									
(60,600)	43.31	8.72									

Table B.1: *Event selection efficiencies, in percent, of the generator-level (ε_{gen}) and detector-level (ε_{AFC}) analyses described in Sections 7.2 and 7.5, respectively, for a signal sample (m_h, m_H) (masses given in GeV/c^2). The efficiencies shown are after all event selection cuts have been applied. Efficiencies at generator-level are contained in the columns titled ε_{gen}, whilst efficiencies at detector-level are contained in the column titled ε_{det}.*

Bibliography

[1] A. L. Read, *Modified frequentist analysis of search results (the CL_s method)*, J. Phys. **G** 25 (CERN-OPEN-2000-205).

[2] T. Junk, *Sensitivity, Exclusion and Discovery with Small Signals, Large Backgrounds, and Large Systematic Uncertainties*, CDF/DOC/STATISTICS/PUBLIC/8128.

[3] A. Einstein, *The Foundation of the General Theory of Relativity*, Annalen der Physik **49**.

[4] F. Halzen, A. D. Martin, *Quarks and Leptons: An Introductory Course in Modern Particle Physics*, John Wiley and Sons, 1984.

[5] D. Griffiths, *Introduction to Elementary Particles, 2^{nd} Edition*, Wiley-VCH, 2009.

[6] Y. Fukada *et al.*, *Evidence for oscillation of atmospheric neutrinos*, PRL **81** (1998) 15621567.

[7] The Super-Kamiokande Collaboration, *Solar neutrino measurements in Super-Kamiokande-II*, PR **D78**.

[8] The SNO Collaboration, *Independent Measurement of the Total Active ^8B Solar Neutrino Flux Using an Array of ^3He Proportional Counters at the Sudbury Neutrino Observatory*, PRL **101**.

[9] H. Weyl, *Gravitation und Elektrizität*, Sitzungsber. Preuss. Akad. Wiss. Berlin (Math. Phys.) (1918) 465.

[10] C. N. Yang, R. L. Mills, *Conservation of Isotopic Spin and Isotopic Gauge Invariance*, Phys. Rev. **96** (1954) 191–195.

[11] S. L. Glashow, *Partial symmetries of weak interactions*, Nucl. Phys. **22** (1961) 579–588.

[12] A. Salam, *Weak and electromagnetic interactions*, Elementary Particle Theory: Relativistic Groups and Analyticity Nobel Symposium No. 8 (1968) p.367.

[13] S. Weinberg, *A model of leptons*, PRL **19** (1967) 1264–1266.

[14] N. Cabibbo, *Unitary Symmetry and Leptonic Decays*, PRL **10** (12) (1963) 531–533.

[15] M. Kobayashi, T. Maskawa, *CP-Violation in the Renormalizable Theory of Weak Interaction*, Progress of Theoretical Physics **49** (2) (1973) 652–657.

[16] P. W. Higgs, *Broken Symmetries and the Masses of Gauge Bosons*, Phys. Rev. Lett. **13** (16) (1964) 508–509.

[17] B. W. Lee, C. Quigg, H. B. Thacker, *Weak interactions at very high energies: The role of the Higgs-boson mass*, *Phys. Rev. D* **16** (5) (1977) 1519–1531.

[18] J. Kuti, L. Lin, Y. Shen, *Upper Bound on the Higgs-Boson Mass in the Standard Model*, PRL **61** (6) (1988) 678–681.

[19] A. Djouadi, P. Gambino, *Leading Electroweak Correction to Higgs Boson Production at Proton Colliders*, PRL **73** (19) (1994) 2528–2531.

[20] A. Djouadi, *The Anatomy of electro-weak symmetry breaking. I: The Higgs boson in the standard model*, arXiv:hep-ph/0503172 457 (2008) 1–216.

[21] T. Hambye, K. Riesselmann, *SM Higgs mass bounds from theory*, arXiv:hep-ph/9708416v1 (1997).

[22] The ALEPH Collaboration, *Observation of an Excess in the Search for the Standard Model Higgs Boson at ALEPH*, Phys. Lett. **B 495** (2000) 1–17.

[23] ALEPH, DELPHI, L3 and OPAL Collaborations, *Search for the Standard Model Higgs Boson at LEP*, Phys. Lett. **B 565** (2003) 61–75.

[24] The Tevatron New Physics, *Combined CDF and D0 Upper Limits on Standard Model Higgs-Boson Production with up to 6.7 fb^{-1} of Data*, arXiv:1007.4587 (2010).

[25] The LEP Electroweak Precision Group, *Precision Electroweak Measurements and Constraints on the Standard Model*, arXiv:0911.2604 (2009).

[26] H. Flacher, M. Goebel, J. Haller, A. Hocker, K. Monig, J. Stelzer, *Revisiting the Global Electroweak Fit of the Standard Model and Beyond with Gfitter*, Eur. Phys. J. **C 60** (2008) 543–583.

[27] The ATLAS Collaboration, *Expected performance of the ATLAS experiment: detector, trigger and physics*, CERN, Geneva, 2009.

[28] A. Arhrib, R. Benbrik, R. B. Guedes, R. Santos, *Search for a light fermiophobic Higgs boson produced via gluon fusion at Hadron Colliders*, arXiv:0805.1603 (2008).

[29] J. F. Gunion, H. E. Haber, *Conditions for CP-Violation in the General Two-Higgs-Doublet Model*, Phys. Rev. **D 72** (095002).

[30] J.F. Gunion, H.E. Haber, G.L. Kane and S. Dawson, *The Higgs Hunter's Guide*, "Addison-Wesley", 1989.

[31] S. Dimopoulos, H. Georgi, *Softly broken supersymmetry and SU(5)*, Nuc. Phys **B 193** (1981) 150 – 162.

[32] P. Fayet, *Supergauge invariant extension of the Higgs mechanism and a model for the electron and its neutrino*, Nuc. Phys. **B 90** (1975) 104 – 124.

[33] A. Barroso, L. Brücher, R. Santos, *Is there a light fermiophobic Higgs?*, Phys. Rev. **D 60** (3) (1999) 35005.

[34] DELPHI Collaboration, *Search for fermiophobic Higgs bosons in final states with photons at LEP 2*, Eur. Phys. J. **C 35** (2003) 313–324.

[35] ALEPH Collaboration, *Search for $\gamma\gamma$ decays of a Higgs boson in e^+e^- collisions at $\sqrt{s}$ up to 209* GeV, Phys. Lett. **B 544** (2002) 16–24.

[36] L3 Collaboration, *Search for a Higgs boson decaying into two photons at LEP*, Phys. Lett. **B 534** (2002) 28–38.

[37] OPAL Collaboration, *Search for associated production of massive states decaying into two photons in e^+e^- annihilations at $\sqrt{s} = 88 - 209$* GeV, Phys. Lett. **B 544** (2002) 44–56.

[38] The LEP Higgs Working Group, *Searches for Higgs Bosons Decaying into Photons: Preliminary Combined Results Using LEP Data Collected at Energies up to 209* GeV, arXiv:hep-ex/0107035 (2001).

[39] D0 Collaboration, *Search for Decay of a Fermiophobic Higgs Boson $h_f \to \gamma\gamma$ with the D0 Detector at $\sqrt{s} = 1.96$ TeV*, Phys. Rev. Lett. **101** (2008) 051801.

[40] CDF Collaboration, *Search for a Fermiophobic Higgs Boson Decaying into Diphotons in $p\bar{p}$ Collisions at $\sqrt{s} = 1.96$ TeV*, Phys. Rev. Lett. **103** (6) (2009) 061803.

[41] O. Deschamps, S. Descotes-Genon, S. Monteil, V. Niess, S. T'Jampens, V. Tisseranda, *The Two Higgs Doublet Model of Type II facing flavour physics data*, arXiv:0907.5135v2 (2010).

[42] O. Stal, *Constraints on the two-Higgs-doublet model*, arXiv:0909.5031 (2009).

[43] A. Denner, R. J. Guth, W. Hollik, J. H. Khn, *The Z-width in the two Higgs doublet model*, Zeit. Phys. **C 51** (1991) 695–705.

[44] A. G Akeroyd and A. Arhrib and E. Naimi, *Note on tree-level unitarity in the general two Higgs doublet model*, Phys. Lett. **B 490** (1-2) (2000) 119–124.

[45] R. Santos, *Private communication*.

[46] O. S. Bruning, P. Collier, P. Lebrun, S. Myers, R. Ostojic, J. Poole, P. Proudlock, *LHC Design Report*, CERN, Geneva, 2004.

[47] L. Evans, P. Bryant, *LHC Machine*, Journal of Instrumentation **3**.

[48] C. Lefevre, *The CERN accelerator complex. Complexe des accelerateurs du CERN*, CDS.

[49] The ATLAS Collaboration, *The ATLAS Experiment at the CERN Large Hadron Collider*, Journal of Instrumentation **3**.

[50] The ATLAS Collaboration, *ATLAS detector and physics performance: Technical Design Report*, CERN, 1999.

[51] C. W. Fabjan, F. Gianotti, *Calorimetry for particle physics*, Rev. Mod. Phys. **75** (4) (2003) 1243–1286.

[52] Comune, G *et al.*, *The Algorithm Steering and Trigger Decision mechanism of the ATLAS High Level Trigger*, hep-ex/0306009 (2003).

[53] ATLAS Computing Group, *ATLAS computing: Technical Design Report*, ATLAS TDR-017 (2005).

[54] The ATLAS Collaboration, *The ATLAS Simulation Infrastructure* arXiv:1005.4568 (2010).

[55] M. L. Mangano, M. Moretti, F. Piccinini, R. Pittau, A. Polosa, *ALPGEN, a generator for hard multiparton processes in hadronic collisions*, JHEP 0307:001 (2003).

[56] J. Alwall, P. Demin, S. de Visscher, R. Frederix, M. Herquet, F. Maltoni, T. Plehn, D. L. Rainwater, T. Stelzer, *MadGraph/MadEvent v4: The New Web Generation*, JHEP 0709:028 (2007).

[57] J. Alwall *et al.*, *A standard format for Les Houches Event Files.*, Comput. Phys. Commun. 176 (**4**) (2006) 300–304.

[58] T. Sjostrand, S. Mrenna, P. Skands, *Pythia 6.4, Physics and Manual*, hep-ph/0603175 (2006).

[59] G. Corcella, I. G. Knowles, G. Marchesini, S. Moretti, K. Odagiri, P. Richardson, M. H. Seymour, B. R. Webber, *HERWIG 6: an event generator for Hadron Emission Reactions With Interfering Gluons (including supersymmetric processes)*, J. High Energy Phys. 1 (2000) 010.

[60] J. M. Butterworth, J. R. Forshaw, M. H. Seymour, *Multiparton Interactions in Photoproduction at HERA*, Zeit. Phys. **C 71**.

[61] M. Dobbs, J. B. Hansen, *The HepMC C++ Monte Carlo Event Record for High Energy Physics*, CERN ATL-SOFT-2000-001.

[62] ATLAS Computing Group, *ATLAS computing: Technical Design Report*, ATLAS TDR-017 (2005).

[63] S. Agostinelli, *et al.*, *GEANT4: A Simulation toolkit*, Phys. Res., **A 506** (3) (2002) 250–303.

[64] A. Rimoldi, *et al.*, *First Report of the Simulation Optimization Group*, CERN ATL-SOFT-PUB-2008-002. ATL-COM-SOFT-2008-004.

[65] E. Barberio, *et al.*, *The GEANT4-Based ATLAS Fast Electromagnetic Shower Simulation*, CERN ATL-SOFT-CONF-2007-002. ATL-COM-SOFT-2007-014.

[66] S. Dean, P. Sherwood, *The ATLAS fast simulation package: ATLFAST-I* `http://www.hep.ucl.ac.uk/atlas/atlfast/`.

[67] E. Richter-Was, D. Froidevaux, L. Poggioli, *ATLFAST 2.0 a fast simulation package for ATLAS*, CERN ATL-PHYS-98-131.

[68] The ATLAS Collaboration, *ATLAS muon spectrometer: Technical Design Report*, CERN ATLAS-TDR-010.

[69] D.Cavalli, *et al.*, *Performance of the ATLAS fast simulation ATLFAST*, CERN ATL-PHYS-INT-2007-005. ATL-COM-PHYS-2007-012.

[70] S. R. Klein, e^+e^- *Pair production from 10* GeV *to 10 ZeV*, Radiat. Phys. Chem **75** (2006) 696.

[71] V. Kostyukhin, *VKalVrt - package for vertex reconstruction in ATLAS*, CERN ATL-PHYS-2003-031.

[72] M. Wielers, *Photon Identification with the ATLAS Detector*, CERN ATL-PHYS-99-016.

[73] M. Escalier, F. Derue, L. Fayard, M. Kado, B. Laforge, C. Reifen, G. Unal, *Photon/jet separation with DC1 data*, CERN ATL-PHYS-PUB-2005-018.

[74] C. Collins-Tooth, S. Ferrag, S. Allwood-Spiers, C. Wright, T. Doyle, *AtlfastC: particle identification efficiencies for ATLFAST-I*, Glasgow University `https://twiki.cern.ch/twiki/bin/view/AtlasProtected/AtlfastC/`.

[75] L. Fayard, G. Unal, *Photon identification in gamma-jet events with Rome layout simulation and background to* $H \rightarrow \gamma\gamma$, CERN ATL-PHYS-PUB-2006-025.

[76] The ATLAS Higgs to $\gamma\gamma$ working group, HiggsAnalysisUtils Package `http://atlas-sw.cern.ch/cgi-bin/viewcvs-atlas.cgi/offline/PhysicsAnalysis/HiggsPhys/HiggsAnalysisUtils/`.

[77] Tsai, Yung-Su , *Pair production and bremsstrahlung of charged leptons*, Rev. Mod. Phys. **46** (4) (1974) 815–851.

[78] P. Golonka, Z. Was, *PHOTOS Monte Carlo: a precision tool for QED corrections in Z and W decays*, Eur. Phys. J. **C 45** (2006) 97.

[79] M. Spira, *HIGLU: A Program for the Calculation of the Total Higgs Production Cross Section at Hadron Colliders via Gluon Fusion including QCD Corrections*, hep-ph/9510347.